

# Sheffield Hallam University

*Brittleness in ferritic Fe-Mn alloys.*

NASIM, Mohammad.

Available from the Sheffield Hallam University Research Archive (SHURA) at:

<http://shura.shu.ac.uk/20109/>

## A Sheffield Hallam University thesis

This thesis is protected by copyright which belongs to the author.

The content must not be changed in any way or sold commercially in any format or medium without the formal permission of the author.

When referring to this work, full bibliographic details including the author, title, awarding institution and date of the thesis must be given.

Please visit <http://shura.shu.ac.uk/20109/> and <http://shura.shu.ac.uk/information.html> for further details about copyright and re-use permissions.

BAR CODE

101 381 285 9.

**Sheffield City Polytechnic  
Eric Mensforth Library**

**REFERENCE ONLY**

This book must not be taken from the Library

PL/26

R5193

2/4 16.59

ProQuest Number: 10697416

All rights reserved

INFORMATION TO ALL USERS

The quality of this reproduction is dependent upon the quality of the copy submitted.

In the unlikely event that the author did not send a complete manuscript and there are missing pages, these will be noted. Also, if material had to be removed, a note will indicate the deletion.



ProQuest 10697416

Published by ProQuest LLC (2017). Copyright of the Dissertation is held by the Author.

All rights reserved.

This work is protected against unauthorized copying under Title 17, United States Code  
Microform Edition © ProQuest LLC.

ProQuest LLC.  
789 East Eisenhower Parkway  
P.O. Box 1346  
Ann Arbor, MI 48106 – 1346

BRITTLENESS IN FERRITIC

Fe-Mn ALLOYS

by

MOHAMMAD NASIM BSc (Met Eng.)

A Thesis submitted to the Council for National Academic  
Awards for the degree of Doctor of Philosophy

Sponsoring Establishment: Department of Metallurgy  
Sheffield City Polytechnic

Collaborating Establishment: Corporate Physical  
Metallurgy Centre  
Swinden Laboratories  
British Steel Corporation

June 1979



79-19278-01

## PREFACE

This thesis is submitted to the Council for National Academic Awards for the degree of Doctor of Philosophy.

The research work was carried out during the period November 1974 to October 1978 at the Department of Metallurgy, Sheffield City Polytechnic. A number of post-graduate courses were attended at the Sheffield City Polytechnic during the above period and included:-

1. High-Strength Steels
2. Electron Microscopy.

The author has attended a conference on "Grain Boundaries" held at Jersey in April 1976 and also attended a conference on "Precipitation in Iron-base Alloys" held in September 1977 at UMIST. A paper from the work entitled, "The nature of Intergranular Embrittlement in Quenched Fe-Mn Alloys" has also been published in Scripta Metallurgica, vol 12, pp 377-380, April 1978. A further paper from the work entitled, "Influence of thermal-cycling treatment on ITT in Fe-Mn Alloys" has also been submitted to the conference on "Phase-Transformations" held at The University of York in April 1979.

The author would like to express his appreciation to the Corporate Physical Metallurgy Centre, Swinden Laboratories, British Steel Corporation for the provision of financial support and supply of the alloys used in the investigation.

Grateful thanks are expressed to Dr E A Wilson for his interest, guidance and constant encouragement throughout the

course of this work. Also, grateful acknowledgement is made to Dr D Dulieu, industrial supervisor, for numerous helpful discussions and to the staff of the Electron Metallography section of the Applied Physics Department for provision of X-ray and Electron Microscopy facilities.

I am also very grateful to Dr B C Edwards, Metallurgy Division, Atomic Energy Research Establishment, Harwell, who carried out Auger Electron Spectroscopic Analysis of some of the alloys. The chemical analysis of alloys was carried out at the Harwell Research Centre and Swinden Laboratories. I extend my thanks to these organisations. Finally, thanks are expressed to the technicians and lecturing staff of the Department of Metallurgy, Sheffield City Polytechnic.

The results obtained and the theories developed are, to the best of my knowledge, original except where reference is made to the work of others. No part of this thesis has been submitted for a degree at any other university or college.

Department of Metallurgy  
Sheffield City Polytechnic

M NASIM  
June 1979

# BRITTLENESS IN FERRITIC Fe-Mn ALLOYS

by

Mohammad Nasim

## Synopsis

The cause of intergranular brittleness in a number of alloys based on Fe-8%Mn has been investigated. The intergranular brittleness in as-water quenched alloys was mainly because of segregation of N to austenite grain boundaries, but some specimens did show the presence of P as well. A de-segregation of carbon in the vicinity of the grain boundaries was also observed which may have also contributed to embrittlement. This embrittlement was further enhanced on air cooling, with segregation of N and Mn to prior-austenite grain boundaries. On ice-brine quenching the alloys, the DBTT was lowered. Intergranular fracture was avoided and the brittle fracture mode changed to cleavage. However, preliminary examination by AES indicated a rise in N content on the cleavage facets.

Aging quenched alloys at 450°C resulted in a rapid rise in DBTT and further embrittlement, with further segregation of Mn, N and at a later time P, to prior austenite grain boundaries. Reverted austenite was not detected until after 60h at 450°C, and the hardness rose <12HV30 on aging. These factors were thought to have little effect on embrittlement.

Analysis of segregation kinetics at 450°C showed that the segregation of Mn and P was consistent with bulk diffusion of Mn and P in  $\alpha$ -Fe, while measurement of the kinetics of embrittlement by tensile ductility tests indicated that diffusion of N in  $\alpha$ -Fe was the main rate controlling factor in isothermal embrittlement.

Above 450°C reverted austenite formed rapidly on aging and was thought to be responsible for de-embrittlement.

A thermal cycling treatment was devised to overcome embrittlement. Such treatment caused improvement in impact toughness through refinement of grain size and introduction of  $\gamma$  and  $\epsilon$  phases into the microstructure. The alloys showed resistance to embrittlement at 450°C and evidence of deformation induced transformation on tensile testing at -78°C.

1.0	<u>INTRODUCTION</u>	1
2.0	<u>LITERATURE REVIEW</u>	2
2.1	Introduction	2
2.1.1	Equilibrium Diagrams	2
2.1.2	Phase Transformations in Fe-Ni and Fe-Mn Alloys	2
	Equi-axed Ferrite	2
	Massive Ferrite	3
	Lath Martensite	3
	Twinned Martensite	4
	Epsilon Martensite	4
	Other Transformation Products	5
2.1.3	Mechanical Properties of Fe-Ni and Fe-Mn Alloys	5
	Nickel Steels	5
	Manganese Steels	9
2.1.4	Comparative aspects in Fe-Ni and Fe-Mn Alloys	11
✓ 2.1.5	Factors affecting toughness in steels	14
	The variation of yield strength of iron with temperature	14
	The Ductile-Brittle Transition in Iron-base alloys	16
	Brittle Fracture by Cleavage	19
	Brittle Fracture by Inter-granular failure	19
	Ductile Fracture through initiation and propagation of ductile cracks	20
2.1.6	Intergranular Brittleness in Fe-Mn alloys	22
2.2	Grain Boundary Embrittlement in Iron-base alloys	26
2.2.1	Grain boundary segregation	26
2.2.2	Influence of oxygen, carbon and sulphur on Intergranular brittleness in Iron and its alloys	32
2.2.3	Influence of Nitrogen and Phosphorus on grain boundary embrittlement of Iron-base alloys	36
2.2.4	Inter-relation of Grain Boundary Embrittlement in Fe-N, Fe-P, Fe-P-C alloys with Temper Brittleness and '350°C Embrittlement'	41
2.2.5	Segregation Predictions in Ternary Systems	44
2.2.6	Grain Boundary Embrittlement due to precipitation	47
	Embrittlement due to precipitation of AlN	47
	Embrittlement due to precipitation of Ti (C,N)	49

2.3	Temper Brittleness in Iron-base alloys	50
2.3.1	History of the Problem	50
2.3.2	Characteristics of Temper Brittleness	57
2.3.3	Measurement of susceptibility to Temper Brittleness	60
	Mechanical Methods	60
	Metallographic Methods	62
	Auger Electron Emission Analysis	62
2.3.4	Theories of Temper Embrittlement	63
2.4	Methods of Improving Low-temperature toughness in steels	68
2.4.1	Grain Refinement	68
2.4.2	Effect of heat-treatment in the ( $\alpha + \gamma$ ) phase region	69
2.4.3	Effect of thermal-cycling treatment in the $\gamma$ and ( $\alpha + \gamma$ ) phase region	72
3.0	<u>EXPERIMENTAL PROCEDURE</u>	
3.1	Alloys Preparation	75
3.2	Heat Treatment	76
3.3	Optical Metallographic Examination	76
3.4	Hardness Measurements	78
3.5	Tensile Testing	78
3.6	Impact Toughness Testing	79
3.7	Dilatometric Analysis	79
3.8	X-ray Diffraction Analysis	80
3.9	Electron Microscopy	84
3.10	Scanning Electron Microscopy	85
3.11	Auger Electron Emission Analysis	86
4.0	<u>EXPERIMENTAL RESULTS</u>	
4.1	Embrittlement Studies	88
4.1.1	Heat-treated alloys and Microstructure	88
	Dilatometric Analysis	88
	Metallographic and X-ray Examination	88
	Effect of Ti and Al additions	89
4.1.2	Impact Toughness Results and Fractography	90
	Impact Toughness Data	90
	Hardness Data	91
	Influence of Ti and Al additions on Impact toughness	92
	Fracture Surfaces Examination	93
	Auger Electron Emission Analysis	94
4.1.3	Effect of aging at 450°C	97
	Hardness Data	97
	X-ray Diffraction Analysis	98
	Metallographic Examination	100
	Impact Toughness Data	100
	Tensile Data	101
	Fracture Surfaces Examination	102
	Auger Electron Emission Analysis	103

4.1.4	Phase Transformations in the upper critical temperature range (450-650°C)	106
	X-ray Diffraction Analysis	106
4.1.5	Kinetics of Embrittlement	107
	Arrhenius Plot Determination	108
4.2	Effect of Thermal-Cycling Treatment	110
4.2.1	Thermal-cycling treatment in Fe-Mn alloys	110
	Heat-treatment cycle	110
	Metallographic Examination	111
	X-ray Diffraction Analysis	111
	Cryogenic Impact Properties	112
	Cryogenic Tensile Properties	112
	Electron Microscopy	114
	Fracture Surfaces Examination	115
4.2.2	Thermal-cycling treatment in Fe-Mn alloys with Ti and Al additions	116
	Impact Data	116
	Hardness Data	116
	X-ray Diffraction Analysis	117
	Metallographic Examination	118
	Fracture Surfaces Examination	118
4.2.3	Effect of aging at 450°C on thermally-cycled alloy	119
	Tensile Data	120
	Hardness Data	120
	X-ray Diffraction Analysis	121
4.2.4	Effect of aging at 450°C on thermally-cycled alloy with Ti and Al additions	122
	Impact Data	122
	Hardness Data	122
	X-ray Diffraction Analysis	122
5.0	<u>DISCUSSION</u>	124
5.1	Embrittlement Mechanisms in Fe-Mn Alloys	124
5.1.1	Intergranular embrittlement in quenched alloys	124
	Water-quenched alloys	124
	Ice-brine quenched alloys	126
5.1.2	Intergranular embrittlement in air-cooled alloys	128
5.1.3	Embrittlement on aging at 450°C	131
	Hardness of alloys	131
	Reverted austenite	133
	Degree of embrittlement on aging	133
	Brittle fracture mode	
	AES results	134
	General discussion of embrittlement on aging at 450°C	136

5.1.4	Phase transformations on aging between 450-650°C	139
5.1.5	Kinetics of embrittlement	140
5.2	Thermal-Cycling Treatment of Fe-Mn alloys	145
5.2.1	Influence of thermal-cycling treatment on cryogenic mechanical properties of alloy K1525 (without Ti and Al additions)	145
	Cryogenic impact properties	145
	Cryogenic tensile properties	149
5.2.2	Influence of Thermal-cycling treatment on Cryogenic mechanical properties of alloy 137 with Ti and Al additions	151
5.2.3	Effect of aging at 450°C on cryogenic mechanical properties in thermally- cycled alloy with and without Ti and Al additions	153
	Alloy K1525	153
	Alloy 137	154
6.0	<u>CONCLUSIONS</u>	156
7.0	<u>RECOMMENDATIONS FOR FURTHER WORK</u>	161
	Further work of general relevance	163
	<u>REFERENCES</u>	164

TABLES I to XXII

Most of the recently developed high-strength and cryogenic steels are expensive since they contain nickel as a major alloying element. Manganese is a cheaper alternative to nickel and produces similar effects upon the austenite to ferrite transformations (1,2) which could allow cheaper alternatives to nickel steels.

Whether Fe-Mn alloys can be used as a basis for cryogenic high-strength steels, however, will depend on the mechanical properties that can be achieved. Earlier work in the department (1,3) indicated that although comparable strength levels could be obtained in Fe-Mn alloys to those of Fe-Ni alloys, such alloys were very brittle. This brittleness occurred at the prior-austenite grain boundaries and was thought to be due to temper brittleness. Subsequent work by Freeman (4) and Gabbitas (19) confirmed these findings but no insight was obtained into the nature of the embrittlement mechanism.

The present studies were undertaken to identify the nature of this embrittlement in ferritic iron-manganese alloys and determine methods of improving the low-temperature toughness of these alloys.

## 2.0 LITERATURE REVIEW

### 2.1 Introduction

The aims of the present research have been described in the introduction. This section examines the structure and properties obtainable in Fe-Ni and Fe-Mn alloys with emphasis on the characteristics of the brittleness phenomenon found in Fe-Mn alloys.

#### 2.1.1 Equilibrium Diagrams

Fig 1 and Fig 2 show the equilibrium diagrams for the Fe-Mn and Fe-Ni systems respectively. Both Mn and Ni have similar effects on austenite stability except that the former element depresses the  $(\alpha + \gamma)/\gamma$  phase boundary more severely than the latter. For both alloy systems at lower temperatures the equilibrium phases are a mixture of ferrite and austenite over a wide range of alloy contents. In practice the equilibrium phases are not formed due to the very slow nature of the equilibrium reaction and instead a variety of transformation products are formed. Figures 1(b), 2(b) show the transformation temperatures observed in these alloys.

#### 2.1.2 Phase Transformations in Fe-Ni and Fe-Mn Alloys

Five basic modes of transformation of austenite, which do not involve carbide separation, have been established for iron alloys and are briefly described as follows:

##### Equiaxed Ferrite:

Austenite decomposes to ferrite during cooling by nucleation and growth. The nucleus is thought to be an incoherent grain-boundary allotriomorph (5). Since the trans-

formation occurs by rapid movement of the incoherent boundary, there is no change in composition and growth is unaffected by prior-austenite grain boundaries. No surface tilting is observed on pre-polished surfaces confirming that no shears are involved in the formation of equiaxed ferrite (6). The resulting structure consists of equiaxed ferrite grains of fairly low-dislocation density (7).

#### Massive Ferrite:

This reaction also occurs by rapid movement of an incoherent boundary to give grains of ragged outline and high dislocation density (7). However in this case the nucleus is thought to be a coherent grain-boundary allotriomorph with a semi-coherent boundary along the austenite grain boundary and a semi-spherical incoherent cap (5). Since the nucleus is semi-coherent, strain energy is produced in the nucleus opposing transformation and forcing transformation to occur at a lower temperature than equiaxed ferrite (5).

#### Lath Martensite:

This has also been referred to as "self-accommodating" (8), massive (12) or "slipped" (10) martensite but is usually termed lath martensite (9). It is generally regarded as the product of austenite decomposition to body-centred cubic ferrite via a shear mode of transformation (9). The structure produced is often characteristically described as "Widmanstätten" ferrite but it should not be confused with the Widmanstätten ferrite formed in carbon steels. Lath martensite consists of parallel laths with a high dislocation density (11). In this martensite the "Inhomogeneous shear" is thought to occur by slip (11).

### Twinned Martensite:

This is sometimes incorrectly referred to as acicular martensite (12). The martensite appears as lenticular plates in optical micrographs, whose internal structure is cross-hatched by transformation twins (13). In Fe-Ni alloys the crystal structure is body-centred cubic but is body-centred tetragonal in carbon steels. The inhomogeneous shear in this case is supplied by the internal twins.

### Epsilon Martensite:

This occurs chiefly in steels whose austenite has a low stacking fault energy (eg 18 Cr 8 Ni stainless steels (14) and Fe-Mn in the composition range 10% to 30% Mn) and is generally believed to represent an intermediate stage in the decomposition of austenite to ferrite. Its structure is hexagonal close-packed and it forms in parallel sided bands bounded by the  $\{111\}$  austenite planes (14).

Breedis and Kaufmann (15) suggest that epsilon martensite is only found in those alloy systems where solute additions decrease the stacking fault energy of austenite to very low values approaching zero. At these very low stacking fault energies, the energy necessary for the  $\gamma \rightarrow \epsilon$  transformation is reduced below that of the  $\gamma \rightarrow \alpha$  transformation and thus a metastable  $\epsilon$  phase is formed. There are a variety of means, eg Cold-working (16,17), tempering (18) or sub-zero treatment by which epsilon can be made to transform to a body-centred cubic ferrite whose structure closely resembles that of lath martensite (19).

## Other Transformation Products

Other products of austenite decomposition such as pearlite or bainite usually involve carbide separation, and so have not been included in the above list. However, the inclusion of a bainitic mode of transformation may be justified, since there are reports (20,21) of an isothermal shear transformation in binary iron alloys containing virtually no carbon. From a structural aspect this isothermal transformation product resembles lath martensite.

### 2.1.3 Mechanical Properties of Fe-Ni and Fe-Mn Alloys

#### Nickel Steels

In the last decades, there has been a considerable development in the production and uses of liquified gases in petrochemical and missiles industries, which inevitably caused a growing need for a suitable material for easy storage and handling of these products in these industries. This led to the development of 9%Ni steel which actually is the only engineering material available covering the needs between 3.5%Ni and austenitic stainless steels. The following table taken from the work of Hardwick (22) indicates the usage of nickel steels for different applications depending on the boiling points of these respective gases.

-45.5°C	Ammonia -33.4°C Propane -42.1°C	Carbon Steel
-59.0°C	Propylene -47.7°C Carbonyl Sulphide -50.2°C	2.25% Ni Steel
-101°C	Hydrogen Sulphide -59.5°C Carbon dioxide -78.5°C Acetylene -84.0°C Ethane -88.8°C	3.5% Ni Steel
-195°C	Ethylene -103.8°C Methane -161.5°C Oxygen -182.9°C Argon -185.9°C Fluorine -188.1°C	9% Ni Steel
	Nitrogen -195.8°C Neon -246.1°C Deuterium -249.8°C Hydrogen -252.6°C Helium -268.9°C	Austenitic Stainless Steel

Steels for low temperatures; used under conditions defined by the normal boiling points of liquefied gases (22)

In all these applications at low-temperature the impact strength is considered most important, in addition to other properties such as strength, fabricability, weldability, availability and cost.

A typical composition of 9%Ni steel is 0.08C, 0.25Si, 0.75Mn, 9.0Ni and the heat treatment originally designed for this steel was a double normalize from 900°C and 790°C followed by a temper at 570°C and air cool to room temperature. But recently this heat treatment has been modified to a single quench in oil or water from 900°C followed by a conventional temper at around 570°C. The mechanical properties obtained after this heat treatment in small section bar and plate are as follows (22):-

0.2%PS N/mm <sup>2</sup>	UTS N/mm <sup>2</sup>	Elongation %	R of A %	Charpy V-notch (J)	
				RT	-196
618	722	30	70	163	61

In this tempered condition the structure consists of an austenite/ferrite mixture with austenite having been nucleated at carbides previously precipitated at the lath boundaries. This austenite has a high alloy content and thus it is stable down to temperatures below  $-196^{\circ}\text{C}$  (23). The tempering temperature and time of tempering are regarded as the important controlling factor for this impact energy value at  $-196^{\circ}\text{C}$ .

In figure 3, the variation in Charpy impact energy at RT and at  $-196^{\circ}\text{C}$  is plotted as a function of tempering temperature. It is shown that 9%Ni steel exhibit good impact energy value when tempered between  $500-600^{\circ}\text{C}$ . From the studies of the effect of cooling rate after the tempering treatment and the examination of microfractographs (23) it was concluded that the drop in the impact energy below  $500^{\circ}\text{C}$  was due to the phenomenon of temper embrittlement. The drop in the impact energy when tempered at  $600^{\circ}\text{C}$  is thought to be due to the instability of reverted austenite islands which form at the tempering temperature and undergo transformation to martensite on cooling to room temperature, resulting in untempered martensite.

Brophy and Miller (24) in 1949 were the first to explain that the improvement in low-temperature toughness of 9%Ni steel after being tempered at  $570^{\circ}\text{C}$  was mainly due to formation of stable austenite islands. Marschall et al (25) extended

their work and confirmed the beneficial effect of stable austenite islands.

During the development of this explanation of the role of austenite islands, Kron et al (26) gave another reason that improvement in low-temperature toughness in 9%Ni steel was mainly through excellent low-temperature properties of high nickel ferrite. According to them, the drop in impact energy at high temperatures was mainly through the formation of un-tempered martensite after being cooled to room temperature. They suggested that appearance of austenite phase was mainly accidental (26).

However, the recent work of Naghashima et al (23) has confirmed that the improvement in low-temperature toughness of 9%Ni steel is predominantly affected by the formation of reverted austenite islands. They actually studied the effect of tempering temperature on the mechanical properties and amount of reverted austenite formation and its stability at room temperature and at  $-196^{\circ}\text{C}$ . Naghashima et al (23) reported that the peak in impact energy did not coincide with the peak in amount of reverted austenite formation as shown in figure (4a, 4b). This observation made it clear that the reverted austenite appearance was not the only contributory factor in this improvement of low-temperature toughness in 9%Ni steels.

The mechanisms of the improvement of low-temperature toughness in 9%Ni steels and the recently developed 6%Ni steels by heat treatment in the  $(\alpha + \gamma)$  phase region will be discussed in detail in sections 2.4.2 and 2.4.3. It is thought that in addition to the crack-blunting effect of austenite islands, the improvement in low-temperature toughness is also through

grain-refinement (27) and possibly removal of the embrittling effect of the small quantities of manganese and other solutes found in these alloys (28) by dissolution in austenite.

### Manganese Steels

Manganese is used extensively in low-alloy steels due to its effect in increasing hardenability and retarding softening on tempering. However, apart from Hadfield's manganese steel which has been known for a number of years, manganese has found very little use in high alloy materials.

Recently Bolton (1) and Freeman (4) examined the phase-transformations and mechanical properties of Fe-Mn alloys following the studies of the mechanical properties and structure of the Fe-Mn systems reported by Schumann (29). The interest has been stimulated mainly by economic and strategic considerations with reference to the use of Mn as a substitute for nickel, especially in high-alloy steels. The use of Fe-Mn alloys as a base for cryogenic and high-strength steels depends on the mechanical properties that can be achieved. Both of these studies indicated that high-strength levels could be attained in Fe-Mn alloys but at the same time these alloys were found exceedingly brittle.

The mechanical properties of Fe-Mn alloys in the composition range 0-20%Mn were first studied by Walter et al (30). It was found that in the normalized condition, a peak in strength of about 770 N/mm<sup>2</sup> was attained at approx 10%Mn but these alloys showed very low toughness. Tempering at 540°C produced a slight decline in strength but toughness was slightly improved.

Examination of the tensile and impact properties of Fe-Mn alloys containing up to 5%Mn(31) showed that the martensitic alloys were extremely brittle with the occurrence of intergranular fractures. As a result of more recent work on the mechanical properties of ferritic Fe-Mn alloys and their relationship to microstructures, it has been suggested (3,4) that the most likely cause of brittleness was a classical temper brittleness effect. This intergranular brittleness in ferritic iron-manganese alloys is discussed more fully in section 2.1.6.

Holden et al (2) found that when the Mn content exceeded 10% in Fe-Mn alloys, a mixture of ( $\alpha + \epsilon$ ) phases were obtained and beyond 15%Mn a mixture of ( $\alpha + \epsilon + \gamma$ ) phases resulted. Also within these compositions austenite was found to be stable even at liquid nitrogen temperatures. Such alloys had excellent impact toughness with an impact transition temperature below  $-80^{\circ}\text{C}$ . Recently Zackay et al (32) attempted to examine the cryogenic properties of this mixture of microstructures, ( $\alpha + \epsilon + \gamma$ ), by varying Mn content (Fig. 6-10). They found that increasing Mn content in  $\alpha$ -solid solution was detrimental to low-temperature toughness (Fig.7). At Mn > 12pct appreciable amounts of  $\epsilon$  and  $\gamma$  phases were formed which consequently lowered the Ductile-brittle transition temperature, (DBTT), rapidly. This work also showed that the drop in DBTT was at the rate of  $1.3^{\circ}\text{C}/\text{vol pct } (\epsilon + \gamma)$  Fig.8. However figure 9, shows that this increase in impact toughness was obtained at the expense of a decrease in yield strength. This decrease in yield strength with increasing amounts of  $\epsilon$  was thought (32) to be due to localised flow in the weaker  $\epsilon$  phase and stress induced transformation of  $\epsilon$  to  $\alpha$ .

## 2.1.4 Comparative aspects in Fe-Ni and Fe-Mn alloys

In the recent studies (1,4) on Fe-Mn alloys, it has been indicated that the approximate phase-composition limits and mode of transformation in the normalized condition are as follows:

Composition Limits	Structure	Mode of Transformation
0-3% Mn	Equiaxed Ferrite	Diffusion dominated
3-4% Mn	Mixture of Bainite and Martensite (1) Intermediate type of structure (4)	
4-10% Mn	Lath Martensite	Shear dominated

Similarly the phase composition limits and mode of transformation in Fe-Ni alloys has been reported to be (4):

Composition Limits	Structure	Mode of Transformation
0-6% Ni	Equiaxed Ferrite	Diffusion dominated
6-9% Ni	Intermediate type of structure	
9-25% Ni	Lath martensite	Shear dominated

These limits have been found to vary with the carbon content and cooling rate. However, it is interesting to note that the composition limits for Fe-Ni system are about twice those observed in Fe-Mn system.

The lath-martensite structure found in Fe-Mn (4-10% Mn) and Fe-Ni (9-25% Ni) systems is independent of cooling rate and is a shear dominated product. It has been found to be structurally identical in the same heat-treated condition eg similar lath sizes and austenite grain size/packet size ratios (4). Thus

similar morphologies are produced in both systems, except that in Fe-Ni systems, the structures are produced at higher alloy content than for the same structure in the Fe-Mn system.

Both manganese and nickel have been found to depress the  $\gamma \rightarrow \alpha$  transformation temperatures, with manganese showing greater effect than nickel. The transformation diagrams for Fe-Mn and Fe-Ni system are shown in (Figure 1, 2). In fig. I(b), fig. 5 it is shown that when manganese concentration exceeds 10 pct, the transformation products at room temperature consist of  $\alpha$ -lath martensite (formed via epsilon martensite) austenite and epsilon martensite. In the Fe-Mn system, this intermediate martensitic transformation resulting in hcp epsilon martensite is thought to be mainly because of the low stacking fault energy of the austenite. In the Fe-Ni system, the austenite is of high stacking fault energy, so the epsilon intermediate transformation product does not form and in this case  $\gamma \rightarrow \alpha$  transformation occurs. Retained austenite is observed at 25%Ni and the martensite morphology changes from lath to plate (twinned) martensite.

The microstructural studies on Fe-Mn and Fe-Ni systems have thus shown that they exhibit similar structures over the composition ranges 0-10% for Fe-Mn and 0-25% Fe-Ni alloys.

It is reported that the same strength level in the normalized condition can be expected in (8-10% Ni) and (4-6% Mn) alloys having lath-martensitic structure (1). Therefore as far as strength level and solid-solution strengthening is concerned both systems are virtually identical and on this basis, it is thought that Mn can be substituted for nickel and both these alloys should have similar mechanical properties.

However, the major difference between the two systems was found when the low-temperature toughness properties were examined. It has been reported that Fe-Mn lath-martensite alloys are very brittle having ductile-brittle transition temperature above the ambient temperature (3,4,32); whereas Fe-Ni martensitic alloys are much tougher having ductile-brittle transition temperature well below the room temperature. This is illustrated in figures 6,7. Moreover, a considerable improvement in impact energy and other mechanical properties was achieved on tempering Fe-Ni alloys (22,23). The beneficial effect of nickel in lowering the ductile-brittle transition temperature (DBTT) of iron-carbon alloys was studied by Brophy and Miller (24) in 1949. Later studies indicated that nickel also lowers the DBTT of carbon-free iron. Although the mechanism for this improvement in notch toughness is not yet clear, it seems possibly that nickel raises the cleavage strength of iron and influences the ease of dislocation movement in the crystal lattice rather than an effect on microstructure (33). Manganese is often thought to improve the low-temperature ductility of Fe but apparently behaves in a different way than nickel. Jolley (34) reported that manganese improved the notch impact properties of Fe only in the presence of carbon and suggested that the effect of Mn was through changes in morphology and distribution of carbides. Roberts (7) studied up to 9 pct Mn alloys using high-purity alloys which had been subjected to wet hydrogen treatment to reduce carbon and nitrogen to low levels. He only observed cleavage fracture below the DBTT on impact testing his alloys, although it should be noted that Roberts only used normalised or quenched specimen for determining DBTT.

The effect of tempering on DBTT and fracture appearance was not studied. Roberts results showed that impact toughness and DBTT were insensitive to the manganese content but were affected by the transformation substructure and grain size, Figure 11. The grain size dependence reported by Roberts also agrees with that reported by Leslie (35) and Sasaki (36) for Fe-Ni alloys.

#### 2.1.5 Factors affecting toughness in steels

In this section the basic mechanisms governing toughness in steels will be discussed before more detailed discussion of embrittlement in particular alloy systems.

#### The variation of yield strength of iron with temperature

One of the most striking differences between the bcc and the fcc metals is the manner in which their resistance to deformation is affected by a decrease in temperature below room temperature. In general, the bcc metals exhibit a sharp rise in yield stress or critical resolved shear stress for slip, whereas the fcc metals do not. The low-temperature brittleness of many of the bcc metals is generally attributed to this change in resistance to plastic deformation. Since crack nucleation becomes more probable and crack propagation becomes easier as the resistance to plastic flow is increased. In figure 12(a), the results of a number of investigations on slightly impure iron where the difference  $\sigma_T - \sigma_{300^{\circ}\text{K}}$  is plotted as a function of temperature. Here  $\sigma_{300^{\circ}\text{K}}$  is the yield point at room temperature and  $\sigma_T$  is the yield point at the lower temperature. It is shown that, despite a range of carbon contents and grain sizes, the general trend is almost the same for all sets of data. Until

recently (41) the rise in the resistance to deformation was attributed to the pinning of dislocations by interstitial impurities; and it was anticipated that if sufficiently pure iron was made, then perhaps both the steep rise in the yield strength and brittleness at low temperatures could be avoided. The contribution of interstitial impurity pinning to these effects has been the subject of controversy by Helsop and Petch (42) and Stein and Low (43). Both authors concluded that the friction stress rather than the pinning stress rises as the temperature was decreased, but they admitted that the impurities also strongly influenced the low-temperature behaviour.

While comparing the behaviour of single crystal and polycrystalline iron, it was found that at low temperature the polycrystalline curve lies above the single crystal curve. This suggested that in addition to an increase in friction stress at low temperature (single crystal curve) there is an increase in the grain boundary interference with slip as well (41).

It is found that at about  $77^{\circ}\text{K}$  and below, the initial yielding appears to occur by twinning rather than by slip (44, 45) and the course of the yield stress-temperature curve is changed to a lower slope. The data reported by London et al (46) on the variation of yield strength with temperature of zone-refined iron also showed that even the yield strength values are not greatly different from an impure iron shown in fig.12(a). This observation also contradicted the suggestion of Conrad (41) who suggested that the steep rise in yield stress at low temperatures was due to interstitials. Later on, Low (43) experimented by removing C and N to the lowest

possible levels from an impure low-carbon steel by wet hydrogen treatment. He decarburized for 16 hours in wet hydrogen at 700°C, the carbon was reduced to (0.006-0.0016%) and the nitrogen to 0.0005% with other elements not affected by decarburization. This treatment even eliminated the yield point and strain aging but it did not greatly affect the rise in the yield strength at low temperature.

Figure 12(b) taken from Stein's work (47) shows that the yield stress of iron is still strongly temperature dependent when the interstitial content is extremely low.

On the basis of all this evidence it seems likely that the steep rise in yield stress of iron at low temperatures is characteristic of the b.c.c. crystal structure rather than due to the presence of small amounts of interstitials, however this conclusion is still one of controversy.

### The Ductile-Brittle Transition in Iron-base Alloys

If the deformation of iron or a ferritic iron alloy is studied at successively lower temperatures, a temperature is eventually reached when the material breaks in a brittle manner rather than ductile behaviour.

Deformation can be carried out by a variety of methods, such as tensile testing or impact testing, but the temperature at which the transition occurs depends upon the method of testing as well as microstructural effects such as grain size. In general high strain rates and/or the presence of notches raises the DBTT while small grain sizes lower the DBTT. The energy required for brittle fracture is very low and considerably

less than that required for ductile deformation.

By experimenting with mild steel and different grain sizes under compression and tension. Low (48) showed that brittle fracture occurred when the fracture stress coincided with the yield stress.

Thus the low-temperature brittleness of iron is due to the steep rise in yield stress which occurs as the temperature is lowered until it eventually exceeds the fracture stress. In f.c.c. materials the temperature dependence of the yield stress is so low that the fracture stress is never exceeded. The effect of notches on increasing the DBTT can also be explained on the basis of the coincidence of the yield and fracture stresses. The effect of the notch is to locally raise the stress in the vicinity of the root of the notch thus exceeding the fracture stress and resulting in premature failure.

In the case of glass, Griffith (49,50) showed that the presence of small cracks was responsible for brittle behaviour. The cracks locally raised the stress acting on the material. Griffith showed the brittle fracture occurred when

$$\sigma > \sqrt{\frac{2E\gamma}{\pi c}} \quad 2.1.(1)$$

where  $\sigma$  = stress applied to material

$E$  = Youngs Modulus

$c$  = one half the crack length

$\gamma$  = Energy required to create unit area of new surface by crack growth.

If crack sizes for brittle failure in iron are calculated, it is found that these are  $\sim 0.3 \mu\text{m}$  ( $3,000 \overset{\circ}{\text{A}}$ ). Atomic sharp cracks of this size are not always present in iron and it is

concluded that a small amount of plastic deformation occurs before brittle failure to create cracks. Plastic deformation also occurs during crack propagation. The Griffith relationship can then be modified to allow for this as follows (58)

$$\sigma > \sqrt{\frac{2E\gamma\rho}{\pi ca}} \quad 2.1.(2)$$

where  $\rho$  = radius of curvature of crack root

$a$  = Interatomic spacing across fracture plane

A variety of dislocation mechanisms have been suggested to produce cracks including twin intersections (45). However Cottrell (40) and Petch (52) have both concluded that crack propagation rather than crack nucleation is the most important and difficult step in brittle fracture, otherwise the known effect of grain size, state of stress and temperature cannot be accounted for. On this basis grain boundaries act as barriers to crack propagation and thus finer grain sizes lead to a lowering of the DBTT (40,52). Petch (52) showed both experimentally and theoretically that in the case of mild steel the DBTT,  $T_c^0$  varied linearly with  $\ln d^{-\frac{1}{2}}$ , where  $d$  is half the grain size diameter, figure 13.

In conclusion the rise in yield stress of iron at low temperatures is the basic cause of low-temperature brittleness. An increase in the yield stress has two effects; first the microcracks which are nucleated by slip or twinning are more likely to propagate and secondly the cracks are less likely to be blunted at their tip since plastic deformation at the crack tip will be reduced by decrease in temperature.

## Brittle Fracture by Cleavage

In ferrite brittle cleavage occurs on {001} planes (53). This plane also satisfies the criterion of possessing the direction of minimum surface energy (54). It is also the cleavage plane in Cottrell's mechanism for crack nucleation (40).

When the ferrite microstructure takes the form of an acicular structure such as bainite or lath martensite, H Ohtani et al (55) have shown that the cleavage facet size corresponds to the packet size. Moreover they obtained a linear relationship between the DBTT and  $\log d_c^{-\frac{1}{2}}$ , where  $d_c$  is the cleavage facet size.

Similarly as remarked earlier, Roberts (7) reported a linear relationship between DBTT and  $\log d$  in lath martensite figure 11. All these results are in agreement with Petch's theoretical equation for the effect of grain size on DBTT (52).

## Brittle Fracture by Inter-granular failure

If segregation occurs at grain boundaries, then generally brittle fracture occurs along these boundaries rather than by trans-granular cleavage. This is because the surface energy term  $\gamma$  in the modified Griffith equation is reduced. For cleavage fracture,  $\gamma$  is equal to  $2\gamma_s$ , where  $\gamma_s$  is the energy per unit area of the cleavage surface. For intergranular fracture

$$\gamma = (2\gamma_s - \gamma_b) \quad 2.1.(3)$$

where  $\gamma_b$  is the grain boundary energy per unit area since the energy of the two new surfaces is partly reduced by the energy of the grain boundary along which fracture is taking place.

When an impurity segregates to the boundary, due to Gibb's adsorption, it reduces  $\gamma_b$ , thus contributing to an increase in  $\gamma$ . Since most grain boundary active impurities are surface active they also decrease  $\gamma_s$ . The degree of this influence determines the embrittling influence of an impurity. But, in general, extremely large reductions in  $(2\gamma_s - \gamma_b)$  have been reported (56) especially in Cu-Bi system where Bi has been found to be an effective embrittler of Cu. Another good example of embrittlement due to segregation is that due to small concentrations of P in iron (57).

Intergranular fracture may also occur due to the presence of a brittle phase at grain boundaries. An example is the precipitation of AlN at grain boundaries in certain steels under certain heat treatment conditions (58). This particular example is discussed in further detail in section 2.2.6.

### Ductile Fracture through initiation and propagation of ductile cracks

Ductile failure by deformation implies a fracture process which takes place after substantial deformation but sometimes brittle fracture can also be preceded by a marked degree of plastic deformation commonly known as delayed cleavage fracture. Ductile fracture is generally exhibited by a necking during tensile testing when a cup-and-cone fracture eventually occurs. The main difference between ductile and brittle fracture, which is of profound practical significance, is that the propagation of a ductile crack involves substantial plastic flow, whereas in a brittle crack the fracture proceeds with a minimum of further

plastic deformation. With cleavage the fracture energy is needed mainly to overcome the cohesive forces between atoms on each side of the crack path, whereas in ductile fracture this contribution is greatly outweighed by that needed for plastic deformation associated with the crack process. Tipper (59) reported that in the early stages of necking only the effects of deformation by slip could be seen but at a later stage small pores were found which gradually multiplied and eventually nucleated a crack by joining together. Ludwik (60) observed that the pores mainly originated at small inclusions on particles of a second phase. Puttick (61) as a result of a study of the nucleation of pores in iron and copper, has concluded that the pores are created by the metal flowing away from the interfaces of small inclusions not wetted by the matrix.

The link between inclusions and the initiation of ductile fracture is thus now well established and explains very adequately the increase in reduction in area as the purity of a metal is raised. Ideally, a pure metal free of inclusions should thus exhibit 100 pct reduction in area in the necked zone, but there is some evidence to support the view that ductile cracks can initiate also in the absence of inclusions (62). In these circumstances, crack nuclei would be expected to form by dislocation coalescence as in the nucleation of brittle cracks, but the subsequent propagation would be different. The propagation of the ductile crack occurs by the joining up of pores and the resulting coalescence has been called a process of internal necking which is a description of the breaking of bridges between adjacent cavities elongated in the tensile direction.

### 2.1.6 Intergranular Brittleness in Fe-Mn alloys

The mechanical properties of iron-manganese alloys have been a matter of considerable interest ever since Walter et al (30) showed that a strength of approx 770 N/mm<sup>2</sup> could be obtained but with low toughness in Fe-10.0% Mn alloys. He also showed that on tempering an improvement in toughness could be expected with a decline in strength. Rees and Hopkin (31) experienced brittleness in Fe-5.0% Mn martensite alloys on examination of tensile and impact properties. As their Fe-Ni alloys exhibited similar characteristics of brittleness with intergranular fractures, they concluded that some kind of grain boundary weakening through impurity segregation was responsible for the brittleness in their Fe-Mn and Fe-Ni alloys. Nicohenko (37) observed brittleness in Fe-8.0% Mn on cold working but it was suggested that possibly this brittleness was due to transformations of retained epsilon martensite to  $\alpha$ -martensite. Boniszewski (38) reported extreme brittleness in Fe-7.0% Mn compared with its counterpart Fe-9.0% Ni but he suggested simply that in Fe-Mn alloys twinned martensite formation was responsible for this brittleness whereas in Fe-9.0% Ni steel, lath martensite transformation was taking place. The presence of twinned martensite was also thought to be responsible for this brittleness in Fe-Mn alloys by F G Wilson (39), while studying the replacement of nickel by manganese in maraging steel at Swinden Laboratories. However recent studies (1) have not been able to show any evidence of twinned martensite in these Fe-Mn alloys. Bolton et al (3) found that the low-carbon Fe-Mn alloys (4-10% Mn) in the lath-martensite condition were brittle in the as-quenched condition due to a weakness at prior-austenite grain boundaries which became even more marked when the alloys

were tempered between 250-400°C. It was suggested that the segregation of the harmful impurities might have occurred during austenitization and led to a potential weakening of grain boundaries in the subsequently quenched martensitic alloys. When the alloys were tempered within the range 250°C to 400°C, interstitial elements would distribute themselves at grain boundaries either as precipitates or solute atmosphere and cause embrittlement by aggravating the effects of the already segregated impurities. On tempering at 600°C it was suggested that the impurities were thermally dispersed from the grain boundary sites and the alloy no longer embrittled unless the impurities were allowed to re-segregate back to the grain boundaries by either slow cooling, or aging, within the range 250°C to 500°C.

It was also found that this brittleness observed in Fe-Mn alloys was neither due to changes in friction stress  $\sigma_i$  or unlocking parameter  $Ky$  in Cottrell equation (40)

$$(\sigma_i d^{\frac{1}{2}} + Ky)Ky = \beta \mu \gamma \quad 2.1.(4)$$

where  $\sigma_i$  = the frictional resistance to dislocation movement

$\mu$  = the shear modulus

$Ky$  = the slope of  $d^{-\frac{1}{2}}$  versus flow stress curve of the Petch relationship

$d$  = one half the grain size

$\beta$  = a constant which varies from 1.0 to 0.3 and represents the level of stress concentration related to test piece geometry

$\gamma$  = the surface energy for fracture.

The main cause of brittleness was suggested to be a classical temper brittleness. More recent research (4,19) determined the

transformations and mechanical properties in Fe-Mn alloys and confirmed the previous observations that similar strength levels to those in Fe-Ni alloys could be obtained but attainment of toughness would be a problem. In this work, it was found that fracture mode in Fe-10.0% Mn alloys depended on heat treatment and testing temperature. Completely intergranular fractures were obtained in the normalized condition, but even on water-quenching the fracture mode was still intergranular. A change in carbon content from (0-0.2%C) did not make any difference in the fracture mode. No precipitates and particles were found on smooth inter-granular grain boundaries. All these observations were found in agreement with the previous research (1,3). In Freemans' work (4) the fracture mode was still completely intergranular even after tempering at 500°C but above this temperature, ie between 520-620°C, the fracture mode was found to change from intergranular to intergranular microvoid coalescence (IMC) when impact tested at room temperature; at -196°C, the fracture mode was quasi-cleavage. These observations along with the published results of Bolton et al (3) led to the conclusion that Fe-Mn alloys exhibited the characteristics of temper embrittlement phenomenon ie:

- (i) Rise in ductile-brittle transition temperature with intergranular fracture when heated in, or slowly cooled through 300-500°C.
- (ii) Embrittled alloys can be de-embrittled by heating above the embrittlement range ie  $\approx 600^{\circ}\text{C}$
- (iii) Re-embrittlement by holding or slowly cooling through 250-500°C after being tempered at 600°C.

It was difficult to decide, however, from the available evidences which impurity was responsible for the embrittlement.

For Fe-Mn alloys containing trace impurities, Bolton speculated that the Mn/Si levels could possibly control the susceptibility to temper embrittlement (1,3). Further evidence which favoured silicon as being responsible was that  $\frac{1}{2}$  pct addition of Mo failed to restrict the embrittlement and this had also been shown to occur with other steels (63,64) where silicon was responsible for embrittlement. The evidence favouring silicon was not conclusive however; phosphorus was also suggested as a possible source of embrittlement, since embrittlement even at concentrations as little as 0.001% P had been reported (65) when in combination with manganese. Bolton's alloys contained 0.002% P to 0.005% P. It was thought that nitrogen (3) could also be responsible for increasing embrittlement, since Capus (63) showed that nitrogen seriously enhanced 350°C embrittlement. Moreover it had also been found that low-carbon Fe-Mn alloys which contained aluminium to scavenge the nitrogen were less brittle than straight Fe-Mn alloys (66).

Later, in another investigation carried out in the department, on Fe-Ni-Mn alloys (67,68) similar loss in impact properties was experienced. The intergranular fracture surfaces were analysed using AES (69) Ni, Mn, P and N were detected on the brittle grain boundaries.

Thus, out of all this research work, it became obvious that possible impurities were P, N or Si although the exact interaction was not clear nor whether manganese would cause embrittlement on its own.

## 2.2 Grain-Boundary Embrittlement in Iron-base Alloys

In this section it is intended to examine the occurrence of brittle intergranular fracture in iron-base alloys in more detail. An attempt will be made to examine the solute-embrittlement in pure iron alloys in order to clarify exactly the role of interstitial and impurities in the embrittlement of iron and its alloys especially Fe-N and Fe-P alloys. Later, some specific conditions will be reviewed where grain-boundary embrittlement is enhanced by AlN, TiC precipitation on prior-austenite grain boundaries.

### 2.2.1 Grain-Boundary Segregation

Mclean (70) developed a theory of interfacial segregation of solutes and demonstrated that the driving force for the segregation of solutes be inferred from a simple elastic model of a foreign atom in a matrix in such a way that its associated lattice strain energy would be reduced by concentration of the solutes at the structural defects, such as dislocations, grain boundaries and free surfaces. There are generally two types of grain boundary segregation:

#### 1. Gibbs Equilibrium Segregation:

Where the segregation of solute atoms to the boundaries result in lowering of the free energy of the boundary and hence the energy of the system as a whole.

#### 2. Non-equilibrium segregation:

Where the segregation occurs from the interaction of solute atoms with vacancies to boundaries which act as sinks.

Modern technique such as Auger electron spectroscopy makes it possible to distinguish between these two types of segregation and also between them and precipitation. By the use of inert ion sputtering to uniformly remove atomic layers from the specimen, a solute atom gradient can be determined for some distance from the boundary. Some typical sputtering profiles are shown in fig. 14(a). With a precipitate, the Auger signal should remain fairly constant until it disappears suddenly, while equilibrium segregation should exhibit a gradient but only over a few atomic layers, whereas the non-equilibrium type of segregation should persist over much larger atomic distances.

In section 2.2.2 and 2.2.3 the grain-boundary embrittlement in iron-base alloys with elements like oxygen, sulphur, nitrogen and phosphorus will be reviewed. As the solute embrittlement in iron-base alloys has been divided into two segregation types it now appears that actually these embrittling elements fall into two clear categories:-

1. Elements which form a true Gibbs mono-layer and embrittle at small concentration for example sulphur, phosphorus, oxygen, nitrogen etc.
2. Elements which form multi-layers at the boundary and in general require high concentrations for embrittlement for example tin, arsenic and antimony.

Actually the distinction between equilibrium and non-equilibrium segregation is made on the basis of whether the amount of segregate satisfies the Gibbs adsorption isotherm for dilute solutions (71).

$$\Gamma_2 = - \frac{C}{RT} \left( \frac{d\sigma}{dC} \right)_T \quad 2.2.(1)$$

where  $\Gamma_2$  = Grain-boundary excess concentration of the second element due to segregation

$\frac{d\sigma}{dC}$  = the change (decrease) in the grain-boundary energy with changes in the bulk concentration C of the second element.

Hondros and McClean (72) have reported that  $\frac{d\sigma}{dC} = 1190$  ergs/sq cm/at pct for phosphorus segregation to grain boundaries in  $\delta$ -iron at 1450°C. It has also been suggested that more precise determination of the amount of segregate can be made with a knowledge of the Activation Energy for adsorption of solutes at grain boundaries in iron.

Another expression derived by Cahn and Hilliard (73) also gives theoretically the upper limiting values of segregants. Accordingly for two-component systems like Fe-P etc

$$\Gamma_2 = \frac{\sigma}{kT [1 + \ln(C_e/C)]} \quad 2.2.(2)$$

where  $\sigma$  = grain-boundary energy of pure iron at the temperature TK under consideration.

$C_e$  = limit of solid solubility in terms of atom fraction

k = Boltzmann constant

Cahn (73) and Hondros (74) suggested an assumed value of  $\sigma$  and  $C_e$  for phosphorus as

$$\sigma = 800 \text{ ergs per sq cm}$$

$$C_e = 0.02$$

Hondros and McClean (72,74) have experimentally shown that  $\frac{d\sigma}{dC}$  is inversely proportional to solubility. It was found that an element

like nickel which has a high solubility in iron, has a  $\left(\frac{d\sigma}{dC}\right)$  value of only 54  $\frac{\text{ergs/sq cm/at pct}}{\text{at}}$  at grain-boundaries in  $\gamma$ -Fe, whereas phosphorus which has a low solubility in iron, has a  $\frac{d\sigma}{dC}$  value of 575  $\frac{\text{ergs/sq cm/at pct}}{\text{at}}$  under the same conditions.

Hence the energy of the grain boundaries was suggested to be affected by the phosphorus alone. If nickel and chromium interact with phosphorus, they increase the activity and diffusivity of P in iron, consequently increasing the theoretical upper limit for segregation to higher values.

The driving force for equilibrium segregation is a reduction of free energy due to the diffusion of impurity atoms to a surface where misfit is more easily accommodated, McLean (70).

For a given boundary segregation, it is possible to show (70) by a statistical thermodynamics argument that segregation is related to temperature by an expression of the form

$$C_b = \frac{AC \exp\left(\frac{E}{RT}\right)}{1 + AC \exp(E/RT)} \quad 2.2.(3)$$

where  $C_b$  is the grain-boundary concentration, C the bulk concentration, T the absolute temperature, A is a constant and E is the excess lattice energy due to the presence of the impurity atoms. Alternatively E can also be regarded as the decrease in energy accompanying the transfer of an atom of solute from the lattice to a boundary site. For the case of P in b.c.c. iron E is estimated by Hondros (74) as 16000 cal/gm atom. The constant 'A' is a factor which accounts for changes in vibrational energy within the boundary region due to segregation and is generally assumed to be unity. The value of  $E_{\max}$  is given by (75,76)

$$E_{\max} = 6\mu\Omega\varepsilon^2 = 6\mu\Omega\left(\frac{r_A - r_B}{r_A}\right)^2 \quad 2.2.(4)$$

where  $\mu$  and  $\Omega$  are the shear modulus and atomic volume of solvent and  $r_A$  and  $r_B$  are the atomic radii of solvent and solutes respectively.

McLean (70) has also shown that the grain-boundary segregation of a solute as a function of time can be described by the following equation

$$\frac{C_{bt} - C_{bo}}{C_{b\infty} - C_{bo}} = 1 - \exp\left\{-\frac{4Dt}{\alpha_2^2 d^2}\right\} \operatorname{erfc}\left\{\frac{2\sqrt{Dt}}{\alpha_2 d}\right\} \quad 2.2.(5)$$

where  $C_{bo}$  is the initial grain-boundary concentration ( $t = 0$ )

$C_{b\infty}$  is the equilibrium grain-boundary concentration  
( $t = \infty$ )

$C_{bt}$  is the grain-boundary concentration at time  $t$

$D$  is the diffusion coefficient

$d$  is the grain-boundary thickness

$\alpha_2$  is the ratio of  $C_{b\infty} / C_{bo}$

2.2.(5)

when  $(4Dt/\alpha_2^2 d^2) < 1$ , equation (5) reduces to

$$\frac{C_{bt} - C_{bo}}{C_{b\infty} - C_{bo}} \sim \frac{4\sqrt{D}}{\sqrt{\pi} \alpha_2 d} \sqrt{t} \quad 2.2.(6)$$

Further if  $C_{b\infty} \gg C_{bo}$  ;

$$C_{bt} \sim \frac{4\sqrt{D}}{\sqrt{\pi} d} C_{bo} \sqrt{t} \quad 2.2.(7)$$

Hondros (74) techniques of studying grain-boundary segregation of solutes by measurement of surface and grain-boundary energies seems to be reasonable as the energies are affected quite substantially by segregation in a number of binary alloys as shown above.

The "Interfacial Activity" of a solute in a

particular solvent is defined as the decrease in interfacial energy per atomic per cent of bulk solute concentration in the limit of zero concentration. Hondros (77) attempted to correlate the interfacial activity in a wide range of systems with other physical parameters. He found a reasonable correlation between grain-boundary activity and maximum solubility, probably because this parameter reflects all types of atomic mismatching and for various systems this correlation is shown in fig 15. Hondros and Seah (78) have also defined, by analogy with the Langmuir isotherm for surface adsorption, a more precise parameter, the grain-boundary enrichment factor,  $\beta$ , with which to compare grain-boundary segregation in different systems

$$\beta = \frac{X_B/X_{Bo}}{C} = \frac{d\sigma/dC}{X_{Bo}RT} = K \frac{1}{C_e}$$

where  $X_B$  = no of moles of solute/unit area of grain boundary  
 $X_{Bo}$  = no of moles of solute/unit area of grain-boundary  
 required to form a close-packed sheet one atom thick  
 $C$  = bulk concentration  
 $C_e$  = limit of atomic solubility  
 $K$  = exp (E/RT)

For temperatures  $\sim 1000$  K and  $E = 0.5$  Kcal mole<sup>-1</sup>,  $K = 1$  to 10. Hondros and Seah (78) reported the correlation between  $\beta$ , the grain-boundary enrichment ratio and atomic solid solubility which is shown in fig 16 for a number of binary systems. The measurement of grain-boundary enrichment was determined by using two techniques; namely, Interfacial energy measurement and recently developed technique of Auger Electron Spectroscopy.

Recently Hondros (74) reported the grain-boundary segregation of tin in iron-tin alloys over a temperature range of 1000°C. In

order to control the segregation by the addition of a third element, the Fe-Sn-S system was also studied. Sulphur is surface active in iron indicating the possibility of a strong competition between sulphur and tin for grain-boundary sites. It was found that the segregation behaviour had close analogies with gas adsorption on surfaces. The important point noticed was that sulphur segregation obeyed Langmuir-type (monolayer) behaviour whereas tin formed grain-boundary multilayers. It was suggested that sulphur and tin showed two segregation behaviour patterns; the sulphur category (akin to surface chemisorption) represent the behaviour of high surface activity elements like O, N and P whereas tin category (akin to multilayer physisorption) represent the behaviour of other elements like As, Sb and Cu. As already pointed out, the important outcome of this work was the prediction that the impurity elements segregating tendency was inversely proportional to the limit of solid solubility of that element. Since this work Seah and Lea (79) have measured grain-boundary and surface segregation tendency of Sn by AES in the temperature range of 500-850°C. They developed a thermodynamic theory to explain the variation of surface and grain-boundary enrichment with temperature by considering the interfacial and surface entropies of the segregants. They found good agreements with the experimental results.

### 2.2.2 Influence of Oxygen, Carbon and Sulphur on Intergranular Brittleness in Iron and its Alloys

It has now become well established fact that segregation of solutes have a great effect on the intergranular cohesive strength of iron. A number of metalloid elements like P, As, Sn and Sb have been found to affect this cohesive strength and result

in raising the ductile-brittle transition temperature and in some cases in lowering the upper shelf energy in the embrittled state; also with a change in brittle fracture mode from cleavage to smooth intergranular. The metalloid elements (P, As, Sn, Sb) were suggested long ago (80) as being responsible for grain-boundary embrittlement but have been confirmed recently with the advent of Auger Electron spectroscopy.

In the early stages, most of the research workers (81) focussed more attention towards the influence of carbon on cohesive strength of iron and found that carbon increased the cohesive strength of iron (81). The tentative model suggested was that carbide precipitation at the grain boundary caused an offsetting in the embrittling elements from the grain boundary (81). Another postulation (31) was that perhaps the effect of carbon might be on the intrinsic bonding in the material at the grain boundary along with the effect resulting from off-setting of the embrittling elements. Low and Feustal (81) also demonstrated that carbon caused an inherent interface strengthening effect (grain-boundary strengthening effect) and they approached this idea by studying carburization and recarburization experiments on a low-carbon rimmed steel. After this interesting work, MacMahon et al (83) found that the equilibration temperature from which iron was quenched had a profound effect on the grain-boundary strength of ferrovac iron, commercially vacuum melted from electrolytic iron containing  $\approx 50$  ppm carbon and  $\approx 20$  ppm oxygen. It was found that if the quenching temperature was lowered, the ductility of the iron at 77 K was increased and the tendency for intergranular fracture was decreased. The reasons suggested for this behaviour was that by decreasing the equilibration temperature (solution

treatment temperature), it enhanced the equilibrium segregation of carbon to grain boundaries. So it means that if the temperature is high, there is less chance for carbon to segregate to grain boundaries (possibly because of increased solubility) and strengthen them and thus the grain boundaries will be weaker. It was not clear from this work whether carbon had an intrinsic effect, or if it had some sort of scavenging interaction with another segregated impurity; for example oxygen. Fast (84) in 1949, found that iron containing 0.015% oxygen had a transition temperature on impact about 50°C higher than that of a similar iron killed with zirconium, titanium or aluminium; the addition of 0.53% of Mn to an iron containing 0.014% of oxygen was also found to lower the transition temperature of about 40°C compared with that of the killed-iron. On the basis of impact tests at room temperature he concluded that more than about 0.002% of carbon could combat the effect of oxygen. Fast (84) associated the presence of oxygen with failure along grain boundaries and mentioned that oxygen reduced the cleavage strength, the reduction being localized at the grain boundaries.

Rees and Hopkins (31) demonstrated in 1952 that oxygen reduced the intergranular strength of iron. An alloy with 0.48%Mn was found to almost counteract the embrittling effect of oxygen (0.006%O). The minimum oxygen content for severe embrittlement was found to be 0.003%. At that time in 1952, the authors could not clearly understand the mechanism involved for this grain-boundary embrittlement by oxygen as there was no intergranular phase present. Oxide inclusions were noticed on increasing oxygen content beyond 0.007% but they were

randomly distributed. The addition of Mn was found to counteract very largely the embrittling effect of oxygen but some grain-boundary failure still remained. Rellick and McMahon (85) recently showed the influence of 0.05 pct aluminium and found that intergranular brittleness associated with high equilibration temperature reported by McMahon earlier (83) was suppressed considerably by the addition of 0.05 pct Al. when quenched from  $\alpha$  high temperature. It was also found that further increase in low-temperature ductility could be achieved if the iron containing 0.05 pct Al was slowly cooled down to  $\approx 560^{\circ}\text{C}$  and then quenched. From this work, the important point to note was the interaction of Al with oxygen. By adding Al to the melt, it lowered the amount of dissolved oxygen to a very small amount and thus decreasing the intergranular brittleness.

It is interesting to see that the effect of these impurities and interstitials on the intergranular brittleness of iron has been the subject of research for 25 years. As indicated above, some impurities by reinforcing the cohesion of the grain boundaries favour transgranular fracture while others lead to fragile intergranular fracture. Oxygen has been regarded as having a considerable embrittling effect; but its specific role remained controversial till the current work by French Workers (86) who concluded that oxygen did not affect the intergranular brittleness (fig.17). They reported that there was a profound effect of carbon and sulphur on the intergranular brittleness of pure iron and demonstrated that the beneficial effect of carbon on the cohesion of the grain boundaries was independent of the oxygen content (fig.18). Thus accordingly it was suggested that all the mechanisms established so far concerning the interaction

between oxygen and carbon at the grain boundaries were invalid. They supported previous observations (87,88) that sulphur segregated to the grain boundaries and caused intergranular fragility very rapidly. It was suggested that all the previous studies on the influence of oxygen (84,89) were made on iron where the concentration of sulphur was already sufficient to cause embrittlement. The segregation of carbon and sulphur was also found to follow the segregation theory proposed by Hondros and Seah (78) that intergranular segregation of an element increases to a maximum when the solubility decreases with temperature to the solubility limit. Thus for an embrittling element like sulphur there will be a maximum boundary fragility and for a strengthening element like carbon, there will be a maximum boundary reinforcement when the alloy containing sulphur and carbon respectively are quenched from a temperature close to the solubility limit.

### 2.2.3 Influence of Nitrogen and Phosphorus on grain-boundary embrittlement of Iron-base alloys

Rees and Hopkins (89) demonstrated in 1954 that high-purity iron with 0.01%N exhibited grain-boundary weakness when cooled at normal rates from the austenitic region and found that severity in this intergranular brittleness could be increased by isothermal treatment in the approximate temperature range of (500-800°C). This intergranular embrittlement was associated with rise in the impact transition temperature and on tensile testing at -196°C, the brittle fracture stress decreased with increase in the degree of embrittlement. Unfortunately at that time in 1954, there was no direct tool like AES available to

determine the fracture surface chemistry. Thus Rees and Hopkin (89), on the basis of these isothermal studies, and the effect of cooling rate finally explained this type of intergranular brittleness, as possibly being caused by segregation of nitrogen atoms to the grain boundaries. Moreover, this intergranular brittleness was found very sensitive to heat treatment. It was found very interesting, but difficult to explain, that if the cooling rate was increased, the fracture mode changed predominantly to intergranular with high-impact transition temperature. By reducing the cooling, ie by air cooling and furnace cooling, the intergranular brittleness was gradually decreased. The reasons suggested for this kind of observation was that on rapid cooling, the precipitation of  $\text{Fe}_{16}\text{N}_2$  was avoided or even eliminated with no clustering, of N atoms taking place. Thus free N atoms segregated to the grain boundaries because of their high diffusion rates and weakened them resulting in enhancement of inter-granular brittleness along with rise in the impact transition temperature. On slow cooling there was sufficient time for precipitation of  $\text{Fe}_{16}\text{N}_2$  to occur. Thus precipitation of  $\text{Fe}_{16}\text{N}_2$  took place rather than segregation of nitrogen to grain boundaries resulting in brittle failure by cleavage and a lowering of the DBTT.

By studying the effects of isothermal treatments and the effects of cooling rate, it was found that precipitation mainly took place below  $300^{\circ}\text{C}$ . In figure 19, the toughest condition was found after furnace cooling down to room temperature but the intergranular brittleness was induced into these alloys by holding for various times at temperatures between  $300\text{-}1000^{\circ}\text{C}$ . From the shape of this curve shown in fig.19, the simplest explanation suggested was that maximum tendency for nitrogen to diffuse to

the grain-boundaries was between 600-700°C.

Above this temperature range, nitrogen atoms tended to diffuse away or boil off from grain boundaries resulting in de-embrittlement while below this temperature range diffusion was too sluggish to produce embrittlement in measurable times. An alternative explanation of the lack of embrittlement at low temperatures was that precipitation of  $\text{Fe}_{16}\text{N}_2$  or clustering of Fe and N atoms occurred within the grains rather than diffusion of nitrogen to grain boundaries.

It was also found in this very interesting work that on prolonged heating at 200°C or 250°C after being furnace cooled to room-temperature  $\text{Fe}_{16}\text{N}_2$  type precipitates disappeared with the formation of  $\text{Fe}_4\text{N}$  type precipitates.

Following their work on Fe-N alloys, Hopkins and Tipler carried out similar studies on Fe-P alloys (57) the effect of isothermal treatments at different temperatures on the brittle fracture stress is shown in figure 20. The curves have similar characteristics to that shown in figure 19 for Fe-N alloys. From figure 20, it is evident that the temperature range over which extreme sensitivity to grain-boundary embrittlement occurs becomes wider as the P content is increased.

Hopkins and Tipler (57) also studied embrittlement in Fe-P-C alloys. They found that rate of isothermal embrittlement was a lot less than in the binary Fe-P alloys ie carbon had a strengthening effect on grain-boundaries.

Direct evidence for the segregation of phosphorus to grain-boundaries was obtained in 1958 by Inman and Tipler (90). The

embrittlement of an Fe-0.09%P alloy was studied by bend tests. They found ductile behaviour of the alloy at room temperature, but it failed in a brittle intergranular manner at  $-78^{\circ}\text{C}$  when furnace cooled from  $1000^{\circ}\text{C}$ . A short isothermal treatment at  $700^{\circ}\text{C}$  followed by a water quench produced a severe intergranular weakness at room temperature. Phosphorus segregation was detected at the embrittled grain boundaries by a radio-active technique.

More recently Stein et al (91) employed AES, a better tool for the analysis of fractured surfaces in Fe-P alloys than that used earlier by Inman and Tipler (90). They reported that phosphorus did segregate to the grain boundaries in ferrite range but not in the austenitic range and the segregation did not conform to Gibb's equilibrium segregation model. This later finding disagrees with that of Hondros (74).

Hondros (74) attempted to explain this intergranular fragility in Fe-P alloys in terms of adsorption of phosphorus to the grain boundaries and consequently lowering of the fracture surface energy. The segregation of solute to interfaces by the application of Gibb's theory, namely the reduction of interfacial free energies have been dealt in detail in section 2.3.1 but here its applicability in Fe-P system would be briefly reviewed following the measurement of interfacial energies of grain boundaries by Hondros (74).

A marked drop in interfacial energy occurred with the addition of P to pure iron (74) eg  $\delta\text{Fe}$  at  $1450^{\circ}\text{C}$ , grain-boundary surface energy dropped from  $\approx 800$  ergs/cm<sup>2</sup> for pure iron to  $\approx 500$  ergs/cm<sup>2</sup> for iron containing 0.15P. As this work referred to segregation characteristics at high temperatures, almost near to

the melting point of the metal, the values had to be corrected to the observed embrittlement temperature range of 600°C to 1000°C (74). The grain-boundary concentration  $C_b$  at different temperatures was determined using equation 2.2(3), section 2.3.1.

i.e. 
$$C_b = \frac{AC \exp (E/RT)}{1 + AC \exp (E/RT)}$$

A was taken as unity. E was estimated to be 16000 cal/gm-atom from the grain-boundary adsorption isotherm. The results are shown in figure 21. This curve shows that the grain-boundary concentration of solute increases with decrease in temperature and the extent of segregation is less in the  $\gamma$ -phase. From these predictions the concentration of solute at grain boundaries in the embrittlement temperature range of 600-1000°C can be estimated (57,90). At 800°C this treatment predicts about 0.7 of a monolayer of phosphorus at the grain boundaries. This work of Hondros (74) gives qualitative support to the view that the intergranular weakness of Fe-P alloys may be attributed to the presence of nearly a monolayer of solute at the grain boundaries. The detailed mechanism of the weakening action is however still not clear but at least it can be said that the presence of nearly a monolayer of phosphorus will create potential intergranular fracture path with reduced energy requirements as explained in section 2.1.5.

Recently in another investigation (91) the grain-boundary embrittlement of pure iron due to P, Sb and S has been studied using fracture appearance transition temperature (FATT°C) measurement and Auger Electron emission spectroscopy to analyse the fractured surfaces. These studies actually confirmed that the

embrittlement occurring in these alloys was different from the reversible temper embrittlement which is generally associated with low-alloy steels. The embrittlement associated with these binary and ternary alloys of Fe-P, Fe-P-S and Fe-Sb-S was found to be irreversible and the segregation of impurities occurred at all temperatures in ferrite and did not follow Gibb's adsorption mechanism. It is thought that possibly some type of phase, type of grain boundary (austenite-ferrite or ferrite-ferrite) or the vacancy solute interaction near the boundary in  $\alpha$ -phase may be responsible for this non-equilibrium segregation.

#### 2.2.4 Inter-relation of Grain-Boundary Embrittlement in Fe-N, Fe-P, Fe-P-C alloys with Temper brittleness and "350°C embrittlement"

Comparing the sensitivities of embrittlement by isothermal treatment, the embrittlement in Fe-P alloys, as measured by the brittle-fracture stress at  $-196^{\circ}\text{C}$  was more severe than that of Fe-P-C alloys. (57) It was found that the degree of embrittlement in Fe-P-C alloys (57) could be of the same order as that found in the phenomenon of temper brittleness in low-alloy steels, as measured by the rise in the impact transition temperature. The time required to develop the brittleness in Fe-N and Fe-P alloys was  $\sim$  minutes whereas that in Fe-P-C alloys it was  $\sim$  hours. Thus the addition of carbon was found to reduce the severity and the rate of development of intergranular brittleness in Fe-P alloys and thus making the situation comparable with temper brittleness in commercial steel. On the basis of similarities between intergranular brittleness in Fe-N, Fe-P, Fe-P-C alloys and temper brittleness in low-alloys steel, they can be briefly

compared as follows:

Intergranular Brittleness in Fe-N, Fe-P and Fe-P-C alloys	Temper Brittleness in Steels
<p>(1) The brittle fractures are partly intergranular and in some cases completely intergranular as a result of reduction of the grain-boundary strength below the cleavage strength possibly through segregation of N, P, etc. (89,57,90).</p>	<p>(1) The brittle fractures are also partly or in some cases completely intergranular as a result of reduction of the grain-boundary strength below cleavage strength through segregation of solutes P, As, Sn, Sb. (92,93)</p>
<p>(2) The maximum embrittlement was obtained by heating in a certain temperature range and it was less above and below that temperature range. (89,57)</p>	<p>(2) Similarly in steels, the maximum embrittlement occurred over a certain temperature range. The degree of embrittlement became less at temperatures above this range but for lower temperatures, the embrittlement occurred after a long time. (94).</p>
<p>(3) The embrittlement in Fe-P, Fe-N alloys occurred very rapidly and the temperature of maximum embrittlement was higher than that in steels. (90)</p>	<p>(3) The embrittlement in steels reported (94) was less rapid and the temperature of maximum embrittlement was lower than that in Fe-P and Fe-N alloys. The embrittlement kinetics was comparable to that in Fe-P-C alloys.</p>

(4) There occurs severe embrittlement in Fe-P and Fe-N alloys under same conditions of heat treatment but the addition of carbon to Fe-P alloys leads to comparable situations with steel.

(4) The embrittlement is less severe than that in Fe-P, Fe-N alloys. The embrittlement has similar characteristics to that in Fe-P-C alloys.

On the basis of comparison outlined above, it was suggested by Hopkins and Tipler (57) that temper-brittleness in steels could be a mild form of the intergranular brittleness in Fe-P and Fe-N alloys.

The influence of nitrogen in a 3%Ni-Cr steel has been reported by Capus (63); room temperature impact properties of a high purity steel and of one containing 0.02% nitrogen are shown in figure 22. Nitrogen appears to have a severely embrittling effect, particularly when tempering temperatures between 200°C and 350°C are used (ie the tempering temperature causing embrittlement is lower than the range required to induce embrittlement in steels containing other impurity elements). The conclusion of Schrader, Wiester and Siepmann, that the presence of nitrogen in steels could result in "350°C embrittlement" was thus confirmed by Capus (63). It is clear, however, that nitrogen is only one of several elements which are liable to have this effect.

In steels containing nitrogen the fractures were predominantly intergranular after tempering in the embrittling range, whereas

steels containing other trace elements showed little evidence of this type of fracture. The fact that commercial steels also show intergranular fracture when embrittled by tempering in that region supports the conclusion that nitrogen is an important factor in relation to "350°C embrittlement".

A clearer comparison of the relative influence of the respective trace elements on impact values at various strength level is given by the room temperature impact value/hardness curves in figure 23 relating to quenched and tempered high-purity steels and some steels of similar base composition but containing embrittling elements (N, P, Sb, As).

These results suggest that the impact properties of hardened and tempered commercial low-alloy steels are controlled to a large extent by the presence of impurity elements. The presence of phosphorus and nitrogen is certainly significant in relation to the occurrence of "350°C embrittlement" whilst other impurity elements, for which the steels are not usually analysed, may also contribute to embrittlement.

#### 2.2.5 Segregation Predictions in Ternary Systems

It is thought (95) that if a ternary element is added in the binary solution of an impurity in a metal, then the solubility of <sup>the</sup> impurity will be decreased and thus increasing the segregation of that impurity to the grain boundaries. Indeed McMahon and his co-workers (118) (97) have demonstrated that this is the case for Fe-Ni-Sb, Fe-Ni-Sn and Fe-Cr-Sn. Seah and Hondros (78) found that if there exist a strong chemical attractive interaction between the substrate and the adsorbed

atoms, then the adsorption on the surface will be increased. Guttman (98) found in ternary solutions that if there existed a strong attraction between solutes then the chemical interaction between solute atom could greatly enhance the segregation of both solutes. He found in temper-embrittled steels that if transition elements 'M' (Ni, Cr, Mn, etc) and impurities 'I' (Sb, P, As, Sn, etc) have a strong attractive interaction <sup>with each other</sup> with respect to iron, they would enhance the segregation compared to the binary system of Fe + I (91) and Fe + M (72). Guttman (95) presented the theoretical treatment of the above mentioned idea in terms of a ternary segregation equation based on equilibrium segregation thermodynamics. He used explicitly the chemical interactions between Fe, I and M in the expressions of the chemical potential, assuming for simplicity the hypothesis that the ternary solution is regular. He defined the relative chemical interaction energy  $\hat{\alpha}_{MI}$  between solute atoms I and M with respect to the solvent Fe as

$$\hat{\alpha}_{MI} = \alpha_{MI} - \alpha_{FeI} - \alpha_{FeM} \quad 2.2.5(1)$$

The coefficients  $\alpha$  are obtained from the enthalpy of mixing  $\Delta H_{XYZ}^M$  of a solution of elements, X, Y, Z with concentrations x, y, z.

$$\Delta H_{XYZ}^M = \alpha_{XY}^{XY} + \alpha_{YZ}^{YZ} + \alpha_{ZX}^{ZX} \quad 2.2.5(2)$$

An average value of  $\hat{\alpha}_{MI}$  consistent with segregation measurement of I in temper-brittle steels (99) was found to be of the order of 10,000-30,000 cal/g-atom and specifically  $\approx 19,000$  cal/g-atom in the Mn-Sb steels (98). This value was found to be in agreement with the rough estimate of the  $\alpha_{XY}$  deduced from the available enthalpies of mixing of various XY compounds.

Guttman actually tried to emphasize the link between limited solubility and segregation potency in ternary systems. It was felt as both these phenomenon express the tendency of the solid solution to reject the impurity first as a segregate than as a precipitate, so they should have some parameter in common and this parameter Guttman identified as the interaction coefficient,  $\alpha_{MI}$ .

In the absence of thermodynamic data to evaluate  $\alpha_{MI}$  an idea of the strength of the interaction between the elements M and I can be obtained from the heat of formation of compounds based on the elements M and I.

It is interesting to see that various recent experimental work has supported Guttman's theory. Clayton and Knott (100) showed that Guttman's segregation equations fitted their segregation measurement of Ni and Sb as did the data of Mulford (101) for Ni and P. Even in systems where a behaviour typical of temper embrittlement had not been suspected, this type of ternary segregation was found to occur. In a high-purity ternary alloy Fe + 2%Mn + 1200ppm Sb, a strong segregation of N was detected (95) besides that of Sb and Mn, although the N content was < 10 ppm. This work by Guttman clearly explained a strong Mn-N interaction when  $\alpha_{MnN} \approx 39000$  cal/g-atom, compared to  $\alpha_{FeN} \approx 1500$  cal/g-atom which yielded  $\alpha_{MnN} \approx 37500$  cal/g-atom. In the presence of Si and/or Al nitrogen did not embrittle the steels because of very high interaction between aluminium, silicon and nitrogen ( $\alpha_{SiN} \approx 100,000$  cal/g-atom,  $\alpha_{AlN} \approx 150,000$  cal/g-atom). On this basis it was suggested that Al addition was beneficial in eliminating brittleness associated with nitrogen.

Another interesting situation was found in rotor steel (95) where a strong segregation of Cu was observed besides that of P, Sn, Ni, Cr and Mo. Generally, Cu was not expected to segregate in Fe because of its relatively high solubility, but in the presence of strongly segregated P, it did segregate since  $\bar{a}_{\text{CuP}} \approx 45000 \text{ cal/g-atom}$ .

#### 2.2.6 Grain-Boundary Embrittlement due to the Precipitation of AlN, TiC,<sup>(1)</sup>etc.

##### Embrittlement due to the precipitation of AlN

In 1960, Woodfine and Quarrell (102) examined in detail the effect of 'Al' and 'N' on the occurrence of "intergranular" or "rock-candy" fracture after the work by Lorig and Elsea (164) who concluded that the precipitation of AlN on the primary austenite grain boundaries could be the major cause of intergranular fracture in carbon and low-alloy steel castings. Woodfine et al (102) also suggested that AlN could produce a form of intergranular fracture in cast steels. They also studied the effect of Ti and Zr additions with and without aluminium as the nitrides formed by Ti and Zr were more stable than AlN. It was found that intergranular fracture could be avoided in these steels by deoxidation with Ti or Zr or by using Ti in combination with Al. It was found that AlN could be taken into solution in austenite by heating in the range 1100-1250°C and on quenching intergranular fracture could be eliminated, but if the steel castings were slowly cooled after solidification or held in the temperature range 800-1100°C, grain-boundary weakness would result with the precipitation of AlN at the austenite grain boundaries established by the

high-temperature heat treatment. Afterwards Wright and Quarrell (58) once again confirmed that AlN could give rise to a form of intergranular fracture in steel castings and in Al-killed steels. It was found that this defect could be only minimized by keeping the nitrogen content of the steel as low as possible and by restricting the aluminium additions to the very minimum required for complete deoxidation coupled with a high-cooling rate after solidification. Another interesting feature of this work was that AlN contents equivalent to about 0.002%N gave rise to intergranular fracture in low-alloy steels on slow cooling after solidification but with AlN contents equivalent to about 0.016%N, when particles of AlN formed within the melt with subsequent precipitation in the solid state occurring on these nuclei, prevented the development of intergranular fracture.

Recently Fukagawa (103) clarified the characteristics and causes of austenite grain boundary embrittlement found in AlN bearing high-strength steels. In this work AlN bearing mild steel and high strength steels were firstly hot rolled and heat treated in various conditions. After these heat treatments the AlN contents of specimens were determined chemically by the bromine-ester method, and then the morphology of AlN precipitates were studied in relation with the mechanical properties, especially the low-temperature notch toughness. Two distinctive peaks were found for the precipitation of AlN from solid solution upon cooling; one at 1200-1050°C in the  $\gamma$ -region and the other at 750-650°C in the  $\alpha$ -iron region, figure 25(a). Upon reheating however, there was found only one broad peak at temperatures between 650 and 1100°C shown in figure 25(b).

It was also found that if the AlN was allowed to precipitate in the austenite, then steels became so embrittled that the ductility could not be recovered by any subsequent heat treatment on hot working. Electron microscopy revealed thin, rectangular plate of AlN precipitated along the austenite grain boundaries. Therefore it was finally suggested that for the manufacture of such AlN-bearing or Nb-bearing steel, the production procedures should be designed to impede the precipitation of nitrides or carbonitrides while the steels are <sup>in the</sup> austenitic condition during cooling.

#### Embrittlement due to the precipitation of Ti(C,N)

The occurrence of intergranular embrittlement in maraging steel due to the precipitation of TiC during slow cooling and/or intermediate annealing in the austenite temperature range has been the subject of a few recent investigations. Spaeder (104) reported in 1970 that if maraging steels were improperly heat-treated ie if subjected to too high solution annealing temperature followed by slow cooling or an intermediate annealing treatment in the austenitic temperature range, the grain boundary embrittlement would result due to the precipitation of TiC and this phenomenon was termed "Thermal Embrittlement". The various mechanisms proposed were all concerned with grain-boundary segregation and/or precipitation of alloy carbides or nitrides. Kalish and Rack (105) established the temperature range of this thermal embrittlement and attributed the major loss of toughness to the diffusion of interstitial impurity atoms as carbon and nitrogen to the austenite grain boundaries during cooling or intermediate isothermal annealing below 1100°C. This discrete precipitation of Ti(CN) at the boundaries was initially

believed to play a role only in the advanced stage of the embrittlement but later on, Johnson and Stein (106) examined the cause of this thermal embrittlement by employing Auger Electron Spectroscopy and showed that the embrittlement was directly correlated with segregation of Ti and C to the prior-austenite grain boundaries. They proposed that embrittlement was due to a subsequent reaction of Ti and carbon to form carbides at the boundaries. It appears from this work that the thermal embrittlement in maraging steels require the presence of Ti and C(N) at the prior-austenite grain boundaries

The mechanism suggested by Thomas (107) is that a too high solution treatment of maraging steel leaves Ti and C in solid solution in sufficient amounts to cause the precipitation of TiC during subsequent slow cooling and or intermediate annealing treatment in the austenitic<sup>phase</sup> region.

## 2.3 Temper Brittleness in Iron-base Alloys

### 2.3.1 History of the Problem

In 1917 it was found (108) that the notch-toughness properties of quenched and tempered low-alloy steels were severely affected if after tempering at 600°C, the steels were either slowly cooled or reheated in the temperature range of 350-550°C. Problems were encountered in assessing the degree of brittleness in embrittled steels. Considerable attempts were made to understand the nature of the embrittlement problem and how different measures could be adopted to combat it. Initially many confusing theories were developed to understand the brittleness exhibited by such steels until in 1919,

Greaves (109) indicated some of the characteristics observed at that time.

- (i) Steels of more or less similar composition might show variation in degree of brittleness when subjected to the same conditions of heat treatment.
- (ii) Notch-toughness decreased as the austenitising temperature was increased.
- (iii) Reheating in the temperature region of around 500°C caused embrittlement irrespective of the subsequent cooling rate.
- (iv) An initially tough steel could be embrittled if slowly cooled or reheated in the critical temperature range. On the other hand an embrittled steel could be made tough by reheating above 600°C and rapidly cooling. For this reason the embrittlement was named as reversible brittleness.

Later on during 1920-25, Greaves and Jones (110) demonstrated the effect of isothermal holding on degree of embrittlement at different temperatures especially in the critical temperature range. It was found that embrittlement could be increased with increasing time in the critical temperature range. The experiments were performed on Ni steels and it was shown that the presence of phosphorus, manganese and chromium enhanced the embrittling characteristics of the steel. This essentially showed an interaction of alloying elements with impurities. Molybdenum was found to be beneficial to some extent and was argued that molybdenum exerted merely a delaying action on the embrittlement process.

In early work the problem of deciding some measure of susceptibility to embrittlement was solved by taking into account

the susceptibility ratio which was defined as the ratio of the fracture energies of quenched and slowly-cooled specimens.

$$\text{Susceptibility Ratio} = \frac{\text{Fracture energy of quenched specimen}}{\text{Fracture energy of slowly-cooled specimen}}$$

This method of comparing the susceptibility of steels to temper brittleness was found to be false when Jollivat and Vidal (111) introduced the concept of ductile-brittle transition temperature in the understanding of this type of brittleness in 1944. It was found that the ductile-brittle transition temperature could be shifted to higher temperatures if the degree of embrittlement was increased either by isothermal holding or slow cooling in the critical temperature range.

By 1946, a clearer picture of the problem started emerging when Holloman (112) plotted the results of Greaves and Jones (110) to show the effect of isothermal holding at different temperatures on temper brittleness. It was found that embrittlement exhibited C-curve behaviour. The similarities of C-curve kinetics with other phase-transformations curves gave rise to theories that some sort of mechanism like precipitation from  $\alpha$ -iron might be responsible for such brittleness and weakness at the prior-austenite grain boundaries. At 600°C ie above the embrittlement range, the precipitate might dissolve and cause de-embrittlement effect in steels; and it was also speculated that the rate of such precipitation was maximum at 500°C and possibly this precipitation might be through a diffusion controlled process. Different types of precipitates such as oxides, phosphides, carbides and nitrides were suggested to precipitate from  $\alpha$ -iron during embrittlement treatment. The

possibility of nitrides was highly favoured by Holloman (112) and thought that perhaps the alloying elements act through changing the solubility of nitrogen in ferrite.

In 1950, Jaffe and Buffum (113) confirmed the original C-curve behaviour of temper-embrittlement process and it was suggested that the composition of the steel was the predominant factor affecting the rate of embrittlement and the maximum temperature at which embrittlement occurred. Other research workers supported this idea by studying isothermal embrittlement and step-cooled embrittlement in the critical temperature range.

In his review (93) in 1953, Woodfine tried to give a more exact picture of the understanding of the problem of temper brittleness and showed how grain coarsening can be harmful in temper brittleness. The response of different microstructures from pearlite to martensite was studied in enhancing the brittleness. Temper brittleness was found to be less in pearlite than in martensite in a Ni-Cr steel.

In 1959, Steven and Balajiva (80) finally showed that different types of impurities are responsible for this brittleness. The impurities such as P, As, Sn and Sb and to a lesser extent Mn and Si were suggested to be associated with temper brittleness. The embrittlement was found to be absent in their high-purity alloys based on Ni-Cr. An attempt was made to explain the role of carbon by studying impurity-doped plain-carbon steels. However, brittleness was not experienced in these steels even in the presence of impurities. This showed that another factor was required other than the presence of impurities to produce brittleness. This factor could be either carbides, major alloying elements or some phase itself.

Low et al (114) showed that the presence of major alloying elements like nickel, chromium, was essential along with the impurities (P, As, Sn, Sb) in order for the alloys to embrittle. The studies were made using autoradiography and electron microscopy to find any grain-boundary precipitation or segregation. But carbide morphology was found to remain unchanged before and after embrittlement. Carbon extraction replicas even failed to show any precipitation on grain boundaries.

There has been different proposals about the behaviour of alloying elements in temper-embrittled steels. Low et al (114) found that alloying elements are merely enhancers of impurities through affecting the diffusion kinetics of impurities. Capus (115) suggested a double segregation model and proposed that alloying elements segregate during austenitising to make sites of chemical attraction for impurities which segregate during the subsequent embrittling treatment. Alternative opinion was made by Restaino and McMahon (116) that pre-segregation of impurities might occur during austenitising as P, As, Sn, Sb are ferrite stabilizers and thus during austenitising treatment these impurities will segregate to  $\gamma$ -boundaries. However, recent work involving the use of Auger Electron Spectroscopy (AES) and back-scattering of energetic ions (BEI) has not supported the suggestion of segregation during austenitising. Most of the research workers after using these analytical techniques agreed that segregation of impurities and alloying elements took place during the embrittling treatment. An exception is due to Shultz and McMahon (117) who detected the prior segregation of P in Ni-Cr-Mo steels.

More recently McMahon et al (118) demonstrated in Ni-Cr steel that Ni and Cr decrease the solubility of Sb and Sn in  $\alpha$ -Fe at certain temperatures and thus increased the tendency of these solutes to segregate to grain boundaries at these temperatures. The driving force resulting from misfit strains in the solvent lattice associated with these impurity elements (Sb and Sn) were also suggested to be an additive effect for segregation of Sb and Sn. This work has at last given some qualitative explanation of the role of alloying elements in temper brittleness, which has been reinforced with Guttman's theoretical analysis of segregation in ternary alloys of iron (95) discussed previously in section 2.2.5.

In an early attempt by Woodfine et al (93) to emphasize the effect of microstructure on temper brittleness, Low et al (114) gave his interpretation that impurity segregation might affect the strength of carbide-ferrite interfaces and make such interfaces an easiest propagation path for brittle cracks. Guttman and Krahe (119) in their explanation about the influence of microstructures classified the boundaries in the lath-martensite steels into two main categories. The boundaries of low-porosity ie the interlath boundaries and the boundaries of high-porosity ie prior-austenite grain boundaries and interpacket boundaries and they suggested that even though the segregation of impurities might occur to both  $\alpha$  and  $\gamma$  boundaries but  $\gamma$ -boundaries are geometrically more favourable for the propagation of brittle cracks. The investigation by Viswanathan et al (120) showed the effect of long-time isothermal embrittling treatment in NiCrMoV steel and suggested that the temper brittleness exhibited by such steels is affected by the strength level of steel, carbide morphology and

ferrite chemistry directly or indirectly through modifying the segregation of impurity and alloying elements. McMahon et al (121) showed that intergranular brittleness in iron-carbon alloys by impurities could be obtained by the build-up of rejected impurities from the precipitating carbides and thus affecting the strength of carbide-ferrite interfaces. Other research workers (122) have recently compared the behaviour of bainite and martensite and showed that at the same degree of embrittlement measured through  $\Delta FATT$ , the amount of grain-boundary segregate and the extent of intergranular fracture was lower in tempered bainite than in martensite thus suggesting that embrittlement of interfaces other than prior-austenite grain boundaries are an important factor in the embrittlement of bainitic structure. Moreover at the same strength level, the segregation in bainite was less than in martensite and it was found to increase with increasing strength level of a given structure.

In 1968, the Auger Electron Spectroscopy technique was developed by Harris (123) which made it possible to study the nature of the surfaces with this technique, very thin surface layers of the order of  $5-10 \text{ \AA}$  could be analysed. Thus the understanding of the problem of temper embrittlement has been enhanced in the recent years with the advent of (AES) and it has been demonstrated that specific impurities are responsible for embrittlement. The behaviour of these impurities depend on the alloy content (124) of the steel and the embrittlement is due to reversible segregation of the impurities to prior-austenite grain boundaries.

In future work it is now necessary to study the effect of alloy content on the rate and degree of embrittlement in the

various classes of steels. This would not only give an understanding of the nature of interaction but may also result in optimisation of the composition of commercial alloy steels to avoid embrittlement.

In spite of this long history of the temper embrittlement problem and the large number of investigations there is still no theory which can explain all the characteristics exhibited by temper-brittleness phenomenon, probably because there are so many interactions involved in it. Secondly the Auger electron spectroscopy has only recently been developed which has made it possible to detect and identify the harmful impurities directly. Stein (124) and McMahon (117) have utilized this technique in the analysis of fracture surfaces and since then, a clearer picture of the phenomenon has started emerging.

### 2.3.2 Characteristics of Temper Brittleness

Temper brittleness is generally found in low-alloy steels and results when the hardened steel after being tempered at  $600^{\circ}\text{C}$  is either allowed to slowly cool or reheated in the temperature range of  $350\text{-}550^{\circ}\text{C}$ . The characteristics of temper-brittleness phenomenon so far established are summarized as follows:

- (1) A rise in the ductile-brittle transition temperature is observed. Thus in most cases notch-bar impact test is employed to differentiate between embrittled and unembrittled steels (111). Low-temperature tensile test has been used where tensile-ductility as measured by reduction of area has been found to drop in severe embrittled cases (67)(120)(125).

- (2) Embrittlement follows "C" curve behaviour when plotted against time and temperature. Maximum embrittlement occurs in the region 450 to 550°C. At low-tempering temperatures (~350) embrittlement only occurs after long holding times, while tempering above 550°C results in de-embrittlement of steel (113).
- (3) Embrittlement caused by certain specific impurity is dependent on particular alloying element. So in order to establish the degree of embrittlement it is always necessary to state alloy content as well as impurity level. Antimony, phosphorus, tin and arsenic are the major embrittlers listed in order of severity. Manganese and silicon have been reported to be active in larger amounts (80). Generally, embrittlement increases with increase in concentration of these impurities but it has been found to saturate with increasing concentration of P, Sn, As (80).
- (4) Temper brittleness is reversible. Even severely embrittled steel after being tempered or slowly cooled in the embrittlement range (350-550°C) can be de-embrittled by tempering above the embrittlement range (~600°C). Brittleness can again be restored by tempering once again in the embrittlement range.
- (5) The degree and rate of embrittlement are greatly affected by the alloy content. Plain-carbon steels with Mn < 0.5% are not susceptible (80). Susceptibility is enhanced greatly by chromium and manganese and less strongly by nickel (65) molybdenum and tungsten are inhibitors in small amounts but larger amount enhance the brittleness (126). A decrease

in carbon content has been reported to decrease but not prevent embrittlement (114).

- (6) Embrittlement results in decohesion along the prior-austenite grain boundaries. Holloman (112), Low (114) interpreted that decohesion actually occurs in the ferritic boundaries which lie along surfaces of the prior-austenite grain boundaries.
- (7) The phosphorus induced embrittlement in steels can be identified metallographically and result in grooving along the grain boundaries with certain etchants (114)(93).
- (8) The rate of embrittlement during embrittling treatment has been found to decrease if the embrittled steel is first de-embrittled ie held above the nose of the embrittlement C-curve but below the  $A_1$  temperature for a long time (127).
- (9) Most of the steels when embrittled above the nose of the C-curve go through a maximum of embrittlement with aging time.
- (10) The susceptibility to temper brittleness as measured by the shift in transition temperature depends upon structure and increases in the order pearlite, bainite and martensite (93).
- (11) With all the other conditions the same, an increase in prior-austenite grain size results in proportionate increase in embrittlement (126).
- (12) Plastic deformation can retard the development of embrittlement (128). Russian workers have shown that plastic deformation after embrittlement but before impact testing can

lower the transition temperature (129).

### 2.3.3 Measurement of Susceptibility to Temper Brittleness

Since the hazards of temper brittleness were known, the methods of testing have been reported along with the understanding of the nature of the problem. The methods used in assessing embrittlement can be classified as follows.

#### Mechanical Methods:

Greaves and Jones in 1920 suggested that the ratio of fracture energies between unembrittled and embrittled states could be taken as a measure of degree of brittleness. However, the long term work of Vidal showed that actually <sup>the</sup> impact transition curve was displaced on embrittlement; so the whole approach to the problem was changed and the rise in the ductile brittle transition temperature was taken as the measure of this intergranular brittleness. The common current practice is to determine the difference in impact transition temperature in the embrittled and non-embrittled condition.

In order that specimens undergo essentially the same tempering treatment, they are given the following heat treatment:

- (a) Embrittled: Austenitised and quenched, tempered for a certain time at a temperature above the embrittling range (eg 1h c600°C) followed by a tempering treatment in the embrittling range or by slow, or by step cooling through the embrittlement range.
- (b) Unembrittling treatment: Austenitised for some time as (a) and quenched. Tempered in the embrittling range using

the same time and treatment as the embrittling treatment in (a) followed by a de-embrittlement treatment using the same time and treatment as the temper above the embrittling range used in (a).

Woodfine (93) emphasized the importance of testing technique which makes the difference clear between 350°C embrittlement and temper brittleness.

The positive detection of segregation was observed by Plateau (130) after finding striations on the intergranular fracture surfaces. Low (114) indicated some sort of segregation through microhardness measurement. Some evidence of segregation was also found by Arkharov (131) in P-doped embrittled steels using a chemical analysis of the fracture surfaces.

Recently it has been shown that tensile plastic flow properties of some steels are affected by embrittlement and the effect of embrittlement was found to be mainly on the plastic strains required to (120) cause fracture. In NCMV steels Viswanathan et al found reduction of area 50 pct below in embrittled condition than in unembrittled condition. Squires and Wilson (68) observed a sharp drop in the reduction of area to zero in severe cases of embrittlement, figure 27, and enabled a time and temperature 'C' curve to be determined for embrittlement in a Fe-Ni-Mn maraging type steel, figure 28. Geniet and Knott (125) measured fracture stresses and tensile ductility at -196°C. Depending on the degree of embrittlement the fracture mode changed from ductile to intergranular as the embrittlement proceeded with a consequent decrease in the strain to fracture and true fracture stress.

## 2. Metallographic Methods

Different etchants have been used to differentiate between embrittled and tough steels. Cohen(160) tried ethereal picric acid solution containing zephiran chloride. This etchant worked well in those specimens where embrittlement was associated with phosphorus. Some other solutions based on picric acid showed similar results. These etchants produced a grooving effect on prior-austenite boundaries but no precipitates were ever found at the boundaries. In some cases ferrite boundaries were also attacked.

## 3. Auger Electron Emission Analysis

When high energy electrons or photons strike a solid matter (atoms), an electron in the inner shell is excited to a higher energy level or ejected making the whole atom unstable. The electron shell is then filled with an electron from the higher energy level and thus returning the atoms to a stable condition. In this process of refilling, the difference in energy between the two shells involved, can be released through emission of photons such as the generation of characteristics X-radiation. Alternatively this energy can be imparted to another electron which is then ejected from the atom. The electrons so ejected are called Auger electrons and occur at discrete energy levels characteristic of the emitting element. However, recent developments in the technique by Harris (123) in which he takes the second derivative of number of electrons emitted versus energy  $d^2N/dE^2$  have made Auger Electron Emission Analysis an attractive tool for studying segregation. Weber and Johnson (163) argued on a theoretical basis that  $dN(E)/dE(d^2N/dE^2$  in figures) that is, the peak height of the Auger electron spectra is proportional to the atomic concentration of the element being analyzed. Since

they were able to support the calculation with experimental results on potassium (deposited on germanium), it appears that the assumption of linearity of peak height with concentration is justified. Thus the height of the  $dN(E)/dE$  peak for each element is a measure of the amount of the particular element.

Auger electrons can be created at considerable depth from the surface depending on the energy of the primary bombarding electrons. However, before these electrons leave the material, most of them lose the discreteness of their energies due to inelastic collisions. Only those Auger electrons emitted from near the surface (5-15<sup>0</sup>Å) retain their discreteness and significantly contribute to the observed Auger peaks. Thus this technique has been used in analysing extremely thin surface layers. After analysing the given surface layer, it can be removed by sputtering using  $Ar^+$  ion bombardment and the next layer can then be analysed.

Prenotched samples having dimensions similar to that shown in figure 14(b) are held in an evacuated chamber at a pressure of  $10^{-9}$  torr. The specimens are fractured with a hammer inside the evacuated chamber at a sub-zero temperature, dependant upon the brittleness range of the particular specimen. Thus freshly fractured uncontaminated surfaces can at once be analysed.

#### 2.3.4 Theories of Temper Embrittlement

The well known phenomenon of temper brittleness found in low-alloy steels has now been established as a problem associated with certain impurity elements like P, As, Sn, Sb (80) and alloying elements like Ni and Cr, (114). The effect of silicon and

manganese has been reported to be enhancing (80). Even after such a long history of the problem some of the aspects of temper brittleness have yet to be described by an adequate theory.

Since the problem was known, a number of theories have been proposed at different stages on the basis of different characteristics exhibited by temper brittleness.

1. At first it was thought on the basis of high interfacial energy involved in the intergranular fracture than in cleavage fracture; that some sort of segregation is possible which might be accountable for this difference in interfacial energy.
2. Second mechanism was thought to be associated with development of hardening near the grain boundaries. This increase in hardening was associated with dislocation multiplication near the grain boundaries and result when any substitutional solute segregate to grain boundary, vacancies in turn, will move away from the grain boundaries and cause dislocation-vacancy interaction resulting in hardening. The embrittlement associated with sulphur was interpreted by this mechanism (132).
3. Thirdly, the embrittlement was again explained as a result of hardening effect near grain boundaries through solid solution hardening effect of segregants at grain boundaries like segregation of intermetallic compound in Ag-Mg type alloy. A similar type of mechanisms might be operating in steels.
4. Fourth theory regarding segregation was proposed by Hill and Martin (133). It is suggested that segregation of

impurity elements to grain boundary result in the development of lath like carbides at the grain boundaries which favour fracture along the length rather than cracking across the width. The result will be an intergranular fracture with fracture path along carbide-ferrite interface. The net effect on brittleness is two-fold; one is the segregation of impurity elements to cause decohesion and another is the development of lath shaped carbides at the grain boundaries.

The above mentioned theories basically favour equilibrium segregation models. Hondros, Low, Joshi and Stein attempted to explain the varying degrees of embrittlement by different elements through change in surface and grain boundary tensions they can produce to a unit change in grain boundary composition as discussed in section 2.2.1.

The problem of temper brittleness was also analysed by Steven and Balajiva (80) and Low et al (114). The following points were not explained by the equilibrium segregation model.

- (a) Steven and Balajiva (80) demonstrated that plain carbon steels in the presence of impurities do not exhibit intergranular brittleness.
- (b) Low et al (114) showed that certain major alloying elements should be present for the embrittlement to occur.
- (c) Another observation is that there is no experimental evidence to explain the role of alloying elements in a quantitative way. Only recently Auger analysis has made it possible to analyse the surface layers and thus the impurities and alloying elements present on the fracture surfaces.

Low et al observed microhardness difference between grain interior and grain boundaries to indicate the local hardening effect. Transmission electron microscopy has failed to show any kind of precipitation at the grain boundaries. If one analyses the segregation model, it is apparent that some sort of driving force is available for the segregation of impurities and this might be the result of misfit strains produced by impurities in the solvent lattice. This misfit strain can be obviously associated with the atomic radii of the corresponding impurity elements. Except phosphorus the remaining impurities Sb, As, Sn have larger radii than the solvent atom of  $\alpha$ -Fe resulting in considerable misfit strain.

Another possible factor affecting the segregation is the diffusion rate of impurities in the solvent lattice. As described in section 2.3.1 McMahon has recently illustrated the enhancing effect of Ni and Cr on embrittlement due to Sb and Sn. It was found that Ni and Cr causes a decrease in solid solubility of Sb and Sn in  $\alpha$ -Fe. McMahon further describes the driving force for segregation as arising from the misfit strain of the impurity in the solvent lattice.

In order to provide another driving force for the impurity element to segregate to grain boundaries, Capus suggested that double segregation involving segregation of alloying element during austenitization provided sites of chemical attraction for impurities to segregate during embrittling treatment. According to his proposal elements such as Ni, Cr, Mn, Mo segregate to austenite grain boundaries during austenitizing treatment and favour the segregation of P, As, Sn, Sb during

embrittling treatment. This theory can to some extent explain the role played by alloying elements in embrittlement but this has yet to be put on a quantitative basis. Another deficiency in this model is that it does not discuss the role of ferrite boundaries.

But recent investigations by McMahon (101) Stein (91, 106) and co-workers (117) have shown with the help of AES that both alloying elements and impurities segregate during embrittling treatment and disagreed with Capus (115) suggestion of double segregation.

Another possible model which explains different manifestations of temper brittleness has been proposed (116). According to this model, during austenitization, embrittling elements segregate to austenite grain boundaries and get entrapped there after quenching. But when the steels are tempered at 600°C, coarser carbides are developed at the prior austenite grain boundaries and embrittling elements are boiled off and disperse away from the carbides. On embrittling below 550°C after being tempered at 600°C, the embrittling elements diffuse back to <sup>the</sup> austenite grain boundaries.

Virtually, all the boundaries namely prior-austenite, carbide-ferrite and ferrite-ferrite boundaries receive a dose of embrittling elements but the effect is significant on carbide-ferrite boundaries owing to the non-plastic nature of carbides. On the other hand at lower temperature after being tempered at 600°C, the embrittling elements cannot segregate because of low diffusion rate, thus inhibiting the brittleness. This model proposed by Restaino and McMahon (116) was tested on Fe-0.02C-600ppm Sb alloy and it explained very well the C-curve behaviour

of temper-brittleness.

In the preceding discussion, it is important to note that not one theory has explained completely the role of alloying elements in embrittlement. Auger analysis has only identified the embrittling elements but the problem is to know the interaction of impurities P, As, Sn, Sb with alloying element like Cr, Ni, Mn etc in order to develop the exact understanding on speculations that alloying elements either enhance the segregation or modify the carbide morphology.

The work of McMahon's group (96) on the effect of Ni and Cr on solubilities of impurities and Guttman's theoretical work on segregation in ternary alloys appears to be a step in the right direction.

Recently Rellick and McMahon (121) proposed another mechanism regarding the embrittling effect of impurities (P, As, Sn, Sb) and the effect of carbide growth on impurities. It is suggested that during slow cooling through the embrittling region, precipitation of carbides takes place and during growth, the impurities are rejected ahead of the growing carbide and thus *the* carbide-ferrite interface is the favourable path for the fracture. This model has been tested on Fe-0.04 pct C with different level of impurities (As, Sn, Sb). This model has been found to be correct for these impurities but has yet to be shown the case for phosphorus.

## 2.4 Methods of Improving low-temperature toughness in steels

### 2.4.1 Grain Refinement

It has been well established fact that grain size can be used to strengthen the material and is also an economical method of

improving toughness.

Hall and Petch (134) proposed the basic relationship between strength and grain-size of any engineering material ie

$$\sigma_y = \sigma_i + d^{-\frac{1}{2}}K_y$$

where

$\sigma_y$  = yield stress

$\sigma_i$  = Lattice friction stress

$$= \sigma_0 + \sigma_*$$

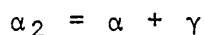
$2d$  = Grain diameter

$K_y$  = Constant - a measure of the difficulty of spreading yielding from grain to grain

Refinement of the grain size also leads to an increase in toughness and decrease in DBTT. In the case of brittle failure by cleavage, grain boundaries act as barriers to propagation of brittle cracks and thus a finer grain size increases toughness. Where brittle failure occurs along grain-boundaries due to segregation of impurities, the amount of segregate/unit area of grain boundary is thought to be reduced as the grain size is refined.

#### 2.4.2 Effect of heat treatment in the ( $\alpha + \gamma$ ) phase region

Allen (135) found that in Fe-Ni alloys if heating be carried out in the two-phase ( $\alpha + \gamma$ ) region of the iron-rich side, austenite is formed by the following diffusion controlled decomposition reaction



where  $\alpha_2$  is the martensite,  $\alpha$  is a low nickel BCC phase and  $\gamma$  refers

to the nickel enriched FCC phase which has been called reverted austenite. This reverted nickel-enriched austenite will transform wholly or in part to martensite while cooling to room temperature depending if nickel enrichment corresponds to an  $M_s$  above room temperature. Thus aging temperature in the two phase region should be such that the reverted austenite should contain sufficient nickel to be stable at room temperature.

The rate of austenite reversion has been found to be affected by austenite grain size (136) and microsegregation if present. Both the degree of microsegregation and grain size vary with the austenitising temperature. The rate of austenite reversion during ageing is also greatly accelerated by the presence of either retained austenite or nickel enriched regions in the martensite resulting from an incomplete austenitizing treatment (25). The 9% nickel cryogenic steels are generally used in quenched and tempered condition. During tempering, the austenite islands are formed and they serve the following purposes:

- a. The austenite islands act as sinks for impurity atoms and causes a scavenging effect during tempering (22,34).
- b. These austenite islands act as shock absorbers since FCC alloys have an excellent toughness even at low temperatures (27).
- c. Grain refining of the ferrite matrix takes place by formation of finely-dispersed austenite islands during tempering (25,27,28).
- d. Formation of austenite islands at prior austenite grain boundaries can also decrease temper embrittlement (23.)

It is necessary that these austenite islands should be made stable at  $-196^{\circ}\text{C}$  by either appropriate alloying elements or by suitable heat treatment (23). These steels show inferior impact energy when tempered at temperatures lower than  $500^{\circ}\text{C}$  and higher than  $600^{\circ}\text{C}$ . This situation can be explained by normal temper-embrittlement below  $500^{\circ}\text{C}$  and by instability of austenite islands formed during tempering at high temperatures.

In order to make a more economical steel, than 9%Ni steel for low-temperature use, 6% nickel steel has been developed (28) with the following objectives in view:-

1. Refinement of the microstructure.

For this purpose an addition of Mn is preferred which lowers the transformation temperature and increases the hardenability.

2. Increase in susceptibility to temper-brittleness by manganese is suppressed by the addition of molybdenum.

3. Molybdenum favours refinement of microstructure and to some extent stabilizes the reverted austenite.

The resulting 6% nickel steels contain 6% Ni, 1.1% Mn, 0.2% Mo and 0.07% C (23,28).

In 9% nickel steel it is found that the impact energy decreases as the tempering temperature rises above  $550^{\circ}\text{C}$  and is recovered above  $650^{\circ}\text{C}$ . The reasons for this recovery is that <sup>a</sup> fine martensite structure is formed from fine austenite grains formed just below the transformation temperature. When this fine martensite is tempered, a further refined structure is obtained by the formation of reverted austenite islands within this fine martensite. This treatment is therefore used in the development of 6% nickel steel for cryogenic applications.

Thus the addition of partial austenitization between conventional quenching and tempering remarkably improves the toughness after tempering. The microstructure obtained consists of fine ferrite matrix divided by many lath like martensite islands after partial austenitising. On tempering the fine austenite islands appear within martensite islands. As a result of this the microstructure of the steel consists of well tempered ferrite, tempered martensite containing fine reverted austenite islands. So this refined microstructure can obviously cause tremendous improvement in low temperature toughness of the alloy: because of the stability of this reverted austenite islands at cryogenic temperatures.

When a crack propagates, the stable austenite acts as a shock absorber and a resisting force acts against the propagation of brittle fracture through stress relaxation due to plastic deformation and partial transformation of austenite.

The benefits of this reversion heat treatment have been reported in Mn-Mo, Mn-Mo-V, Mn-Ni-Mo-Nb (137, 138) and 5-6% Ni steel (28). Wada (139) demonstrated the effect of partial austenitizing treatment on martensitic and bainitic NCMV steels containing high phosphorus and high tin levels and found a remarkable reduction in temper embrittlement in both steels.

#### 2.4.3 Effect of thermal-cycling treatment in the $\gamma$ and $(\alpha + \gamma)$ phase region

This technique (140)(141) involves repetitive austenitising treatment, each of very short duration, at a temperature barely sufficient to austenitize. In this process the grain refining effect of austenite transformation and the tendency for each

ferrite grain to transform on rapid heating to a single austenite grain is utilized to develop ultrafine grains. The extent of grain-refinement and its effect on mechanical properties depends upon the number of cycles.

The grain size is not a well defined concept in martensitic structure where laths or plates of martensite form. It is thought that by decreasing the mean size of martensite plate the yield strength of the martensitic structure can be increased. In almost all the investigations prior-austenite grain size is refined which causes refinement in the packet and lath size. In the past a number of techniques has been developed by Grange (142) Porter and Dabkowski (143) for refining prior austenite grain size in Fe-Ni alloys but the basic principle utilised in these techniques was to austenitize and then cool to room temperature. Miller (144) employed another technique for refining prior-austenite grain in Fe-Ni alloys and it consisted of severe cold work at room temperature followed by annealing in the  $(\alpha + \gamma)$  phase region and grain sizes  $\sim 1\mu\text{m}$  were achieved.

The cyclic treatment consists of holding the alloy in the  $\gamma$ -range just above the  $A_f$  temperature followed by holding in the  $(\alpha + \gamma)$  phase region just below the  $A_s$  temperature. The austenitizing temperature should be low to minimize grain growth while the temperature in the  $(\alpha + \gamma)$  phase region should be high enough to maximize the rate of decomposition. In the first part of the cycle when austenite transforms to ferrite through shear transformation, the grain-refinement effect is presumably through relieving the internal strain built up during the shear transformation. During holding in the  $(\alpha + \gamma)$  phase region nucleation of reverted austenite takes place through diffusional and

growth process. The microstructure is divided up by the nucleation of this reverted austenite at the boundaries of the martensite plates or prior-austenite grain-boundaries and time of holding during each cycle influences the extent of grain-refinement and mechanical properties of the alloy.

### 3.0 EXPERIMENTAL PROCEDURE

#### 3.1 Alloys Preparation

The alloys shown in Table 1 were prepared by vacuum melting. A nominal composition of Fe-8.0% Mn alloy was chosen in order to ensure a lath-martensitic structure on air cooling essentially free of epsilon martensite and retained austenite.

Alloy K1525 was prepared at British Steel Corporate laboratories, Hoyle Street, Sheffield in 1970 as a 9 Kg melt using Japanese electrolytic iron and electrolytic manganese and subsequently hot-rolled to 76 x 16 mm plate.

Alloys 134 and 137 were prepared in the department to give two ingots of approximately 4 Kg each. These alloys were prepared from Glidden iron and electrolytic manganese. An addition of 0.1% Ti and 0.1% Al was made to alloy 137 in order to scavenge residual carbon, nitrogen and oxygen. Unfortunately on analysis it was found that alloy 134 and alloy 137 contained 0.03% N. This contamination arose during the melting procedure. During vacuum melting it was found difficult to melt the iron due to poor coupling between the charge and the HF coil; by mistake the alloys were then prepared by air melting. However, it was decided to continue work on these alloys 134 and 137 until high purity alloys free of nitrogen become available.

Ingots of alloys 134 and 137 approximately of 55 x 55 x 150 mm were hot-rolled to 25 x 50 mm bar. In order to reduce banding in the material, these bars were coated in Berkatec after machining and soaked in an argon atmosphere for 50 hrs at 1100°C followed by oil quenching. These bars were then subsequently hot rolled to 6.4 x 50 mm plate.

### 3.2 Heat treatment

Alloy K1525 was austenitised for one hour at 1000°C in the form of 76 x 60 x 16 mm plate followed by water quenching.

Specimens of alloys 134 and 137 approximately 60 x 12 x 6.4mm were austenitised for  $\frac{1}{2}$  hour at 900°C followed by ice-brine quenching and air cooling. Tempering was carried out in neutral salt baths at 450°C. The heat treatment cycle designed for grain refinement is shown in figure 68 and V-notch Charpy specimens of K1525, and 137 were heat treated in salt baths at 740°C and 655°C with intermittent air cooling to room temperature. Hounsefield tensile specimens of K1525, used to measure the drop in reduction of area as a function of aging time, were heat treated at 450°C before and after thermal cycling treatment to study the kinetics of embrittlement. X-ray specimens were heat treated in the upper critical temperature range (450-650°C) in neutral salt baths to study the phase transformations in alloys 134, 137 and K1525.

### 3.3 Optical Metallographic Examination

Specimens in the heat treated condition were examined metallographically. It was found that mechanical polishing could be the simplest technique for metallographic study. Sometimes electropolishing was also carried out. The electrolyte used consisted of 10 pct perchloric acid in methanol.

Different etching techniques were tried. A single etch with 2 pct nital was used and also a double etch using 2 pct nital to lightly etch the polished surface followed by immersion in an aqueous solution of sodium thiosulphate plus sodium metabisulphite. This was a stain etchant and it developed a

blue-brown staining of the surface. This later etchant was developed by Schumann (29) and it was found satisfactory and independent of solution concentration. In practice, solutions of approx 35 pct concentrations were tried.

Another etchant consisting of one gram picric acid in 5 pct HCl in absolute alcohol was tried to reveal the pre-existing austenite grain boundaries. This etchant also worked reasonably if the quenched specimens were annealed at 230°C for 15 mins prior to etching.

Finally in alloy K1525, an attempt was made by heat treating the specimen for one hour at 500°C after being solution treated and etching in 2 pct nital for 10 secs. With this technique, the prior-austenite grain boundaries were successfully revealed and thus grain size, packet size were measured accurately.

#### Grain Size Measurements

Mean linear intercept method, often called the Heyn intercept method, was used to measure the grain size. It measures the chord length defined by the intersection of a random straight line by the grain boundaries in the plane section of the polish.

The mean linear intercept, m.l.i, is often given the symbol  $\bar{d}$ , where:-

$$\bar{d} = \frac{L}{n}$$

and L = length of the random line on the planar surface

and n = No. of grains occupying this line.

For each microstructure about 200 intercepts were measured giving an accuracy ~10% in the grain size.

The grain size quoted is the mean true grain diameter  $\bar{D}$  given by:-

$$\bar{D} = 1.75\bar{d}$$

### 3.4 Hardness Measurements

Hardness measurements were made on a Vickers Hardness machine using a load of 30 kg. An average of ten impressions were made per treatment. The errors quoted are the 90% confidence limits.

For aging experiments at a particular temperature the same specimen was used, aged intermittently.

The variation of hardness with aging time for alloy K1525, was determined at 350°C, 400°C and 450°C to establish the kinetics of aging in this alloy. Changes in hardness of alloys 134 and 137 were monitored during aging at 450°C up to aging times of 100 hours.

Hardness measurements were also taken of all the alloys in different heat-treated condition in relation with their ductile-brittle transition temperatures including thermally cycled alloys of K1525, and 137.

### 3.5 Tensile Testing

The reduction in area of tensile specimens was used as a measure of the ductility of the material. Modified Hounsefield tensile specimens with a diameter of 3.047 mm and gauge length of 10 mm were tested at a strain rate of 0.5 min<sup>-1</sup> at -78°C in an Instron tensile testing machine. In alloy K1525, embrittlement kinetics was studied through tensile ductility tests after aging the tensile specimens over a temperature range of 300-600°C. In the same alloy, the cryogenic tensile properties were also

determined before and after thermal-cycling treatment.

### 3.6 Impact Toughness Testing

Ductile-brittle transition temperatures of the alloys were determined in various heat treated conditions using sub-standard Charpy V notch specimens 5 x 10 x 55 mm.

Low-temperature tests were carried out using cardice and acetone ( $-78^{\circ}\text{C}$ ) and liquid nitrogen ( $-196^{\circ}\text{C}$ ).

Temperatures above room temperature were obtained with an oil bath and fluidised sand bath.

Thermocouples were spot welded to the specimen close to the V-notch and connected to a temperature recorder, and the temperature at the moment of fracture was noted within  $\pm 3^{\circ}\text{C}$  in order to avoid any temperature drop due to time delay in transferring the test pieces from its temperature environment to the impact testing machine.

### 3.7 Dilatometric Analysis

To determine the austenite and martensite transformation temperatures of the alloys, dilatometric analysis was performed on specimens 3 mm diameter x 20 mm long machined from the as solution-treated Charpies. The tests were performed on a 'Linseis' horizontal dilatometer. A simultaneous recording was made of the dilation and temperature on a 2 pen recorder. In alloy K1525 the test was performed by first heating the specimen to  $1000^{\circ}\text{C}$  at the heating rate of  $50^{\circ}\text{C}/\text{min}$  and the austenite transformation temperatures noted during this heating up period. After soaking for approximately 10 minutes, the specimen was

allowed to cool at a cooling rate of  $50^{\circ}\text{C}/\text{min}$  and the martensite transformation points noted. Table 3 summarizes the  $A_s$ ,  $A_f$ ,  $M_s$ ,  $M_f$  temperatures of alloys K1525, 134 and 137. In the case of alloys 134 and 137 the heating was done up to  $900^{\circ}\text{C}$  under the same heating and cooling conditions as those employed on alloy K1525.

### 3.8 X-ray Diffraction Analysis

Previous work on Fe-Ni-Mn type maraging steel (67) and low carbon manganese steel (1,3) indicated that rapid embrittlement occurred on tempering these alloys at  $450^{\circ}\text{C}$ . It was therefore decided to temper quenched alloys at  $450^{\circ}\text{C}$  to examine if embrittlement could be induced at this temperature. However, in order to isolate the effect of tempering time at  $450^{\circ}\text{C}$  on impact properties, it was necessary to monitor changes in hardness and formation of reverted austenite which may by themselves affect impact properties.

X-ray examination using a Philips Diffractometer was therefore carried out on heat treated samples and on specimens subjected to grain-refinement through thermal-cycling treatment, to analyse for austenite and epsilon martensite. Copper radiation was chosen in order to separate the diffraction peaks at small differences in Bragg angle, as chromium and cobalt radiations also give good dispersion of the lines, but low intensity, and molybdenum radiation gives a large number of intense lines, but poor dispersion. Thus copper radiation was a good compromise as the tube can be operated at high intensity and gives adequate dispersion of the diffraction lines. Using copper radiation there is of course a high level of fluorescent radiation from ferritic materials, but by carefully selecting the pass band of the

discriminator it is possible to reduce the level of fluorescent radiation by approximately two orders of magnitude for a 20% reduction in the intensity of the  $\text{CuK}_\alpha$ . This small loss in intensity is more than compensated for by the fact that the dispersion of the lines is sufficiently high for the  $(111)_\gamma$  and  $(110)_\alpha$  reflections to be measured.

### Method for X-ray Analysis

The method for X-ray analysis was based on comparing the integrated intensities of reflection planes (hkl) of martensite and austenite phases.

The integrated intensity of a diffraction line was calculated from the following equation as shown by Durnin and Ridal (161).

$$I_{(hkl)} = n^2 V m (LP) e^{-2M} (F.f)^2$$

where  $I_{(hkl)}$  = Integrated Intensity of (hkl) reflection

$n$  = Number of cells in  $1 \text{ cm}^3$

$V$  = Volume exposed to X-ray beam in  $\text{cm}^3$

$LP$  = Lorentz-Polarization factor

$m$  = Multiplicity of (hkl) planes

$e^{-2M}$  = Debye-Waller temperature factor

$F$  = Structure factor

$f$  = Atomic Scattering factor

For  $n^2 V$  it is possible to substitute  $\frac{V}{v^2}$  where  $v$  is the volume of the unit cell.

$$I_{(hkl)} = \frac{V}{v^2} m (LP) e^{-2M} (F.f)^2$$

If  $\alpha$  and  $\gamma$  are the two phases present, hence

$$\frac{V_\alpha}{V_\gamma} = \frac{I_\alpha}{R_\alpha} / \frac{I_\gamma}{R_\gamma}$$

where  $R_i$  = Theoretical intensity for phase i at a particular reflection angle.

And  $V_\alpha + V_\gamma = 1$

$$\therefore V_\gamma = \frac{I_\gamma/R_\gamma}{\frac{I_\gamma}{R_\gamma} + \frac{I_\alpha}{R_\alpha}}$$

If  $\alpha, \gamma, \epsilon$ , three phases are present then for random orientation:

$$V_\epsilon = \frac{I_\epsilon/R_\epsilon}{\frac{I_\alpha}{R_\alpha} + \frac{I_\gamma}{R_\gamma} + \frac{I_\epsilon}{R_\epsilon}}$$

The theoretical intensity factor 'R' was calculated from

$$R = \frac{1}{v^2} m (LP) e^{-2M} (F.f)^2$$

where R = Theoretical Intensity

v = Volume of the unit cell

m = Multiplicity factor of particular plane (hkl)

LP = Lorentz Polarization factor

$$= \frac{1 + \cos^2 2\theta_c \cos^2 2\theta}{\sin \theta \sin 2\theta}$$

where  $\theta$  = Bragg Angle for the particular reflection

$\theta_c$  = Bragg Angle for the monochromating crystal

$e^{-2M}$  = Debye-Waller temperature factor

F = Structure factor

f = Atomic Scattering factor

In polarization factor, account is taken of the fact that a beam of X-rays monochromatised by a graphite crystal is not completely unpolarized. Thus LP is calculated with correction factor  $\theta_c$  (160).

## Assumptions

The following assumptions have been made while calculating the theoretical intensity of different reflections (hkl).

- (i) The Debye-temperature has only been determined for ferrite and it is assumed that this value applies to both austenite and martensite. A range of values is given in "International Tables for X-ray Crystallography" but an average 420 K used by Averbach and Cohen (160) has been taken.
- (ii) As the radiation used ( $\text{CuK}_\alpha$ ,  $\lambda = 1.542 \text{ \AA}$ ) is close to the absorption edge of iron, correction has been made to the usual atomic scattering factor for different reflections to allow for dispersion. Averbach and Cohen used the following correction.

$$f = f_0 - \Delta f$$

f = Effective Scattering factor

$f_0$  = Usual Atomic Scattering factor

$\Delta f$  = Decrement in the Atomic Scattering due to interaction with the K electrons usually taken as 4.0 units.

The Multiplicity factor for hkl reflections is as follows:

Cubic System		Hexagonal System	
h00	6	h0.0	6
hhh	8	00.1	2
hh0	12	h0.1	6
hk0	24	10.1	6
hkl	48	hk.0	6

Structure Factor 'F' is given by

$\alpha$ (B.C.C.)

F = 2f when (h + k + l) even

$\gamma$ (F.C.C.)

F = 4f when h + k, k + l, h + l are even integers

$\epsilon$ (c.p.h.)

$$|F|^2 = 4f^2 \text{Cos}^2 \pi \left\{ \frac{h + 2k}{3} + \frac{l}{2} \right\}$$

'f' Atomic Scattering factor for different reflections (hkl) depends on composition of the alloys and <sup>were</sup> taken from the International Tables.

Calculated values of R for various phases and reflections are shown in Table 4.

### 3.9 Electron Microscopy

#### Transmission Electron Microscopy

Thin foils were prepared from discs cut from machined cylinders of 3 mm diameter. Discs were grounded on 600 grade paper. Different solutions were tried for dishing and polishing with varying success. A solution of 10 pct perchloric acid in methanol and 25 pct perchloric acid in methanol (methanol containing water <0.01%) was finally used for dishing and polishing respectively. Final thinning was carried out by electropolishing using what is essentially a "window" technique with the polishing potential being controlled through a potentiostat. The problems with oxide contamination of the foil were solved by controlling the temperature in the polishing tank at -40°C with the ~~acid~~ of liquid nitrogen.

After thinning the foils were examined using JEM 100B electron microscope at 100 kv.

### Replication

A replica technique has been developed to extract carbides from polished surface and fracture surfaces. Preparation of the carbon extraction replicas consisted of the following steps:

- (1) Evaporation of a carbon layer in vacuo on to the surface to be replicated.
- (2) Immersion in a 2% Bromine in methanol solution at  $-20^{\circ}\text{C}$  for 1 to  $1\frac{1}{2}$  hours to loosen the carbides along with the carbon film (165).
- (3) Washing the replicas in ethyl alcohol and water, then mounting on a grid.

After mounting, they were examined with JEM 100B at 50 kv.

### 3.10 Scanning Electron Microscopy

Specimens for the SEM were selected by sectioning the fractured part of the Charpy specimen, and standard Hounsfield specimen. After tensile testing the fractured parts were kept in a desiccator to protect them from contamination. Often the surfaces were cleaned especially when the fractures were not fresh to remove extraneous material and anything that would outgas in the vacuum. The percentage fracture mode was determined by point counting and ten different regions were selected from one fracture surface.

The EDAX energy dispersive X-ray analysis system mounted within the SEM system was used to analyse the unidentifiable particles on the fracture surface.

### 3.11 Auger Electron Emission Analysis

The embrittled alloys which exhibited intergranular fracture were subjected to Auger Analysis to analyse the fracture surfaces. Specimens were machined from broken sub-standard Charpies.

#### AES Measurements

AES measurements were made on small cylindrical specimens 3 mm diameter x 20 mm long with a 60° V-notch in the centre, held in a Fe-9%Ni specimen holder. The design of the holder and sample geometry is shown in figure 14(b). The samples were cooled to -80°C and were fractured in situ at pressures  $\sim 10^{-10}$  torr, using the Harwell impact stage. AES analyses were performed immediately after fracture.

A vacuum Generator cylindrical mirror analyser (CMA) of the type described by Bishop et al (166) was used for the AES analysis with an integral electron gun providing a spot size on the sample of 4  $\mu\text{m}$ . The differential energy spectra were recorded at a modulation of 3v peak to peak, a primary energy of 2.5 keV and a specimen current of 4  $\mu\text{A}$ .

Argon-ion sputtering was used to remove layers progressively from the surface, thus allowing the determination of the composition profile of the elements as a function of distance from the fractured surface. Each ion-bombardment comprised 9  $\mu\text{A}$ -minutes at 3 kV, which may be approximated to a removal of  $\sim 5$  monolayers.

## Quantification of AES spectra

It is well established that to a good approximation the amplitude of an Auger Peak in the  $dN(E)/dE$  spectrum is proportional to the atomic concentration of the element giving rise to that peak (163). Problems of absolute quantification can be avoided by expressing results as ratios of prominent peaks of alloying or impurity elements to a chosen prominent peak of the matrix, provided that the matrix elements always dominate the surface composition. The latter condition was not fulfilled in the present experiments. Accordingly the peak heights of Mn(540 eV), P(120 eV), and N(380 eV) were first expressed as percentage ratios of the Fe703 eV peak. The Mn spectra were calibrated using AES spectra obtained from both cleavage and ductile fracture surfaces, which were approximated to the bulk Mn concentration.

Conversion from such peak ratios to approximate atomic percentages requires information about relative elemental sensitivities. A widely used and comparatively simple approach to the conversion is to use the elemental spectra and scale factors in the "Handbook of Auger Electron Spectroscopy" published by Physical Electronics Industries Inc (PHI) (168). This approach was used in the present investigation using the elemental sensitivities. The values for Mn, N and P are 0.79, 1.60 and 2.07 respectively.

Carbon concentrations were calculated relative to the Fe (703 eV) peak height.

## 4.0 EXPERIMENTAL RESULTS

### 4.1 Embrittlement Studies

#### 4.1.1 Heat-treated Alloys and Microstructure

##### Dilatometric Analysis

The results from the dilatometric tests are given in Table III. All the alloys, K1525, 134, 137, showed more or less the same transformation temperatures when they were heated and cooled at the rate of 50°C/minute.

##### Metallographic and X-ray Examination

Originally alloy K1525 was solution treated at 1000°C followed by water quenching. Subsequently alloys 134 and 137 were austenitised at 900°C followed by ice-brine quenching or air cooling. The austenitising temperature and quenching condition were altered to reduce the austenite grain size and try and achieve brittle failure by cleavage (7) rather than intergranular failure.

The first series of alloys of K1525 and 134 were solution treated at 1000°C for 1 hour and water quenched, and/or ice-brine quenched. Both alloys showed  $\alpha$  lath-martensite structure. The optical micrographs are shown in figure 75. The prior-austenite grain size was found to be ~80-90  $\mu\text{m}$  in both these alloys. Each austenite grain was found to contain at least (3-4) packets of (20-25  $\mu\text{m}$  approx) in size. The X-ray analysis in both these heat-treated conditions showed that the alloys were completely  $\alpha$  lath martensitic with  $\epsilon$ -martensite only <2 pct. The X-ray analysis of alloys in the water quenched, ice-brine quenched and air-cooled states are given in table II along with other microstructural details.

Some metallographic specimens of alloy 134 were heat treated at  $900^{\circ}\text{C}/\frac{1}{2}$  hour and ice-brine quenched or air cooled to room temperature. Optical metallographic studies in both these heat-treated conditions once again indicated that the heat-treated microstructure was completely  $\alpha$  lath martensite. But this time the prior-austenite grain size was found to be  $\sim 65-70 \mu\text{m}$ . An optical micrograph is shown in fig. 75(b). Once again the X-ray analysis in ice-brine quenched and air cooled condition also showed that the alloys are completely  $\alpha$  lath martensitic with  $\epsilon$ -martensite less than 2 pct. Only  $(10.1)\epsilon$  reflection of  $\epsilon$ -phase was found in all these heat-treated conditions. The X-ray analysis are given in Table II.

#### Effect of Titanium and Aluminium Additions

In another series of alloys the addition of 0.1Ti and 0.1Al was added to scavenge free nitrogen and carbon as  $\text{Ti}(\text{C},\text{N})$ ,  $\text{AlN}$  and to cause grain refinement. This alloy is designated as 137 and was first given the same solution treatment conditions as K1525 ie  $1000^{\circ}\text{C}/1\text{h-WQ}$ . Some specimens of this alloy 137 were heat treated at  $900^{\circ}\text{C}/\frac{1}{2}$  hour - IBQ, or air cooled.

The optical metallographic examination showed the prior-austenite grain size around  $(60-70 \mu\text{m})$  after  $1000^{\circ}\text{C}/1\text{h}$  in water-quenched states. The grain size was  $(45-50 \mu\text{m})$  after  $900^{\circ}\text{C}/\frac{1}{2}\text{h}$  in ice-brine quenched and air-cooled states. In each case the number of packets within the austenite grains were around  $(3-4)$  approx in each grain. A typical optical micrograph of alloy 137 showing lath-martensitic structures is shown in fig. 76.

Transmission Electron microscopic studies indicated that in all cases, the packets were further composed of bundles of parallel laths with high density of dislocations but there was found no

internal twins in these laths. Electron micrographs of a typical lath-martensitic structure is shown in figures 77, 78.

#### 4.1.2 Impact Toughness Results and Fractography

##### Impact Toughness Data

The ductile-brittle transition curves of the alloys K1525, 134, 137 in various heat-treated condition are shown in Figs. 31-35. Table XIX summarizes the impact transition temperatures and low-temperature fracture mode along with AES analysis results. Figs. 31, 3 illustrate the effect of cooling rate on the shift in impact transition temperatures irrespective of the difference in N level between K1525 (low N level) and 134 (high N level). Alloy K1525 after being solution treated at 1000°C/1h-water quenched showed impact transition temperature around +115°C at 40.0J whereas alloy 134 after ½ hour at 900°C but ice-brine quenched showed impact transition temperature of around +35°C in spite of its higher N level. Evidently this difference in impact transition temperature is primarily because of difference in cooling rate. The low temperature fracture mode was predominantly cleavage in IBQ state while it was completely IG in the water-quenched state.

On the basis of this critical effect of cooling rate after solution treatment on the shift in impact transition temperature, it was decided to carry out the effect of air-cooling on high N alloy 134. Thus one batch of specimens of 134 were ice-brine quenched and the other were air-cooled after solution treatment, but this time they were solution treated at 900°C/½ hour. The ductile-brittle transition curves of alloy 134 in the ice-brine quenched state and air-cooled state are plotted in fig 32. In this

case, the impact transition temperature at 30.0J was  $+35^{\circ}\text{C}$  in ice-brine quenched state but on air-cooling it shifted to  $+375^{\circ}\text{C}$ . The low temperature fracture mode was almost <sup>completely</sup> cleavage in IBQ but in air cooled state, it was 100 pct intergranular.

Thus the effect of cooling rate was found to be more critical if one compares the ductile-brittle transition temperatures in IBQ, WQ and AC states. In the air-cooled condition, it was decided to look at the intergranular fracture surfaces with the aid of electron microscopy using carbon-extraction replicas as an attempt to find any precipitates or any second-phase particles on the fracture surfaces.

#### Hardness Data

Table XX summarizes the hardness data for alloys 134, 137, K1525 in different heat treated conditions. The as water-quenched hardness in alloy 134 after solution treatment of  $1000^{\circ}\text{C}/1\text{h-WQ}$  was  $\approx 29\text{Hv}_{30}$  higher than that in alloy K1525. Presumably this rise in hardness could be attributed to the presence of higher N level (0.03%) in solid solution in alloy 134 than that in alloy K1525 (0.003%).

Another noticeable difference in the hardness value was that in air cooled and ice-brine quenched alloy of 134 from same solution treated conditions ie ( $900^{\circ}\text{C}/\frac{1}{2}\text{h}$ ), the as air-cooled hardness was  $\approx 18\text{Hv}_{30}$  higher than that in ice-brine quenched state, presumably due to precipitation of carbides and nitrides on air cooling.

In alloy 137 the initial hardness in the water quenched condition after  $1000^{\circ}\text{C}/1\text{h}$  treatment was  $\approx 44\text{Hv}_{30}$  less than its

counterpart alloy 134 with no titanium and aluminium additions. This difference seems primarily because of interstitial tieing-up effect of Ti and Al additions and to cause drop in initial hardness. A similar situation was observed in ice-brine quenched state and air-cooled state after solution treatment of  $900^{\circ}\text{C}/\frac{1}{2}\text{h}$ . The hardness drop in 137 in the ice-brine quenched and air-cooled conditions was  $\approx 37\text{Hv}_{30}$  and  $\approx 27\text{Hv}_{30}$  respectively, compared with its counterpart alloy 134 in the same heat treated condition; ice-brine quenched and air cooled.

### Influence of Ti and Al additions on Impact Toughness

Figure 33 shows the impact transition temperature in alloy 137 in ice-brine quenched and air-cooled conditions. The impact transition temperature in air-cooled state was  $+135^{\circ}\text{C}$  higher than that in ice-brine quenched state. This rise in (ITT $^{\circ}\text{C}$ ) could be partly reflected from rise in  $\text{Hv}_{30} \approx 19$  in the air-cooled state and partly could be by segregation of untied nitrogen during air-cooling to room temperature.

The hardness data and the impact transition temperature results are given in Table XX along with fractographic and Auger analysis results. Figs 34 and 35 show the comparative effect of Ti and Al additions on the shape of impact transition curve in the ice-brine quenched and air-cooled states in alloys 134 and 137. In figure 34, the shift in the impact transition temperature was negligible in the ice-brine quenched state but a rise of 36.0J in the upper shelf energy was found in alloy 137. This effect of Ti and Al addition was quite marked in the air-cooled condition as shown in figure 35. The impact transition temperature at 30J dropped from  $+375^{\circ}\text{C}$  (134) to  $+271^{\circ}\text{C}$  in alloy 137. Once again a similar rise of nearly 70.0J was noticed in the upper shelf energy in alloy 137. It seems from figure 34 and figure 35 that the addition of Ti and Al not only

depresses the impact transition temperature but also raises the upper shelf energy.

### Fracture Surfaces Examination

The fracture surfaces of the alloy K1525, 134 showed completely intergranular fractures under impact testing at room temperature after being water quenched from the solution treatment of 1000°C/1h. The scanning electron micrographs are shown in figs 80 and 81 (a). But the fracture mode completely changed to cleavage on ice-brine quenching and very occasionally grain-boundary facets were observed. Figure 82 shows SEM of fracture surface of alloy 134 (high N) ST1000°C/1h - ice-brine quenched.

In alloy 137 (0.1Ti-0.1Al) the fracture mode was once again predominantly intergranular after solution treatment of 1 hr, 1000°C-WQ. At this time only 70-80 pct was intergranular, whereas the remaining 20-30 pct was quasi-cleavage. The interesting point to note was the fine precipitation of Ti(C,N), AlN particles on the grain-boundary facets. A typical scanning electron micrograph of fracture surface of alloy 137 after being solution treated at 1000°C/1h water quenched and impact tested at room temperature is shown in figure 83.

In the second series of alloys of 134 and 137 solution treated at 900°C/½h followed by ice-brine quenching and air-cooling, showed completely cleavage fracture mode on impact testing in the ice-brine quenched state but it changed to smooth-intergranular mode on air cooling. Figures 84, 85 show scanning electron micrographs of fracture surfaces in the ice-brine quenched state of alloys 134, 137 respectively. The fracture mode was almost cleavage (100 pct cleavage) below the transition in alloy 134 but again in 137

even on ice-brine quenching, fracture mode is 80-90% cleavage but still the remaining 10% is grain-boundary facets. A typical micrograph taken from three different portions of fracture surface is shown in figure 85. 85(a) shows the fracture mode in the centre of the fracture surface. On the grain boundary facets, a fine ppt of Ti(C,N), AlN were noticed. Figure 86,88 shows the scanning electron micrographs of alloys 134,137 in the air-cooled condition. The fracture mode was almost <sup>completely</sup> intergranular in both these cases below the transition. In alloy 134, a change in fracture mode was observed from completely intergranular in the centre to small amount of cleavage towards notch and opposite to notch. A typical scanning fractograph is shown in figure 86(a,b,c). In alloy 137 this difference was not found in the fracture mode away from the centre as shown in figure 88 (a,b,c). The carbon extraction replicas from the fracture surface of Charpy impact specimen having predominantly intergranular fracture mode, showed no evidence of precipitation. The fracture surface was found almost <sup>completely</sup> clean as shown by the electron micrograph in figure 87.

For all the alloys at temperatures above the ductile-brittle transition, the fracture mode consisted of ductile dimples. Sometimes these dimples were associated with inclusions. A typical example of the ductile fracture observed is shown in figure 81(b).

#### Auger Electron Emission Analysis

In alloy K1525 in the as water-quenched condition, in situ impact testing produced a predominantly intergranular failure mode with crack propagating along the prior-austenite grain boundaries. A typical fractograph of alloy K1525 (low N) and alloy 134 (high N) in the water-quenched state after being solution treated at 1000°C/1 hour is shown in figure 80 (a,b), figure 81(a)

respectively. The fracture mode was almost <sup>inter</sup>intergranular with some transgranular areas, possibly having been produced at the intersection of an annealing twins with the prior-austenite grain boundaries.

Representative spectra taken from the as fractured surface in the water-quenched condition are shown in figure 55. The quantification of AES spectra, in terms of atomic concentrations is presented in Table XIV for the alloy K1525. The spectra of the as-quenched material exhibited several important features. Firstly, no evidence was obtained for the grain-boundary segregation of any of the classical embrittling elements of temper embrittled steels (ie Sb, Sn, P or As). Secondly, the enhanced levels of S and N relative to the bulk were detected on the fracture surface. Although the sulphur signal probably originated at the MnS particles which were present on the ~~inter~~intergranular areas. Thirdly, the Mn concentration on the fracture surface, as deduced by the quantification procedure, approximated to that of the bulk.

These results therefore demonstrated that no significant segregation of alloying or impurity elements has occurred during the austenitizing treatment and a possible contributory factor in the intergranular fracture of the as-quenched material is the presence of N at the grain boundaries.

The concentration profiles of the elements Mn, N and C as a function of distance from the grain boundary for the alloy K1525 in the as-water-quenched condition is shown in figure 58. It should be noted that the Mn signal decreases on ion-bombardment to levels below that of the bulk value due to the preferential sputtering of Mn (155) and hence no positive conclusions can be made regarding Mn

distributions as a function of distance from fracture surface. However, from a comparison of the sputtering profiles shown in figure 58 it can be deduced that the enhanced N concentration was limited to the first few monolayers of the boundary.

Another interesting feature of the sputtering profiles in the as quenched condition was that the C level increased with bombardment. This suggests a possible 'C' de-segregation during austenitisation and quenching which could also strengthen the matrix relative to the boundary, resulting in intergranular fragility. But still the predominant factor affecting intergranular brittleness in the as water-quenched state is the segregation of N to the prior-austenite grain boundaries. The results of the quantification of the AES spectra (Figs 60-62) in terms of atomic concentration taken from the fracture surfaces of alloy 134, 137 in the ice-brine quenched condition and air-cooled condition after being solution treated at  $900^{\circ}\text{C}/\frac{1}{2}$  hour are shown in Table XVI. In situ impact testing produced a predominantly cleavage fracture in the ice-brine quenched state whereas it was completely intergranular in the air-cooled condition.

The results of the Auger analysis on sputtering in alloy 134 (high N) in the air-cooled condition are given in Table XV. As shown the build-up of both Mn and N above the bulk level was detected on the prior-austenite grain boundaries. Once again on sputtering, the AES results indicated the de-segregation of carbon.

In Table XVI, in the ice-brine quenched state of alloys 134, 137 the N level on the fracture surface, possibly on the interpacket or other low-angle boundaries, was above the bulk level, although such enhancement lies within the experimental error of the bulk.

The smaller amount of N in alloy 137 could be because of Ti and Al addition. But in <sup>the</sup> air-cooled condition, the level of Mn and N <sup>were</sup> both raised considerably higher than the bulk level in both alloys 134, 137. Once again the N level was less  $\approx 3.5$  at pct in alloy 137 where as in 134, N level was  $\approx 5.4$  at pct in one specimen and  $\approx 8.3$  at pct in another specimen. The increase in N level at the grain boundaries resulted in rise of Mn level which indicated a strong N-Mn interaction.

Figs. 63, 64 show the effect of cooling rate on the shift in impact transition temperature along with the variation in grain-boundary concentration of Mn, N in alloys K1525, 134, 137. This curve shows that on air cooling the impact transition temperature <sup>increased to a</sup> maximum in alloy 134 with increase in Mn and N concentration at the grain boundaries.

#### 4.1.3 Effect of Aging at 450°C

##### Hardness Data

The variation of hardness with aging time at 450°C for alloys 134 and 137 after being solution treated at 900°C/½h and ice-brine quenched, is shown in figs 42, 44. The errors shown are the 90% confidence limits.

Alloy 134 (Fig.42) showed a higher as-quenched hardness than alloy 137 and exhibited two age-hardening peaks with a rise in hardness of  $\approx 10\text{Hv}_{30}$  after 1.0 minute and 10 mins of aging respectively. The first peak is thought to be due to  $\text{Fe}_4\text{N}$  which appears to be replaced by  $\text{Mn}_3\text{N}_2$  on longer aging (89, 96). Hardness dropped rapidly after approximately 2 hours, falling  $\approx 50\text{Hv}_{30}$  after 100 hours of aging: whereas the reverted austenite started appearing after 60 hours of aging at 450°C.

In contrast alloy 137 (0.1Ti-0.1Al) Fig 44, showed negligible hardening  $\approx 5Hv_{30}$  after 6 minutes, but hardness started falling after nearly 10 minutes at  $450^{\circ}C$ . In this case the hardness only fell  $\approx 20Hv_{30}$  after 2 hours but remained constant over the rest of aging time till 100 hours.

Alloy K1525 showed slight hardening at  $450^{\circ}C$ . The hardness first increased by  $\approx 12Hv_{30}$  in 10 minutes but it started falling after 12 minutes and had fallen nearly  $25Hv_{30}$  after 100 hours of aging at  $450^{\circ}C$ . In figure 50, the variation in hardness with aging time in alloy K1525 after being solution treated at  $1000^{\circ}C/1h$ , water quenched and aged at  $350^{\circ}C$ ,  $400^{\circ}C$ ,  $450^{\circ}C$ , is shown. The hardening characteristics of alloy K1525 aged between  $350-550^{\circ}C$ , is plotted in an Arrhenius manner in Fig 52 and will be reported in section 4.1.5.

### X-ray Diffraction Analysis

The results of phase analysis during aging at  $450^{\circ}C$  are summarized in Tables (V-vIII) for alloys 137, 134, K1525 after being solution treated at  $900^{\circ}C/1/2$  hour, air cooled, ice-brine quenched and  $1000^{\circ}C/1h$  water-quenched respectively. In alloy 137, the aging was carried out up to 100 hours in order to see the rate of formation of reverted austenite and its stability at liquid nitrogen temperature. It is interesting to see in Table V & VI that after 100 hours of aging, the amount of reverted  $\gamma$  is 3.3% in alloy 137 (0.1Ti-0.1Al) after being ice-brine quenched and 5.7% after being air-cooled from the solution treated condition. Another point to note was the difference in the amount of reverted  $\gamma$  from 3.3 pct after 100 hours to 7.4 pct after 1000 hours in IBQ state but in air-cooled condition the amount of reverted  $\gamma$  remained more or less the same

ie nearly 5.7 pct after 100 hours and 1000 hours of aging at 450°C. In both these heat-treated conditions, the reverted  $\gamma$  started appearing after 60 hours of aging at 450°C, first only (111) reflection appeared and a measurable amount formed after 75 hours of aging at 450°C. In all the X-ray traces (10.1) <sub>$\epsilon$</sub>  reflection was so faint that it could not be measured and moreover, it seemed that  $\epsilon$ -martensite formation was merely taking place via plastic deformation induced martensitic transformations. In all these measurements of %age phases, the combination of six peaks were taken in order to even out the error due to preferred orientation etc. It was interesting to find that the reverted austenite which formed after 1000 hours at 450°C was stable at liquid nitrogen temperatures in both ice-brine quenched and air cooled.

As the prime objective for these phase-transformation studies was to isolate the embrittlement during aging at 450°C, in  $\alpha$  lath-martensitic state from being affected through phase-transformation effects of forming  $\gamma$  and  $\epsilon$ -martensite, thus in alloys 134 (high N) and K1525 (low N), the aging studies were made up till 100 hours at 450°C. In both these alloys, once again (111) peak started appearing after 60 hours but measurable amount formed after 75 hours; 1.6% $\gamma$  in alloy 134 (high N) and 1.5% $\gamma$  in alloy K1525 (low N), after being ice-brine quenched and water-quenched from 900°C/½ hour and 1000°C/1 hour respectively. It was interesting to find that in 134 (high N) and K1525 (low N) the amount of reverted austenite after 100 hours of aging was nearly 1.8%; almost the same in both cases. At this stage it would be worth mentioning that the amount of reverted austenite was 1.5 pct greater in IBQ and 3.9 pct greater in AC in alloy 137 (0.1Ti and 0.1Al) than its counterpart alloy 134 (high N). Perhaps this difference could be attributed to

the presence of Ti and Al in alloy 137.

### Metallographic Examination

Optical metallographic studies failed to show any difference in the micro-structure <sup>of these alloys</sup> on aging even after 1000 hours <sup>at 450°C</sup> in these alloys. Electron microscopy <sup>showed</sup> the interlath appearance of reverted  $\gamma$  along with highly annealed structure of  $\alpha$ -martensite after longer aging of 1000 hours at 450°C. Fig 79 shows the transmission electron micrograph of alloy 137 (0.1Ti & 0.1Al) aged for 1000 hours at 450°C after being solution treated at 900°C/½ hour and ice-brine quenched. Note <sup>the</sup> sub-boundaries in the micrograph in this highly polygonised structure.

### Impact Toughness Data

The effect of holding time at 450°C on the shift in ductile-brittle transition temperature in alloys 134 (high N) and 137 (0.1Ti & 0.1Al) is shown in figures 43, 45. In alloy 134 (high N) the aging at 450°C was found to have a profound effect on the shift in ductile-brittle transition temperatures. In the first six minutes, the transition temperature shifted from +25°C to +175°C. In one hour of aging, the DBTT <sup>increased</sup> to +225°C. But on aging up till 10 hours at 450°C, the transition temperature again dropped back to +150°C. Similarly, the effect of holding time at 450°C on the shift in ductile-brittle transition temperature in alloy 137 (0.1Ti & 0.1Al) is shown in fig 45 and it will be seen that the effect is less profound than that in alloy 134. In the first 1.5 minutes, the DBTT shifted from 0°C in the IBQ state to +100°C and it raised to +135°C in six minutes of aging at 450°C. But by increasing the holding time up to 1 hour and 10 hours, the DBTT°C dropped back to 110°C and 100°C respectively. In alloy 137 (0.1Ti & 0.1Al) the highest shift, ~135°C, was obtained after six minutes at 450°C.

The effect of holding time at  $450^{\circ}\text{C}$  on the shift in ductile-brittle transition temperature and hardness is shown in figure 46. It would appear that the shift in transition temperature on aging at  $450^{\circ}\text{C}$  seemed to be enhanced by the age-hardening response of the alloys, along with some other effects. In both these alloys 134, 137, especially in the first six minutes of aging at  $450^{\circ}\text{C}$ , it appeared that in addition to change in hardness, there is some other mechanism causing such a drastic rise in ductile-brittle transition temperature. Although a small rise in hardness after six minutes of aging has also occurred in both the alloys; another notable difference was the age-hardening response of alloy 134 which was greater than alloy 137 possibly as 137 alloy contained 0.1Ti and 0.1Al which might have tied up any free interstitials. It seems from figure 46 that the softening stage have more effect on the drop in ductile-brittle transition temperature especially in alloy 134. Alloy 137 started softening after six minutes with a consequent drop in ductile-brittle transition temperature whereas alloy 134 showed drop in hardness after 1 hour with consequent fall in the ductile brittle transition temperature. In alloy 137, no change in hardness was found between 1 hour to 10 hours of aging and as shown in figure 46 no marked change in the ductile brittle transition temperature was noticed for this aging time at  $450^{\circ}\text{C}$ .

#### Tensile Data

In alloy K1525, the effect of aging at  $450^{\circ}\text{C}$  was monitored by tensile-ductility <sup>tests</sup> at  $-78^{\circ}\text{C}$  and at a strain rate of  $0.5 \text{ min}^{-1}$ .

Figure 51 shows that the reduction of area fell to zero percent after five minutes at 450°C. The effect of holding time on tensile ductility was studied on various tensile specimens after being aged for various times at different temperatures between 350-600°C figure 54. The embrittlement data was also plotted in an Arrhenius manner, figure 52 and will be discussed in section 4.1.5.

The tensile data of embrittlement kinetics showed that the rapid embrittlement occurred in alloy K1525 between 450-550°C and figure 54 shows the embrittlement kinetics curve which coincidentally represents a C-curve behaviour.

### Fracture Surfaces Examination

The fractographic characteristics of different alloys in various heat treated conditions along with impact data and Auger analysis have been summarized in table XIX. In alloy K1525, the low-temperature fracture mode after being solution treated at 1000°C/1 h and water quenched was 100 pct intergranular with the crack propagating along the prior-austenite grain boundaries. A scanning electron micrograph showing a typical fracture mode is shown in figure 80. No difference was noticed in the appearance of the fracture surfaces as a function of aging time at 450°C. Some transgranular areas were present, having been produced at the intersection of annealing twins with the prior-austenite grain boundaries. The perturbation of the grain-boundary structure produced by the annealing twin was sufficient in some cases as shown in figure 80 to change the mode of fracture from inter-granular to cleavage across the twin. On traversing the twin the fracture reverted to an intergranular mode.

In alloy 134 (high N) the fracture mode was found to change from cleavage in the ice-brine quenched state to 5-10 pct IG on aging

for six minutes at 450°C. The intergranular mode increased to 10-15 pct after aging 1 hour, but even after 10 hours of aging the percentage intergranular fracture mode remained almost the same. In all these heat-treated conditions in alloy 134, in addition to intergranular fracture mode, the remaining 80-85 pct fracture mode consisted of quasi-cleavage.

In alloy 137, the influence of aging on the change in fracture mode from quasi-cleavage in the ice-brine quenched state to intergranular was rapid. Even in the ice-brine quenched condition, the fracture mode was nearly 10 pct intergranular. But on aging at 450°C it changed rapidly. In the first six minutes as shown in figure 92 fracture occurred by 50 pct IG and 50 pct cleavage, but in one hour of aging, it almost changed to 90 pct intergranular with smooth grain-boundary facets. A typical fractograph showing this fracture mode is given in figure 93. The percentage fracture mode remained almost the same till 10 hours but as shown in figure 94 a localized coarse precipitates were observed on the fracture surface.

### Auger Electron Emission Analysis

#### AES Measurements of the As Fractured Surfaces

The results of quantification of AES peak ratio for alloys K1525, 134, 137 on aging at 450°C are summarized in table XIV, XVII, XVIII. Representative AES spectra of alloy K1525 are shown in figure 55 and the quantification of the spectra, in terms of atomic concentration is presented in table XIV. The grain boundary concentrations of Mn, P and N as a function of aging time at 450°C are presented in figure 57. A rapid grain-boundary enrichment of Mn was observed especially in the first

six minutes of aging. As tabulated in Table XIV and plotted in figure 57 the Mn level increased from 7.6 at pct in the WQ state to 18.5 at pct after aging for six minutes at 450°C. It should be noted that the nitrogen level also increased from 2.2 at pct in the as quenched condition to 4.4 at pct after six minutes of aging at 450°C. Another intriguing aspect of aging studies in alloy K1525 was the gradual build up of phosphorus as the aging progressed but initially at a much slower rate than for N. The degree of embrittlement as measured by tensile ductility increased on aging at 450°C, figure 51. (The effect of aging at 450°C on DBTT in K1525 were not studied due to lack of material). In some of the specimens carbon ~~was~~ was also noted which was attributed to ~~the~~ carbide precipitation or possibly contamination in ~~the~~ the AES equipment (I48) by contamination.

Tables XVII and XVIII summarizes the quantification of the AES spectra of alloys 134 and 137 on aging at 450°C for six minutes, 1 hour and 10 hours. The AES spectra for these aging times are shown in figures (60) for alloy 134 (high N) and in figure 62 for alloy 137 (0.1Ti and 0.1Al). The variation in grain boundary concentration of Mn and N as a function of aging time in alloy 134 and alloy 137 has been plotted in figures 65,66 on aging for six minutes, 1 hour, 10 hours at 450°C respectively.

By comparing the aging results of alloy K1525 and 134 in figure 57 and figure 65 it seems ~~that~~ in alloy K1525 (0.003%N) during the first six minutes of aging, the concentration of Mn on the fracture surface increased significantly and rapidly with a slight rise in N concentration as well, whereas in alloy 134 (0.03%N) in the first six minutes, <sup>the</sup> Mn level ~~rose~~ only a small amount while the N concentration remained more or less the same. It appears as if in alloy

K1525 because of less N (0.003%) the Mn atoms have segregated freely and have also induced P segregation through Mn-P interaction.

In alloy 137 (0.1Ti and 0.1Al) the situation was a little different as it contained 0.1Ti, 0.1Al and obviously the level of free nitrogen would be less. In figure 66, the variation in grain-boundary concentration of Mn and N with aging time in alloy 137 has been plotted.

Figure 67 gives the comparative picture of the fracture surface concentration of Mn and N in alloy 134 and alloy 137 (0.1Ti - 0.1Al) in the ice-brine quenched state and on aging at 450°C. It is shown in this figure that the overall level of Mn segregation to the fracture surface is more in alloy 137 than in alloy 134, although it should be noted that in alloy 134 (high N) Auger signals may have come from the cleavage facets rather than the grain boundaries. The N concentration after six minutes also remains the same in both alloys as that in the ice-brine quenched state, being possibly lower in alloy 137.

#### AES Measurements As a Function of Ion Bombardment

The concentration profiles of the elements Mn, N, P and C as a function of distance from the grain-boundary are shown in figure 58 for the as-quenched condition and for the material aged for 12 minutes at 450°C in alloy K1525. It should be noted that the Mn signal decreases on ion-bombardment to levels below that of the bulk value due to the preferential sputtering of Mn (155). However, from a comparison of the sputtering profiles shown in figure 58, it can be deduced that the enhanced Mn concentration on aging was limited to the first few monolayers of the boundary. Similarly the N, P segregation was limited to the first few

monolayers of the boundary suggesting that the segregation of N and P was enhanced by equilibrium segregation of Mn atoms during aging at 450°C but it appears that there might have existed a site competition process between N and P atoms.

In the as quenched material, the carbon level increased with bombardment whereas it remained approximately constant for the aged material (>3 minutes 450°C). This also suggests a possible C desegregation during austenitization and quenching which can strengthen the matrix relative to the boundary, resulting in an intergranular fracture.

#### 4.1.4 Phase Transformations in the Upper Critical Temperature Range 450-650°C

In order to study the kinetics of embrittlement during holding in the ( $\alpha+\gamma$ ) phase region, the phase transformations were first studied in the upper critical temperature range ie between 450-650°C below the  $A_s$  temperature.

#### X-ray Diffraction Analysis

Table VIII, IX, X summarize the peak combinations and the percentage phase-analysis on aging alloy K1525 at 450°C, 550°C, 650°C respectively. The volume pct reverted austenite and epsilon martensite as a function of aging time is plotted in figure 53.

#### Phase-Transformations at 450°C

In alloy K1525 while holding at 450°C, the strongest reflection of austenite ie  $(111)_\gamma$  started appearing after 60 hours but measurable amount of reverted  $\gamma$  formed after 75 hours of aging when  $(200)_\gamma$  peak also appeared. After 100 hours of aging  $(220)_\gamma$  peak was also measurable. The amount of reverted austenite was

1.5 pct after 75 hours and 1.8 pct after 100 hours of aging at 450°C and the remaining was  $\alpha$ -martensite. The results of phase transformations occurring at 450°C are shown in Table VIII and plotted in figure 53.

#### Phase Transformations at 550°C

Table IX summarizes the peak combinations and the percentage phase analysis on aging at 550°C. The results have also been plotted in figure 53. It appears that the amount of  $\epsilon$ -martensite first increases then decreases on isothermal holding while the amount of austenite shows a gradual increase.

#### Phase transformations at 650°C

Table X summarizes the peak combinations and the average %age phase analysis on isothermal holding at 650°C shown in figure 53. A similar behaviour to that at 550°C is occurring on isothermal holding although in this case the percentages of  $\epsilon$  and  $\gamma$  are greater.

#### Metallographic Examination

Optical metallographic examination failed to show any microstructural changes produced by aging treatments. In some cases stain etchant like Schumann's reagent was tried with a hope to get blue, brown and yellow colours for  $\alpha$ ,  $\gamma$  and  $\epsilon$ -martensite but it did not work. Electron microscopy helped to show the microstructural and phase-changes and these will be discussed in detail in section 4.2.1. under the effect of thermal-cycling treatment. The cycling treatment employed not only refined the prior-austenite grain size but also produced phase changes like the formation of epsilon martensite and reverted austenite.

#### 4.1.5 Kinetics of Embrittlement

After studying the phase transformations in the upper critical

temperature range of (450-650°C) the kinetics of embrittlement was studied by determining the drop in tensile-ductility as measured by reduction in area as a function of aging time between 350-650°C. Tensile specimens were tested at -78°C at a strain rate of 0.5 min<sup>-1</sup>. The variation in hardness as a function of aging time was also studied in an attempt to see any relationship between hardening and embrittlement on aging in alloy K1525.

Figure 54 shows the ductility transitions over the range of temperature from 300-650°C as a function of aging time. It is interesting to see that when all the ductility transitions at different temperatures for different times were plotted together <sup>the data</sup> took the form of a C-curve. In this figure, the dashed portion shows the region during which phase-transformations comprising of reverted austenite and epsilon martensite occurs. Thus the ductility transition shown in the figure occurred in the α-martensite state. The fracture mode in the brittle region was 100 pct intergranular. Figures (95,96) show scanning electron micrographs of fracture surfaces of Hounsfield tensile specimen aged at 550°C, 650°C respectively for 10 minutes after being solution treated at 1000°C/1 hour and water quenched.

#### Arrhenius Plot Determination

In order to determine the activation energy for embrittlement the data from the tensile-ductility transition was plotted in an Arrhenius manner. It is interesting to see that the variation of tensile-ductility with time and temperature on aging alloy K1525 gave an activation energy of 77 kJ/gm atom for embrittlement. From the aging curves at different temperatures in alloy K1525 shown in figure 50, the aging time to peak hardness was used to determine the Arrhenius plot for hardening. The hardening plot gave an activation energy of 147 kJ/g-atom.

Both the plots for hardening as well as embrittlement are shown in figure 52.

## 4.2 Effect of Thermal-Cycling Treatment

### 4.2.1 Thermal-Cycling Treatment in Fe-Mn Alloys

#### Heat-treatment Cycle

In order to devise the thermal-cycling treatment for refinement of the prior-austenite grain size, dilatometric studies were conducted to determine the transformation temperatures in these alloys. Table III summarizes the transformation temperatures in alloys 134, 137, K1525. Earlier studies on Fe-Ni alloys (145) indicated that when the alloys were heated or cooled rapidly between room temperature and the  $\gamma$ -field, both the transformations of  $\alpha \rightarrow \gamma$  and  $\gamma \rightarrow \alpha$  occur primarily through a diffusionless shear mechanism, while if the alloys are annealed within the two-phase ( $\alpha + \gamma$ ) field, the transformation proceeds through a diffusional nucleation and growth process leading to an equilibrium partitioning of Ni between the two phases. On the similarities between Fe-Ni and Fe-Mn systems, both the transformation mechanisms could be used for grain-refinement in Fe-Mn alloys as well. If  $\alpha$  is heated to the  $\gamma$ -field and then cooled to room temperature, a decrease in apparent grain size (or martensite packet size) results, presumably to relieve the internal strain built-up during the shear transformation. If  $\alpha$  is annealed inside the two-phase region, a very fine lath-like structure results with the formation of reverted austenite and its preferential nucleation in the boundaries of the martensite plates and prior-austenite grain boundaries, thus refining the whole microstructure. Based on these theoretical principles, a cycling treatment was devised, the schematic illustration of which is shown in figure 68. In this treatment, the austenite reversion was alternated with two-phase decompositions. The annealing temperatures were chosen from the results of dilatometric studies. The austenitising

temperature was selected to be low enough to minimize grain growth, while the two-phase decomposition temperature be high enough to maximize the rate of decomposition. The annealing times and total number of cycles were chosen from metallographic studies of grain refinement, X-ray analysis results and low-temperature mechanical testing.

### Metallographic Examination

Table II summarizes the microstructural details of alloy K1525 before and after thermal cycling treatment. A typical optical micrograph is shown in figure 97 (a,b) where the prior-austenite grain size has been reduced to 21  $\mu\text{m}$  from 80-90  $\mu\text{m}$  after first complete cycle comprising of ( $I_A+I_B$ ) stages as shown in figure 68. The white bead-like decoration predominantly along the prior-austenite grain boundaries is presumably the reverted austenite network. Optical micrograph in figure 98 (a,b) shows further refinement of the prior-austenite grain size to 10-15  $\mu\text{m}$  after second cycle comprising of ( $I_A+I_B+II_A+II_B$ ) stages as shown in figure 68.

### X-rays diffraction Analysis

Table XI summarizes the results of phase-transformations on thermal cycling treatment in alloy K1525 after being solution treated at 1000<sup>o</sup>C/1 hour and water quenched and subjected to heat-treatment cycle of ( $I_A+I_B+II_A+II_B$ ) stages as shown in figure 68. Four peak combinations were chosen to find average %age phases on cycling at each stage. After  $I_A$  stage ie 740<sup>o</sup>C/2h-air cooled, the  $\epsilon$ -martensite was only less than 2 pct, but after ( $I_A+I_B$ ) ie 650<sup>o</sup>C/2 hour - air cooled, the phase analysis consisted of  $\gamma=5.8\%$ ,  $\epsilon=28.0\%$  and  $\alpha=66.2\%$ . It should be noted that during the 740<sup>o</sup>C/2 hour anneal of the second cycle ie  $II_A$  stage, even

though  $740^{\circ}\text{C}$  is above the  $A_F$  temperature, 4.1 pct reverted austenite was still present, but the amount of epsilon martensite was decreased down to 4.0 pct whereas  $\alpha = 91.9$  pct. After completion of the second cycle ( $II_A + II_B$ ) ie  $650^{\circ}\text{C}/2$  hours anneal, the phase-analysis consisted of  $\gamma = 8.0\%$ ,  $\epsilon = 24.6$  pct and  $\alpha = 67.4\%$ . Note that the amount of reverted austenite has increased,  $\epsilon$ -martensite has decreased while  $\alpha$ -martensite remained more or less the same after the completion of second cycle.

This indicated that the reverted austenite formed at  $650^{\circ}\text{C}$  was so enriched in manganese, that the  $M_s$  for the  $\gamma \rightarrow \epsilon$  transformation lay below room temperature and thus there was an increase in the amount of austenite and a decrease in the amount of epsilon martensite observed at room temperature.

In Table XI it is shown that by holding the thermally-cycled alloy in liquid  $\text{N}_2$ , some of the transformations seemed to occur, especially  $\gamma \rightarrow \epsilon$  as the amount of  $\gamma$  has dropped from 8.0 % to 6.0 % while the amount of  $\epsilon$ -martensite has increased by the same amount. Another interesting aspect was that the amount of reverted austenite possibly increased by increasing the number of cycles.

#### Cryogenic Impact Data

Figure 70 shows the influence of thermal-cycling treatment on impact transition temperature in alloy K1525. It is evident that at 30J the shift in impact transition temperature has taken place from  $+115^{\circ}\text{C}$  to  $-60^{\circ}\text{C}$ . This shift in impact transition is attributed to grain refinement of the prior austenite from 80-90  $\mu\text{m}$  to 10-15  $\mu\text{m}$  and phase transformations to reverted austenite and  $\epsilon$ -martensite which are generally regarded to improve the low-temperature toughness.

#### Cryogenic Tensile Data

Figure 71 shows the effect of thermal cycling treatment on engineering stress - elongation curves for alloy K1525. The tensile

testing was carried out at  $-78^{\circ}\text{C}$  at a strain rate of  $0.5 \text{ min}^{-1}$ . It is shown that 8% Mn alloy after solution treatment ( $1000^{\circ}\text{C}/1 \text{ h} - \text{WQ}$ ) having bcc matrix exhibited fairly high yield strength but rather poor elongation. But after thermal cycling treatment, the yield strength seems to be decreased but elongation increased almost three times. As the alloy consisted of triple phase microstructure ( $\alpha = 67.2\%$ ,  $\epsilon = 26.8\%$ ,  $\gamma = 6.0\%$ ) at  $-80^{\circ}\text{C}$ , thus it appears that with increasing amount of  $\epsilon$  in a primarily  $\alpha$  microstructure, the yield strength decreased.

The above behaviour can be rationalized if account is taken of the differences in yield strength between phases and the changing stability of  $\epsilon$  phase. In this phase microstructure ( $\alpha + \gamma + \epsilon$ ), the  $\epsilon$  phase is predominant, it appears that as the load is increased, the flow or strain tends to concentrate in the weaker  $\epsilon$  phase and  $\gamma$  phase as well, because  $\gamma$  and  $\epsilon$  phases are reported (32) to have comparable strengths, thus the overall yield strength was controlled by the strength of the ( $\gamma + \epsilon$ ) phases. The shape of the curve indicates that as the load was increased during tension testing at  $-78^{\circ}\text{C}$ , the  $\epsilon$  phase has transformed to  $\alpha$ . It is probable that a stress-induced martensitic transformation of  $\epsilon$  to  $\alpha$  has contributed to low yield strength but apparently increased in %age elongation because of localized flow. Stress-induced transformations have been reported in several metastable austenitic steels of low austenite stability (156,157). It was shown (158) that these stress-induced transformations could significantly raise the ductility and fracture toughness of alloys having metastable matrices. In the Fe-Mn system, the possible stress-induced transformations are those of the hexagonal  $\epsilon$  phase transforming during deformation to bcc  $\alpha$  and of the retained austenite transforming to either  $\epsilon$  or  $\alpha$  or both. White and

Honeycombe (17) and, more recently, Holden et al (2) found phase transformations of this kind to occur during cold-working of Fe-Mn alloys.

### Hardness Data

Thermal cycling increased the hardness from  $258 \pm 2 \text{Hv}_{30}$  to  $392 \pm 6 \text{Hv}_{30}$ . This high hardness must be partly due to grain refinement but also due to high work hardening rate shown by the stress-strain curve, figure 71.

### Electron Microscopy

Figures (102-107) show the transmission electron micrograph in alloy K1525 after <sup>the</sup> thermal-cycling treatment. Figure 101 shows the initial lath-martensitic structure with high density of dislocations in alloy K1525 as solution treated at  $1000^\circ\text{C}/1\text{h}$  and water quenched. On thermal cycling as shown by the X-ray diffraction analysis (Table XI) triple phase microstructure comprising of  $(\alpha+\epsilon+\gamma)$  is developed. Thin foil electron micrograph in figure 102 shows the presence of  $\gamma$  and  $\epsilon$  phases at  $\alpha$ -lath boundaries, since the nucleation at these sites is much easier than in the body of the  $\alpha$ -laths. The grain refining effect of the continuous  $\gamma \rightarrow \epsilon \rightarrow \alpha$  transformation can be seen from figure 102 (a,b) which shows the parallel sided laths of  $\alpha$ -martensite formed from the highly faulted  $\gamma$ -phase. A high local density of dislocations may be seen in these  $\alpha$ -laths producing the 'banding' contrast which is also observed. Figure 104 (a,b,c,d) show the increasing  $\gamma$  and  $\epsilon$  phase content of the thermally-cycled alloy, determined by X-ray diffraction analysis.

The specimens subjected for the further  $\text{II}_A$ ,  $\text{II}_B$  treatment (figures 103,104) also show the effect of heat treatment on the dislocation substructure by mutual annihilation of positive and negative

dislocations and formation of subgrain boundaries in the  $\alpha$ -phase.

Dark-field electron microscopy was used in figures (105-107) to show the nucleation and precipitation of  $\gamma$ -phase at interlath boundaries and within the  $\alpha$ -laths.

### Fracture Surfaces Examinations

Figures 99,100 show the scanning electron fractograph of the fracture surface of impact and tensile specimens respectively in alloy K1525 after thermal-cycling treatment.

Comparing the fracture mode on impact testing in figure 99 with that in figure 80 where the fracture mode is completely intergranular in alloy K1525 after solution treatment at 1000°C for 1 hour and water quenched, it is noticed that in the thermally-cycled condition the fracture mode has changed from intergranular to ductile+cleavage due to so called 'flaking' effect (4) on brittle facet walls indicating the breakdown of true cleavage due to the presence of  $\gamma$  and  $\epsilon$  phases at the lath and packet boundaries. Another interesting feature in these scanning electron fractographs is that the size of the areas shown by these ductile regions correspond to the grain size of the prior austenite as shown by the bead-like network of austenite islands along the grain boundaries as shown in optical micrographs (figures 97,98).

Figure 100 shows the scanning electron fractograph of the fracture surface in tensile specimen. As during thermal cycling (figure 68) the specimens have been actually tempered at 655°C in the ( $\alpha+\gamma$ ) field and the X-ray diffraction analysis has shown a mixture of triple phase ( $\alpha+\epsilon+\gamma$ ), a complex fracture mode is observed. On tensile testing at -196°C at a strain rate of 0.5 min<sup>-1</sup>, the reduction of area dropped to zero per cent with fracture mode predominantly cleavage

with random ductile regions, Figure 100(a,b).

#### 4.2.2 Thermal-cycling Treatment in Fe-Mn alloys with Ti & Al Additions (Alloy 137)

Charushnikova (66) pointed out that an improvement in impact toughness in manganese steels could be expected from the addition of aluminium or titanium due to the high affinity of these elements for nitrogen and it was suggested that combining nitrogen into stable nitrides, these elements would substantially neutralize its harmful effect as an element blocking dislocations. Keeping these ideas in mind, it was decided to apply <sup>the</sup> thermal-cycling treatment to alloy 137 (0.1Ti-0.1Al) which already showed slight refinement in the prior austenite grain size.

#### Impact Data

Figure 73 shows the influence of thermal-cycling treatment on the shift in impact transition temperature from +150°C after solution treatment (1000°C/1h)-WQ state to -40°C. The likely factors responsible for this shift are attainment of grain refinement of prior austenite from 60-70 µm in the water quenched state to 10-15 µm after thermal cycling treatment and beneficial effect of phase transformation products like  $\gamma = 39.6\%$ ,  $\epsilon = 20.6\%$ ,  $\alpha = 39.8\%$  at room temperature. Alloy 137 (0.1Ti-0.1Al) showed inferior toughness even with the addition of 0.1 titanium and 0.1 aluminium in comparison with the toughness shown by alloy K1525 when they were both subjected to the same thermal cycling treatment.

#### Hardness Data

The hardness results in alloy 137 (0.1Ti+0.1Al) and in alloy K1525 in the water quenched condition after being solution treated at 1000°C/1h shows that the starting hardness of solid solution in 137

is  $Hv_{30} = 244$  whereas it is  $Hv_{30} = 258 \pm 2$  in K1525 ie  $\approx Hv_{30} = 15$  lesser in 137. This decrease in hardness could be ~~due~~ to the tieing-up of free interstitials by the addition of titanium and aluminium in alloy 137. On thermal cycling the hardness of this alloy increased to  $Hv_{30} = 333$  at R.T. This rise in hardness could be mainly by grain refinement and may be through triple-phase structure as well. By comparing the hardness values in alloy K1525 after thermal-cycling treatment ie  $Hv_{30} \approx 400 \pm 20$  with same degree of grain refinement as in alloy 137 but difference in %age phase analysis ( $\gamma = 8.0\%$ ,  $\epsilon = 24.6\%$ ,  $\alpha = 67.4\%$ ) it seems likely that a decrease in hardness in alloy 137 ~~has~~ <sup>mainly</sup> come from %age phases ( $\gamma = 39.6\%$ ,  $\epsilon = 20.6\%$ ,  $\alpha = 39.8\%$ ) but could also be partly from Ti(C,N), AlN precipitates coarsening during the course of thermal cycling treatment. This decrease in hardness in alloy 137 ie  $Hv_{30} \approx 60$  suggest that the alloy should show improvement in impact toughness. ~~However~~ <sup>However</sup> the toughness properties were impaired and will be discussed later.

### X-ray Diffraction Analysis

The phase-transformations on thermal-cycling in alloy 137 (0.1Ti+0.1Al) are shown in Table XIII and the stability of the resulting phases is also shown at  $-196^{\circ}\text{C}$ . The phase analysis after thermal-cycling treatment consisted of  $\gamma = 39.6\%$ ,  $\epsilon = 20.6\%$ , and  $\alpha = 39.8\%$ . After holding the specimen at liquid nitrogen temperature for 15 minutes, the phase analysis showed  $\gamma = 17.5\%$ ,  $\epsilon = 20.6\%$ , and  $\alpha = 56.5\%$ . By cooling down to sub-zero temperature it seems likely that  $\gamma \rightarrow \epsilon \rightarrow \alpha$  transformation has occurred consistent with the observation of White and Honeycombe (17) who reported that  $\epsilon$ -phase formed by the  $\gamma \rightarrow \epsilon$  transformation may be transformed to  $\alpha$  by sub-zero treatment. Whether these transitions are good for impact properties, will be discussed later.

## Metallographic Examination

Optical micrographs of alloy 137 (0.1Ti+0.1Al) after being solution-treated and thermally-cycled (ST1000°C/1h-WQ+I<sub>A</sub>+I<sub>B</sub>+II<sub>A</sub>+II<sub>B</sub>) are shown in figure 108. When etched in 2 pct Nital, the thermally-cycled specimens showed chain-like alignment of etch pits delineating the austenite grain boundaries as shown in figure 108 (a,b,c,d). Similar alignments are often seen in cast steels which are embrittled due to the presence of AlN inclusions (103). On the contrary, the alloy K1525 which do not contain AlN or Ti(C,N) do not exhibit such etch pit lines even though alloy K1525 has also been thermally-cycled in the similar manner. Optical micrograph shown in figure 108 is an example for comparison with those shown in figure 97. In addition to the precipitation of these AlN, TiC, Ti(C,N), the formation of reverted austenite is believed to occur preferentially at the prior-austenite grain boundaries and one of the usual morphologies (140), it consists of a bead-like particles in the grain boundaries. The lighter phase along the grain boundaries in optical micrograph shown in figure 108, is thought to be reverted austenite. As the X-ray analysis showed the formation of considerable amount of reverted  $\gamma$ ,  $\epsilon$ -martensite,  $\alpha$ -phase, so it was decided to do stain-etching using the Schumann's (29) technique of light etch with 2 pct Nital followed by immersion in 30 pct aqueous solution of <sup>sodium</sup> thiosulphate and dium meta-bisulphite. Schumann found blue-brown and yellow phases with  $\alpha$ -as blue,  $\gamma$  as brown and  $\epsilon$ -phase gives yellow colour. The grain boundary network did in fact etch brown/yellow indicating the presence of  $\gamma$  and  $\epsilon$ . The optical micrographs shown in figure 109 shows grain boundary network fairly darker along with clearly identified precipitation of nitrides and carbonitrides.

## Fracture Surfaces Examination

The scanning electron fractographs of the fracture surface of

alloy 137 after being thermally cycled are shown in figure 110-112. Examination of these impact specimens, having been fractured below the transition temperature, revealed various fracture modes depending upon the phase present. As the X-ray diffraction analysis have shown that after thermal-cycling treatment, the alloy consisted of triple-phase microstructure containing  $\gamma = 39.6\%$ ,  $\epsilon = 20.6\%$ ,  $\alpha = 39.8\%$  at R.T. but at  $-196^{\circ}\text{C}$  it consisted of  $\gamma = 17.5\%$ ,  $\epsilon = 26.0\%$  and  $\alpha = 56.5\%$  thus at low temperatures below the transition the fracture mode will be governed by the amount of phases stable at sub-zero temperature and phases transformed by mechanical deformation during testing. The fracture mode shown in figure 110(a) shows cleavage and ductile. It seems as if ductile region follows irregular network all over the fracture surface blunting the cleavage crack propagation. This could be because of the presence of  $(\gamma+\epsilon)$  phase mixture. Another important feature to note is the presence of Al rich (Fig 110), Ti rich (Fig 111), precipitates in the close vicinity of ductile phases. This once again confirms that decoration of precipitates of AlN, TiC, Ti(C,N) and bead-like formation of reverted austenite network lies preferentially along the austenite grain-boundaries as shown in the optical micrographs in figures 108, 109. The X-ray spectra taken from the fracture surfaces is shown in figs 110(b), 111(b), 112(b). The precipitates identified were richer in Al, Ti and S presumably thought to be AlN, Ti(C,N), MnS.

#### 4.2.3 Effect of Aging at $450^{\circ}\text{C}$ on Thermally-cycled Alloy

As the alloy K1525 showed an increase in the degree of embrittlement on aging at  $450^{\circ}\text{C}$  so it was decided to study the resistance of thermally-cycled alloy to embrittlement by tensile-ductility tests on aging this alloy at  $450^{\circ}\text{C}$ . Tables XXI, XXII summarises the results in this alloy.

## Tensile Data

In alloy K1525, after being subjected to thermal-cycling treatment, drop in R.A. was measured as a function of aging time at 450°C. Specimens were tested at -78°C at a strain rate of 0.5 min<sup>-1</sup>. The tensile ductility was measured after 10 mins, 1 hour and 2 hours of aging at 450°C but no drop in R.A. was found. On the other hand before thermal cycling the alloy showed severe embrittlement with R.A. dropped to 0% on aging for 5 minutes at 450°C. Engineering stress-elongation curves for alloy aged for 10 minutes, 1 hour and 2 hours at 450°C are shown in figure 72. It seems by comparing these curves in view of the percentage phase-analysis results, that as the load is increased, the  $\gamma \rightarrow \epsilon \rightarrow \alpha$  transformations occur resulting in the change in slope of the curve and after certain load the slope of the curve is almost parallel to each other in differently aged condition having difference in percentage phases. The slope of the curve after passing through the maximum load is again almost the same down to fracture even with more or less the same fracture strength. Out of these studies, it seems as  $\epsilon$ -phase formed by the  $\gamma \rightarrow \epsilon$  transformation may be transformed to  $\alpha$  by cold working on mechanical deformation as reported by Parr (16), White and Honeycombe (17) or by sub-zero treatment, reported by Cina (18) and Schumann (29).

## Hardness Data

Table XXI summarises the variation in hardness on aging at 450°C in alloy K1525 after thermal cycling treatment at R.T. and at -78°C. The hardness value seems to increase with increase in the amount of  $\epsilon$ -phase which is suggested in literature (4) to be a harder phase. As the variation in phase analysis occur on aging at 450°C, thus the changes in hardness are mainly thought to be

due to phase changes.

### X-ray Diffraction Analysis

Phase-transformation studies on aging alloy K1525 at 450°C after thermal cycling treatment are shown in Table XII. It is interesting to note that in the first ten minutes, the phase changes are considerable, amount of  $\gamma$  increased from 8.0% to 12.5%, epsilon martensite decreased from 24.7% to 11.8% while  $\alpha$ -martensite increased from 67.3% to 75.7%. After 1 hour, the amount of  $\alpha$  remains more or less the same, but there occurs transition between  $\gamma$  and epsilon martensite. Amount of  $\epsilon$ -martensite increases to 14.5% while amount of  $\gamma$  decreases to 9.5% which indicated  $\gamma \rightarrow \epsilon$  transformation occurring after aging 1 hour at 450°C. Again on further aging to 2 hours, the situation becomes very interesting, amount of  $\gamma$  remains nearly 10.6% but  $\epsilon$ -phase decreases to 8.8% while  $\alpha$ -martensite increases to 80.5% showing that  $\epsilon \rightarrow \alpha$  transformation has occurred. It seems likely that  $\gamma \rightarrow \epsilon \rightarrow \alpha$  transformations have been thermally activated. This result is consistent with the observations reported by Cina (18) and Schumann (29) who found that a low-temperature annealing treatment gave rise to an initial increase in  $\epsilon$ -phase due to decomposition of retained austenite. As the tensile-ductility to measure the R.A. was carried out at -78°C so the stability of these phase-transformation products were checked at -78°C by keeping the specimen after being aged for 2 hours at 450°C, in cardice and acetone mixture for 15 minutes. The phase analysis was found to be  $\gamma = 6.0\%$ ,  $\epsilon = 9.5\%$ ,  $\alpha = 84.5\%$ . It appears that  $\gamma$  has been decreased by 4.0% while  $\alpha$  has been increased by the same amount.

#### 4.2.4. Effect of aging at 450°C on thermally-cycled alloy with Ti and Al additions

In order to study the effect of grain refinement and phase-transformations on embrittlement in the presence of 0.1Ti and 0.1Al, the alloy 137, after being solution treated and thermally cycled was subjected to embrittling treatment at 450°C for 6 minutes and the results are summarised below.

##### Impact Data

In figure 73, at 30.0J, the impact transition temperature was more or less the same before aging at 450°C and after aging for 6 minutes at 450°C ie -50°C.

##### Hardness Data

The hardness values  $Hv_{30}$  after these various thermal treatments were very interesting. After solution-treatment of 1000°C/1 hour and WQ the  $Hv_{30} = 243.5 \pm 5$  at room temperature but after thermal-cycling treatment ie (ST-WQ+I<sub>A</sub>+I<sub>B</sub>+II<sub>A</sub>+II<sub>B</sub>) it rose to  $Hv_{30} = 332.8 \pm 5$ . This increase in hardness could be attributed to grain refinement from 60-70  $\mu\text{m}$  to 10-15  $\mu\text{m}$  and phase transformations to  $\gamma = 39.6\%$ ,  $\epsilon = 20.6\%$  and  $\alpha = 39.8\%$ . On further aging at 450°C, this thermally-cycled alloy having multiple-phases, the hardness dropped slightly from  $Hv_{30} = 332.8 \pm 5$  to  $Hv_{30} = 322.0 \pm 5$ . No difference in grain size was noticed but a slight change in phase transformations occurred and it resulted in  $\gamma = 41.6\%$ ,  $\epsilon = 29.7\%$ ,  $\alpha = 28.7\%$  at 20°C. The various phase transformations are summarised below.

##### X-ray Diffraction Analysis

X-ray diffraction analysis results in alloy 137 on thermal cycling and on aging at 450°C after being thermally cycled have

been summarized in Table XIII. The results were very interesting at different temperatures of holding. The phase transformations of alloy after being solution treated at  $1000^{\circ}\text{C}/1$  hour - WQ +  $I_A + I_B + II_A + II_B$  + 6 minutes at  $450^{\circ}\text{C}$  consisted of  $\gamma = 416\%$ ,  $\epsilon = 29.7\%$ ,  $\alpha = 28.7\%$  at room temperature. At  $-78^{\circ}\text{C}$ , the amount of  $\epsilon$ -martensite decreased with a slight increase in  $\gamma$  and  $\alpha$ -martensite and phase analysis consisted of  $\gamma = 44.8\%$ ,  $\epsilon = 21.7\%$ ,  $\alpha = 33.5\%$ . At  $-196^{\circ}\text{C}$ , the phases were analysed as  $\gamma = 12.4\%$ ,  $\epsilon = 41.9\%$  and  $\alpha = 45.7\%$ . Thus a significant decrease in the amount of  $\gamma$  occurred while  $\epsilon$ -martensite and  $\alpha$ -martensite increased on refrigeration. These transformations have possibly occurred through  $\gamma \rightarrow \epsilon \rightarrow \alpha$  transitions depending upon the stability of  $\gamma$  reverted austenite and epsilon martensite.

## 5.0 DISCUSSION

### 5.1 Embrittlement Mechanisms in Fe-Mn Alloys

#### 5.1.1 Intergranular embrittlement in quenched alloys

Bolton (1,3) and later Freeman (4) found that the Fe-Mn alloys containing between 4-10% Mn in the lath-martensite condition exhibited brittleness in as-quenched condition due to a weakness at prior-austenite grain boundaries. Bolton (3) suggested that the segregation of some harmful impurities might have occurred during austenitization and led to the potential weakening of the grain boundaries in the subsequently quenched condition. Freeman also reported that, in the 10% Mn alloy, enhancement of embrittlement occurred in the normalized condition but even on water quenching the brittle fracture mode was still intergranular. In contrast with these results, Roberts (7) did not find intergranular brittleness in his alloys. However, the results of the present investigation table XIX are in agreement with both these previous observations (1,3,4,7). Alloys K1525 (0.003N), 134 (0.03N) showed intergranular brittleness in the as water quenched condition in agreement with Bolton (1) and Freeman (4) whereas alloys 134 (0.03N) and 137 (0.03N, 0.1Ti, 0.1Al) showed also cleavage fractures in agreement with Robert (7) on ice-brine quenching. The same alloys 134 and 137 also showed completely intergranular fractures on air cooling as was found by Freeman (4).

#### Water-Quenched Alloys

In alloy K1525 it is shown (Table XIX) that the intergranular fractures were associated with segregation of nitrogen ( $\sim 2.3 \pm 1.5$  atomic %). However, some AES specimens also showed the presence of P but the build up of N was detected consistently on the intergranular facets.

Alloy K1525 also showed the presence of C on brittle grain boundaries and ion bombardment revealed a de-segregation of this element in the vicinity of the boundary, figure 57. According to recent French work (86) C segregation to grain boundaries is considered to strengthen the grain boundaries and reduce embrittlement. It is therefore concluded that a possible contributing factor in the intergranular fracture of K1525 on water quenching is de-segregation of C at grain boundaries as well as segregation of N. However, these results must be treated with caution as it is possible that the C signal in the AES spectra could have risen from contamination in the AES apparatus.

In addition sulphur was also detected on grain boundary AES spectra of K1525, although it seems likely that the sulphur signal probably originated at MnS particles which were present on the intergranular areas. From these results it seems likely that segregation of nitrogen to prior-austenite grain boundaries is the main embrittling effect in water-quenched alloys. The increase of N at the grain boundaries reduces the inter-facial energy and promotes intergranular low energy fracture. Support for the segregation of N to prior austenite grain boundaries is also provided by the work of Krahe and Guttman (151) in an Fe-1.92%Mn-0.2%C alloy. Wilson and McMahon (69) also report P and N on brittle prior-austenite grain boundaries in a water-quenched Fe-1.2Ni-6Mn alloy. Rees and Hopkins (89), Tipler (57) in the early NPL work on pure iron also suggest that segregation of N and P could also be responsible for intergranular brittleness in their iron-base alloys.

The driving force for segregation of N to prior austenite grain boundaries could be due to three factors.

(a) The misfit strain of interstitial nitrogen in the austenite

lattice, which is more easily accommodated at grain boundaries.

- (b) Reduced solid solubility of N during quenching.
- (c) Chemical interaction with major alloying elements which have previously concentrated at the grain boundaries.

Since rapidly quenched alloys failed by cleavage it is unlikely that substantial segregation of N to grain boundaries occurred during austenitising. Also since the level of Mn on brittle grain boundaries was characteristic of the bulk, (c) did not occur. It therefore seems likely that a combination of (a) and (b) is responsible for the segregation of N to prior austenite grain boundaries. This will be particularly so when the  $\gamma/(\alpha + \gamma)$  solvus is crossed and austenite is metastable. Segregation to austenite grain boundaries of impurities will continue in this metastable austenite down to the  $M_s$  temperature  $\sim 355^\circ\text{C}$ . At  $M_s$  many other sinks such as packet boundaries, interlath boundaries and dislocations would arise for impurities. In other words the misfit due to these impurity atoms (P and in particular N) would then be accommodated in all the martensitic boundaries.

#### Ice brine-quenched alloys

All the ice brine-quenched alloys failed by a quasi-cleavage mode below the DBTT. Thus it appears that the quench rate has been sufficiently fast to prevent impurity segregation, particularly N, to prior austenite grain boundaries during the quench.

However, at the  $M_s$  temperature and below the cooling rate will slow down due mainly to the release of latent heat of transformation and the smaller temperature difference between the material and the quenching media. Thus it is possible that segregation of impurities to all the martensite boundaries could also occur below  $M_s$ . Support

for this is provided by the AES finding of 2.37 atomic % N on cleavage facets in alloy 134 (0.03 mass % N, 0.12 atomic % N) after ice brine-quenching from 900°C. Spluttering back the cleavage facet reduced this to 0.18 atomic % more characteristic of the bulk (0.12 atomic %). Variations in nitrogen content were observed by AES from facet to facet, for example in one case 1.73 atomic %, nevertheless they were all above the bulk level of 0.12 atomic %.

Similarly in alloy 137 containing 0.1 Ti and 0.1 Al, 1.2 atomic % N was observed on a facet by AES compared with a bulk level of 0.12 atomic %. In this case some of the nitrogen will be tied up as TiN and AlN, reducing the amount of free nitrogen available for segregation.

Although the observation of enhanced N concentration on cleavage facets above the bulk lies within the error band  $\pm 1.5$  atomic % N, it is thought that this is real effect and the explanation advanced here for this is a credible one.

Recently Kalish and Rack (105) reported a similar situation where the severity of embrittlement in 18% Ni maraging steel was found to increase with decreasing cooling rate after solution treatment. The major loss in toughness was thought to be associated with diffusion of interstitial impurity atoms to the austenite grain boundaries in the metastable  $\gamma$  field during cooling. The brittle fracture mode in such steel was found to be intergranular on air cooling whereas on water quenching it changed to quasi-cleavage.

In summary, the as-quenched brittleness in Fe-Mn alloys in the present investigation was mainly because of N segregation to the austenite grain boundaries in the metastable  $\gamma$  field on

water quenching. These results are in agreement with the observations of (69,89,148).

On ice brine quenching, segregation of N to prior austenite grain boundaries is thought to be avoided or at least considerably reduced while in the metastable  $\gamma$  field. However segregation of N is thought to occur to all high angle boundaries below  $M_s$  giving rise to quasi-cleavage brittle fracture with an enhanced N level at such fracture surfaces.

### 5.1.2 Intergranular Embrittlement in Air-cooled alloys

The work on alloys 134 (0.03N) and 137 (0.03N, 0.1Ti, 0.1Al) has shown that brittle fracture by cleavage can occur in Fe-8.0% Mn alloys on ice-brine quenching in agreement with Roberts (7). In contrast to this intergranular fractures could be induced in these alloys by air cooling from the austenitizing treatments as was found by Freeman (4) in 10Mn alloys. The rise in ductile brittle transition temperature of nearly 350°C occurred in alloy 134 (0.03N) on air cooling from that on ice-brine quenching as shown in figure 32. The hardness data also showed a slight rise in hardness ( $\sim 10\text{HV}_{30}$ ) on air cooling, but this small rise in hardness is unlikely to explain completely the large shift of 350°C in DBTT.

Similarly alloy 137 (0.03N-0.1Ti-0.1Al) showed a rise in DBTT of nearly 150°C on air cooling from that on ice-brine quenching (figure 33), the rise in hardness being  $\sim 18\text{HV}_{30}$ . Evidently the magnitude of embrittlement was more in alloy 134 than that in alloy 137 and this could be understood by a decrease in the amount of free N in solid solution and partly from the grain refinement in alloy 137 (65-70  $\mu\text{m}$  to 40-45  $\mu\text{m}$ ).

Recently, Nickbaht (150) has investigated embrittlement in high purity Fe-8.0Mn alloys containing 0.008%N. One alloy was a pure binary, 181, while the other alloy 193, contained 0.1% Ti and 0.1% Al to scavenge residual C & N. Both alloys exhibited a brittle quasi-cleavage fracture mode after an ice brine quench from 900°C, and intergranular fractures below the DBTT on air-cooling. Alloy 181 (0.008N) showed a rise of 50°C in the DBTT from 70°C to 120°C on air cooling and alloy 193 (0.008N-0.1Ti-0.1Al) a rise of 85°C in the DBTT from 25°C to 110°C. Clearly the severe embrittlement exhibited by alloy 134 (0.03N) on air cooling is due to the high nitrogen content, although the larger rise in DBTT of 85°C by alloy 193 (0.008N-0.1Ti-0.1Al) compared with 50°C in alloy 181 (0.008N) is anomalous. This effect of N is further illustrated in figure 39 showing a drop of nearly 250°C in DBTT by decreasing the amount of N from 0.03% in alloy 134 to 0.008% in alloy 181, both alloys being in the air cooled condition, exhibiting completely intergranular fracture below the DBTT.

Carbon extraction replicas failed to show any sign of second phase particles on the smooth intergranular fractures of alloy 134, figure 85.

Auger analysis of brittle grain boundaries of alloy 134 in the air-cooled condition showed segregation of N and Mn, and in one case desegregation of C, table XV. Ion-profiling showed that this segregation was confined to the first few monolayers of the fracture surface. The results of AES analysis in alloys 134 and 137 are summarized in table XVI. Figure 63 shows that the segregation of Mn and N to prior austenite grain boundaries is associative, larger concentrations of Mn being associated with higher concentrations of N. While figure 64 shows that in turn, the DBTT depends on the

concentration of Mn and N at the grain boundaries. It seems very clear that in all the alloys on air cooling the larger shift in DBTT was mainly associated with enhancement in grain boundary concentration of Mn and N.

Since water quenched alloys do not exhibit an increase in manganese concentration at brittle grain boundaries, it is postulated that segregation of Mn and N to austenite boundaries has occurred during air cooling while austenite is in the metastable condition.

The possible driving forces for segregation of Mn could be as follows:

- (a) The grain boundary segregation of N would occur by the mechanisms discussed in section 5.1.1 under water quenched alloys. Due to the strong chemical interaction between Mn and N (95), Mn atoms would be attracted by the N atoms, to the grain boundaries, thus lowering the chemical potential of the system. Evidence for a strong Mn-N interaction was first reported by Fuller and Garwood (96) who reported a strong secondary hardening peak due to precipitation of  $Mn_3N_2$  on tempering  $\lambda$  martensites at 450°C. Fe-Mn-N figure 24
  
- (b) The second driving force available in the system could be the equilibrium segregation of Mn to the prior austenite grain boundaries during cooling through the  $(\alpha+\gamma)$  phase field. However, the bulk reaction  $\gamma(\text{metastable}) \rightarrow (\alpha + \gamma)$  equilibrium is extremely slow in the Fe-Mn system (145)

The present results are in agreement with no Mn segregation

in the stable  $\gamma$  field (147,151) but with segregation of Mn in the metastable austenite and ( $\alpha + \gamma$ ) phase field with enhanced concentration of Mn and N at the austenitic grain boundaries.

In summary it is suggested that the embrittlement in as water quenched Fe-8.0% Mn alloy was mainly because of segregation of N to austenite grain boundaries, but some specimens did show the presence of P as well. The embrittlement is further enhanced on air-cooling with segregation of N and Mn in the metastable austenite and ( $\alpha + \gamma$ ) phase field.

### 5.1.3 Embrittlement on aging at 450°C

Bolton first reported (1,3) that the embrittlement in Fe-Mn alloys became more marked when the alloys were tempered between 250-450°C. Later, Squires (68) also observed embrittlement on aging between 300°C and 500°C in Fe-Ni-Mn maraging alloys. This embrittlement was studied by tensile ductility tests and found to be a maximum at 450°C. Thus in the present investigation it was decided to examine the effect of aging at 450°C on embrittlement. All the alloys K1525 (0.003N), 134 (0.03N) and 137 (0.03N-0.1Ti-0.1Al) showed enhancement in the degree of embrittlement on aging at 450°C.

These experimental results will be first discussed individually and then related to the degree of embrittlement experienced on aging. Also included in the discussion will be Nickbaht's result on low nitrogen alloys 181 (0.008%N) and 193 (0.008%N-0.1%Ti-0.1%Al), figure 47,48.

### Hardness of Alloys

In the as quenched condition the high purity alloy K1525 had a

hardness of  $258 \pm 5$  HV30, alloy 134 (0.03N)  $289 \pm 6$  HV30 and alloy 137 (0.03N-0.1Ti-0.1Al)  $253 \pm 5$  HV30, table XIX. Clearly the low hardness of K1525 and 137 is due to the lower level of interstitial in solid solution. Alloy K1525 contains 0.003N and 0.004C and the Ti and Al additions in alloy 137 will have scavenged the interstitials in this alloy to very low levels.

On aging, maximum hardening was experienced in alloy K1525 rising from 258 HV30 to a peak hardness of 272 HV30 in 12 minutes. In the higher nitrogen alloy 134 (0.03%N) the hardness rose from 289HV30 to a peak hardness of 300HV30 in 4 minutes. The rise in hardness of both alloys is presumably due to the precipitation of  $Mn_3N_2$  as reported by Fuller and Garwood (96). The faster aging response of alloy 134 is due to the higher nitrogen content, although it is surprising that the rise in hardness in alloy 134 is less than in K1525. It must be assumed that some of the nitrogen in alloy 134 has segregated and/or precipitated in the martensite during the quench as suggested in section 5.1.1 under ice-brine quenched alloys.

Little aging occurs in alloy 137 at  $450^{\circ}C$ , the hardness rising from 253HV30 to a peak of 258HV30 in 6 minutes. Evidently the Ti and Al additions have reduced interstitials to very low levels.

The fall in hardness on overaging in all the alloys must be primarily due to recovery and possible recrystallisation of the lath martensitic structure. Coarsening of precipitates will also cause a decrease in hardness, particularly in alloy 137 where aluminium nitride and titanium carbo-nitrides are presumably present.

Hardness variations on aging in Nickbaht's alloys have still to be determined.

## Reverted Austenite

Reverted austenite was not detected until after 60 hours at 450°C in all the alloys. The formation of this phase will not therefore affect the embrittling kinetics, the maximum embrittling time examined being 10 hours at 450°C.

## Degree of embrittlement on aging

Alloy K1525 (0.003N) embrittled very rapidly on aging at 450°C, with a drop in tensile ductility at -78°C to zero after 5 minutes at 450°C. The higher N alloy 134 (0.03N) also embrittled rapidly on aging at 450°C with a rise in DBTT from 40°C to 200°C in 6 minutes. In alloy 137 (0.03N) containing Ti and Al additions, the rise in DBTT was less pronounced, from 10°C to 145°C in 6 minutes. In alloy 181 (0.008N) the rise in DBTT on aging was considerable; from 65°C to 330°C in 6 minutes. The rise in DBTT in alloy 193 (0.008N, 0.1Ti, 0.1Al), +30°C to +140°C in 6 minutes, was comparable to that in alloy 137.

In general the results suggest that embrittlement on aging is a maximum for some intermediate level of free nitrogen (alloy 181) and less for higher levels of N (alloy 134) or very low levels of N (alloys 137 and 193).

Subsequent changes in DBTT in all the alloys appeared to reflect changes in hardness, figure 46.

## Brittle fracture mode

Alloy K1525 gave a completely intergranular brittle fracture mode along prior austenite grain boundaries on water quenching and the same type of brittle fracture mode on subsequent aging, figures 95, 96.

In alloy 134 the fracture mode changed from cleavage in the ice-brine quenched state to 5-10%IG and cleavage after 6 minutes at 450°C (figure 85). But the percentage intergranular mode increased to 15 pct after 1 hour and remained the same till 10 hours of aging (figure 90,91).

In contrast, alloy 137 showed a rapid change in fracture mode from predominantly cleavage in the ice-brine quenched state (figure 85) to 50%IG after 6 minutes of aging (figure 92) to almost 90%IG after 1 hour of aging (figure 93). The percentage of each fracture mode remained the same till 10 hours of aging (figure 94).

Alloys 181 and 193 showed completely intergranular fractures below the DBTT on aging. (150)

### AES Results

The grain boundary concentration of Mn, P and N in alloy K1525 as a function of aging time at 450°C is shown in figure 57. A rapid grainboundary enrichment of Mn is observed accompanied by a slight rise in N content. After 1.5 minutes, P starts appearing in the AES spectra but builds up at a slower rate than that of Mn and N. The Mn level approaches that of equilibrium austenite (24 atomic % at 450°C). Reverted austenite (equilibrium austenite) has been reported as forming at prior austenite grain boundaries and inter-lath boundaries in 18%Ni maraging steels (25). Clearly one of the major driving forces for segregation of Mn to prior austenite grain boundaries is this tendency to form equilibrium reverted austenite at such sites, as discussed in section 5.1.1.

Inoue reported segregation of P atoms during austenitising in

a Fe-Mn-P alloy. He suggested that Mn could segregate to the prior austenite grain boundaries during tempering in the ferrite range due to a P-Mn interaction (147). Although such an interaction will increase the rate of Mn segregation to boundaries, it is now clear that for steels containing a reasonable level of manganese (greater than the solid solubility level of Mn at 450°C), segregation of Mn to high angle boundaries will occur on its own as a preliminary step in the formation of reverted austenite at such sites.

Guttman's work (151) on Sb-doped Mn steel shows that both Mn and Sb segregate simultaneously to all the boundaries in ferrite but failure occurs along prior austenite grain boundaries because these are paths of easiest fracture propagation (151). Clearly, once again, although there exists a Mn-Sb interaction manganese will segregate on its own for the reasons discussed previously, *i.e.* tendency to form reverted austenite at prior-austenite grain boundaries and inter-lath boundaries.

Alloys 134 (0.03N) and 137 (0.03N-0.1Ti-0.1Al) have a lower level of P than K1525 (0.003N) and no P was detected in AES spectra of these alloys. Instead Mn and N were detected on fracture surfaces. Figure 67 gives the comparative picture of the fracture surface concentrations of Mn and N in alloys 134 and 137 after ice-brine quenching and aging at 450°C. It is clearly shown that the overall level of Mn segregation to the fracture surface is more in alloy 137 than in alloy 134 which could account for the greater percentage of intergranular fracture mode in alloy 137 than in alloy 134.

However this difference in Mn concentration between alloy 134 and 137 should be interpreted with caution for the following reasons. There is a low percentage of intergranular fracture

(~10%) in alloy 134. Although the fracture surface concentration was calculated from the maximum AES signal, it is possible that the AES signal could have arisen from cleavage facets rather than intergranular surfaces. It seems reasonable to assume that the concentration of Mn would be less on cleavage facets rather than intergranular surfaces.

Alloy 137 (0.03N, 0.1Ti, 0.1Al) shows a drop in Mn and N level on fracture surfaces after 10 hours aging at 450°C. This could be from cleavage portion of the fracture surface. However these results were only obtained on one specimen and need to be confirmed.

The nitrogen level on aging alloy 134 (0.03N) appears greater than that in alloy 137 (0.03N, 0.1Ti, 0.1Al). This is presumably due to the presence of Ti and Al in alloy 137 scavenging N to low levels.

AES spectra on alloys 181 and 193 have yet to be determined.

#### General discussion of embrittlement on aging at 450°C

The maximum rise in hardness on aging the alloys at 450°C was 14HV30 in K1525, and was even less in the other alloys. It is thought that this small rise is unlikely to account for the large rise in DBTT on aging and embrittlement must be due to segregation of alloying elements and impurities to boundaries within the structure.

On comparison of segregation behaviour of Mn and N in alloys K1525 (0.003%N), 134 (0.03%N) and 137 (0.03%N-0.1%Ti-0.1%Al) on aging at 450°C, it appears that Mn segregation will take place on its own, but N will segregate to the boundaries due to a strong Mn-N interaction (96),

provided there is a small amount of N present in solid solution of ferrite. Support for this is available by comparison of Mn and N built-up in aging in alloy K1525 (0.003%N) and 137 (0.03%N, 0.1%Ti, 0.1%Al) figures 57 and 66. It appears that in both these alloys on aging at 450°C, Mn atoms segregate more freely and the concentration build up approaches the equilibrium concentration ( $\approx 24$  atomic % at 450°C).

In alloy K1525 the embrittling effect of Mn at 450°C was enhanced at  $\gamma$ - $\gamma$  boundaries because of N availability at these boundaries in the as water quenched condition (this alloy showed intergranular fracture in the water quenched condition prior to aging).

In alloy 137, the amount of Mn segregated was high enough to cause intergranular fragility (50-60%IG) on aging at 450°C with a rise in DBTT  $\sim 135^\circ\text{C}$  in six minutes (this alloy showed quasi-cleavage fracture mode on ice-brine quenching with a low DBTT  $\sim 10^\circ\text{C}$  prior to aging).

In alloy 134 on aging at 450°C the rise in DBTT occurs with predominantly cleavage fracture mode below the transition. This behaviour is puzzling. It is possible that at high N levels, clustering of Mn and N atoms occurs within the grains rather than segregation to grain boundaries on aging at 450°C. Evidence for this is provided by the double peak in the age hardening curve of alloy 134, figure 42. Presumably the first aging peak is due to the formation of an iron nitride, while the second peak is due to the formation of a secondary alloy nitride,  $\text{Mn}_3\text{N}_2$ . However at present there is no direct evidence for the precipitation of  $\text{Mn}_3\text{N}_2$  in alloy 134 during aging. The rise in percentage intergranular fracture on further aging alloy 134 at 450°C (5% to 15% IG after

10 hours) could be due to segregation of Mn to grain boundaries at a latter stage of aging. Evidence for this is provided by the increase in Mn concentration at fracture surfaces given by the AES spectra at longer aging times.

The extremely rapid embrittlement in alloy 181 (0.008N) on aging compared with 134 (0.03N) figure 41 also suggests that a small amount of N in solid solution may cause more embrittlement than a high level. Alloy 181 also showed mainly intergranular fracture on aging, while the high N alloy 134 only showed 10-15% IG on aging. As suggested previously it is thought that in the high N alloy 134 a strong Mn-N interaction occurs within the grains before segregation of Mn to grain boundaries.

The fact that alloy 181 (0.008N) de-embrittles on aging faster than alloy 134 (0.03N), figure 49, may be due to greater segregation of Mn to grain boundaries in alloy 181 compared with 134. Thus it is possible that the same embrittled boundaries in 181 start becoming de-embrittled earlier due to the greater concentration of Mn and a tendency to form reverted austenite at such boundaries at an earlier stage on aging. However these suggestions are very speculative and await confirmation by AES measurements on alloy 181.

In contrast to alloy 181, alloys 193 (0.008N, 0.1Ti, 0.1Al) and 137 (0.03N, 0.1Ti, 0.1Al) showed more or less the same shift in DBTT on aging at 450°C. The amount of free N in solid solution in these alloys on quenching from 900°C will be very small due to the scavenging effect of Ti and Al to form TiN and AlN. Thus at these very low levels of N, embrittling on aging is quite low. In addition the smaller grain size of these alloys (40-45 µm in alloy 137) compared with 134 (65-70 µm) and 181 will reduce the degree

of embrittlement due to segregation of Mn and N to grain boundaries.

As stated previously it is now fairly clear that Mn will segregate on its own to all the boundaries in ferrite on aging at 450°C. Whether segregation of Mn can cause embrittlement per se is not so clear although the results on alloys 137 and 193 suggests it may. However, these results do not eliminate a Mn-N interaction being responsible for embrittlement. This is because there will be a small but significant level of nitrogen left in solid solution after quenching alloys 137 and 193 from 900°C, which may segregate to boundary sites on aging at 450°C.

In summary, it is suggested that the embrittlement in Fe-8.0%Mn alloys is enhanced on aging at 450°C and AES analysis suggest that it is associated with the build up of Mn and N and sometimes P at the embrittled grain boundaries.

#### 5.1.4 Phase transformations on aging between 450-650°C

The phase transformations to reverted austenite and epsilon martensite on isothermal holding between 450-650°C have been plotted in figure 53 and tabulated in tables VIII-X. The basic reason for the study of these phase transformations between this temperature range was

- (1) to ensure that embrittlement reactions were only occurring in the  $\alpha$ -phase
- (2) to examine their effect on de-embrittlement at temperatures above 500°C.

As shown in figure 53, the reverted austenite was only detected after 60 hours of aging at 450°C, but no epsilon martensite was found. Since the longest embrittlement time was 10 hours at 450°C (section 5.1.3), thus it would not be affected by the formation of reverted austenite and epsilon martensite.

The results above 550°C, figure 53, show that the percentage of  $\epsilon$ -phase first increases and then decreases as the percentage of  $\gamma$  increases. The amounts of these phases increases with temperature as does the speed at which they form. The fact that the amount of  $\epsilon$  decreases while the amount of  $\gamma$  increases is consistent with the fact that  $\epsilon$  forms from  $\gamma$ . Overall the results are in agreement with those of the Russian workers (37) in quenched alloys containing 6 to 8.4%Mn after annealing between 600-625°C in the ( $\alpha + \gamma$ ) phase region.

On tempering above 500°C, considerable amounts of reverted austenite and epsilon martensite were produced. Schumann (29) and Charushnikova (66) have reported the beneficial effects on impact toughness of similar heat treatments to produce such phases in Fe-Mn alloys. Presumably these phases act as ductile areas to arrest the propagation of brittle cracks and/or sinks for embrittling impurities such as N. Bolton (3) reports an improvement in impact toughness of Fe-Mn alloys by tempering for 1 hour at 600°C and suggests that this is due to de-segregation of impurity elements at prior-austenite grain boundaries. It is now evident that although de-segregation may occur, the main de-embrittling effect is due to the formation of reverted austenite and epsilon martensite. Freeman (4) also concludes that the formation of reverted austenite and epsilon martensite above 520°C improves impact toughness.

#### 5.1.5 Kinetics of Embrittlement

Since any hardening of the alloy during aging will affect the kinetics of embrittlement to some extent, the variation in hardness in alloy K1525 with time was studied at 350°C, 400°C and 450°C,

figure 50, as well as tensile ductility tests, figure 54. At 450°C the hardness rose by  $\sim 12\text{HV}_{30}$  in 10-12 minutes, while the tensile ductility dropped to zero after 5 minutes.

In order to examine the interrelation of hardening with embrittlement the data was plotted in an Arrhenius form, figure 52. The activation energy for hardening, 147 kJ/gm.atom in this alloy appears to be close to the values of activation energies reported for hardening in nickel maraging steels, 126-189 kJ/gm.atom (136). In both cases hardening will be controlled by diffusion of substitutional elements in lath martensite; diffusion of manganese in alloy K1525 to form  $\text{Mn}_3\text{N}_2$ , and diffusion of nickel in the case of maraging steels to form intermetallics.

The lower value of activation energy for embrittlement, 77 kJ/gm.atom, suggests that the embrittlement during aging is not mainly due to hardening or diffusion of manganese to grain boundaries. The particular value of the activation energy is closer to that of diffusion of interstitials in ferrite. Hume & Rothery (169) gives an activation energy value of 80.4 kJ/gm.atom for diffusion of C in  $\alpha\text{-Fe}$  and 76.2 kJ/gm.atom for diffusion of N in  $\alpha\text{-Fe}$ . Examination of figure 57 shows a slight rise in the N concentration at brittle grain boundaries on aging. Although such a rise is within the error band, it seems plausible that the N concentration at the boundaries is rising with aging time and that diffusion of N in ferrite is the main rate controlling factor in embrittlement.

Capus (63) reported embrittling effects of N in Ni-Cr steels, figure 22, as did Rees and Hopkins (89) in high purity Fe-N alloys. H C Feng et al (69) reported N on brittle prior

austenite grain boundaries on aging an Fe-12Ni-6Mn maraging type alloy at 450°C although its significance was not realised at that time. The AES spectra published in Guttman's work of 1973 (151) showed a slight build up of N but no reference was made to this, only to the segregation of Mn and Sb in ferrite during aging. However recently Guttman clarified this point in his current publication on the Mn-N interaction (93) and suggested that in spite of N level being <10ppm, its segregation was noted along with segregation of Mn and Sb.

The work of Charasknikova et al (66) strongly supports the segregation of N in controlling embrittlement in Fe-8.0Mn alloys. These workers found that the addition of Ti and Al to an 8%Mn steel eliminated embrittlement below 350°C and suggested this was due to Ti and Al scavenging N. However grain boundary embrittlement still occurred between 400°C and 500°C which these workers attributed to temper embrittlement. The steels were quenched from 820°C and then tempered for an unspecified time (presumably 1h) at various temperatures. Embrittlement between 400°C and 500°C could be due to diffusion of Mn and N to prior austenite grain boundaries as found in the present investigation. There will be a small but significant amount of N left in solid solution on quenching from 820°C even in the presence of Ti and Al which could segregate and cause embrittlement on tempering at 400°C and 500°C.

Another comparison with previous research (1, 147) can be made for the de-embrittlement effect above 550°C shown in figure 54. Bolton (1) observed a drop in DBTT on holding at 600°C and suggested that the impurities causing embrittlement were de-segregated and the embrittlement was a reversible, whereas Inoue (147) found that embrittlement in Fe-Mn alloys was irreversible.

In the present investigation, figure 54 suggests that de-embrittlement above  $550^{\circ}\text{C}$  is occurring in ferrite and the shaded portion indicates the formation of  $\gamma$  and  $\epsilon$  phases on longer aging at the respective temperatures. It is noticed that the time gap between de-embrittling effect and the appearance of  $\gamma$  and  $\epsilon$  phases is so short that it is suggested that at temperatures above  $550^{\circ}\text{C}$  because of faster diffusion of Mn to grain boundaries a thin film of reverted austenite is formed which causes de-embrittlement effect at a microscale but measurable amounts of these phases start appearing after 5-10 minutes. Thus in conflict with Bolton (1) the de-embrittlement in Fe-Mn alloys is through formation of these ductile phases rather than thermal dispersal of any impurity. The present results are in agreement with Inoue (147) that embrittlement in such alloys is irreversible. It is suggested that the irreversible effect is through the presence of ductile phases.

In summary, the embrittlement in alloy K1525 during aging between  $300-650^{\circ}\text{C}$  exhibited C-curve behaviour (figure 54). Its kinetics depend on several factors such as segregation of Mn, N and P and to a lesser extent changes in hardness. The main embrittlement effect is due to a strong Mn-N interaction at prior austenite grain boundaries.

De-embrittlement above the nose of the C-curve is thought to be mainly due to formation of reverted austenite and epsilon martensite.

Edwards and Bishop (170) have analysed the kinetics of the build up of Mn and P on grain boundaries of alloy K1525 (0.003N) on aging at  $450^{\circ}\text{C}$ , figure. 59.

For manganese segregation the approximate equation 2.2.(6) was used:

$$\text{i.e.} \quad \frac{C_{bt} - C_{bo}}{C_{b\infty} - C_{bo}} \sim \frac{4\sqrt{D}}{\sqrt{\pi} \alpha_2 d} \sqrt{t}$$

$C_{b\infty}$  was taken as 24 atomic %, the equilibrium concentration of reverted austenite.

For phosphorus segregation it was further assumed that  $C_{bo} \ll C_{b\infty}$  and equation 2.2(7) was used:

$$\text{i.e.} \quad C_{bt} \sim \frac{4\sqrt{D}}{\sqrt{\pi} d} C_{bo} \sqrt{t}$$

The results of the analysis are shown in figure 59.

Taking the grain boundary thickness,  $d$  as  $2.9\text{\AA}$ , the derived coefficient for Mn turns out to be  $2.0 \times 10^{-18} \text{cm}^2/\text{sec}$  and for P  $2.0 \times 10^{-15} \text{cm}^2/\text{sec}$ . These values are in good agreement with the predicted values of  $0.1 \rightarrow 3.6 \times 10^{-18} \text{cm}^2/\text{sec}$  for manganese and  $5.7 \times 10^{-15} \text{cm}^2/\text{sec}$  for phosphorus using expressions obtained by Irmer (153) and Gruzin (154) for the diffusion of Mn and P in ferrite respectively.

Although one might expect slightly different values for diffusion coefficients than those for binary alloys due to the Mn-N and Mn-P interaction, such differences are thought to lie within the experimental error.

## 5.2 Thermal-Cycling Treatment of Fe-Mn Alloys

### 5.2.1 Influence of thermal-cycling treatment on cryogenic mechanical properties of alloy K1525 (without Ti and Al additions)

#### Cryogenic Impact Properties

A primary objective in using thermal cycling treatments was to explore the feasibility of designing an Fe-8%Mn alloy for cryogenic purposes which should exhibit minimum embrittlement.

In the Fe-Mn system a variety of substructural changes occur during the transformation of austenite to ferrite as shown by Roberts (7). Bolton and Holden (2) showed that when the Mn content exceeded about 10 pct, austenitized and quenched, alloys exhibited ( $\alpha+\epsilon$ ) micro-structures. When the Mn content was increased beyond 15 pct,  $\gamma$  phase appeared and was resistant to transformation even when cooled to liquid nitrogen temperature. Thus by increasing the Mn content, mixed microstructures of ( $\alpha+\epsilon+\gamma$ ) could be obtained which have been reported (32) to lower the DBTT but decrease the yield and tensile strength of Fe-Mn alloys as shown in figures 6-10.

In contrast, triple-phase microstructures comprising of ( $\alpha+\epsilon+\gamma$ ) were produced in alloy K1525 with 8% manganese by tempering, coupled with refinement of the prior-austenite grain size by thermal cycling (fig 68). Optical micrographs in figure 98(a,b) shows refinement of the prior-austenite grain size to 10-15  $\mu\text{m}$  after thermal cycling treatment. Table XI summarises the results of X-ray diffraction on phase transformations by thermal cycling treatment in alloy K1525. It appeared that after the second cycle the  $\gamma$  content had been slightly increased by  $\approx 2.2\%$  accompanied by a decrease in the amount of  $\epsilon$ -phase. This is

presumably due to an increase in the manganese content of the reverted austenite resulting in less transformation to  $\epsilon$ -martensite on cooling to room temperature. The Thermal cycling treatment resulted in the formation of favourable transformation products and with the attainment of a fine grain size, the ductile-brittle transition temperature was depressed from  $+115^{\circ}\text{C}$  to  $-60^{\circ}\text{C}$ .

*Transmission* electron micrographs in figures (102-105) show the appearance of interlath precipitation of reverted austenite and epsilon martensite developed by the thermal cycling treatment.

The technical basis of the cycling treatment has been discussed in section 4.2.1. Zackay (32) from his examination of the impact toughness and X-ray analysis of higher Mn alloys (12-20%Mn) concluded that the DBTT was lowered by  $1.3^{\circ}\text{C}$  per volume percent of  $(\epsilon+\gamma)$ . In alloy K1525 after thermal cycling, the volume percent of phases was 8.0% $\gamma$ , 24.7% $\epsilon$  and 67.3% $\alpha$  and the total shift in DBTT was  $\approx 175^{\circ}\text{C}$ . Clearly this improved impact toughness of this alloy K1525 must be due to introduction of these ductile phases into the microstructure as well as grain refinement. Using Zackay's analysis the shift in DBTT due to the formation of ductile phases  $(\gamma+\epsilon)$  is  $\approx 45^{\circ}\text{C}$  and  $\approx 130^{\circ}\text{C}$  due to grain-refinement, assuming the validity of Zackay's model. This later figure ( $130^{\circ}\text{C}$ ), would appear to be rather large for grain refinement (7) alone and indicates a synergistic interaction between grain refinement and the presence of  $(\gamma+\epsilon)$  phases. From Roberts' work (figure 11) the reduction in grain size from 80-90  $\mu\text{m}$  to 10-15  $\mu\text{m}$  in the alloy K1525 should correspond to a shift in DBTT  $\approx 50^{\circ}\text{C}$ .

The exact role of the  $(\gamma+\epsilon)$  phases in reducing embrittlement is not clear. It has been suggested that:

- (a) Austenite may act as a sink for impurities, in this case N, reducing embrittlement during heat treatment (25).

- (b) The ductile phases ( $\gamma+\epsilon$ ) may act as crack arresters blunting the propagation of brittle cracks (27,28,67).
- (c) Transformation of austenite to  $\alpha$  martensite and/or  $\epsilon$  martensite may occur during impact testing improving toughness (158).

In order to take full benefit of all these characteristics of austenite islands, the important factor is to make the austenite islands more stable, even at temperatures as low as  $-196^{\circ}\text{C}$ , by either adding appropriate alloying elements or suitable heat treatments (27,28). In spite of the introduction of ductile phases and grain refinement in alloy K1525 after thermal cycling, its impact energy value was negligible at liquid nitrogen temperature, although reverted austenite was stable down to  $-196^{\circ}\text{C}$  as shown in Table XI.

Zackay et al (32) achieved better impact toughness in their alloy Fe-12Ni-0.25Ti compared with the present investigation. This must partly be due to the finer grain size ( $0.5-2\mu\text{m}$ ) achieved by these workers. However another factor must be the solid solution effect of Ni on the DBTT (33). In the case of Fe-Mn alloys it has been concluded (7) that Mn does not exert a similar effect on the DBTT. In fact Mn in solid solution in ferrite neither raises nor lowers the DBTT per se, but only through its effect on microstructure. There is clearly scope for increasing the low temperature toughness of Fe-Mn alloys if further grain refinements could be achieved.

Zackay (140) reported that with multiple cycles the austenite was apparently stabilized and retained at room-temperature in several unusual morphologies. One of these <sup>in a morphology</sup> consisted of bead-like particles in the grain-boundaries as was observed in the present investigation.

in alloy K1525 (figure 97,98) where the bead-like network of reverted austenite delineates the prior austenite grains. However, Zackay has not confirmed this observation by TEM studies. Presently, TEM Studies are being made to confirm this bead-like morphology of reverted austenite in alloy K1525 after thermal cycling treatment. Freeman (4) observed with the help of transmission electron microscopy that austenite could appear as thin long bands and small islands separated by regions of recovered ferrite in 10%Mn alloy on tempering at 520°C for 10 hours. On tempering at 620°C, both  $\gamma$  and  $\epsilon$  phases were found as precipitates at  $\delta$  lath-boundaries. The transmission electron microscopic studies in alloy K1525 in the thermally-cycled *condition* agrees with these observations (4). Figure 102 shows the interlath precipitation of  $\gamma$  and  $\epsilon$  phases with a dislocation substructure in the  $\delta$  laths radically changed from that shown in figure 101. The effects of annealing in straightening of dislocation lines are evident. The austenite also lies along the former lath boundaries (figure 104) consistent with the observations of Freeman (4).

Bolton (1) and Freeman (4) sought to improve toughness by first ice-brine quenching from the austenitizing temperature and then tempering at 575-620°C for 10 hours followed by quenching from the tempering treatment. This led to improvements in low-temperature toughness with decline in strength in 10Mn alloy. In the present investigation in alloy K1525 it should be noted that during the thermal cycling treatment employed (2h, 740°C-AC; 2h, 655°C-AC; 2h, 740°C-AC-2h; 655°C-AC) the alloy has been subjected to air cooling continuously i.e. the condition of maximum embrittlement as confirmed by alloy 134 and alloy 181. Above all, the solution treatment used was 1h at 1000°C before cycling only in order to actually study the resistance of this alloy against

embrittlement as shown in the as water quenched alloy before thermal cycling. Thus it becomes obvious that the alloy K1525 after being thermally cycled has not only shown the resistance against as-water quenched brittleness but also embrittlement resulting due to air-cooling. It is clear that if the goal is to lower the DBTT, then brine-quenching rather than air-cooling should be employed. However, this would not be possible commercially. It should be possible to employ short austenitizing time at a lower temperature than that used in the present work (1000°C).

### Cryogenic Tensile Properties

Beside a low DBTT, an adequate yield strength must also be developed in an alloy which is to be considered for cryogenic applications. Therefore alloy K1525 after being thermally cycled was tensile tested at -78°C. The tensile results are summarized in figure 71 and Table XX.

It is shown that the alloy K1525 after being solution treated (1h, 1000°C) and water quenched exhibited a low elongation to UTS ( $\approx 11$  pct) followed by high reduction in area to fracture at -80°C. After thermal cycling treatment alloy K1525 showed no definite yield point but considerable increase in elongation especially to tensile strength ( $\approx 42.5$  pct) under the same conditions of testing. It appears from this curve (figure 71) that deformation induced transformations of the metastable phases  $\gamma$  and/or  $\epsilon$  to  $\alpha$  are occurring during tensile testing at -78°C and causing improvement in impact toughness as well (156,157,158). The shape of the stress-strain curve suggests that this transformation is stress induced. The increase in work hardening could be partly from grain refinement and partly from the barriers to slip propagation caused by the twin boundaries of the twin-related martensite  $\alpha$  formed from the  $\epsilon$  phase

(15) during the deformation induced transformation of epsilon and austenite to  $\alpha$ . It has been shown (15) that this  $\alpha$  martensite formed from the epsilon phase consists of twin-related plates rather than laths.

It appears from Zackay's work (32) that with increasing amounts of  $\epsilon$  in a primarily  $\alpha$  microstructure, the yield strength decreased which also seems to occur in alloy K1525 after thermal cycling treatment. It is also suggested (32) that in a ( $\alpha+\epsilon$ ) duplex structure the flow or strain tends to concentrate in the weaker  $\epsilon$  phase and the yield strength is controlled by the strength of the  $\epsilon$  phase. Using X-ray analysis after tension testing it was found (32) that a greater volume fraction of  $\epsilon$  transformed to  $\alpha$  in the 16%Mn alloy than that in 20%Mn alloy. It is suggested that beyond 12%Mn, when the hexagonal  $\epsilon$  phase begins to form, the DBTT of the alloys begin to drop and the alloys begin to lose their strength due to localised flow in the weaker  $\epsilon$  phase and a stress-induced transformation of  $\epsilon$  to  $\bar{\alpha}$  (157,158).

However, in alloy K1525 after the thermal-cycling treatment it is thought that the drop in the yield strength would have been greater without the grain refinement. Thus with a combination of  $\alpha$ ,  $\epsilon$  and  $\gamma$  phases along with grain refinement a reasonable compromise in strength and toughness was achieved.

Although the 'yield' or 'proof' stress of the alloys is low at  $-78^{\circ}\text{C}$ , which would not be desirable in a commercial materials this could be perhaps overcome by prior cold working the alloy (144).

### 5.2.2 Influence of Thermal-cycling treatment on Cryogenic mechanical properties of alloy 137 with Ti and Al additions

An attempt was made to see the **effect** of the same thermal cycling treatment on the impact toughness of alloy 137. It was thought that Ti and Al additions would act as grain refiners as well as scavengers for interstitials leading to an improvement in cryogenic properties.

In fact after thermal cycling, the impact transition temperature shifted from  $+150^{\circ}\text{C}$  (1h,  $1000^{\circ}\text{C}$ -WQ) to  $-40^{\circ}\text{C}$  as shown in figure 73. It appears from figure 108 that the grain refinement also occurred to the same extent as was noticed in alloy K1525 ( $10$ - $15\mu\text{m}$ ) in spite of the addition of Ti and Al. Scanning electron fractographs in figures (110-112) show ductile-cleavage fractures with precipitates of AlN, Ti(C,N) and MnS on the fracture surface as identified by dispersive X-ray analysis.

The total shift in impact transition temperature due to thermal cycling in alloy 137 was  $190^{\circ}\text{C}$  compared with  $170^{\circ}\text{C}$  in alloy K1525. Analysing this shift in alloy 137 in terms of Zackay's estimate (32) of  $1.3^{\circ}\text{C}/\text{volume } \% (\gamma+\epsilon)$  gives a shift of  $\sim 80^{\circ}\text{C}$  due to the presence of ductile phases and  $\sim 110^{\circ}\text{C}$  due to grain refinement. This later result of  $\sim 110^{\circ}\text{C}$ , due to grain refinement is in reasonable agreement with the estimated shift in DBTT of  $\sim 130^{\circ}\text{C}$  due to grain refinement in thermally cycled K1525, but is considerably more than that due to grain refinement, calculated from Roberts' work. Once again a synergistic interaction between grain refinement and the presence of  $(\gamma+\epsilon)$  phases is suspected.

Nevertheless although alloy 137 has the same grain size and a

greater concentration of ductile phases as alloy K1525 after thermal cycling it has a higher DBTT. ( $-40^{\circ}\text{C}$  compared with  $-60^{\circ}\text{C}$ ).

This difference is thought to be due to grain boundary precipitates of AlN and Ti(C,N).

Quarrell (58,102) and Fukagawa (103) reported that the precipitation of AlN on the primary austenite grain boundaries in low alloy steels resulted in embrittlement (see section 2.2.6). Thus it seems that similar kind of precipitation of AlN, Ti(C,N) has also occurred during solution treatment at  $1000^{\circ}\text{C}$  for 1 hr followed by water quenching as shown by the scanning electron fractograph in figure 83. The fracture mode is predominantly intergranular with small precipitates on the grain-boundary facets. It is possible that these precipitates may have caused intergranular fracture together with possible segregation of N during the quench. On thermal cycling (2h,  $740^{\circ}\text{C}$ -AC-2h,  $655^{\circ}\text{C}$ -AC-2h,  $740^{\circ}\text{C}$ -AC-2h,  $655^{\circ}\text{C}$ -AC) these precipitates have actually coarsened along with some more precipitation, figs. 110-112.

It is suggested that this precipitation of AlN, Ti(C,N) during thermal cycling treatment actually result in the acceleration of the whole diffusion process, causing an increase in the volume percent of  $\gamma$  and  $\epsilon$  phases in alloy 137. Support for this suggestion is provided by the work of Freeman and Knott (4) on Fe-10Mn-0.04C. Austenite precipitates were observed in their alloy after one hour at  $570^{\circ}\text{C}$  or 24 hours at  $520^{\circ}\text{C}$ . The austenite was found at the lath and prior austenite grain boundaries and grew into long narrow islands along these boundaries. The lath and prior austenite grain boundaries were also the sites for precipitation of  $\text{Fe}_3\text{C}$  and it was

suggested that the austenite was nucleated by these carbide particles. This process has also been observed to occur in a Fe-9%Ni steel (22,23,24) where it was found that austenite nucleated at carbide particles which had precipitated at the lath boundaries during the quench.

In summary, although alloy 137 has a greater concentration of ductile phases than alloy K1525 after thermal cycling, the presence of Ti(C,N) and AlN precipitates at prior austenite grain boundaries has resulted in loss of impact toughness below  $-40^{\circ}\text{C}$ . The Ti(C,N) and AlN particles are thought to aid the nucleation of reverted austenite.

### 5.2.3 Effect of aging at $450^{\circ}\text{C}$ on cryogenic mechanical properties in thermally-cycled alloy with and without Ti and Al additions

#### Alloy K1525

Unfortunately because of shortage of material in alloy K1525 the effect of aging at  $450^{\circ}\text{C}$  on the shift in DBTT could not be studied. Instead, the effect of aging on tensile ductility at  $-78^{\circ}\text{C}$  was studied in alloy K1525. Prior to thermal cycling this alloy after being austenitised for 1 hour at  $1000^{\circ}\text{C}$  followed by water quenching, showed a drop in ductility after aging for 5 minutes at  $450^{\circ}\text{C}$ , figure 51. After thermal cycling no signs of embrittlement were detected by tensile ductility measurement at  $-78^{\circ}\text{C}$  up to aging times of 2 hours. Engineering stress-strain curves at  $-78^{\circ}\text{C}$  for alloy K1525 after thermal cycling and aging for 10 mins, 1 hour and 2 hours are shown in figure 72. The effect of aging at  $450^{\circ}\text{C}$  on hardness, microstructure and tensile-ductility in alloy K1525 after thermal cycling treatment is summarized in tables XXI, XXII.

Slight variations in hardness could be associated with changes

in the phase analysis; <sup>4</sup> Optical metallography failed to show any changes in prior-austenite grain sizes.

As shown in figure 72, no definite yield point was noticed in this alloy in all heat-treated conditions. It appears from these tensile curves that <sup>deformation</sup> induced transformations of the metastable phases  $\gamma$  and/or  $\epsilon$  to  $\alpha$  are occurring during tensile testing at  $-78^{\circ}\text{C}$  and causing increase in %age elongation. The increase in tensile strength could be associated with increase in work hardening which could be partly because of grain-refinement and partly from the barriers to slip propagation caused by the twin boundaries of the twin-related martensite  $\alpha$  as stated previously in section 5-2.1

This deformation induced transformation of both  $\epsilon$  to  $\alpha'$  and of the  $\gamma$  to either or both  $\epsilon$  or  $\alpha$  could cause significant rise in ductility and impact toughness of the alloy.

#### Alloy 137 (with Ti and Al additions)

In alloy 137 on aging for 6 mins at  $450^{\circ}\text{C}$  after being thermally cycled, the DBTT at 40J remained about the same. This behaviour could be attributed to the increase in volume percent of  $(\epsilon+\gamma)$  phases from 60.2% after thermal cycling treatment to 71.3% after thermal cycling and aging for 6 mins at  $450^{\circ}\text{C}$ .

However there was little difference in the Charpy impact fractures in thermally-cycled specimens of alloy 137 before and after aging. The same typical ductile+cleavage mode at  $-78^{\circ}\text{C}$  with high proportion of precipitates of AlN, Ti(C,N) was noted, figures 110-112.

From these results, it would seem that both alloys K1525

and 137 are fairly resistant to embrittlement on aging at 450°C after the thermal cycling treatment.

## 6.0 CONCLUSIONS

Grain boundary embrittlement has been investigated in alloys based on Fe-8.0Mn. Such alloys had a lath martensitic structure essentially free of retained austenite or epsilon martensite at all cooling rates from the austenitising temperature.

1. An Fe-8.0Mn alloy containing 0.003%N (K1525) exhibited brittle intergranular failure at prior austenite grain boundaries in the quenched condition. Auger analysis showed that there was no segregation of Mn or impurities to these boundaries but nitrogen was detected on prior austenite grain boundaries. It is suggested that N segregation occurred to the prior austenite grain boundaries in the metastable  $\gamma$  field during cooling from the austenitising temperature. This segregated layer led to brittle intergranular fracture. A possible desegregation of carbon at the brittle grain boundaries was also observed by AES which may have also contributed to the grain boundary weakness.
2. Alloys with 8%Mn and 0.03%N (134) and 0.03%N with addition of 0.1%Ti and 0.1%Al (137) exhibited brittle cleavage fracture on ice-brine quenching. The AES analysis showed a slight rise in N concentration even on the cleavage fracture and the concentration of N varied from one region to another. The concentration of Mn was found equal to that of the bulk but no impurities were detected on the cleavage facets. It is suggested that, on rapid quenching, N segregation to austenite grain boundaries was suppressed in the metastable austenitic field, instead it segregated to dislocation complexes on the martensitic transformation on cooling below  $M_s$ .

3. Alloys 134 (0.03N) and 137 (0.03N-0.1Ti-0.1Al) showed intergranular fracture on air cooling with a rise in DBTT compared to the quenched condition. AES analysis in these air-cooled alloys indicated the simultaneous build up of N and Mn on the intergranular facets. It is suggested that the segregation of both N and Mn to grain boundaries occurred in the metastable austenitic field during air-cooling. The driving force for Mn segregation is thought to be the N-Mn interaction (95) and possibly the equilibrium segregation of Mn to austenite grain boundaries in the ( $\alpha + \gamma$ ) phase region.
4. Aging quenched alloys of K1525, 134, 137 at 450°C resulted in further embrittlement as detected by a drop in tensile ductility and a rise in the DBTT. The fracture mode was already intergranular in the water-quenched condition in alloy K1525 and on aging fracture mode remained intergranular but embrittlement was intensified as found by a fall in tensile R.A. to zero. In alloys 134 and 137, the fracture mode was predominantly cleavage in the ice-brine quenched condition, but on aging alloy 134 showed mixed fracture with only 10-15% intergranular and remaining cleavage whereas in alloy 137 it changed to predominantly intergranular.
5. The variation in hardness and appearance of reverted austenite which may affect embrittlement was also studied on aging at 450°C. Reverted austenite was not detected by X-ray analysis until after 60 hours and therefore did not affect the embrittling kinetics on aging at 450°C. The increase in hardness on aging was less than 12HV30 in all the alloys and was therefore thought to make only a small contribution to the rise in DBTT on aging.

6. In alloy K1525 (0.003N) a small rise in N content at the brittle grain boundaries occurred and after 2 minutes at 450°C a phosphorus build up occurred on the grain boundaries. A Mn build up on the grain boundaries was detected and approached the equilibrium concentration, 24 atomic per cent ie that of reverted austenite after 12 minutes. Examination of the kinetics of segregation of Mn and P at 450°C was consistent with bulk diffusion of Mn and P in  $\alpha$ -Fe, while measurement of the kinetics of embrittlement at various temperatures by tensile ductility indicated that diffusion of N in  $\alpha$ -Fe was the main rate controlling factor in isothermal embrittlement. It is suggested that in this alloy, Mn segregation takes place in ferrite to all the boundaries in the lath martensitic structure as a preliminary step in the formation of reverted austenite at such sites. Segregation of N and P also occurs to the same boundaries due to Mn-N (95) and Mn-P (147) interactions. Failure occurs along prior austenite grain boundaries because these boundaries were already embrittled prior to aging and they are easiest paths for brittle fracture (151).
7. At high N contents such as in alloy 134 (0.03N) only a small amount of intergranular fracture occurred on aging and the build up of Mn and N on fracture boundaries was a lot slower compared with alloy K1525 (0.003N) and alloy 137 (0.03N, 0.1Ti, 0.1Al). It is thought that at this high N level, Mn and N first form clusters within the matrix rather than diffusion to grain boundary sites. The driving force for this is thought to be the formation of  $Mn_3N_2$  within grains. Nevertheless some segregation of Mn and N to boundary sites occurs on aging resulting in a rise in DBTT.

8. On the other hand in alloys such as 137 (0.03N, 0.1Ti, 0.1Al) with a small percentage of dissolved N, Mn and N were observed to build up freely on fracture surfaces causing embrittlement. In this case it is thought that segregation of Mn and N occurs to boundary sites in the lath martensite rather than clustering of Mn and N atoms within the grains. The degree of embrittlement was less on aging compared with alloy 134 (0.03N) possibly because of the lower content of N in solid solution and the smaller grain size (40-45  $\mu\text{m}$  compared with 65-70  $\mu\text{m}$ ) due to refinement from the Ti and Al additions.
9. In all the alloys de-embrittlement occurred on overaging at 450°C. This is thought to be mainly due to the formation of thin layers of reverted austenite at embrittled grain boundaries by the diffusion to them of Mn.
10. Embrittlement in alloy K1525 (0.003N) was found to exhibit a 'C' curve behaviour with time and temperature. Maximum embrittlement occurred at 450°C. Above 450°C, reverted austenite formed rapidly on aging after embrittlement. It is suggested that segregation of Mn to boundary sites within the lath martensite occurs resulting in the formation of thin layers of reverted austenite giving de-embrittlement.
11. A thermal cycling treatment has been devised to overcome embrittlement.

In alloy K1525 (0.003N) the DBTT was reduced from +115°C to -60°C and the grain size from 80-90  $\mu\text{m}$  to 10-15  $\mu\text{m}$ . Reverted austenite and epsilon martensite were also produced in the structure. Such heat treated material appears resistant to embrittlement on aging at 450°C. Evidence of deformation induced transformation of the  $\gamma$  and  $\epsilon$  phase was obtained on

tensile testing at  $-78^{\circ}\text{C}$ . This transformation is thought to exhibit a TRIP effect and improve toughness.

In alloy 137 (0.03N, 0.1Ti, 0.1Al) although twice the amount of  $\epsilon$  martensite and reverted austenite were obtained on thermal cycling compared with alloy K1525, only the same grain size and DBTT was obtained. Impact toughness was thought to be impaired by intergranular precipitation of AlN and Ti (C,N) in alloy 137.

## 7.0 Recommendations for further work

1. The alloy 134 (0.03N) and alloy 181 (0.008N) both showed mainly intergranular fracture below the transition temperature on air-cooling. The DBTT value of alloy 181 was  $\approx 120^{\circ}\text{C}$  and of alloy 134  $\approx 375^{\circ}\text{C}$ . The AES results in alloy 134 supported the build up of both N and Mn on the grain boundaries thus enhancing the grain boundary fragility. The AES analysis work on alloy 181 is therefore needed to confirm the relationship between the amount of N and Mn segregating to grain boundaries.

2. Embrittlement studies on aging alloy 134 and alloy 181 at  $450^{\circ}\text{C}$  showed that the alloys exhibited severe embrittlement in the first six minutes with greater embrittlement in the low nitrogen alloy 181. Preliminary fractographic studies indicated that the fracture mode was 100 pct intergranular in the low nitrogen alloy 181 (0.008N) compared to 10-15% intergranular in high nitrogen alloy 134 (0.03N). It is therefore necessary to do the Auger analysis work in alloy 181 after being aged for 6 minutes, 1 hour and 10 hours.

It is hoped that this part of the work would be able to further clarify that Mn itself could also be responsible for brittleness especially during aging at  $450^{\circ}\text{C}$ . Alternatively, it is also suggested that aging studies be carried on in these alloys after being air cooled, especially in alloy 193 (0.008N, 0.1Ti, 0.1Al) where Ti and Al may tie up residual N on air cooling. In alloy 193, it is anticipated in the light of results of alloy 137, that a higher concentration of Mn will develop at the grain boundaries during aging but the enhancement in embrittlement will be suppressed because of grain refinement in these alloys.

3. The drop in tensile ductility as a function of aging time in alloy K1525 showed that the embrittlement occurred over a temperature range of 300-650°C. It is therefore recommended that Auger analysis be done on specimens embrittled at temperatures below 350°C, as Capus (63) reported in Ni-Cr steel that N embrittled alloys below 350°C and addition of small amounts of Mn was also found to embrittle above 350°C. Bolton (1,3) also found in his alloys that the embrittlement was pronounced when they were aged between 250-400°C. Charushnikova (66) reported that severe embrittlement occurred in his Fe-Mn alloys on aging between 250-500°C and embrittlement was eliminated over the range 250-350°C by the addition of Ti and Al but the alloys still remained brittle over 350-500°C. Thus this part of work will help substantially in understanding the mechanisms of brittleness on aging over this temperature range (ie 250°C-350°C).

4. In thermal cycling treatments, it is suggested that further improvement in cryogenic mechanical properties could be obtained by using a lower solution treatment temperature of nearly 800°C. Instead of air cooling during cycling, the specimens should be ice-brine quenched since the present work shows that air cooling results in considerable embrittlement. In alloy 137 containing 0.1Ti and 0.1Al, the cycling treatment should be modified to avoid the critical temperature ranges during which the precipitation of AlN and Ti(C,N) occurs along austenite grain boundaries and impairs the toughness.

5. Thermal cycled material showed evidence of a TRIP effect on tensile testing at -78°C. Further work is needed to determine whether transformations occurred during elastic or plastic deformation.

## Further work of general relevance

In order to develop Mn-base low carbon steels for cryogenic applications it is suggested that weldability and formability of steels based on Fe-8.0Mn needs to be examined especially after a heat treatment to produce optimum toughness.

The present work shows that free nitrogen is mainly responsible for embrittlement. Therefore further studies are required on alloys which are stabilised with Ti and/or Al. However care is required to achieve the correct balance between Ti and/or Al levels and the nitrogen content and also heat treatment to avoid intergranular precipitation of AlN and/or Ti(C,N).

A study of the resistance of the alloys containing various levels of impurities (N, Si, P, Sn, As, Sb) to embrittlement is required. In this respect alloys made with commercial alloy additions such as low-carbon ferro-manganese rather than high purity materials needs to be investigated.

## REFERENCES

1. J D Bolton PhD Thesis 1970, Sheffield City Polytechnic.
2. A Holden, J D Bolton, E R Petty, JISI, Sept 1971, pp 721-728.
3. J D Bolton, E R Petty and G B Allen, Met Trans, 2, p 2915, 1971.
4. B Freeman PhD Thesis, University of Cambridge, 1973.
5. E A Wilson - Private communication (1978).
6. E A Wilson - PhD Thesis, University of Liverpool, 1965.
7. M J Roberts, Met Trans, 1, p 3287, 1970.
8. J W Christian, Physical properties of Martensite and Bainite, ISI, Spec Rep 93, p 1, 1965.
9. P M Kelly, J Nutting, JISI, 1961, 197, p 199.
10. T Homa, J Japan Inst Metals, 21, p 126, 1957.
11. A Kelly, Proc Phys Soc (London) A66, 403, 1953.
12. W S Owen, E A Wilson and T Bell; High strength Materials, p 167, John Wiley and Sons, New York, 1965
13. P M Kelly, J Nutting, Proc Royal Soc, 1960, 259A, p 45.
14. J A Venables, Phil Mag, 1962, 7, p 35.
15. J F Breedis and L Kaufman, Met Trans ASM, vol 2, pp 2359-2371, 1971.
16. J G Parr, JISI, 171, (2), 1952.

17. C H White and R W K Honeycombe, JISI, 200 (6), 457, 1962.
18. B Cina, Acta Met, 6, 748, 1958.
19. B L Gabbitas, PhD thesis, University of Leeds, 1973.
20. R H Goodenow, R F Heheman, Trans Met Soc, AIME, 233, p 1777
21. A J McEvily , R G Davies et al, Symposium on Transformation and Hardenability in Steels, University of Michigan, p 179, 1967.
22. D Hardwick, Metallurgical Developments in High Alloy Steel, ISI, Special Report 86, 50, (1964).
23. S Nagashima - Toward improved ductility and toughness, Climax Molybdenum Co, Kyota, pp 353-358, 1971.
24. G R Brophy, A J Miller, Trans Am Soc Metals, 41,185, 1949.
25. C W Marshall et al, Trans ASM, Vol 55, p 135-148, 1962.
26. K Born et al, Arch, Eisenh, 40, 57, 1960.
27. Yana, Mimura et al, Trans ISIJ, vol 13, pp 133-140, 1973.
28. Haga ibid, vol 13, pp 141-144, 1973.
29. H Schumann, Arch Eisen, 38, 743, 1967.
30. F M Walters Jr et al, AIMME (Iron and Steel Division), 150, 401, 1942.
31. W P Rees and B E Hopkins, JISI, pp 403-409, 1952.
32. M J Yokota, J W Morris Jr, U F Zackay, ASTM, STP 579, pp 361-377, 1975.

33. W Jolley, Trans TMS-AIME, vol 242, pp 306-14, 1968.
34. W Jolley, JISI, vol 206, pp 170-173, Feb 1968.
35. W C Leslie, Met Trans ASM, vol 2, p 1989, 1971.
36. G Sasaki et al, "Fracture Mode Determinations by SEM" LBL 3120, Lawrence Berkeley. Laboratory, Berkeley Calif, Aug 1974
37. A S Nikonenko et al, Fiz Metal-Metalloved, 18, No 1, pp 126-129, 1964.
38. T Boniszewski, Brt Welding Journal 12, p 349, 1965.
39. F G Wilson, United Steels (Swindon Labs) Report No. PM5055/12/66, 1966.
40. A H Cottrell, Trans AIME, 212, 192 (1958).
41. H Conrad, Phil Mag, 5, 745 (1960).
42. J Helsop and N J Petch, Phil Mag 1, 866, 1956.
43. J R Low, Acta Met, 7, 171, 1959.
44. J R Low, Acta Met 5, 405, 1957
45. G T Hahn, W S Owen, B L Averbach, M Cohen, in Fracture, Wiley, New York, p 91, 1959.
46. G London et al, Franklin Inst Rept, FA2035, 1960.
47. D F Stein, Acta Met vol 14, 99, 1966.
48. J R Low, "Symposium on Relation of Properties to Microstructure, 163, ASM, 1954.
49. A A Griffith, Phil Trans R Soc, Vol A221, 163, 1920.

50. A A Griffith, Proc Inst Congr Appl Mech; vol 55, 1924.
51. E Orowan, Rep Prog Phys Vol 12, p 185, 1948.
52. N J Petch, in Fracture, Wiley, New York, p 54, 1959.
53. N P Allen, B E Hopkins et al, Proc Royal Soc (London) A234, 221 (1956)
54. J J Gilman, in Fracture, Wiley, New York, 1959, p 193.
55. H Ohtani, Toward Improved ductility and toughness, Climax Moly Co, Kyota, 1971.
56. A Joshi, D F Stein, JIM, London, Vol 99, pp 178-181, 1971.
57. B E Hopkin, H R Tipler, JISI, March 1958, pp 218-237.
58. J A Wright and A G Quarrell, JISI, pp 299-307, April 1962.
59. C F Tipper, Metallurgia, 39, 133, 1949.
60. P Ludwick, Z Metallk, 18, 269, 1926.
61. K E Puttick, Phil Mag, 4, 164, 1959.
62. C J Beevers, R W K Honeycombe, Phil Mag, 7, 763, 1962.
63. J M Capus et al, Metallurgia, Vol 62, pp 133-138, 1960.
64. G C Gould ASTM, Spec Tech Publ 407, p 90, 1968.
65. A Preece, R D Carter, JISI, vol 173, p 387-398, 1953.
66. G A Charushnikova et al, Metal Science and Heat Treatment No.7, pp 539-542, 1969.
67. D R Squires PhD Thesis 1972, Sheffield City Polytechnic.

68. D R Squires, E A Wilson, Met Trans, vol 3, pp 575-581, 1972.
69. H C Feng, E A Wilson, C J McMahon Jr, Third International Conference on High Strength Alloys, Cambridge, England, August 1973.
70. D Mclean 1957, Grain Boundaries in Metals, London, Oxford University Press.
71. R A Swalin, Thermodynamics of Solids, John Wiley and Sons, N.Y., p 191, 1967.
72. E D Hondros and D Mclean, Soc Chem Ind, London, Monograph, No 28, p 39, 1968.
73. J W Cahn and J E Hilliard, Acta Met, 1958, vol 7, p 219.
74. E D Hondros Proc Royal Soc, A286, pp 479-498, 1965.
75. F R Nabarro, Proc Phy Soc, vol 52, p 90, 1940.
76. F R Nabarro, Proc Royal Soc, Vol 175, p 519, 1940.
77. E D Hondros, 1969, In Interfaces, Proc Conference in Melbourne (ed R C Gifkins) pp 77-100, Butterworth, London.
78. E D Hondros and M P Seah, Scripta Met, 6, pp 1007-1012, 1972.
79. M P Seah, C Lea, Proc Royal Soc, pp 627-645, 1975.
80. W Steven and K Balajiva, JISI, vol 193, p 141-147, 1959.
81. J R Low and Feustel, Acta Met, Vol 1, p 185, 1953.
82. M P Seah and E D Hondros; Proc Royal Soc, 1973, 335A, 191.
83. C J McMahon Jr, Acta Met, 1966, vol 14, p 839.

84. J D Fast, Metalan, pp 171-181, 1949.
85. J R Rellick and C J McMahon Jr, Met Trans Vol 1, p 929, 1970
86. C Pickard, J Rieu and C Goux, Met Trans Vol 7A, Dec 1976, pp 1811-1815.
87. P Jolly and C Goux, Mem Sci Rev Met Vol 2, p 172, 1969.
88. C Pichard et al, Mem Sci Rev Met, p 13, Vol 70, 1973.
89. B E Hopkins and H R Tipler, JISI, May, pp 110-117, 1954.
90. M C Inman and H R Tipler, Acta Met, vol 6, pp 73-84, 1958.
91. D F Stein et al, Met Trans, vol 4, pp 1735-1742, 1973.
92. A R Entwisle, JISI, vol 169, pp 36-38, 1951.
93. B C Woodfine, JISI, vol 173, pp 229-255, 1953.
94. L D Jaffe and D C Buffum, Trans AIMME vol 209, p 8-16, 1957.
95. M Guttmann, Metal Science, pp337-341, Oct 1976.
96. B A Fuller, R D Garwood, JISI, pp 206-208, March 1972.
97. H Ohtani, H C Feng, C J McMahon Jr, Met Trans, 7A, 87, 1976.
98. M Guttmann, Surface Science 53, pp 213-227, 1975.
99. M Guttmann, P R Krahe, Met Trans, 5, 167, 1974.
100. J Q Clayton and J F Knott, Private Communication.
101. R A Mulford, C J McMahon Jr et al, Met Trans Vol 7A, pp 1183-1195, 1976.

102. B C Woodfine and A G Quarrell, JISI, August 1960, pp 409-414.
103. M Fukagawa et al, Proceedings ICSTIS, Suppl Trans ISIJ  
Vol 11, p 1092-1096, 1971.
104. G F Spaeder Met Trans vol 1, p 2011, 1970.
105. D Kalish and H F Rack, Met Trans, vol 2, p 2665, 1971.
106. W C Johnson and D F Stein, Met Trans, vol 5, pp 549-554, 1974.
107. E Nes, G Thomas, Met Trans vol 7A, pp 967-975, 1976.
108. H Brearly, Proceedings Institute of Automotive Engineers,  
Vol 11, p 347, 1916-17.
109. R H Greaves, JISI, Vol 100, pp 329-339, 1919.
110. R H Greaves, J A Jones, JISI, Vol 111, p 231-255, 1925.
111. H Jollivet and G Vidal, Revue des Metallurgie, vol 41,  
pp 378-388, 1944.
112. J H Holloman, Trans ASM, vol 36, p 473-540, 1946.
113. L D Jaffe and D C Buffum, Trans ASM, vol 42, pp 604-618, 1950.
114. J R Low Jr et al, Trans ASM, vol 242, p 14, 1968.
115. J M Capus, Temper Embrittlement in Steel, ASTM, STP 407, 1967.
116. P A Restaino, C J McMahon Jr, Trans ASM, vol 60, p 699, 1967.
117. B J Schultz, C J McMahon Jr, Temper Embrittlement of Alloy  
Steel ASTM, STP 499, p 104, 1971.
118. C J McMahon Jr, H Herman, Met Trans, Vol 5, p 1061-1068, 1974.

119. M Guttman, P R Krahe, Mem Sci, Rev met, vol 70, No 9, pp 657-668, 1973.
120. R Viswanathan and Sherlock, Met Trans, vol 3, p 459, 1972.
121. J R Rellick, C J McMahon Jr, Met Trans vol 5, pp 2439-2448, 1974.
122. R Viswanathan, A Joshi, Met Trans vol 6A, pp 2289, 1973.
123. L A Harris, Journal of Applied Physics, vol 39, 1968.
124. D F Stein, A Joshi, R Laforce, Trans ASM, vol 62, pp 776-783, 1969.
125. L C Geniets, J F Knott, Proceedings of the Conference on Grain Boundaries Structure and Segregation - Institute of Metals, p 69-70, 1972.
126. A E Powers JISI, 186, 323, 1957.
127. G W Austin et al, JISI, 173, 376, 1953.
128. T Suzuki - Bulletin of the Tokyo Institute of Technology, No. 112, p 61-70, 1972.
129. E N Sokolov; Fiz Met, Metallov, 7, 784, 1959.
130. J Plateau, ISI, Special Report No.64, p 157, 1959.
131. V I Arkharo, Fizika, Metallov, vol 2, p 57, 1956.
132. J H Westbrook and D L Wood, J Inst Met, 91, 174, 1963.
133. R G C Hill and J W Martin, Met Treat, Drop Forg, 29, 301, 1962.
134. N J Petch, Phil Mag, 1, 186 (1956)

135. N P Allen et al, JISI, p 281, 166, 1950.
136. D T Peters, Trans ASM, vol 61, pp 62-74, 1968.
137. S Yano et al, Tetsu-to-Hagane, 57, No 4, p 199, 1971.
138. J H Roux, Rev Met, 57, 507, 1960.
139. T Wada, Met Trans, Vol 5, 1974, pp 231-239.
140. V F Zackay, Third international conference on the Strength of Metals and Alloys. Cambridge, England. August 1973, paper no. 125, p 591.
141. S Jin, J W Morris Jr, V F Zackay, Met Trans, vol 6A, pp 141-149, Jan 1975.
142. R A Grange, Trans ASM, vol 59, pp 26-48, 1966.
143. L F Porter, D S Dabkowski, Ultrafine Grain Metals, Proc 16th Sagamore Conf, p 183, 1970.
144. R L Miller, Met Trans, vol 3, pp 905-912, 1972.
145. M Hansen, Constitution of Binary alloys. McGraw-Hill, New York, pp 664-668, 1958.
146. M J Yokota, Harwood, Mat Sc and Engg 19, pp 129-138, 1975.
147. T Inoue, K Yamamoto et al, Trans ISIJ, vol 14, p 372, 1974.
148. B C Edward, J C Riviere, Acta Met, vol 24, pp 957-967, 1976.
149. T Inoue, Proceedings of the fourth Bolton Landing Conference, p 553, 1974.
150. Nickbaht M.Sc thesis Sheffield City Polytechnic 1978.

151. M Guttman, P R Krahe, Scripta Met, vol 7, pp 387-394, 1973.
152. J H Little et al, ISI/BSC Conference on the effect of second phase particles on the mechanical properties of Steel (March 1971)
153. V Irmer et al, J Phys Chem 33, 2141, 1972.
154. P L Gruzin, Fiz Metalloved, Metal, 16 (4), 551, (1963).
155. K Karraya et al, J Appl Phys, 12, 1297, 1973.
156. V F Zackay et al, Metallurgical Transactions, ASM, vol 3, 1972, pp 2619-2631.
157. R P Reed, G J Guntner, Transactions Metallurgical Society of the American Institute of Mining and Metallurgical Engineers, vol 230, 1964, pp 1713-1720.
158. W Gerberich, V F Zackay, Met Trans, ASM, vol 2, 1971, pp 2243-2253.
159. N S Stoloff, Fracture, vol 6, H Liebowitz Academic Press, New York, 1969, p 1-81.
160. B L Averbach, M Cohen, Metals Technology, 15, February 1948.
161. J Durnin, K A Ridal, JISI, Jan 1968, pp 60-67.
162. R L Miller, Trans of the ASM, vol 57, pp 892-899, 1964.
163. R E Weber and A L Johnson, J Appl Phys, 40, 314 (1969).
164. C H Lorig and A R Elsea; Trans AFS, 55, 1947, 160-173.
165. S R Keown and F B Pickering, Iron and Steel, December 1965.

166. H E Bishop, J P Coad and J C Riviere, J Electron Spectroscopy, 1, 389, 1973.
167. G W B Ashwell, C J Todd and R Heckingbottom, J Phys E Sci Instrum, 6, 435 (1973).
168. P W Palmberg, G E Riach, R E Weber, and N C MacDonald, Handbook of Auger Electron Spectroscopy. Physical Electronics Industries Inc, MN (1972).
169. W Hume-Rothery. "The Structure of alloys of iron", Pergamon Press, 1966, p 82.
170. B C Edwards and H E Bishop: AERE Report No R8516, September 1976.

TABLE I : CHEMICAL ANALYSIS OF CASTS INVESTIGATED

Cast No.	N	C	Si	S	P	Ni	Cr	Cu	Sn	Ti	Al	Sb	As	Mo	Mn	Co
134	0.03	0.001	0.03	0.005	0.002	0.007	0.13	0.01	0.005	<0.01	0.005	<10ppm	<100ppm	0.013	7.93	Ni:
137	0.03	0.001	0.07	0.012	0.005	0.017	0.06	0.004	0.006	0.128	0.071	<10ppm	<100ppm	0.018	7.78	-
K1525	0.003	0.004	0.011	0.010	0.006	0.0027	0.002	-	0.005	-	-	-	0.0027	-	8.1	-
181	0.008	0.014	0.037	0.009	0.004	0.06	0.04	-	-	<0.01	0.004	~10ppm	<100ppm	0.02	7.89	-
193	0.008	0.018	0.05	0.010	0.004	0.06	0.07	-	-	0.17	~0.18	~10ppm	<100ppm	0.02	8.54	-

TABLE II: HEAT-TREATED ALLOYS AND MICROSTRUCTURE

ALLOY	HEAT-TREATMENT	PHASE-ANALYSIS	PRIOR-AUSTENITE GRAIN-SIZE	PACKET SIZE
134 Fe-8.0Mn	ST1000°C/1h - WQ	$\alpha > 98\%$ $\epsilon < 2\%$	80-90 $\mu\text{m}$	20-25 $\mu\text{m}$
	ST1000°C/1h - IBQ	$\alpha > 98\%$ $\epsilon < 2\%$	80-90 $\mu\text{m}$	20-25 $\mu\text{m}$
	ST900°C/½h - IBQ	$\alpha > 98\%$ $\epsilon < 2\%$	65-70 $\mu\text{m}$	15-20 $\mu\text{m}$
	ST900°C/½h - AC	$\alpha > 98\%$ $\epsilon < 2\%$	65-70 $\mu\text{m}$	15-20 $\mu\text{m}$
1525 Fe-8.0Mn	ST1000°C/1h - WQ	$\alpha > 98\%$ $\epsilon < 2\%$	80-90 $\mu\text{m}$	20-25 $\mu\text{m}$
	ST1000°C/1h-WQ+IA+IB +IIA+IIB	$\alpha = 67.33\%$ $\gamma = 8.02\%$ $\epsilon = 24.65\%$	10-15 $\mu\text{m}$	3-4 $\mu\text{m}$
	ST1000°C/1h-WQ+IA+IB+IIA +IIB+2h/450°C-WQ	$\alpha = 80.57\%$ $\gamma = 10.64\%$ $\epsilon = 8.79\%$	10-15 $\mu\text{m}$	3-4 $\mu\text{m}$
	ST1000°C/1h - WQ	$\alpha > 98\%$ $\epsilon < 2\%$	60-70 $\mu\text{m}$	15-20 $\mu\text{m}$
137 Fe-8.0Mn -0.1Ti-0.1Al	ST900°C/½h - IBQ	$\alpha > 98\%$ $\epsilon < 2\%$	40-45 $\mu\text{m}$	10-15 $\mu\text{m}$
	ST900°C/½h - AC	$\alpha > 98\%$ $\epsilon < 2\%$	40-45 $\mu\text{m}$	10-15 $\mu\text{m}$
	ST1000°C/1h-WQ+IA+IB +IIA+IIB	$\gamma = 17.53\%$ $\epsilon = 26.02\%$ $\alpha = 56.45\%$	10-15 $\mu\text{m}$	3-4 $\mu\text{m}$
	ST1000°C/1h-WQ+IA+IB +IIA+IIB+6min/450°C-WQ (-196)	$\gamma = 12.39\%$ $\epsilon = 41.90\%$ $\alpha = 45.71\%$	10-15 $\mu\text{m}$	3-4 $\mu\text{m}$

TABLE III: TRANSFORMATION TEMPERATURES IN Fe-8%Mn ALLOYS

K1525	$M_S = 360 \pm 5^\circ\text{C}$ $M_f = 336 \pm 5^\circ\text{C}$	$A_S = 677 \pm 5^\circ\text{C}$ $A_f = 723 \pm 5^\circ\text{C}$
137	$M_S = 355 \pm 5^\circ\text{C}$ $M_f = 325 \pm 5^\circ\text{C}$	$A_S = 678 \pm 5^\circ\text{C}$ $A_f = 721 \pm 5^\circ\text{C}$
134	$M_S = 357 \pm 5^\circ\text{C}$ $M_f = 330 \pm 5^\circ\text{C}$	$A_S = 670 \pm 5^\circ\text{C}$ $A_f = 710 \pm 5^\circ\text{C}$

TABLE IV:  $\text{CuK}\alpha$  RADIATION  $\lambda = 1.542\text{\AA}$  THEORETICAL INTENSITY FOR (hkl), 'R' FACTOR

hkl	$\theta$	$\text{Sin } \theta$	d-spacing	$\text{Sin } \theta/\lambda$	m	L.P.	$e^{-2M}$	V	f	F	R
(110)	22.41	0.382	2.027	0.25	12	4.41	0.976		13.14	26.28	66.909
(200)	32.30	0.535	1.433	0.346	6	2.17	0.955	23.38	10.35	20.70	10.39
(211)	41.20	0.659	1.170	0.427	24	1.53	0.929	(KX) <sup>3</sup>	9.25	18.50	21.35
(220)	49.50	0.740	1.013	0.48	12	0.504	0.912		7.09	14.18	2.02
(310)	58.30	0.581	0.906	0.552	24	0.55	0.886		6.85	13.70	4.03
(111)	21.85	0.372	2.07	0.251	8	4.64	0.975		13.14	52.56	47.25
(200)	25.45	0.430	1.793	0.28	6	3.56	0.969		11.54	46.16	20.78
(220)	37.40	0.607	1.268	0.394	12	1.75	0.941	46.0	9.25	37.00	12.78
(311)	45.48	0.712	1.081	0.461	24	1.40	0.919		8.36	33.44	16.31
(222)	48.15	0.745	1.035	0.482	8		0.912		7.56	30.24	
(10.0)	20.30	0.347	2.22	0.225	6	5.12	0.980		12.34	12.34	8.66
(00.2)	22.32	0.38	2.03	0.246	2	4.45	0.976	23.0	13.14	26.28	11.34
(10.1)	23.28	0.395	1.95	0.256	6	4.07	0.974		12.92	22.37	22.49
(10.2)	30.95	0.514	1.50	0.334	6	2.4	0.955		10.35	10.35	2.78
(11.0)	37.0	0.602	1.28	0.390	6	1.78	0.941		9.25	18.50	6.50

TABLE V: X-RAY DIFFRACTION ANALYSIS

Alloy 137 Fe-8.0Mn-0.03N-0.1Ti-0.1Al

Solution treated 900°C/½h - Ice-brine Quenched and Aged at 450°C

Heat Treatment	%age Phases with Different Peak Combinations								%age Ph
	(200) <sub>α</sub> -(200) <sub>γ</sub>	(200) <sub>α</sub> -(220) <sub>γ</sub>	(200) <sub>α</sub> -(311) <sub>γ</sub>	(211) <sub>α</sub> -(200) <sub>γ</sub>	(211) <sub>α</sub> -(220) <sub>γ</sub>	(211) <sub>α</sub> -(311) <sub>γ</sub>	(211) <sub>α</sub> -(311) <sub>γ</sub>	AV γ	
ST 900°C/ ½h-IBQ	-	-	-	-	-	-	-	-	-
Aged 450°C/ 100 hours-WQ	3.3	-	-	3.3	-	-	-	3.3	3.3
Aged 400 hours WQ	5.6	4.5	3.4	5.9	4.7	3.6	3.6	4.6	4.6
Aged 1000 hours WQ	9.2	6.5	7.0	8.7	6.2	6.7	6.7	7.4	7.4
400 hrs-WQ- kept in liquid N <sub>2</sub> for 15 mins	3.6	-	-	3.7	-	-	-	3.6	3.6
1000 hrs-WQ- kept in liquid N <sub>2</sub> for 15 mins	6.2	7.4	4.7	8.0	9.5	6.1	6.1	7.0	7.0

TABLE VI: X-RAY DIFFRACTION ANALYSIS

Alloy 137 Fe-8.0Mn-0.03N-0.1Ti-0.1Al

Solution treated 900°C/½h-Air-Cooled and Aged at 450°C

Heat Treatment	%age Phases with different Peak Combinations								%age P]
	(200) <sub>α</sub> - (200) <sub>γ</sub>	(200) <sub>α</sub> - (220) <sub>γ</sub>	(200) <sub>α</sub> - (311) <sub>γ</sub>	(211) <sub>α</sub> - (200) <sub>γ</sub>	(211) <sub>α</sub> - (220) <sub>γ</sub>	(211) <sub>α</sub> - (311) <sub>γ</sub>	(211) <sub>α</sub> - (311) <sub>γ</sub>	AV γ	
ST 900°C/ ½h-A.C.	-	-	-	-	-	-	-	-	10
100 hours-WQ	5.2	8.1	3.8	5.3	8.2	3.8	3.8	5.7	
700 hours-WQ	6.1	7.4	5.4	5.8	7.0	5.2	5.2	6.2	
1000 hours-WQ	5.6	4.7	4.9	6.8	5.7	5.9	5.9	5.6	
100 hrs-WQ- kept in liquid N <sub>2</sub> - 15 mins	7.3	6.1	4.6	6.2	5.2	3.8	3.8	5.5	
1000 hrs-WQ- kept in liquid N <sub>2</sub> - 15 mins	6.0	4.5	5.2	7.1	5.3	6.2	6.2	5.7	

TABLE VII: X-RAY DIFFRACTION ANALYSIS

Alloy 134 ST900°C/½h-Ice-brine quenched-Aged at 450°C

Heat Treatment	%age Phases with Different Peak Combinations								Average %age $\beta$
	(200) <sub>α</sub> -(200) <sub>γ</sub>	(200) <sub>α</sub> -(220) <sub>γ</sub>	(200) <sub>α</sub> -(311) <sub>γ</sub>	(211) <sub>α</sub> -(200) <sub>γ</sub>	(211) <sub>α</sub> -(220) <sub>γ</sub>	(211) <sub>α</sub> -(311) <sub>γ</sub>	(211) <sub>α</sub> -(311) <sub>γ</sub>	AV $\gamma$	
ST-IBQ	-	-	-	-	-	-	-	-	-
ST-IBQ-A450°C for 25 hrs-WQ	-	-	-	-	-	-	-	-	-
ST-IBQ-A450°C for 50 hrs-WQ	-	-	-	-	-	-	-	-	-
ST-IBQ-A450°C for 75 hrs-WQ	$\gamma = 1.8\%$ $\alpha = 98.2\%$	$\gamma = 1.4\%$ $\alpha = 98.6\%$	-	-	-	-	-	-	1.6% $\gamma$
ST-IBQ-A450°C for 100 hrs-WQ	$\gamma = 1.8\%$ $\alpha = 98.2\%$	$\gamma = 1.8\%$ $\alpha = 98.2\%$	-	-	-	-	-	-	1.8% $\gamma$

TABLE VIII: X-RAY DIFFRACTION ANALYSIS

Alloy K1525 - ST1000°C/1h-Water Quenched - Aged at 450°C

Heat Treatment	%age Phases with Different Peak Combinations							Average %age P
	(200) <sub>α</sub> - (200) <sub>γ</sub>	(200) <sub>α</sub> - (220) <sub>γ</sub>	(200) <sub>α</sub> - (311) <sub>γ</sub>	(211) <sub>α</sub> - (200) <sub>γ</sub>	(211) <sub>α</sub> - (220) <sub>γ</sub>	(211) <sub>α</sub> - (311) <sub>γ</sub>	% γ	
(i) ST 1000°C/ 1h-WQ	-	-	-	-	-	-	-	-
(ii) ST-WQ- Aged 25h/ 450°C	-	-	-	-	-	-	-	-
(iii) ST-WQ- Aged 50h/ 450°C	-	-	-	-	-	-	-	-
(iv) ST-WQ- Aged at 450°C for 75 hrs	γ = 1.5% α = 98.5%	-	-	-	-	-	-	1.5% 9
(v) ST-WQ-Aged at 450°C for 100hrs	γ = 1.8% α = 98.2%	γ = 1.8% α = 98.2%	-	-	-	-	-	1.8% 9

TABLE IX: X-RAY DIFFRACTION ANALYSIS

Alloy K1525 ST1000°C/1h - Water Quenched - Aged at 550°C

Heat Treatment	%age Phases with different Peak Combinations					AV Pha.
	(200) <sub>α</sub> - (200) <sub>γ</sub> - (10.1) <sub>ε</sub>	(200) <sub>α</sub> - (220) <sub>γ</sub> - (10.1) <sub>ε</sub>	(211) <sub>α</sub> - (200) <sub>γ</sub> - (10.1) <sub>ε</sub>	(211) <sub>α</sub> - (220) <sub>γ</sub> - (10.1) <sub>ε</sub>	(211) <sub>α</sub> - (220) <sub>γ</sub> - (10.1) <sub>ε</sub>	
ST1000°C/1h- WQ	-	-	-	-	-	α > ε <
ST-WQ -550°C/30 mins -WQ	γ = 2.1% ε = 2.6% α = 95.3%	γ = 1.5% ε = 2.7% α = 95.8%	γ = 1.6% ε = 2.1% α = 96.3%	γ = 1.6% ε = 2.1% α = 96.3%	γ = 1.2% ε = 2.9% α = 95.9%	γ = ε = α =
ST-WQ -550°C/1 hour -WQ	γ = 2.0% ε = 4.7% α = 93.3%	γ = 1.2% ε = 4.7% α = 94.1%	γ = 2.5% ε = 6.2% α = 91.3%	γ = 2.5% ε = 6.2% α = 91.3%	γ = 1.6% ε = 6.2% α = 92.2%	γ = ε = α =
ST-WQ -550°C/5 hrs -WQ	γ = 2.5% ε = 1.0% α = 96.5%	γ = 0.6% ε = 1.0% α = 98.4%	γ = 5.4% ε = 2.1% α = 92.5%	γ = 5.4% ε = 2.1% α = 92.5%	γ = 1.3% ε = 2.2% α = 96.5%	γ = ε = α =
ST-WQ -550°C/ 33 hrs -WQ	γ = 16.0% ε = 1.7% α = 82.3%	γ = 11.1% ε = 1.7% α = 87.2%	γ = 16.3% ε = 1.7% α = 82.0%	γ = 16.3% ε = 1.7% α = 82.0%	γ = 11.3% ε = 1.8% α = 86.9%	γ = ε = α =

TABLE X: X-RAY DIFFRACTION ANALYSIS

Alloy K1525 Solution treated 1000°C/1hr - Water Quenched and Aged at 650°C

Heat Treatment	%age Phases with Different Peak Combinations					Ave % P
	(200) <sub>α</sub> - (200) <sub>γ</sub> - (10.1) <sub>ε</sub>	(200) <sub>α</sub> - (220) <sub>γ</sub> - (10.1) <sub>ε</sub>	(211) <sub>α</sub> - (200) <sub>γ</sub> - (10.1) <sub>ε</sub>	(211) <sub>α</sub> - (220) <sub>γ</sub> - (10.1) <sub>ε</sub>	(211) <sub>α</sub> - (220) <sub>γ</sub> - (10.1) <sub>ε</sub>	
ST-WQ	-	-	-	-	-	ε < α >
ST-WQ-650°C/ 30 mins-WQ	γ = 1.1% ε = 9.1% α = 89.8%	γ = 5.9% ε = 8.7% α = 85.4%	γ = 1.2% ε = 9.8% α = 89%	γ = 6.4% ε = 9.2% α = 84.4%	γ = 12.2% ε = 24.6% α = 63.2%	γ = ε = α =
ST-WQ-650°C/ 1 hour-WQ	γ = 5.6% ε = 21.2% α = 73.2%	γ = 10.0% ε = 20.2% α = 69.8%	γ = 6.9% ε = 26.1% α = 67.0%	γ = 8.4% ε = 25.4% α = 66.2%	γ = 44.3% ε = 9.0% α = 46.7%	γ = ε = α =
ST-WQ-650°C/ 5 hours-WQ	γ = 4.3% ε = 28.1% α = 67.6%	γ = 8.9% ε = 26.7% α = 64.4%	γ = 4.1% ε = 26.6% α = 69.3%	γ = 54.9% ε = 7.2% α = 37.9%	γ = 44.3% ε = 9.0% α = 46.7%	γ = ε = α =
ST-WQ-650°C/ 20 hours-WQ	γ = 55.4% ε = 7.4% α = 37.2%	γ = 44.9% ε = 9.1% α = 46.0%	γ = 54.9% ε = 7.2% α = 37.9%	γ = 44.3% ε = 9.0% α = 46.7%	γ = 44.3% ε = 9.0% α = 46.7%	γ = ε = α =

TABLE XI: PHASE-TRANSFORMATIONS ON THERMAL CYCLING TREATMENT

Alloy K1525 Solution Treated 1000°C/1 hour - WO + I<sub>A</sub>+I<sub>B</sub>+II<sub>A</sub>+II<sub>B</sub> (Figure 68)

Heat Treatment	%age Phases with Different Peak Combinations					Ave % P
	(200) <sub>α</sub> - (200) <sub>γ</sub> - (10.1) <sub>ε</sub>	(200) <sub>α</sub> - (220) <sub>γ</sub> - (10.1) <sub>ε</sub>	(211) <sub>α</sub> - (200) <sub>γ</sub> - (10.1) <sub>ε</sub>	(211) <sub>α</sub> - (220) <sub>γ</sub> - (10.1) <sub>ε</sub>	(211) <sub>α</sub> - (220) <sub>γ</sub> - (10.1) <sub>ε</sub>	
Solution Treated (ST) & Water Quenched (WQ)	-	-	-	-	-	Max
ST-WQ+I <sub>A</sub>	-	-	-	-	-	Max
ST-WQ+I <sub>A</sub> +I <sub>B</sub>	γ = 1.5 ε = 27.0 α = 71.5	γ = 9.3 ε = 24.9 α = 65.8	γ = 1.7 ε = 31.6 α = 66.7	γ = 10.7 ε = 28.6 α = 60.7	γ = 4.0 ε = 4.5 α = 91.5	γ = ε = α =
ST-WQ+I <sub>A</sub> +I <sub>B</sub> +II <sub>A</sub>	γ = 4.1 ε = 3.6 α = 92.3	γ = 3.2 ε = 3.6 α = 93.2	γ = 5.1 ε = 4.4 α = 90.5	γ = 4.0 ε = 4.5 α = 91.5	γ = 12.9 ε = 26.2 α = 60.9	γ = ε = α =
ST-WQ+I <sub>A</sub> +I <sub>B</sub> +II <sub>A</sub> +II <sub>B</sub>	γ = 3.8 ε = 22.6 α = 73.6	γ = 10.5 ε = 21.3 α = 68.2	γ = 4.8 ε = 28.6 α = 66.6	γ = 12.9 ε = 26.2 α = 60.9	γ = 8.7 ε = 29.3 α = 62.0	γ = ε = α =
ST-WQ+I <sub>A</sub> +I <sub>B</sub> +II <sub>A</sub> +II <sub>B</sub> kept in Liq.N <sub>2</sub> for 15 min	γ = 3.8 ε = 24.2 α = 72.0	γ = 7.0 ε = 23.4 α = 69.6	γ = 4.7 ε = 30.3 α = 65.0	γ = 8.7 ε = 29.3 α = 62.0	γ = 8.7 ε = 29.3 α = 62.0	γ = ε = α =

TABLE XII: PHASE TRANSFORMATIONS PRODUCED ON AGING THERMALLY CYCLED ALLOY AT 450°C

Alloy K1525, Fe-8.0Mn; Solution treated 1h at 1000°C, water quenched

Thermally cycled, I<sub>A</sub>+I<sub>B</sub>+II<sub>A</sub>+II<sub>B</sub> according to figure 68 and aged at 450°C

Heat Treatment	%age Phases with different Peak Combinations						Average % I
	(200) <sub>α</sub> - (200) <sub>γ</sub> - (10.1) <sub>ε</sub>	(200) <sub>α</sub> - (220) <sub>γ</sub> - (10.1) <sub>ε</sub>	(211) <sub>α</sub> - (200) <sub>γ</sub> - (10.1) <sub>ε</sub>	(211) <sub>α</sub> - (220) <sub>γ</sub> - (10.1) <sub>ε</sub>	(211) <sub>α</sub> - (220) <sub>γ</sub> - (10.1) <sub>ε</sub>	(211) <sub>α</sub> - (220) <sub>γ</sub> - (10.1) <sub>ε</sub>	
Solution Treated (ST) & Thermally Cycled (Th.Cy)	γ = 3.8% ε = 24.2% α = 72.0%	γ = 10.5% ε = 21.3% α = 68.2%	γ = 4.8% ε = 28.6% α = 66.6%	γ = 12.9% ε = 26.1% α = 60.9%	γ = 12.9% ε = 26.1% α = 60.9%	γ = 12.9% ε = 26.1% α = 60.9%	γ = 12.9% ε = 26.1% α = 60.9%
ST and Th.Cy and 10min, 450°C-WQ	γ = 10.2% ε = 12.3% α = 77.5%	γ = 15.1% ε = 11.7% α = 73.2%	γ = 9.9% ε = 11.9% α = 78.2%	γ = 14.7% ε = 11.3% α = 74.0%	γ = 14.7% ε = 11.3% α = 74.0%	γ = 14.7% ε = 11.3% α = 74.0%	γ = 14.7% ε = 11.3% α = 74.0%
ST and Th.Cy 1h, 450°C-WQ	γ = 8.6% ε = 14.5% α = 76.9%	γ = 10.2% ε = 14.3% α = 75.5%	γ = 8.7% ε = 14.9% α = 76.4%	γ = 10.4% ε = 14.6% α = 75.0%	γ = 10.4% ε = 14.6% α = 75.0%	γ = 10.4% ε = 14.6% α = 75.0%	γ = 10.4% ε = 14.6% α = 75.0%
ST and Th.Cy +2h 450°C-WQ	γ = 9.2% ε = 8.6% α = 82.3%	γ = 11.3% ε = 8.4% α = 80.3%	γ = 9.9% ε = 9.3% α = 80.8%	γ = 12.2% ε = 9.0% α = 78.8%	γ = 12.2% ε = 9.0% α = 78.8%	γ = 12.2% ε = 9.0% α = 78.8%	γ = 12.2% ε = 9.0% α = 78.8%
ST and Th.Cy +2h, 450°C-WQ +kept in Cardice & Acetone for 15mins.	γ = 5.6% ε = 9.0% α = 85.4%	γ = 5.8% ε = 9.0% α = 85.2%	γ = 6.3% ε = 10.0% α = 83.7%	γ = 6.5% ε = 9.9% α = 83.6%	γ = 6.5% ε = 9.9% α = 83.6%	γ = 6.5% ε = 9.9% α = 83.6%	γ = 6.5% ε = 9.9% α = 83.6%

TABLE XIII: X-RAY DIFFRACTION ANALYSIS

Alloy 137 Phase-Transformations on Thermal-Cycling Treatment and on Aging at 450°C for 6 minutes

Heat Treatment	%age Phases with Different Peak Combinations					AVG % I
	(200) <sub>α</sub> - (200) <sub>γ</sub> - (10.1) <sub>ε</sub>	(200) <sub>α</sub> - (220) <sub>γ</sub> - (10.1) <sub>ε</sub>	(211) <sub>α</sub> - (200) <sub>γ</sub> - (10.1) <sub>ε</sub>	(211) <sub>α</sub> - (220) <sub>γ</sub> - (10.1) <sub>ε</sub>	(211) <sub>α</sub> - (220) <sub>γ</sub> - (10.1) <sub>ε</sub>	
ST1000°C/1h-WQ	-	-	-	-	-	α ε
ST1000°C/1h-WQ +I <sub>A</sub> +I <sub>B</sub> +II <sub>A</sub> +II <sub>B</sub> at 200°C	γ = 32.5% ε = 19.1% α = 48.4%	γ = 37.8% ε = 17.6% α = 44.6%	γ = 41.2% ε = 24.1% α = 34.7%	γ = 46.8% ε = 21.8% α = 31.4%		γ ε α
ST1000°C/1h-WQ +I <sub>A</sub> +I <sub>B</sub> +II <sub>A</sub> +II <sub>B</sub> at -196°C	γ = 13.7% ε = 23.1% α = 63.2%	γ = 16.8% ε = 22.2% α = 61.0%	γ = 17.9% ε = 30.1% α = 52.0%	γ = 21.7% ε = 28.7% α = 49.6%		γ ε α
ST1000°C/1h-WQ +I <sub>A</sub> +I <sub>B</sub> +II <sub>A</sub> +II <sub>B</sub> +6min at 450°C	γ = 37.8% ε = 30.1% α = 32.1%	γ = 43.1% ε = 27.5% α = 29.4%	γ = 40.1% ε = 32.0% α = 27.9%	γ = 45.5% ε = 29.1% α = 25.4%		γ ε α
ST1000°C/1h-WQ +I <sub>A</sub> +I <sub>B</sub> +II <sub>A</sub> +II <sub>B</sub> +6min at 450°C +15min at -78°C	γ = 42.8% ε = 20.4% α = 36.8%	γ = 41.7% ε = 20.7% α = 37.6%	γ = 47.8% ε = 22.7% α = 29.5%	γ = 46.7% ε = 23.2% α = 30.1%		γ ε α
ST1000°C/1h-WQ +I <sub>A</sub> +I <sub>B</sub> +II <sub>A</sub> +II <sub>B</sub> +6min at 450°C +15min at -196°C	γ = 9.6% ε = 42.2% α = 48.2%	γ = 14.6% ε = 39.8% α = 45.6%	γ = 10.1% ε = 44.1% α = 45.8%	γ = 15.3% ε = 41.5% α = 43.2%		γ ε α

TABLE XIV:      RESULTS OF QUANTIFICATION OF AES PEAK RATIO  
 Alloy 1525      ST1000°C/1 hour - WQ+Aged at 450°C

Heat Treated Condition	Atomic % on Fracture Surface		
	Mn	N	P
As Quenched	7.6 ± 1.4	2.2 ± 1.5	-
1.5 min 450°C	14.2 ± 1.2	3.3 ± 0.04	-
3 min 450°C	14.9 ± 1.6	3.4 ± 2.3	0.24 ± 0.10
6 min 450°C	18.5 ± 2.8	4.4 ± 1.1	0.29 ± 0.10
12 min 450°C	17.8 ± 2.0	2.8 ± 0.6	0.67 ± 0.16

TABLE XV: AUGER ELECTRON EMISSION ANALYSIS

Alloy 134 ST900°C/½ hour - Air-cooled (100 pct Intergranular)

	%age of Fe. (703 eV) Peak				Atomic %age	
	P	C	N	Mn	N	Mn
<u>Sample 1</u>						
As Fractured	-	7.7 ± 3.4	8.8 ± 1.4	8.7 ± 1.3	5.5 ± 0.87	11.0 ± 1.6
1st ion B, 3µA min.	-	7.5 ± 2.6	4.1 ± 0.7	4.2 ± 0.9	2.6 ± 0.4	5.3 ± 1.1
2nd ion B, 9µA min	-	9.1 ± 2.9	-	2.9 ± 0.7	-	3.6 ± 0.88
3rd ion B, 53µA min	-	7.9 ± 0.6	-	2.6	-	3.4
<u>Sample 2</u>						
As Fractured	-	5.7 ± 2.4	13.6 ± 2.1	9.1 ± 1.7	8.5 ± 1.3	11.51 ± 2.1
1st ion B, 3µA min	-	11.9 ± 1.1	8.6 ± 1.1	6.8 ± 1.2	5.4 ± 0.7	8.6 ± 1.5
2nd ion B, 9µA min	-	13.9 ± 2.7	-	3.9 ± 1.8	-	4.93 ± 2.3

Elemental sensitivities (PHI book)

Mn ≈ 0.79

N ≈ 1.60

P ≈ 2.07

TABLE XVI: RESULTS OF QUANTIFICATION OF AES PEAK RATIO IN ALLOYS 134 and 137

Alloy No.	Heat Treated Condition	Atomic pct on Fracture Surfaces and Fracture mode		
		Fracture Mode	Mn (At%)	N (At%)
134	SOLUTION TREATED AT 900°C/½h-IBQ	CLEAVAGE	8.2	1.73
			5.36*	2.37*
137	SOLUTION TREATED AT 900°C/½h-IBQ	CLEAVAGE	7.9	1.2
134	SOLUTION TREATED AT 900°C/½h-AC	INTERGRANULAR	14.7	5.4
			15.1*	8.3*
137	SOLUTION TREATED AT 900°C/½h-AC	INTERGRANULAR	12.8	3.5

\* Analysis figures taken from the second specimen.

TABLE XVII: SUMMARY OF AES RESULTS

Alloy 134 ST900°C/½ hour - IBQ - Aged at 450°C for 6 min, 1 hour, 10 hours

Heat Treated Condition		%age of Fe(703 eV) Peak				Atomic %age		
		P	N	Mn		N	Mn	
ST900°C/½ hour - Ice-Brine-Quenched	As Fractured	-	3.8	4.24		2.37	5.36	
	1st Ion B, 3µA min	-	1.1	3.3		0.68	4.17	
	2nd Ion B, 13µA min	-	0.3	1.9		0.18	2.40	
ST900°C/½ hour - IBQ - Aged for 6 min at 450°C	As Fractured	-	3.7	6.6±0.87		2.31	8.35	
	1st Ion B, 5µA min	-	2.4	4.7		1.5	5.94	
	2nd Ion B, 15µA min	-	-	0.96		-	1.21	
ST900°C/½ hour - IBQ - Aged for 1 hour at 450°C	As Fractured	-	5.6±0.98	13.3±2.3		3.5	16.83	
	1st Ion B, 5µA min	-	3.0	7.0		1.87	8.86	
	2nd Ion B, 25µA min	-	0.84	1.9		0.52	2.40	
ST900°C/½ hour - IBQ - Aged for 10 hours at 450°C	As Fractured	-	5.13±0.24	13.82±0.65		3.20±0.15	17.49	
	1st Ion B, 10µA min	-	0.83	2.92		0.51	3.69	
	2nd Ion B, 90µA min	-	-	0.78		-	0.98	

TABLE XVIII: SUMMARY OF AES RESULTS

Alloy 137 (0.03N-0.1Ti-0.1Al)

Heat Treated Condition		%age of Fe (703 eV) Peak						Atomic %age				
		P	C	N	O	Mn		P	C	N	O	Mn
ST900°C/½ hour - IBQ - Aged for 6 min at 450°C	As Fractured	-	6.55±1.3	1.45±0.16	15.5	12.4±1.4				0.90±0.1		15.6
	1st Ion B, 4µA min	-	29.3	1.01		6.26				0.63		7.9
	2nd Ion B,	-	34.7	-	24.0	5.35				-		6.7
	3rd Ion B, 8µ	-	36.7	-	21.1	3.91				-		4.9
	4th Ion B, 20µ	-	20.8	-	20.0	3.38				-		4.2
ST900°C/½ hour - IBQ - Aged for 1 hour at 450°C	As Fractured	-	13.1	4.2	-	16.3				2.62		20.6
	1st Ion B, 1µA min	-	20.7	4.9	-	10.7				3.06		13.5
	2nd Ion B, ~1µA min	-	33.9	5.2	-	13.4				3.25		16.9
	3rd Ion B, ~1µA min	-	25.5	-	-	13.4				-		16.9
	4th Ion B, ~8µA min	-	24.8	2.13	-	2.8				1.33		3.5
	5th Ion B, ~18µA min	-	47.0	1.92	-	1.3				1.2		1.6
6th Ion B, ~78µA min	-	34.0	2.3	-	1.4				1.43		1.7	
ST900°C/½ hour - IBQ - Aged for 10 hours at 450°C	As Fractured	-	12.94±3.8	1.63±0.36	23.1±9.0	11.4±1.5				1.01±0.22		14.4

TABLE XIX: SUMMARY OF IMPACT, FRACTOGRAPHIC AND AUGER ANALYSIS RESULTS

Alloy	Heat-Treated Condition	Hardness Hv <sub>30</sub>	Impact Transition Temperature °C	Reduction in Area % at a Strain Rate of 0.5 min <sup>-1</sup>	Low Temp Fracture Mode	AES Analysis		
						Mn (At%)	N (At%)	P (At%)
K1525	ST1000°C/1h-WQ	258±2	+115°C	60%	Intergranular	7.6±1.4	2.2±1.5	-
	ST1000°C/1h-WQ +1.5min/450°C-WQ	261±2	-	55%	100pct Intergranular AES Test at -80°C	14.2±1.2	3.3±0.04	-
	ST1000°C/1h-WQ +3min/450°C-WQ	263±2	-	52%	100% IG AES Test at -80°C	14.9±1.6	3.4±2.3	0.24±0.1
	ST1000°C/1h-WQ +6min/450°C-WQ	267±2	-	0%	100% IG AES Test at -80°C	18.5±2.8	4.4±1.1	0.29±0.1
	ST1000°C/1h-WQ +12min/450°C-WQ	272±2	-	0%	100% IG AES Test at -80°C	17.8±2.0	2.8±0.6	0.67±0.1
134	ST1000°C/1h-WQ	287±2	-	-	Intergranular	-	-	-
	ST1000°C/1h-IBQ	275±2	-	-	Cleavage	-	-	-
	ST900°C/½h-IBQ	289±6	+35°C	-	Cleavage	8.2 5.36	1.73 2.37	-
	ST900°C/½h-AC	298±2	+375°C	-	Intergranular	11.25 14.7	7.0 5.4	-

Alloy	Heat Treated Condition	Hardness Hv <sub>30</sub>	Impact Transition Temperature °C	Low Temp Fracture Mode	AES Analysis		
					Mn (At%)	N (At%)	P (At%)
137 Fe-8.0Mn +0.1Ti +0.1Al	ST900°C/½h - IBQ + 6 mins at 450°C-WQ	295±5	+200	5-10% IG + Quasi- Cleavage	8.35	2.31	-
	ST900°C/½h - IBQ +1 hour at 450°C - WQ	294±5	+215	10-15% IG + Cleavage	16.83	3.5	-
	ST900°C/½h - IBQ +10 hours at 450°C - WQ	265±5	+150	10-15% IB + Cleavage	17.49	3.20	-
	ST1000°C/1h - WQ	243.5±4.0	+150	Intergranular	-	-	-
	ST900°C/½h - IBQ	252.7±4.0	+10	10% IG + All Cleavage	8.0	1.2	-
	ST900°C/½h - AC	271.5±5.8	+145	Intergranular	12.8	3.5	-
	ST900°C/½h - IBQ +6mins at 450°C-WQ	259±5	+140	50-60% IG + Cleavage	15.69	0.90	-
	ST900°C/½ h - IBQ +1 hour at 450°C - WQ	242±5	+100	90% IG + 10% QC	20.63	2.62	-
	ST900°C/½ h - IBQ + 10 hours at 450°C - WQ	238±5	+110	80% IG + Cleavage	14.43	1.01	-

TABLE XX: COMPARATIVE CRYOGENIC TENSILE PROPERTIES

Alloy	Testing Conditions	Yield Stress Ksi	UTS Ksi	Total Elongation %age	Reduction of Area %age
K1525 Fe-8.0 Mn ST1000°C/1h - WQ	Test Temp = -78°C Cross Head Speed = 0.5cm/min	138 Ksi	140 Ksi	20%	59%
K1525(Fe-8.0 Mn) ST1000°C/1h - WQ +I <sub>A</sub> +I <sub>B</sub> +II <sub>A</sub> +II <sub>B</sub>	Test Temp = -78°C Cross Head Speed = 0.5cm/min	No Definite Yield Point	162.38 Ksi	59%	70%
Fi-Ni-Ti Alloy After Thermal- Cycling Treatment	Test Temp = -196°C Cross Head Speed = 0.05cm/min	149 Ksi	154 Ksi	26.8%	72.1%
9-Ni Steel	Test Temp = -196°C Cross Head Speed = 0.05cm/min	146 Ksi	172 Ksi	29.6%	66.8%
304 Stainless Steel	Test Temp = -196°C Cross Head Speed = 0.05cm/min	81 Ksi	235 Ksi	47.3%	65.6%

TABLE XXI: EFFECT OF AGING AT 450°C ON HARDNESS, MICROSTRUCTURE IN ALLOY K1525 AFTER THERMAL CYCLING TREATMENT

Heat Treated Condition	Austenite Grain Size	%age Phase Analysis		Hardness VPN	
		At R.T.	At -78°C	At R.T.	At -78°C
ST1000°C/1h - WQ +I <sub>A</sub> +I <sub>B</sub> +II <sub>A</sub> +II <sub>B</sub>	10-15 μm	γ = 8.0% ε = 24.6% α = 67.4%		392.5 ± 6.6	407.7 ± 11.6
ST1000°C/1h - WQ +I <sub>A</sub> +I <sub>B</sub> +II <sub>A</sub> +II <sub>B</sub> +10 minutes at 450°C	10-15 μm	γ = 12.5% ε = 11.8% α = 75.7%	-	384.50 ± 6.0	376.4 ± 8.8
ST1000°C/1h - WQ +I <sub>A</sub> +I <sub>B</sub> +II <sub>A</sub> +II <sub>B</sub> + 1 hour at 450°C	10-15 μm	γ = 9.5% ε = 14.6% α = 75.9%	-	369.4 ± 9.8	386.8 ± 12.8
ST1000°C/1h - WQ +I <sub>A</sub> +I <sub>B</sub> +II <sub>A</sub> +II <sub>B</sub> + 2 hours at 450°C	10-15 μm	γ = 10.6% ε = 8.8% α = 80.6%	γ = 6.0% ε = 9.5% α = 84.5%	377.4 ± 15.8	388.0 ± 17.2

TABLE XXII: EFFECT OF AGING AT 450°C ON TENSILE-DUCTILITY OF THERMALLY-CYCLED MATERIAL

Alloy K1525 Fe-8.0 Mn

Solution-treated 1h at 1000°C, water-quenched

Thermally-cycled according to figure 68 (I<sub>A</sub>+I<sub>B</sub>+II<sub>A</sub>+II<sub>B</sub>)

Tensile Tested at -78°C at a strain rate of 0.5 min<sup>-1</sup>

Condition	Average % Phases	Prior-Austenite Grain Size	Tensile Strength Kg/mm <sup>2</sup>	Total Elongation %	Reduction in Area %
After Thermal-Cycling Treatment	γ = 8.0% ε = 24.7% α = 67.3%	10-15 μm	114	59%	70%
Thermally Cycled & Aged 10 mins at 450°C - WQ	γ = 12.5% ε = 11.8% α = 75.7%	10-15 μm	109	46%	68%
Thermally Cycled & Aged 1 hour at 450°C - WQ	γ = 9.5% ε = 14.5% α = 76.0%	10-15 μm	115	46%	66%
Thermally Cycled & Aged 2 hours at 450°C - WQ	γ = 10.6% ε = 8.8% α = 80.4%	10-15 μm	120	63%	70%

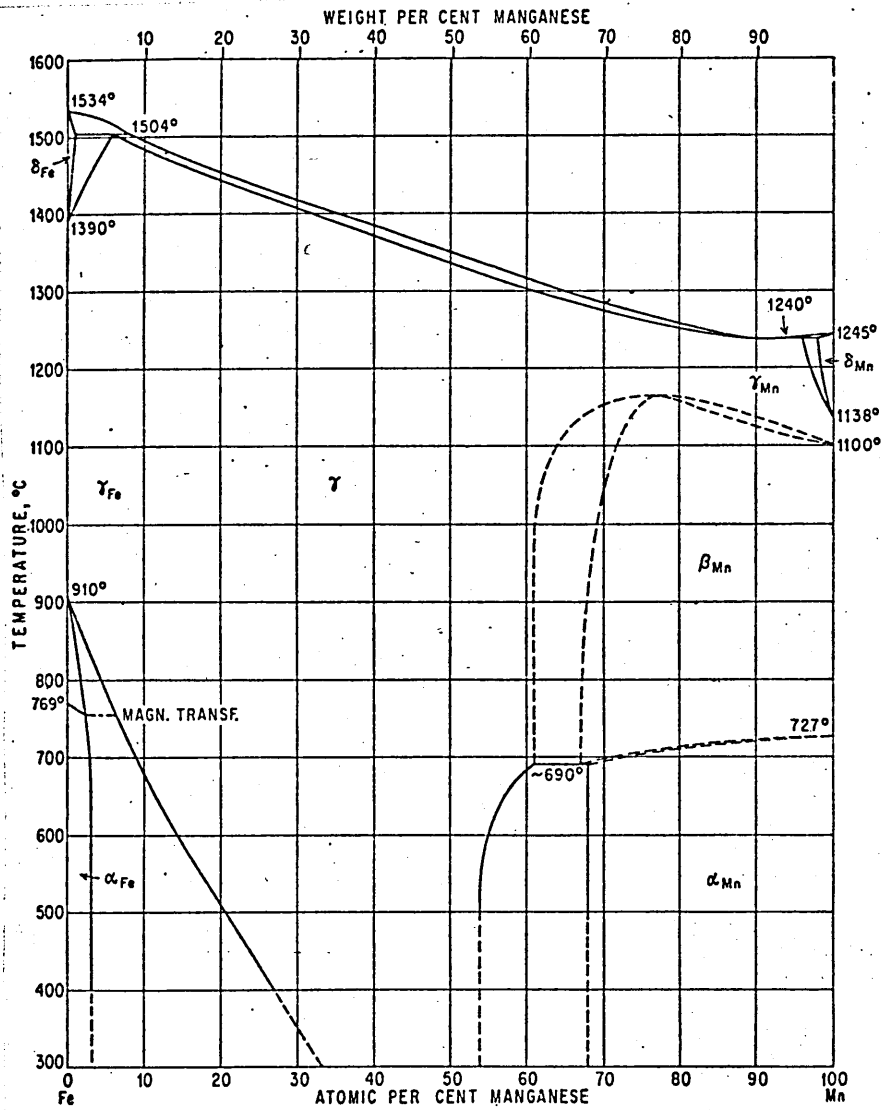


Fig I(a). Equilibrium diagram of the Fe-Mn system.  
 Constitution of Binary Alloys by Hansen  
 McGraw-Hill Book Company p665.

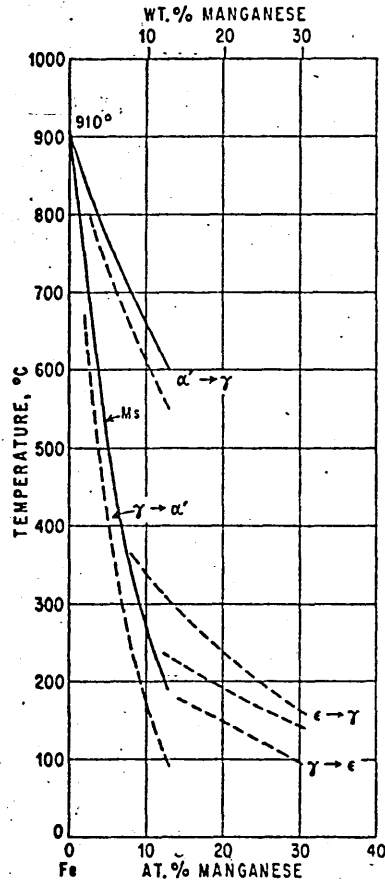


Fig I(b). Fe-Mn metastable phase diagram showing non equilibrium  $\alpha$  and  $\epsilon$  martensitic transformation temperatures (I45, p666)

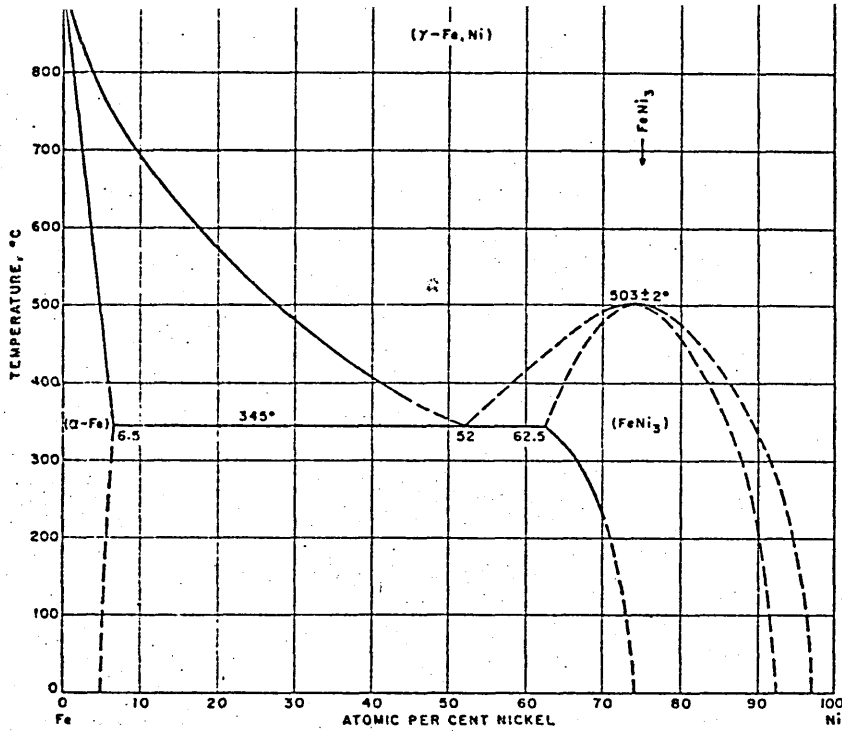


Fig 2(a) Equilibrium diagram of the Fe-Ni system.  
 Constitution of Binary Alloys, second supplement  
 McGraw-Hill Book Company by Francis A. Shunk.  
 P335.

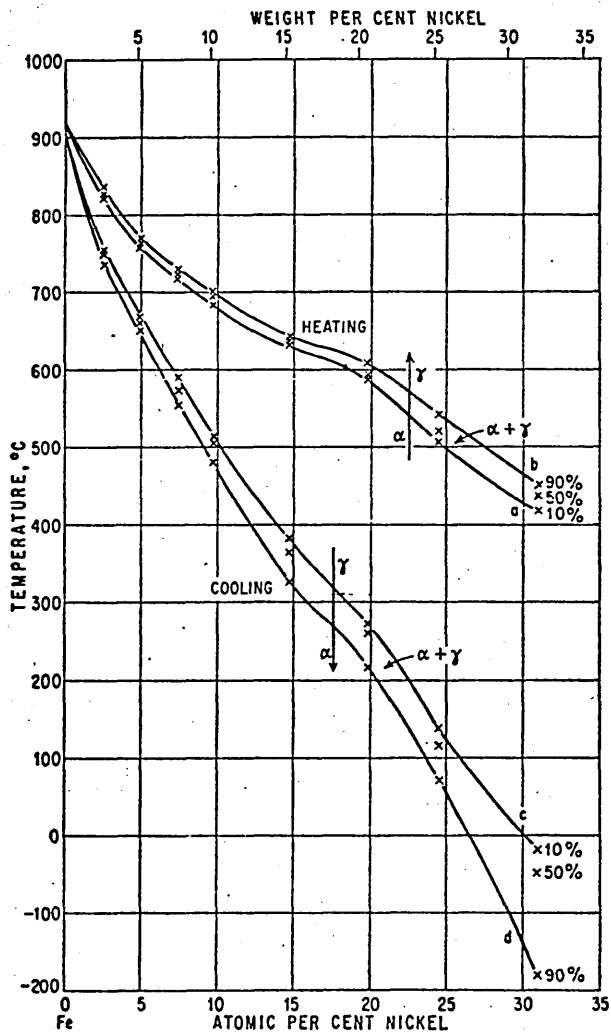


Fig 2(b) Fe-Ni metastable phase diagram.  
 Constitution of Binary Alloys by Hansen  
 McGraw-Hill Book Company, P681

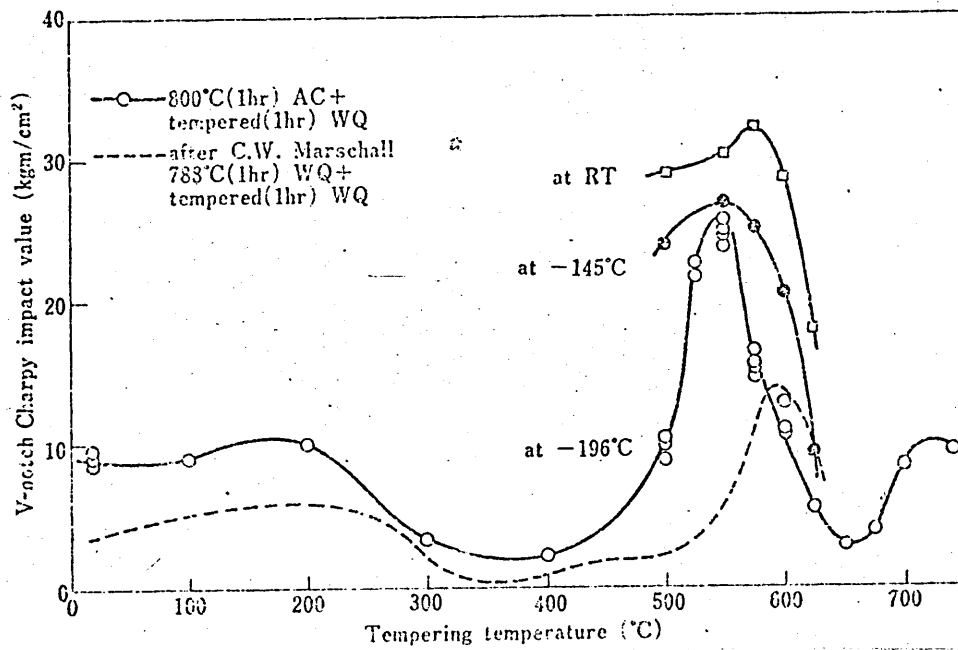


Fig 3. Effect of tempering temperature on the Charpy impact value of 9% Ni steel. (23)

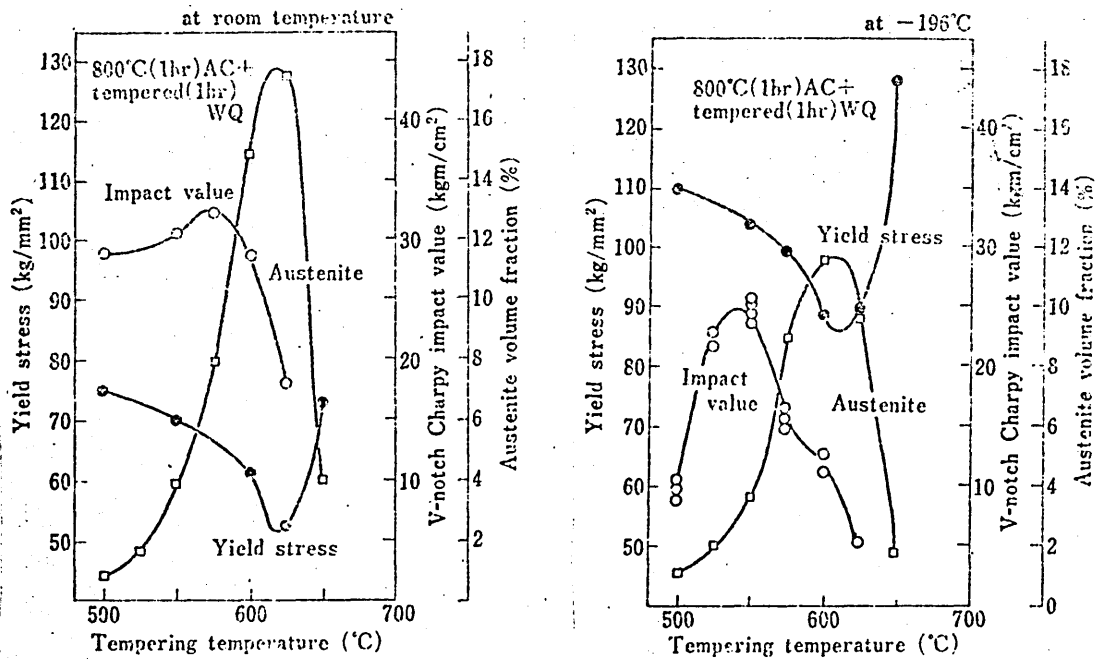


Fig 4. Effect of tempering temperature on the mechanical properties and volume fraction of austenite in 9% Ni steel at room temperature and at -196°C. (23)

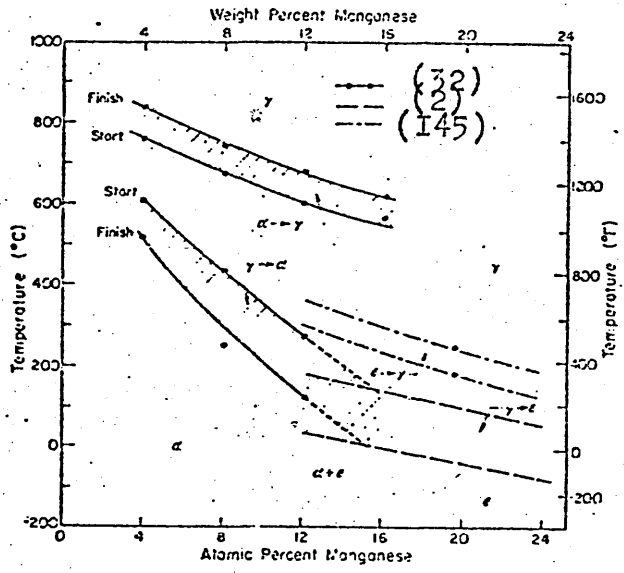


Fig 5. Phase transformation temperatures for Fe-Mn alloys(32  
Also shown are some results of other investigations  
(2,I45)

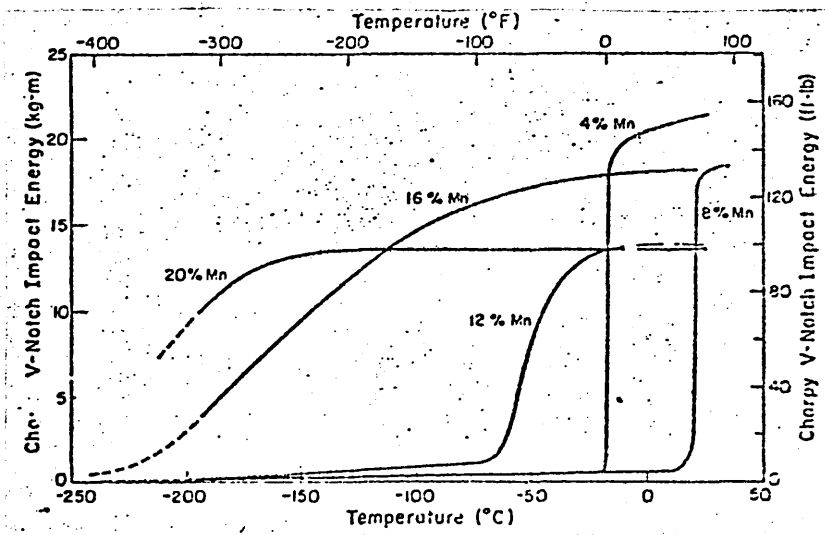


Fig 6. Charpy V-notch impact toughness versus testing  
temperature for Fe-Mn alloys (After Zackay, 32)

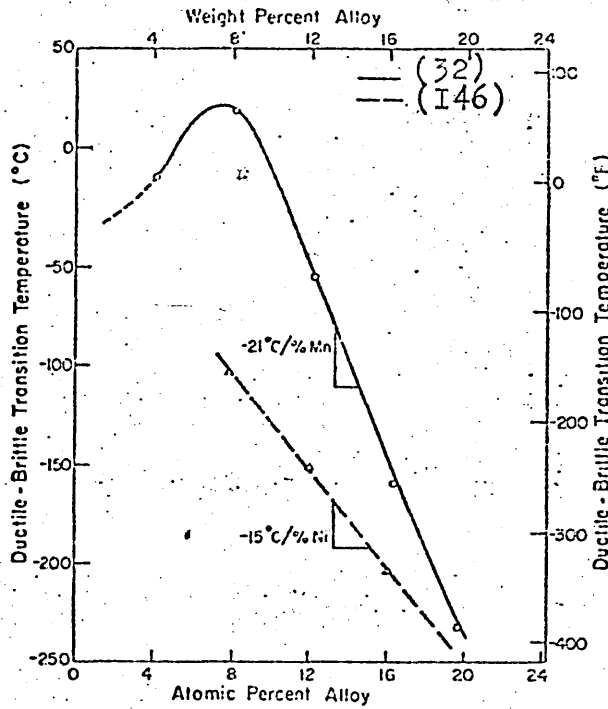


Fig. 7. DBTT versus Mn content for Fe-Mn alloys (32)  
 Also plotted are the data of Yokota et al (I46) on  
 DBTT versus Ni content for noninterstitial Fe-Ni alloy

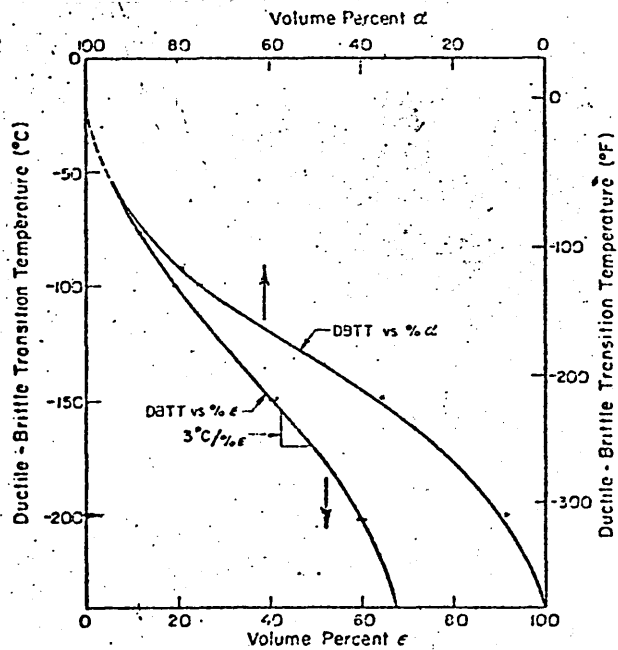


Fig 8. DBTT versus volume percent epsilon and alpha phasea in  
 Fe-Mn alloys (After Zackay, 32 )

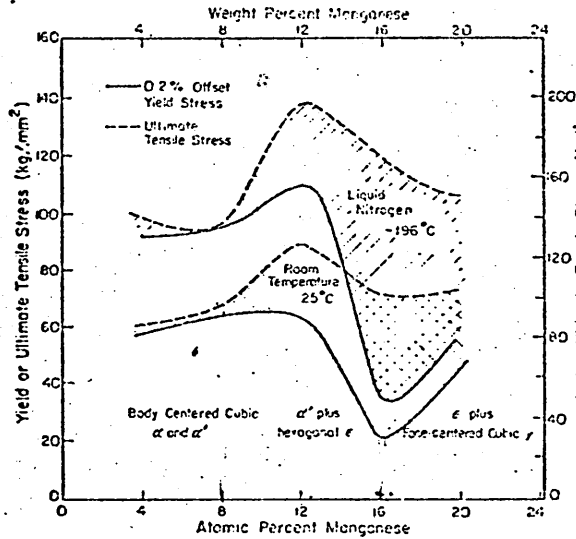


Fig 9. Plots of yield and ultimate tensile strengths at both 25°C and -196°C versus Mn content for Fe-Mn alloys (After Zackay, 32 )

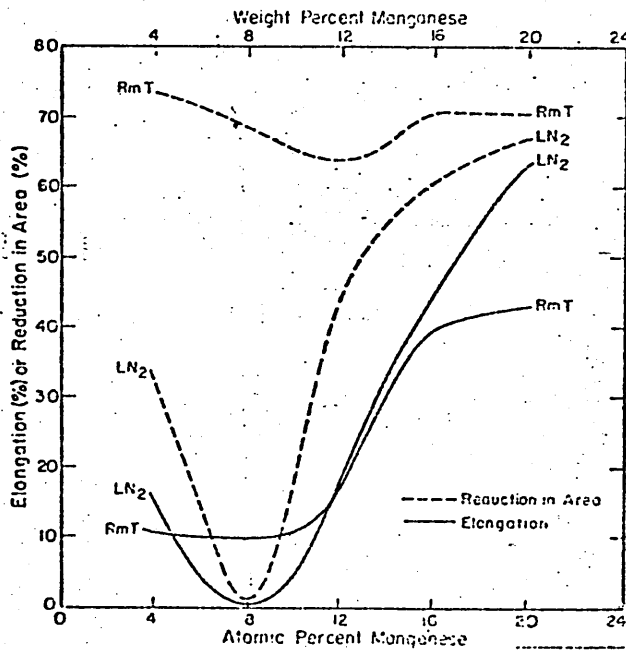


Fig 10. Plots of elongation and reduction in area at both 25 and -196°C versus Mn content for Fe-Mn alloys. (After Zackay, 32 )

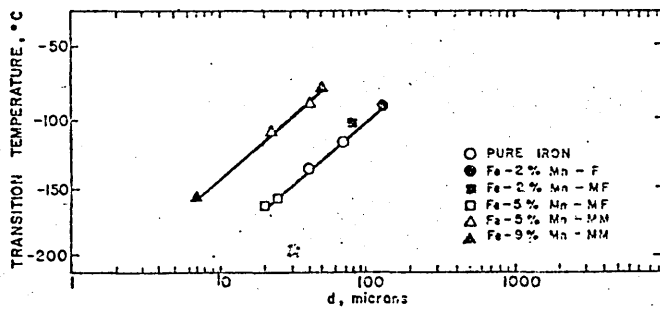


Fig II. The influence of grain size on the impact transition temperature of Fe-Mn alloys. (After Roberts 7)

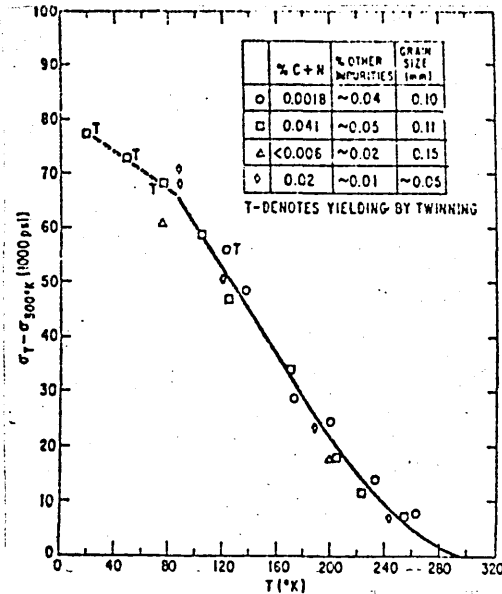


Fig I2(a). Increase in yield stress at low temperatures for several impure polycrystalline irons. (45)

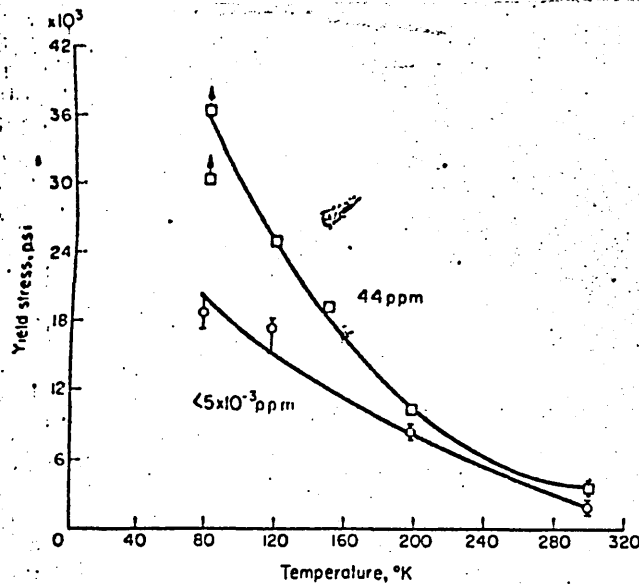


Fig I2(b). Temperature dependence of yield stress of iron (approx. 44 p.p.m. carbon) and very pure iron (0.005 p.p.m. carbon). (After Stein, 47)

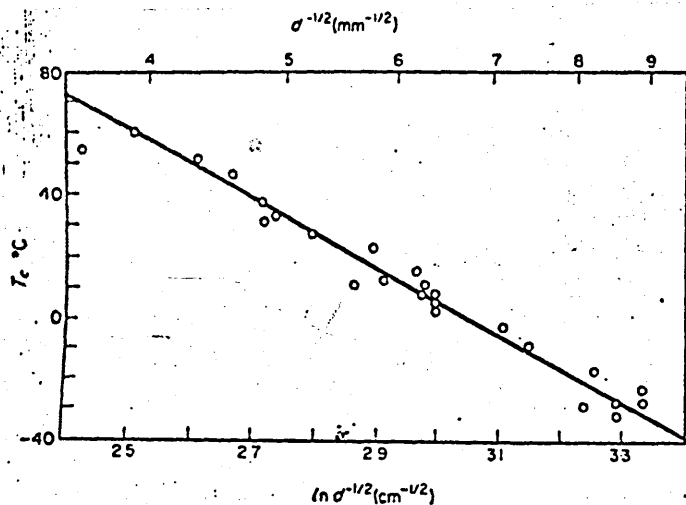


Fig I3. The dependence of the transition temperature of mild steel on the grain size. (52)

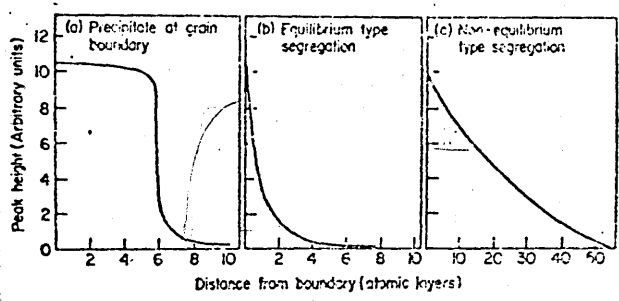
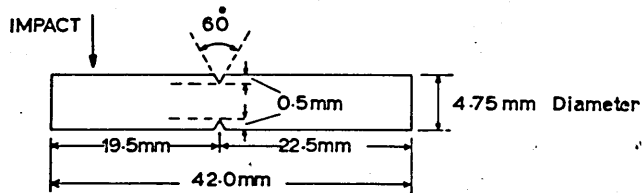


Fig I4(a) Typical sputtering profiles (56)

AUGER SAMPLE DESIGN FOR HARWELL STAGE



PROPOSED MODIFIED DESIGN FOR IMPACT SPECIMEN

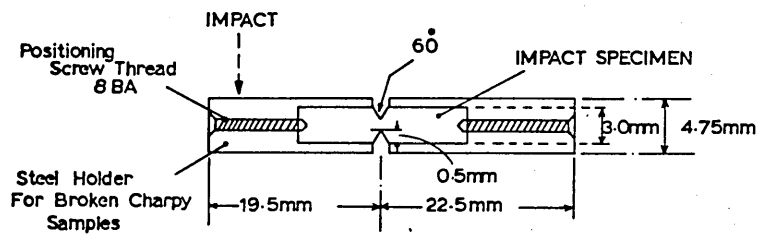


Fig I4(b)

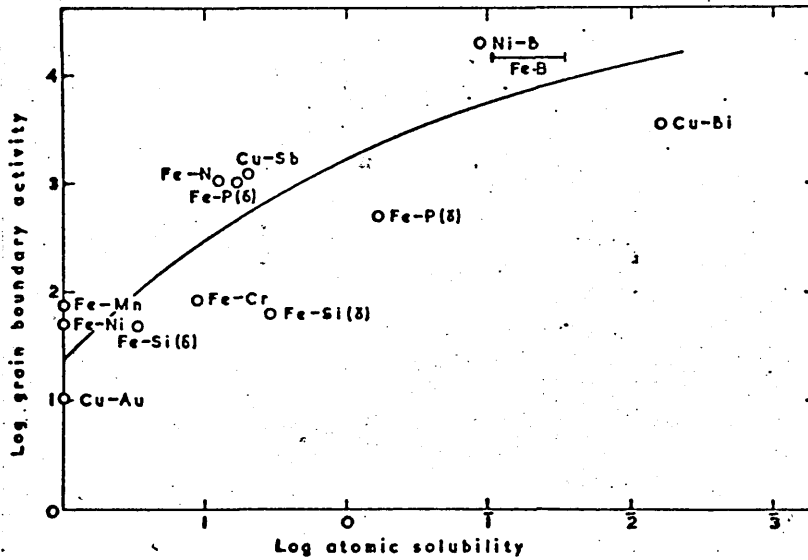


Fig 15. Grain-boundary activity versus maximum solubility. (After Hondros, 77)

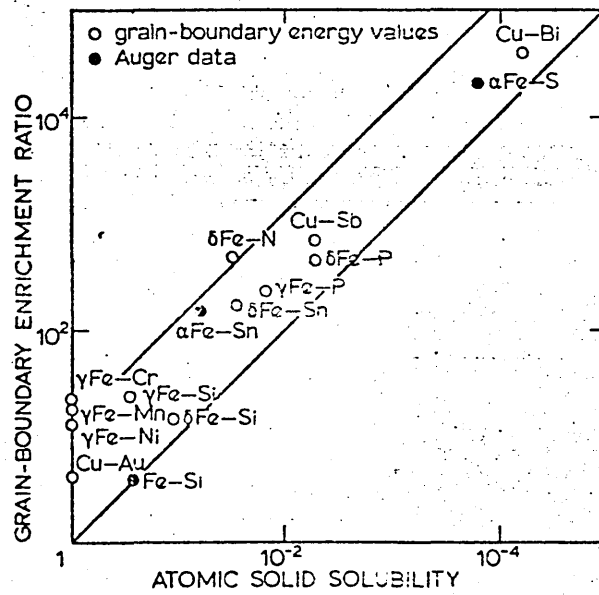


Fig 16. Grain-boundary enrichment factor versus inverse solid solubility (After Seah and Hondros, 82)

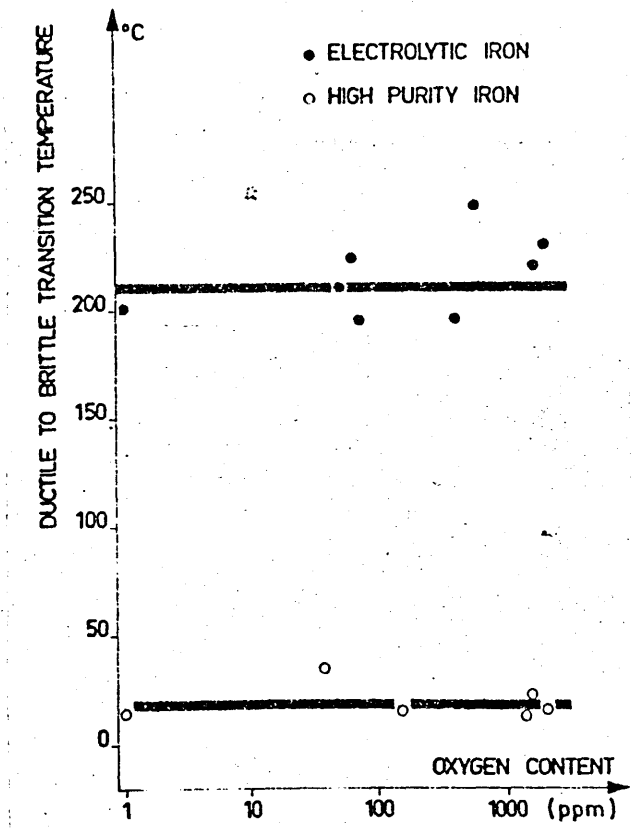


Fig I7. Influence of oxygen concentration on the transition temperature of a decarburized electrolytic iron and high purity iron (C:10ppm) (86)

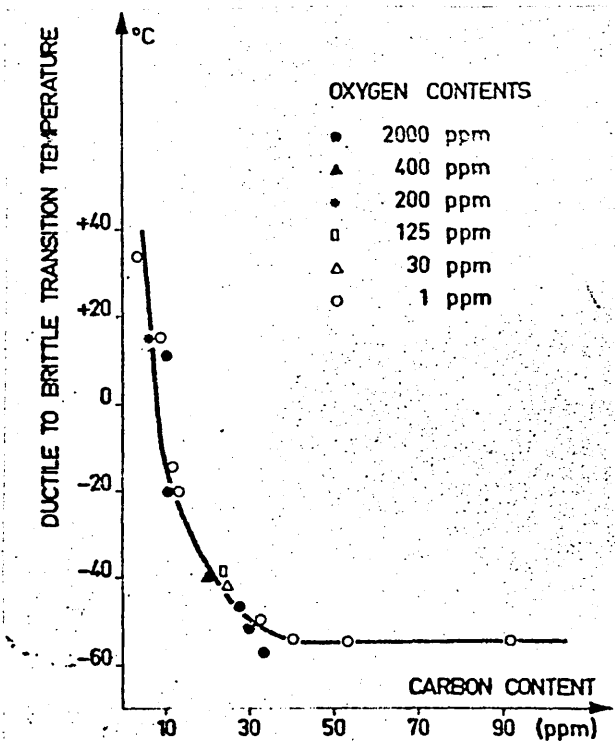


Fig I8. Influence of oxygen concentration on the variation of transition temperature with the carbon content in high purity iron. (86)

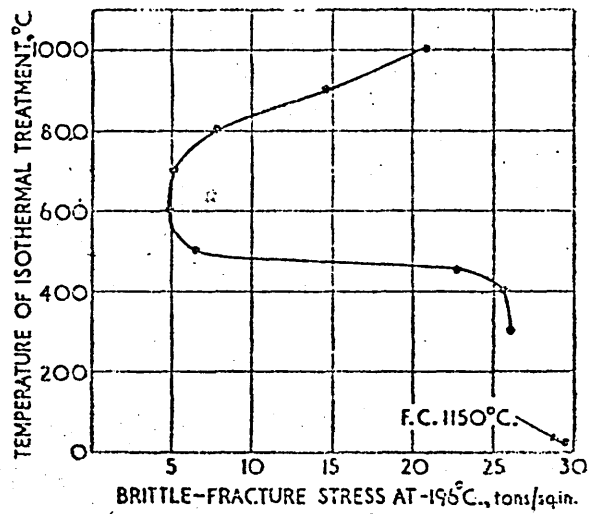


Fig 19. Brittle-fracture stresses at  $-196^{\circ}\text{C}$  of alloy (Fe-N) furnace-cooled from  $1150^{\circ}\text{C}$  and subsequently heated at the temperature shown for times adjusted to give equal opportunity for diffusion of nitrogen, and then water quenched. (89)

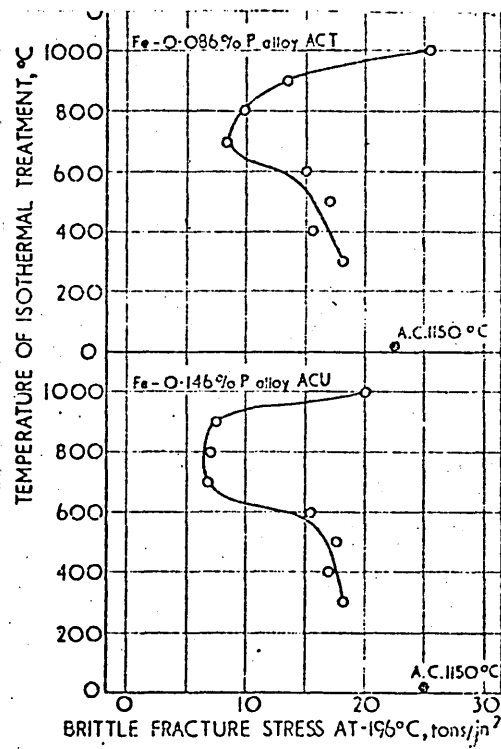


Fig 20. Brittle fracture stresses at  $-196^{\circ}\text{C}$  of Fe-P alloys air-cooled from  $1150^{\circ}\text{C}$  and subsequently water-quenched from various temperatures. Alloys made from refined Norwegian electrolytic iron base. (57)

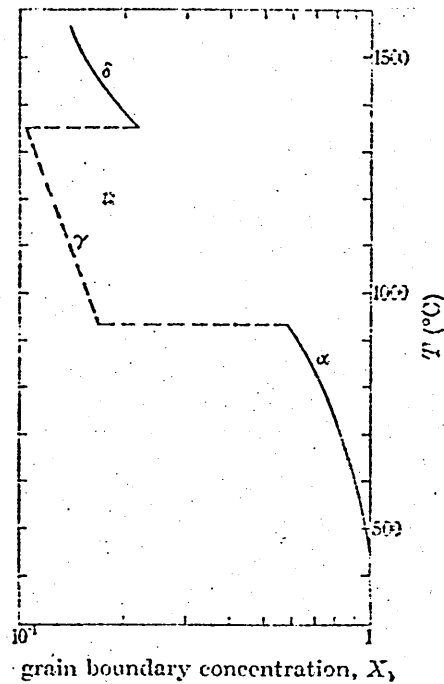


Fig 21. Calculated curve for the variation of grain-boundary concentration of phosphorus with temperature for a specimen having a bulk concentration of 0.15 percent phosphorus. (After Hondros 74)

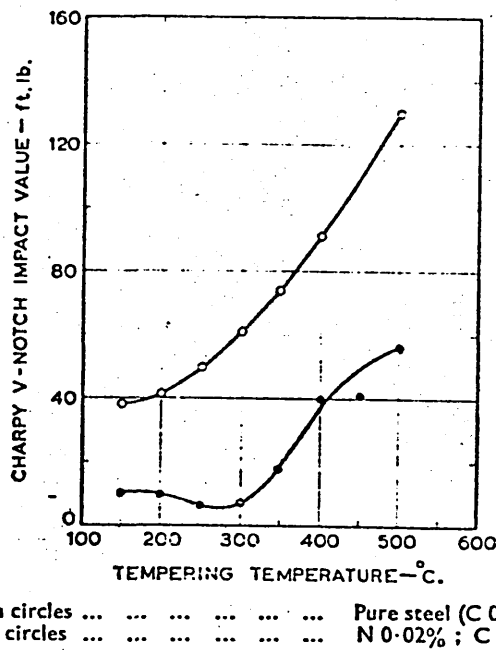
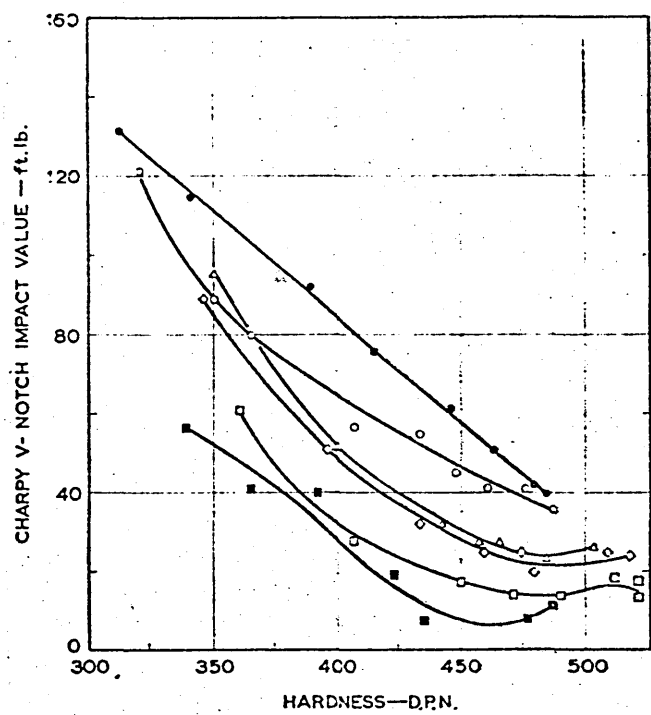


Fig 22. The influence of nitrogen on the impact values at 20°C of hardened and tempered high purity 3%Ni-Cr steels(63)



3% Ni-Cr-Steels

Solid circles ... .. Pure steel (C 0.27%)  
 Solid squares ... .. N 0.02% ; C 0.29%

1 1/2% Ni-Cr-Mo Steels

Open circles ... .. Pure steel (C 0.28%)  
 Open squares ... .. P 0.045% ; C 0.32%  
 Open diamonds ... .. Sb 0.001% ; C 0.32%  
 Open triangles ... .. As 0.084% ; C 0.31%

Fig 23. The influence of impurity elements on the relationship between impact and hardness values at 20°C. of hardened and tempered high-purity-base steels. (63)

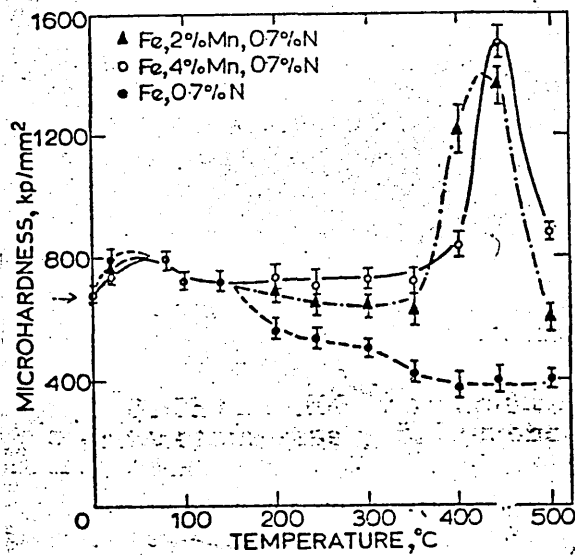


Fig 24. Variation of microhardness of Fe-N and Fe-Mn-N alloys tempered 30 min at temperature. (96)

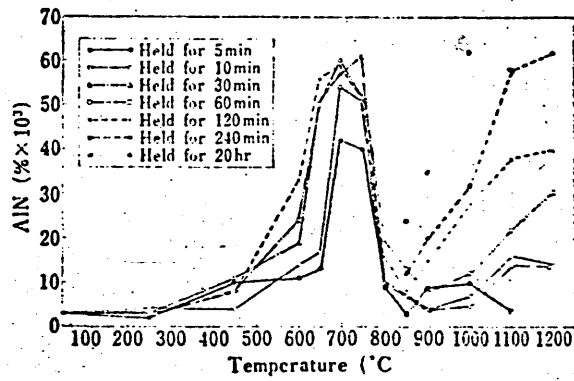


Fig 25(a). Amount of AlN precipitated isothermally during cooling of AlN-bearing mild steel. (I03)

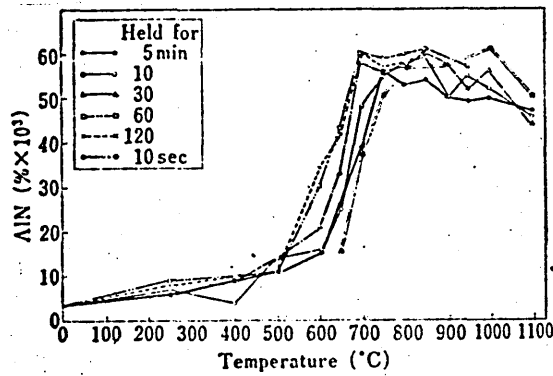


Fig 25(b). Amount of AlN precipitated isothermally during reheating of the same steel. (I03)

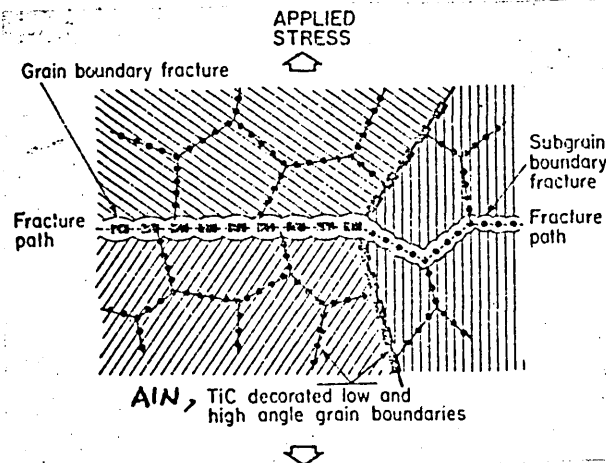


Fig 26. Schematic representation of the embrittlement due to the finer dispersion of TiC, AlN decorating the high and low angle prior austenite boundaries. (I07)

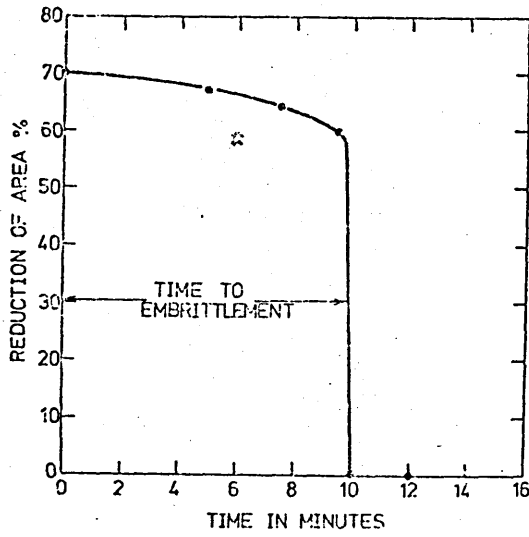


Fig 27. Tensile ductility on aging at 400C in Fe-12Ni-6Mn alloy (68)

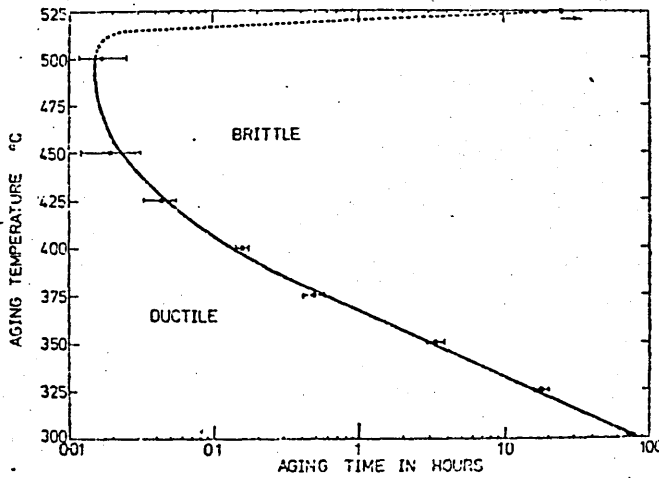


Fig 28. Embrittlement c curve determined on aging from tensile ductility data in Fe-12Ni-6Mn alloy(68)

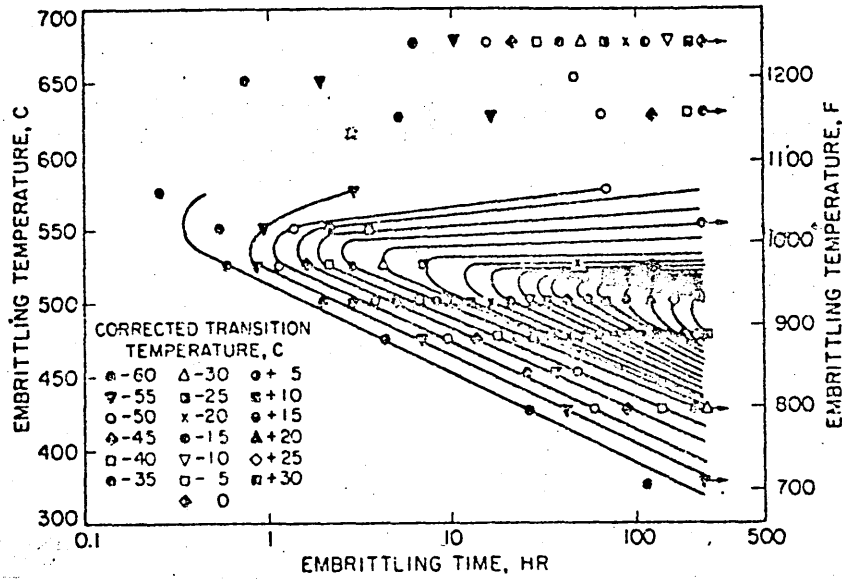


Fig 29. Isoembrittlement curves of Jaffe and Buffum (II3) plotted as a time-temperature diagram, for a Ni-Cr steel (0.39 percent carbon, 0.79 percent manganese, 0.77 percent chromium, 1.26 percent nickel, 0.015 percent phosphorus)

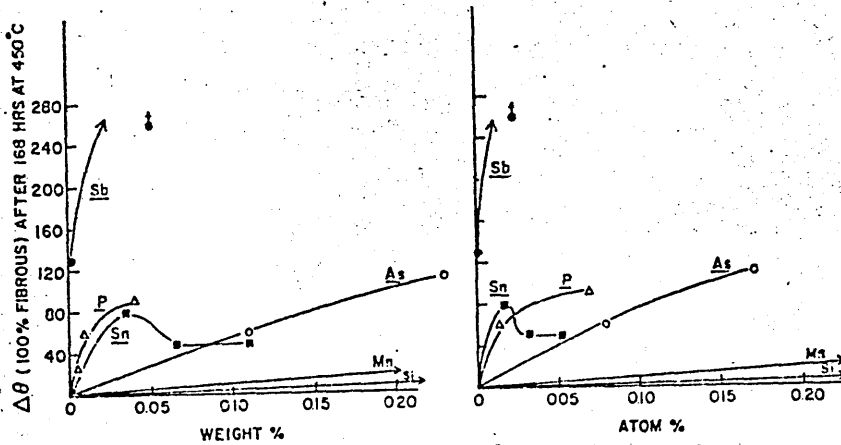


Fig 30. Data of Steven and Balajiva (80) plotted to show amount of embrittlement produced by various elements for an arbitrary embrittling treatment of 168h at 450C. Base steel was 0.2 to 0.3 per cent carbon, 3 per cent nickel, 0.8 per cent chromium.

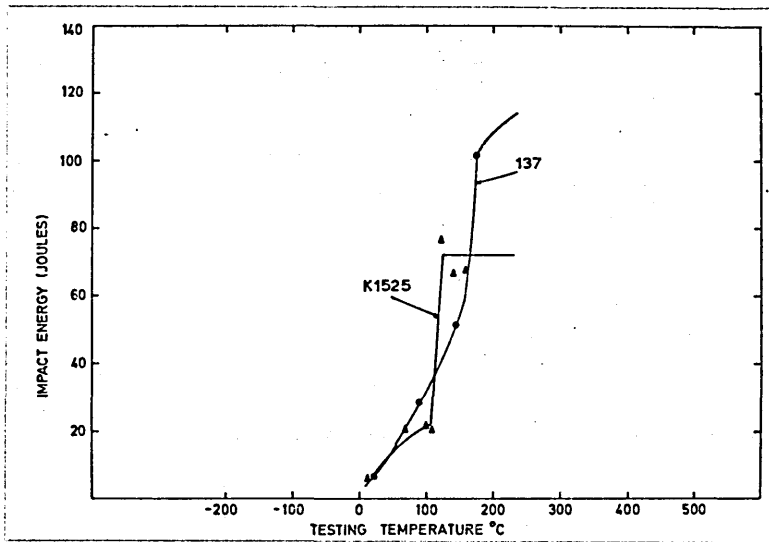


Fig 31. Impact Transition curves for alloys KI525, I37. Solution treated 1 hour at 1000°C and water quenched.

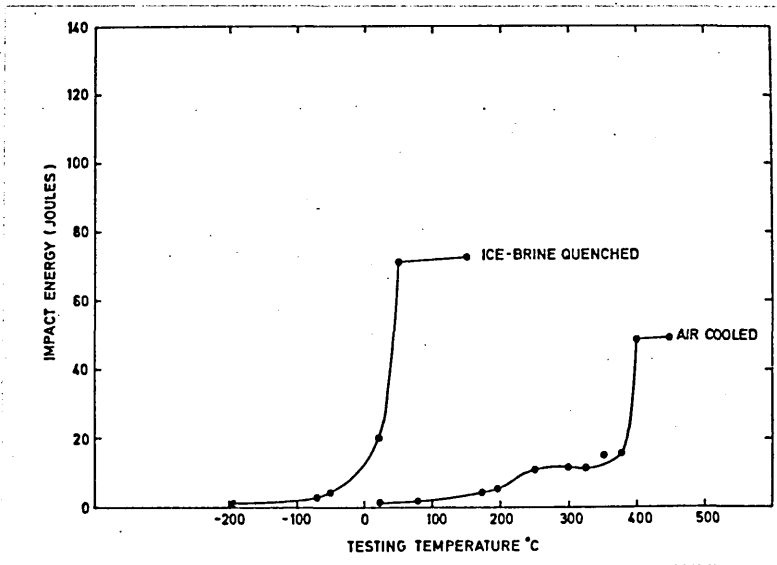


Fig 32. Impact Transition curves for alloy I34 in the ice-brine quenched and air-cooled condition after being solution treated at 900°C for 30 minutes

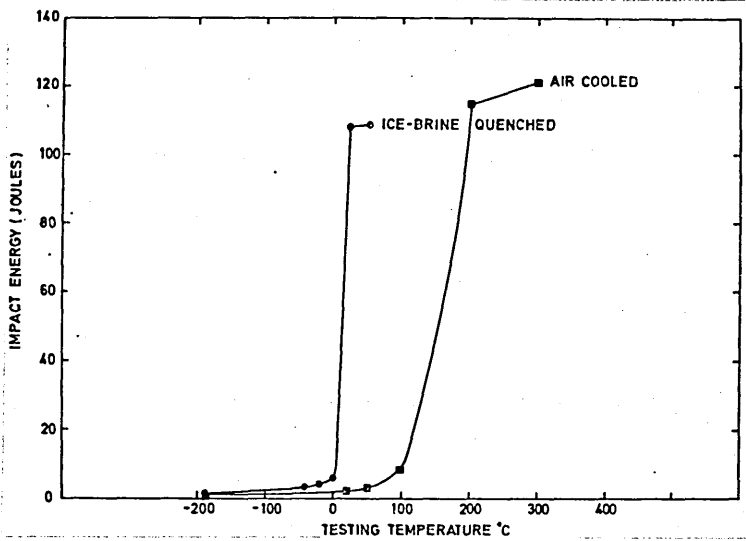


Fig 33. Impact Transition curves for alloy I37 in the ice-brine quenched and air-cooled condition after being solution treated at 900C for 30 minutes.

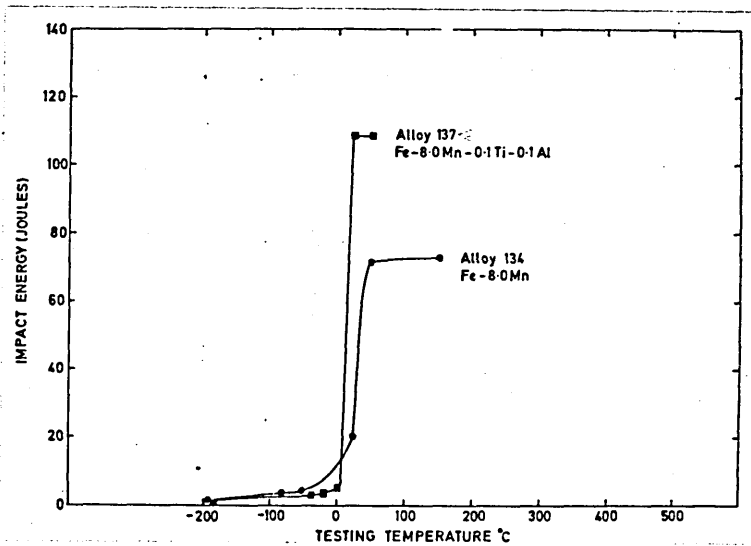


Fig 34. Comparison of impact transition curves for alloys I34 and I37 as ice-brine quenched.

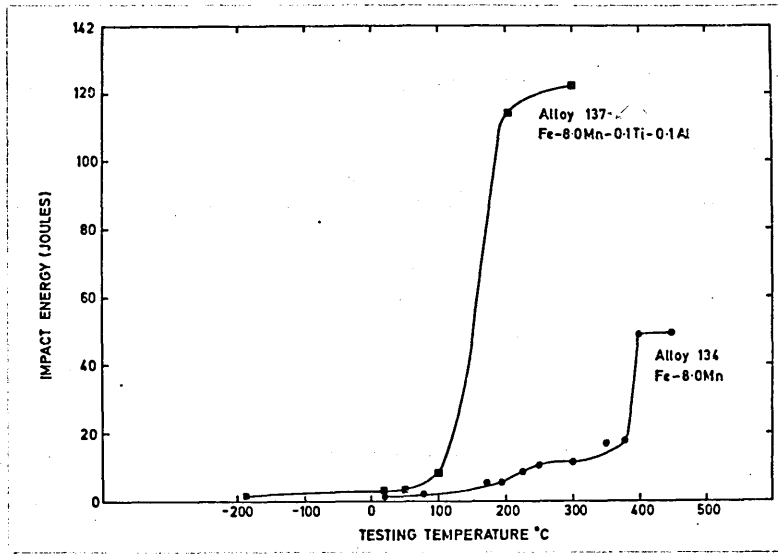


Fig 35. Comparison of impact transition curves for alloys I34 and I37 as air-cooled.

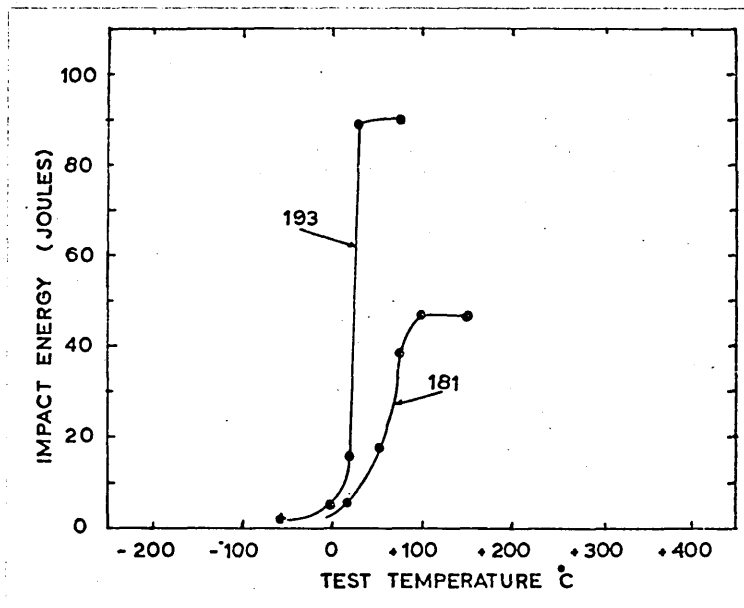


Fig 36. Comparison of impact transition curves for alloys I81 and I93 as ice-brine quenched. (Impact Data taken from Nickbaht et al, I50)

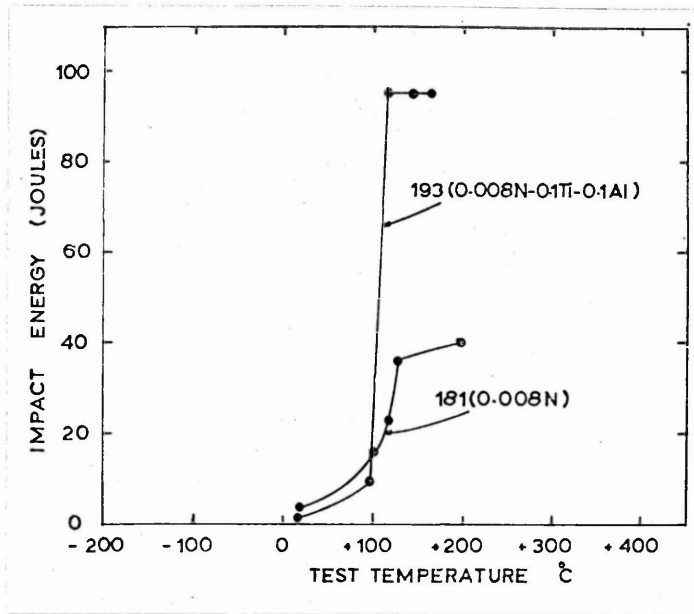


Fig 37. Comparison of impact transition curves for alloys I8I and I93 as air-cooled. After Nickbaht (I50)

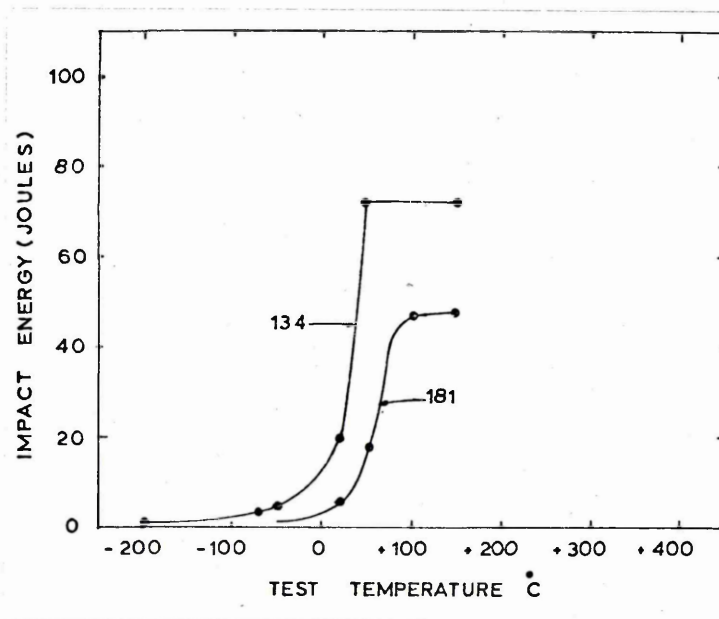


Fig 38. Comparison of impact transition curves for alloys I34(0.03N) and I8I(0.008N) as ice-brine quenched.

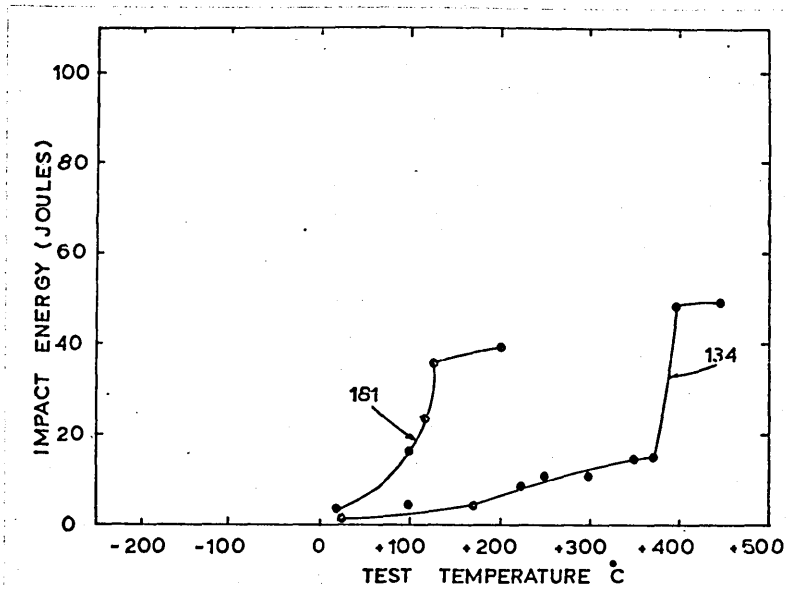


Fig 39. Comparison of impact transition curves for alloys I34(0.03N) and I8I(0.008N) as air-cooled.

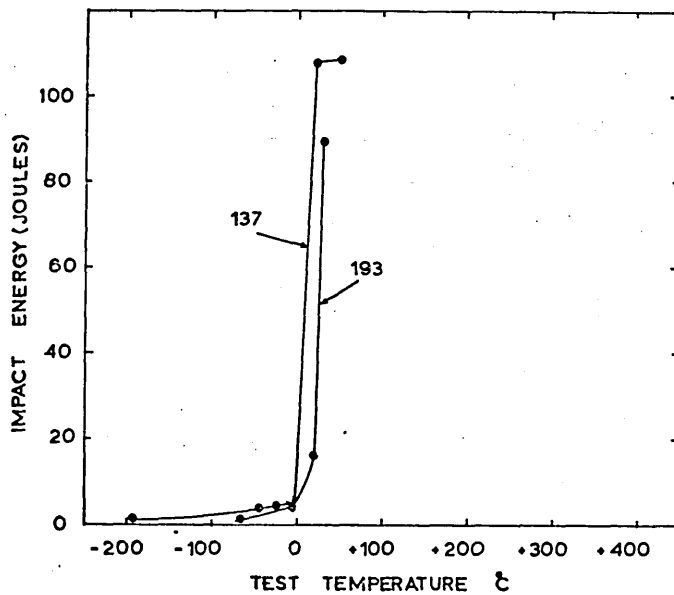


Fig 40. Comparison of impact transition curves for alloys I37(0.03N-0.1Ti-0.1Al) and I93(0.008N-0.1Ti-0.1Al) as ice-brine quenched.

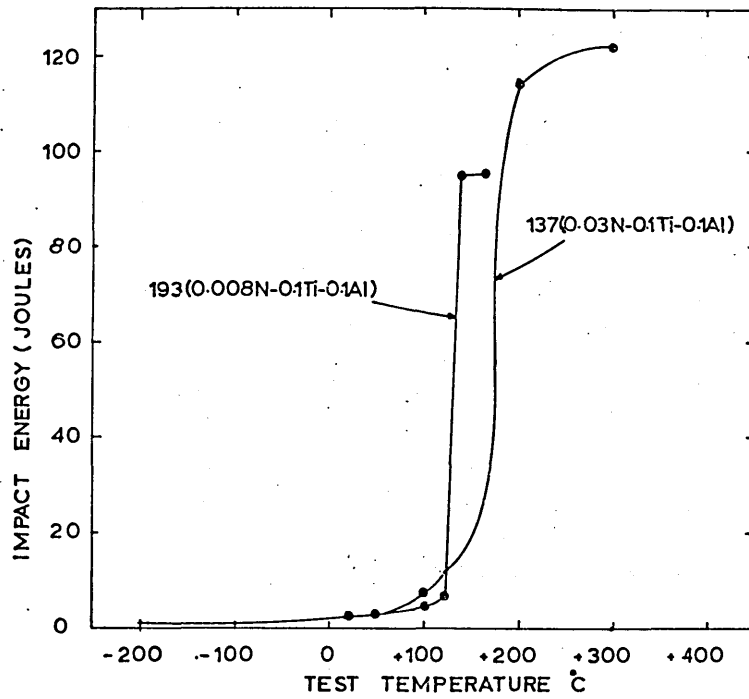


Fig 41. Comparison of impact transition curves for alloys I37 and I93 as air-cooled.

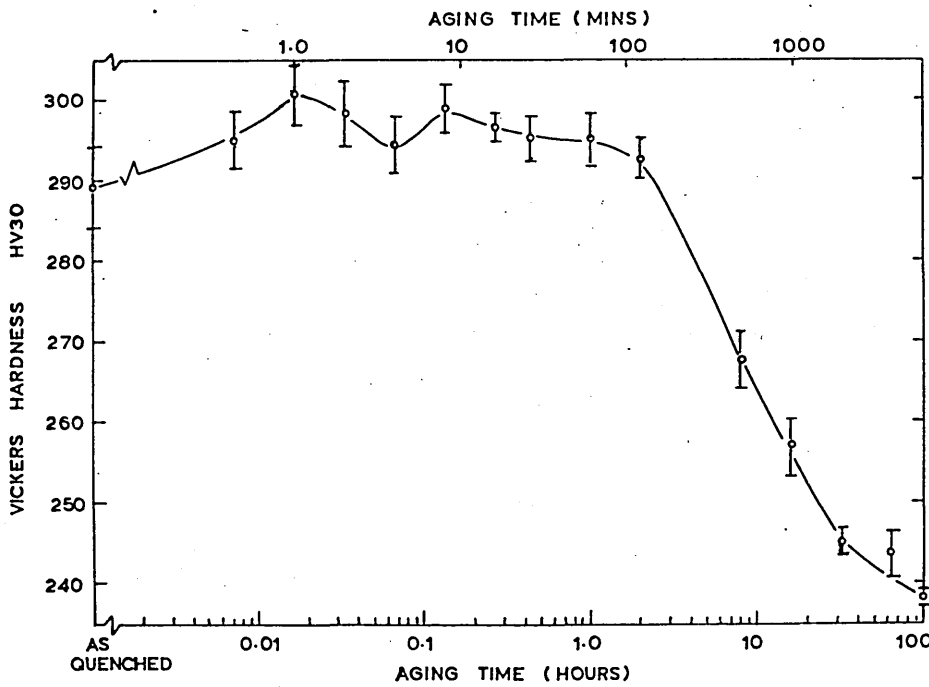


Fig 42. Effect of aging at 450°C on hardness in alloy I34 after being ice-brine quenched.

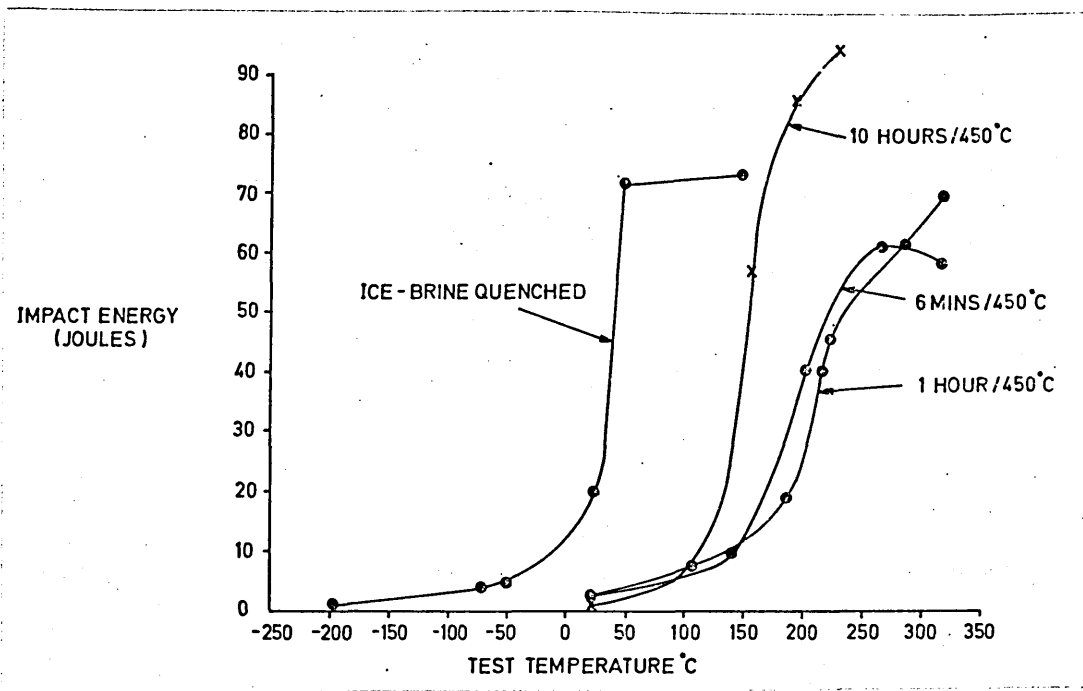


Fig 43. Effect of holding at 450°C on ductile-brittle transition temperature in alloy I34 after being ice-brine quenched.

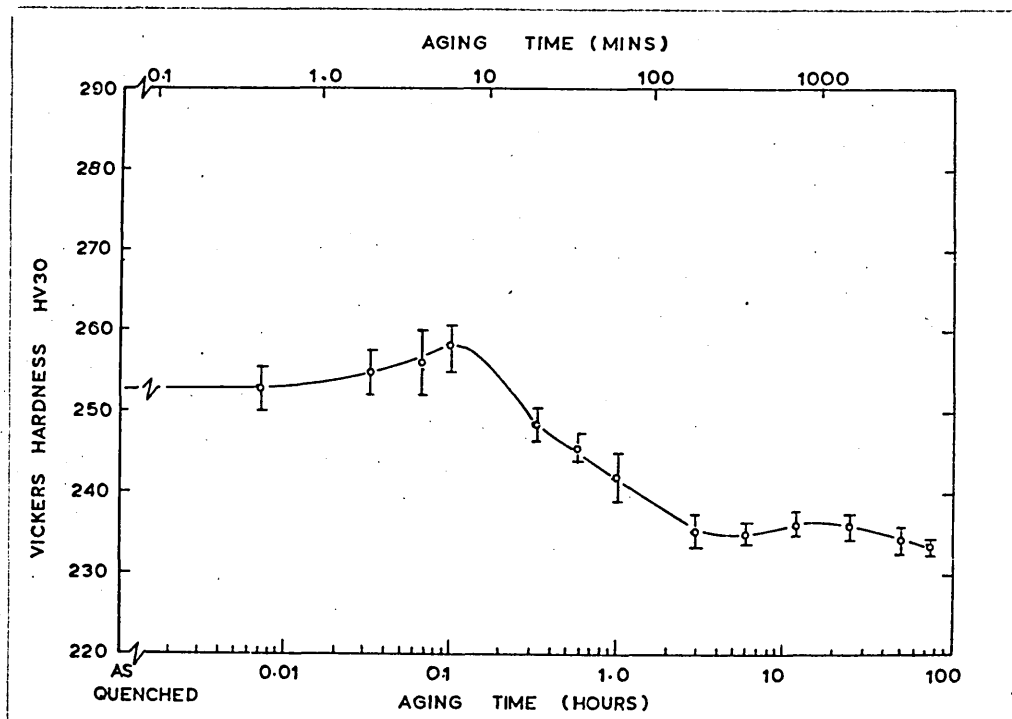


Fig 44. Effect of aging at 450°C on hardness in alloy I37 after being ice-brine quenched.

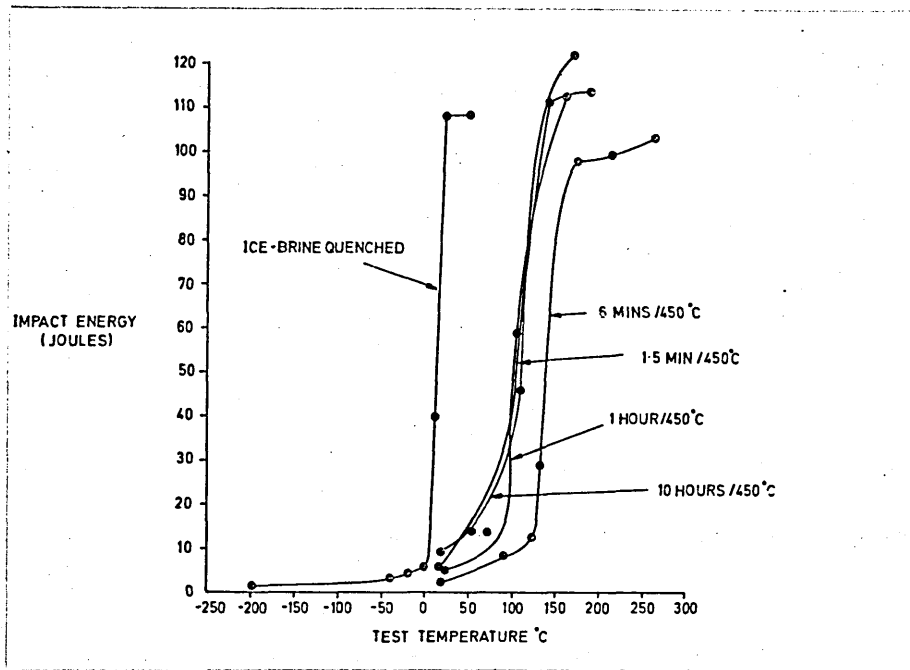


Fig 45. Effect of holding at 450°C on ductile-brittle transition temperature in alloy I37 after being ice-brine quenched.

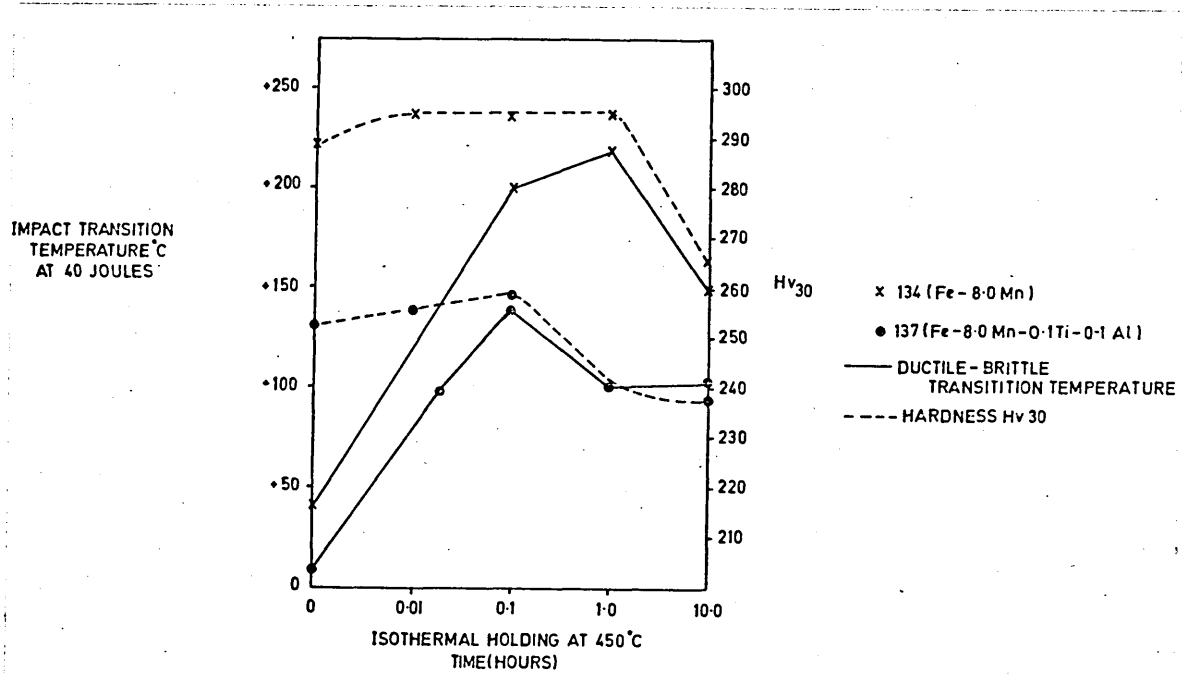


Fig 46. Effect of holding time at 450°C on ductile-brittle transition temperature and hardness in alloys I34 and I37 after being ice-brine quenched.

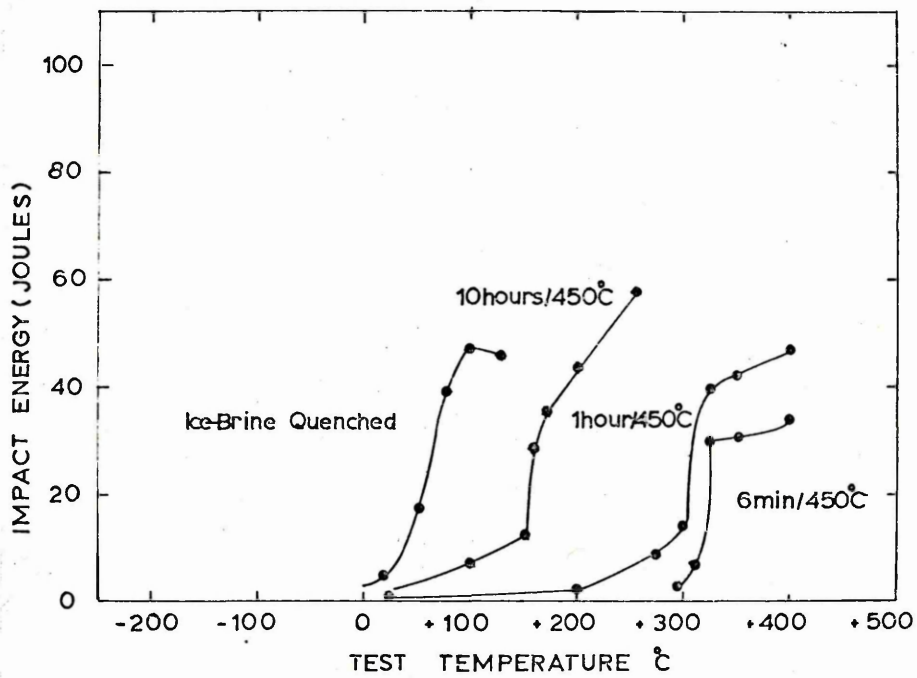


Fig 47. Effect of holding at 450°C on ductile-brittle transition temperature in alloy 181, after being ice-brine quenched. After Nickbaht (150)

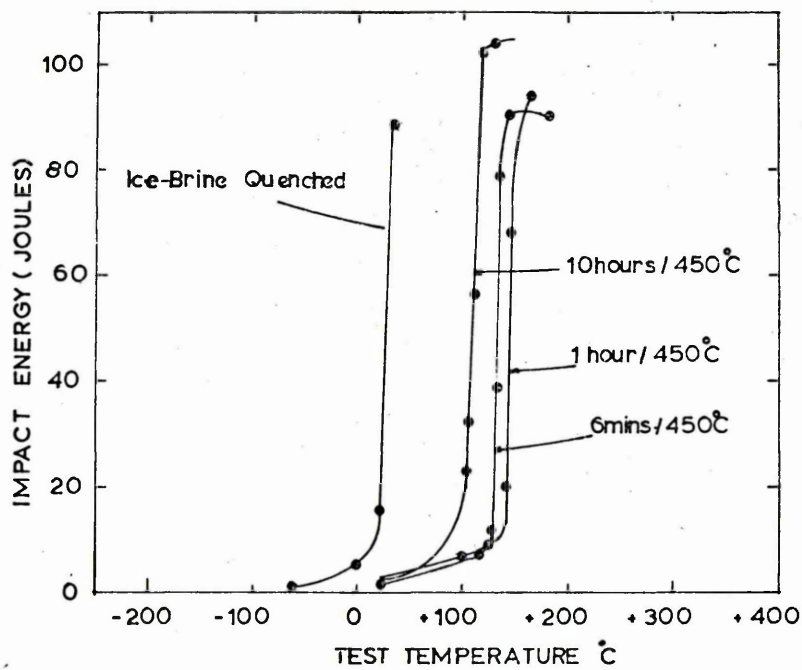


Fig 48. Effect of holding at 450°C on ductile-brittle transition temperature in alloy 193 after being ice-brine quenched. After Nickbaht (150)

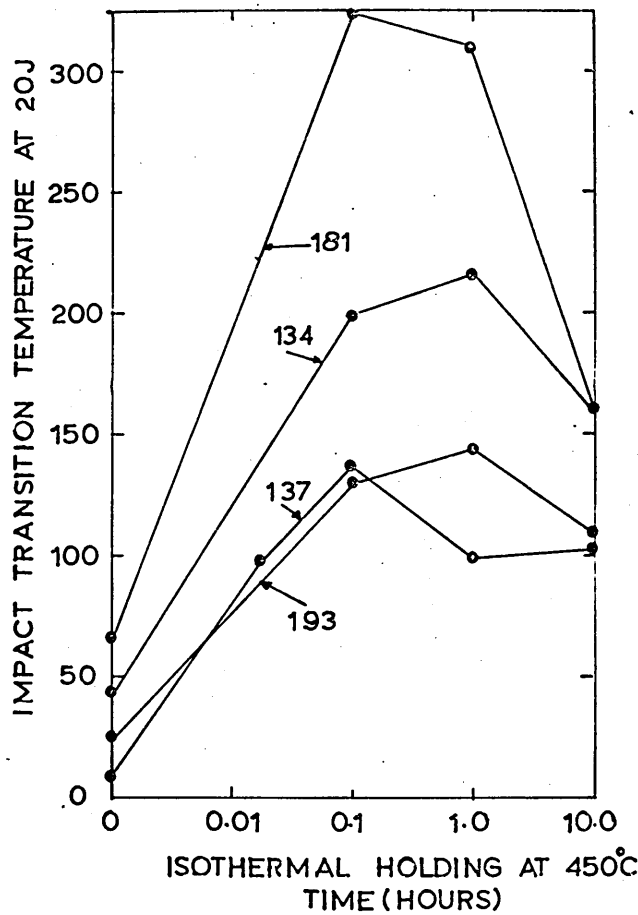


Fig 49. Effect of holding time at 450°C on ductile-brittle transition temperature in alloys 181, 134, 137, 193.

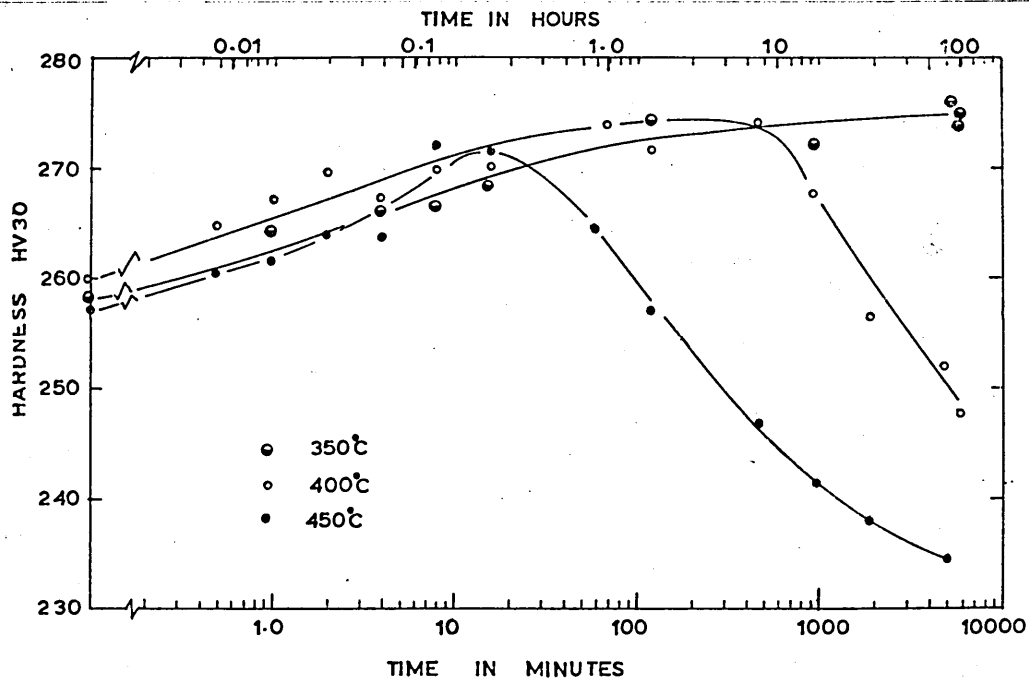


Fig 50. Variation of hardness on aging alloy KI525 at 350°C, 400°C, 450°C after being solution treated at 1000°C for 1 hour and water quenched.

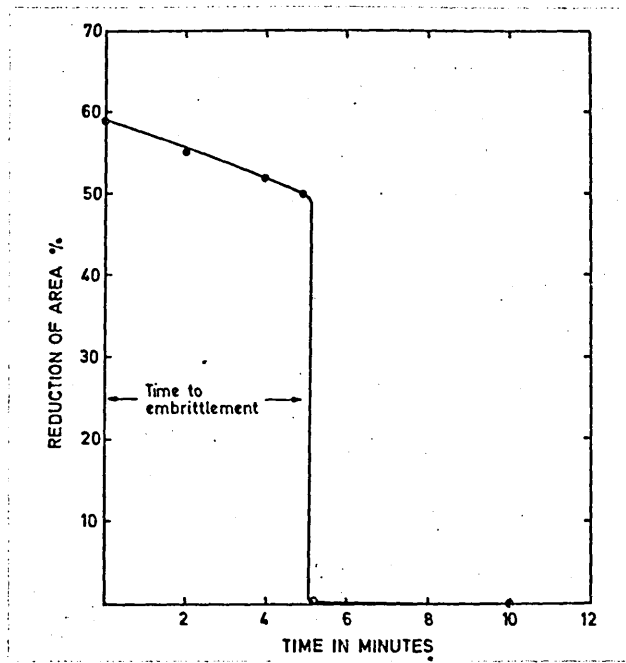


Fig 51. Variation of tensile ductility with aging time at 450C in KI525. Tensile tested at -78C at a strain rate of  $0.5\text{min}^{-1}$

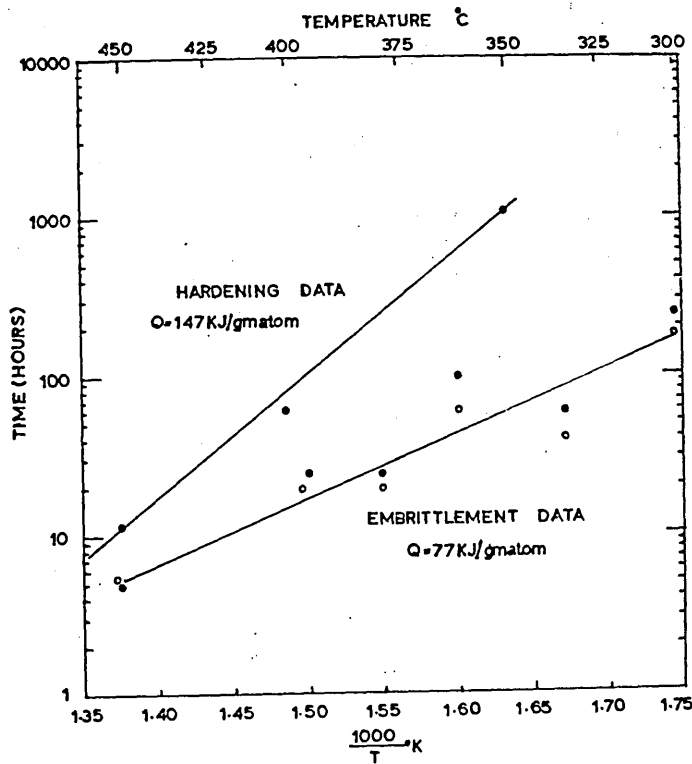


Fig 52. Arrhenius plot of hardening and embrittlement in alloy KI525.

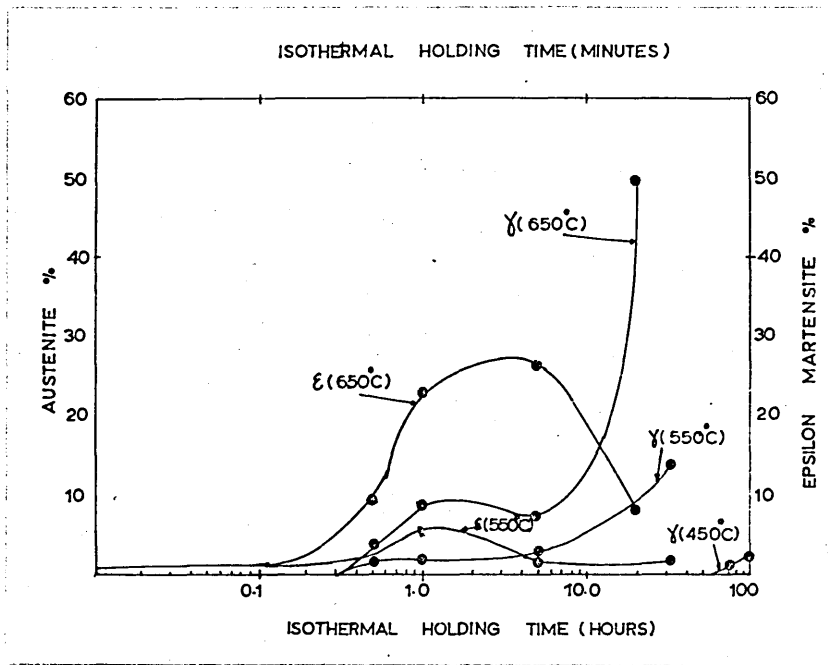


Fig 53. The volume percent austenite and epsilon martensite as a function of aging time in alloy KI525 at 450°C, 550°C and 650°C.

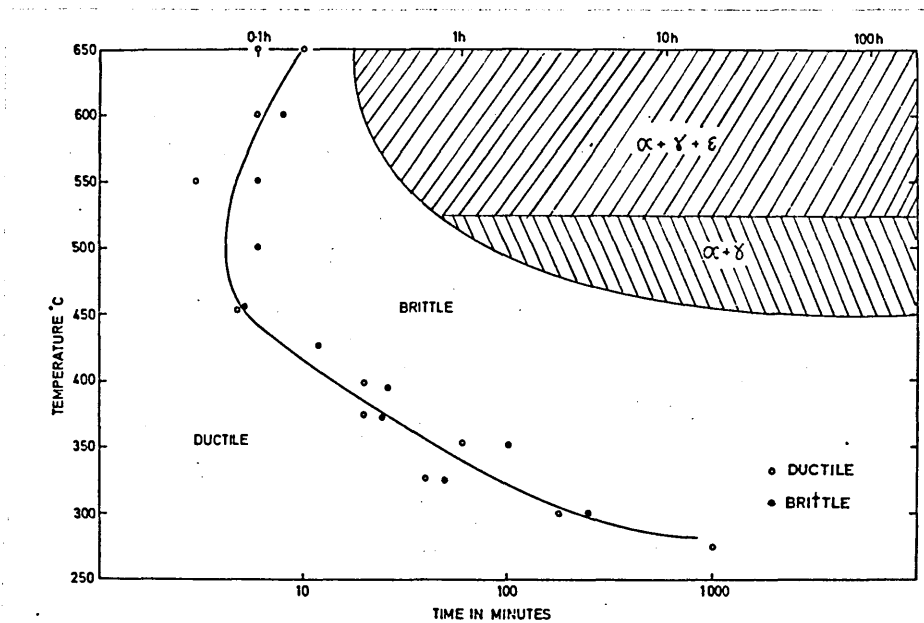


Fig 54. Embrittlement Kinetics curve determined from tensile ductility transition. Shaded portion shows the region during which phase-transformations occur on isothermal holding in alloy KI525.

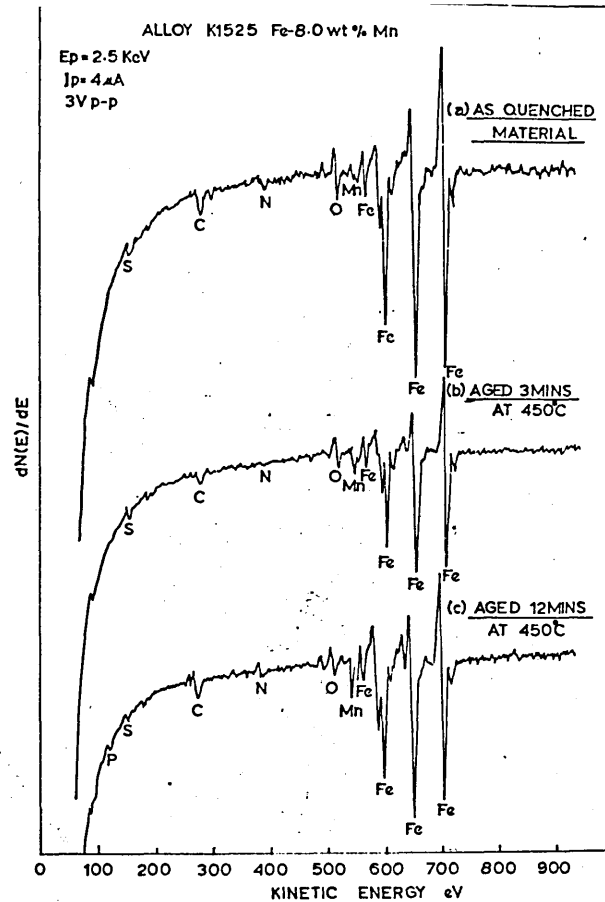


Fig 55 AES spectra of the fracture surfaces of the as quenched and aged material in alloy KI525.

Boundary Situation in lath-martensitic Structure  
in Fe-8.0 Mn alloy

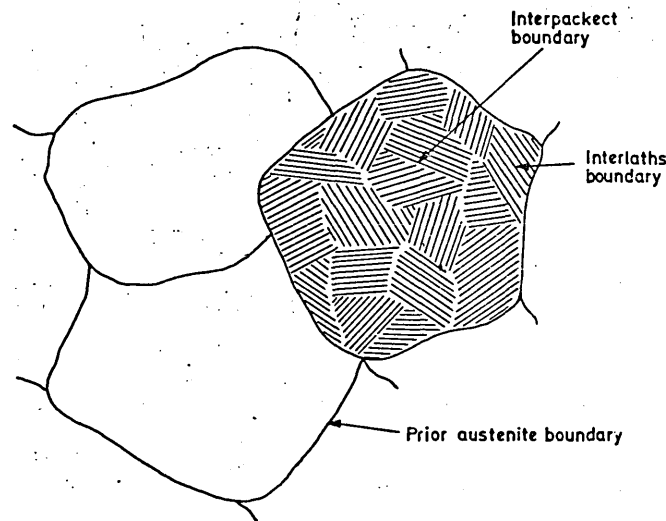


Fig.56

Lath-martensite structure composed of three types of boundaries.

1. Prior austenite grain boundary (Austenitic boundary)
2. Interpacket boundary (Ferritic boundary)
3. Interlath boundary (Ferritic boundary)

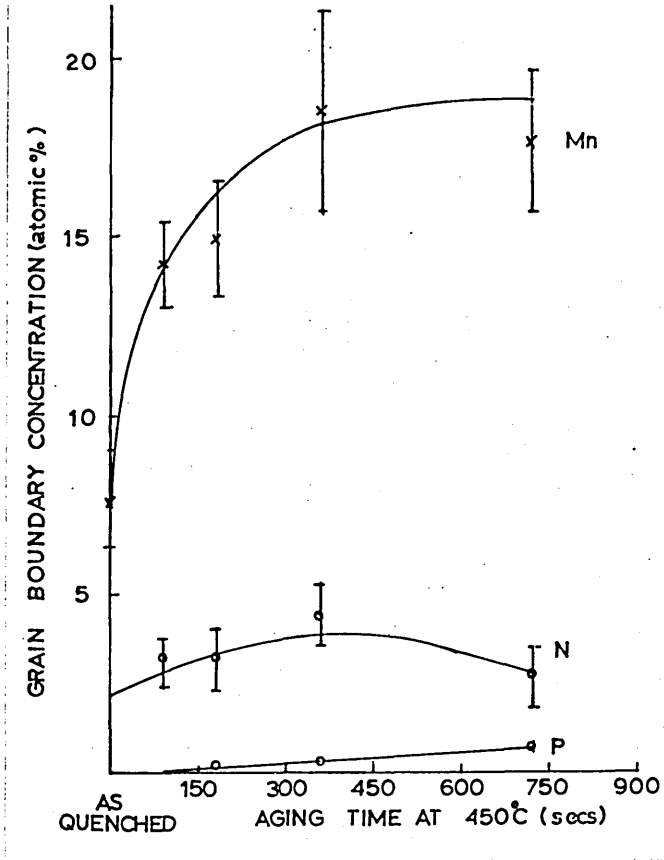


Fig 57. The grain boundary concentration of Mn, N and P as a function of aging time.

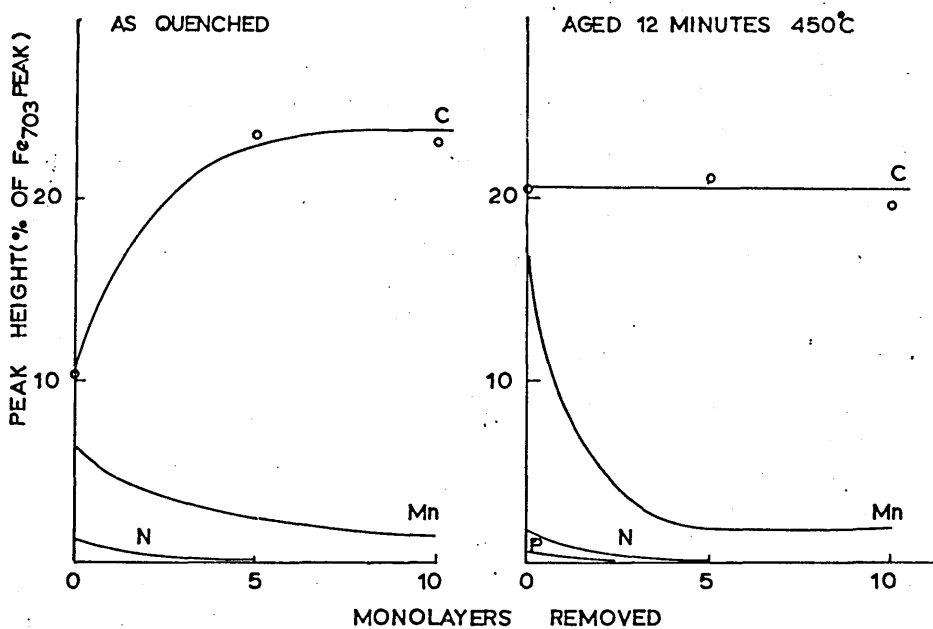


Fig 58. The concentration of Mn, P, N and C as a function of distance from the grain boundary determined using argon ion bombardment.

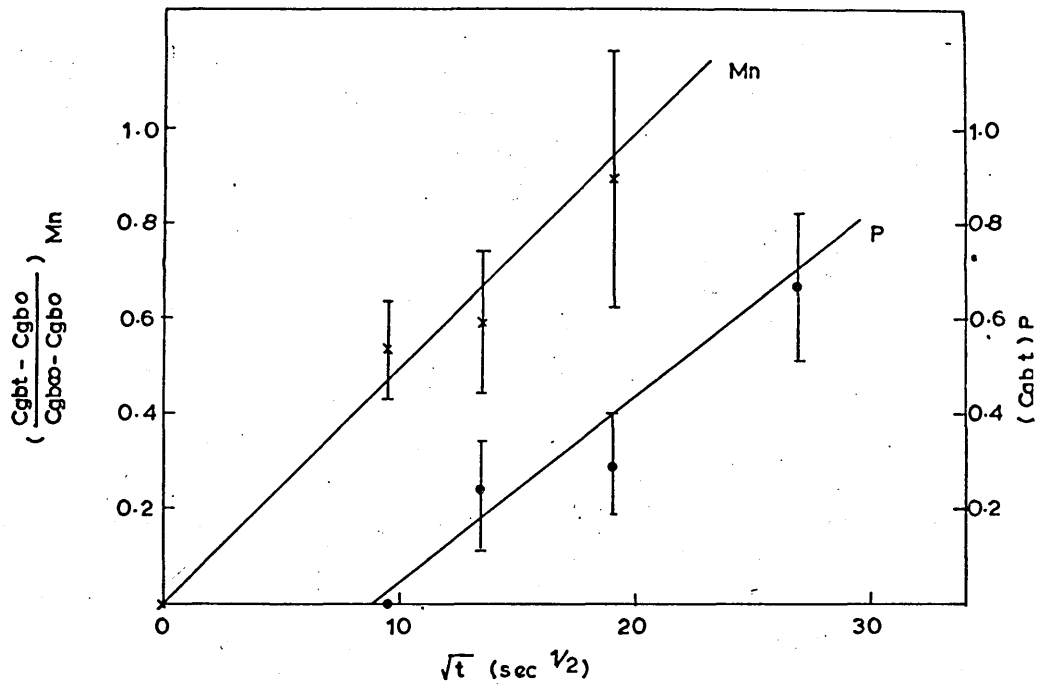


Fig 59. The concentration parameters  $\frac{C_{g_{bt}} - C_{g_{bo}}}{C_{g_{bo}} - C_{g_{bo}}}$  for Mn and  $C_{g_{bt}}$  for P as a function of  $\sqrt{t}$  (170)

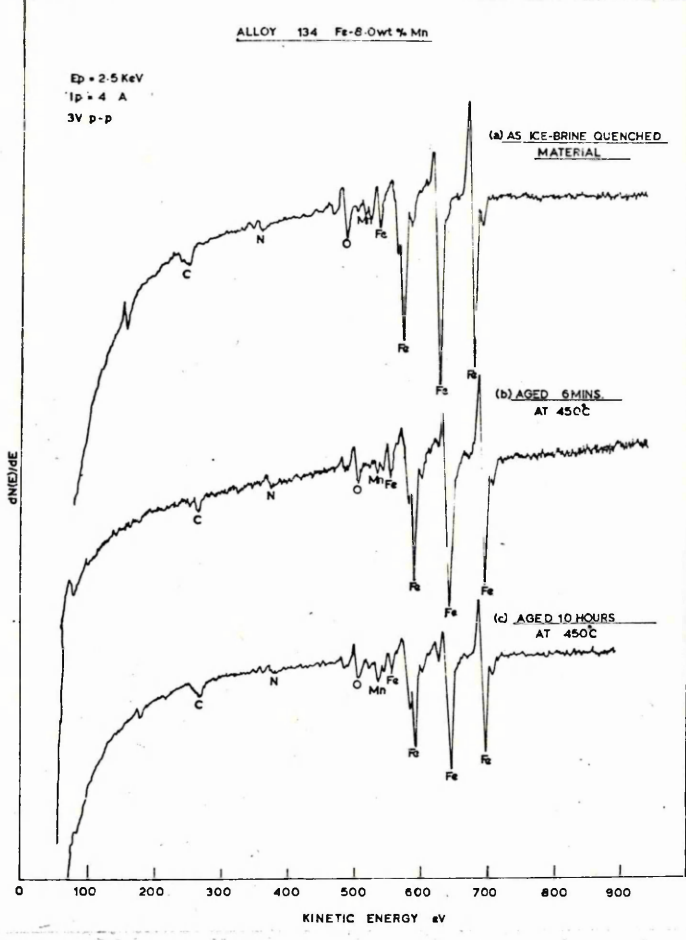


Fig 60. AES spectra of the fracture surface of as ice-brine quenched and aged material in alloy I34.

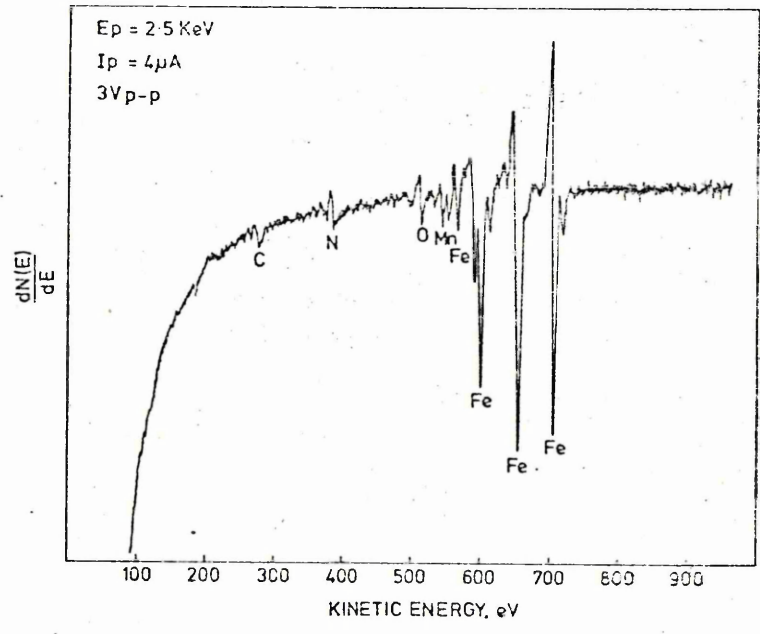


Fig 61. AES spectra of alloy I34-air cooled.

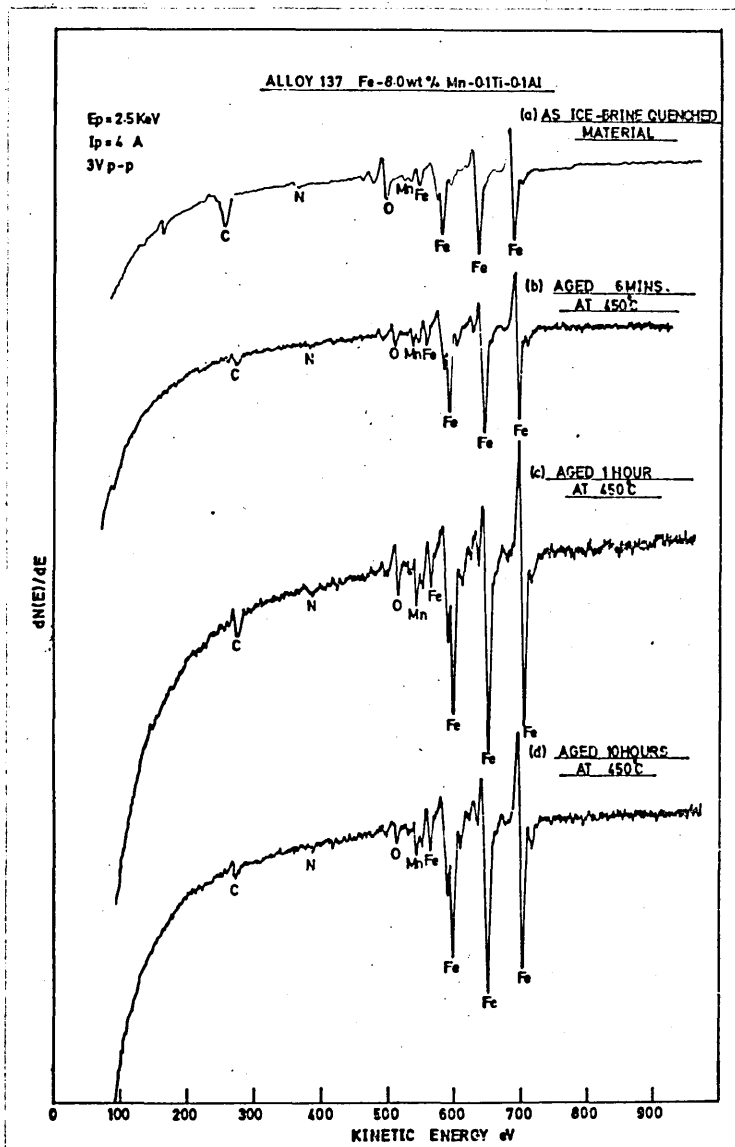


Fig 62. AES spectra of the fracture surface of as ice-brine quenched and aged material in alloy 137.

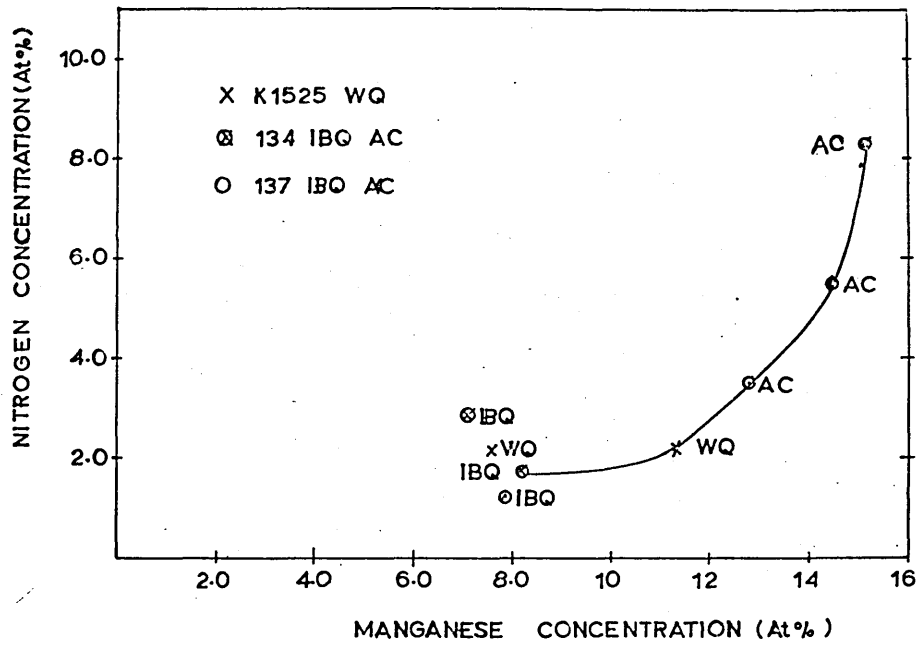


Fig 63. The effect of cooling rate on the variation in grain boundary concentration of Mn and N in alloys KI525 I34, I37.

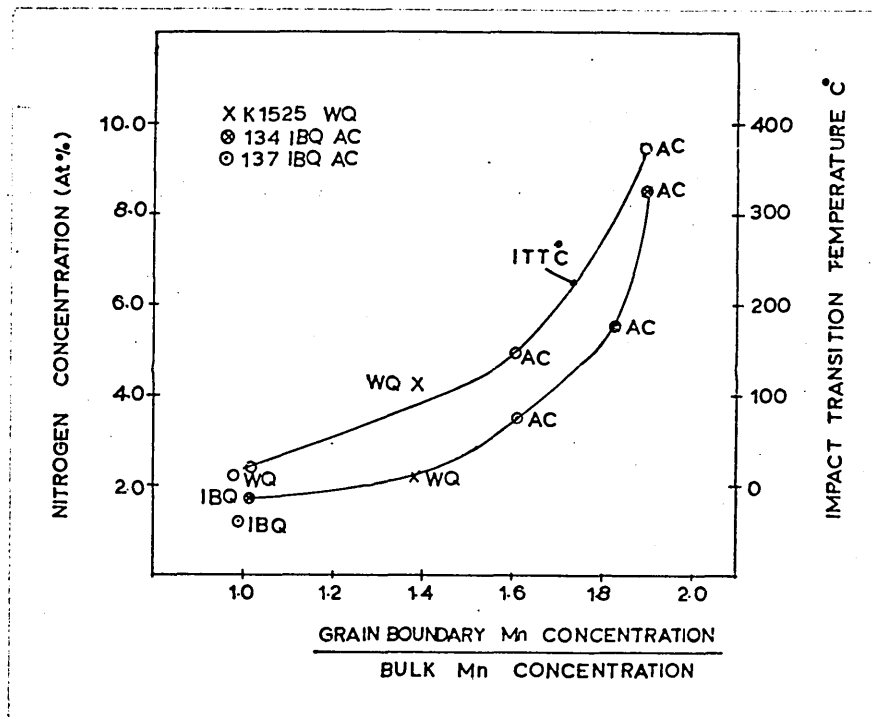


Fig 64. The effect of cooling rate on the shift in impact transition temperature and the variation in grain boundary concentration of Mn and N in alloys KI525, I34, I37.

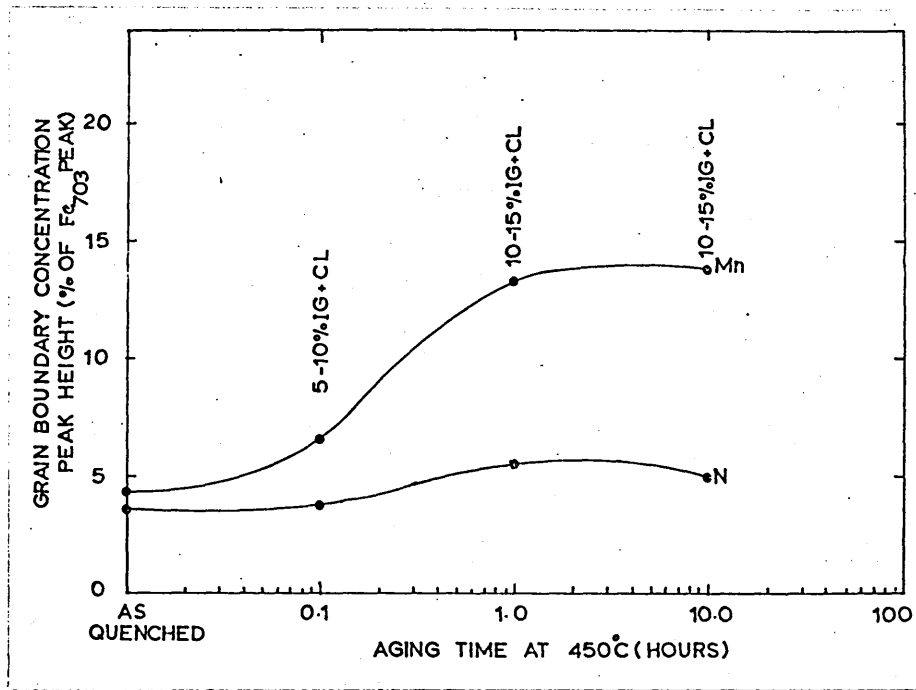


Fig 65. The grain boundary concentration of Mn and N as a function of aging time in alloy I34.

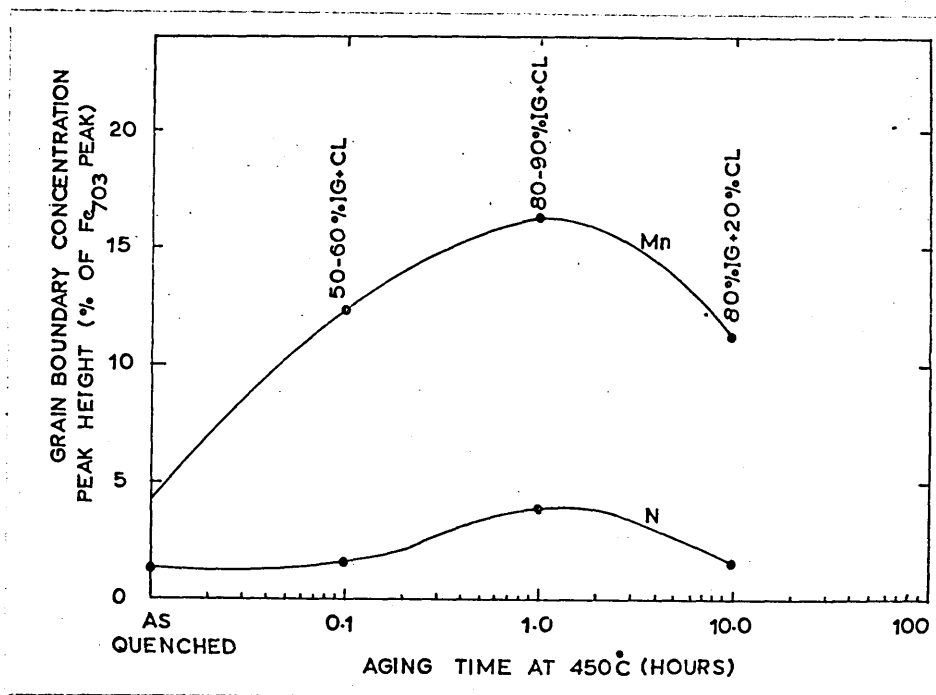


Fig 66. The grain boundary concentration of Mn and N as a function of aging time in alloy I37.

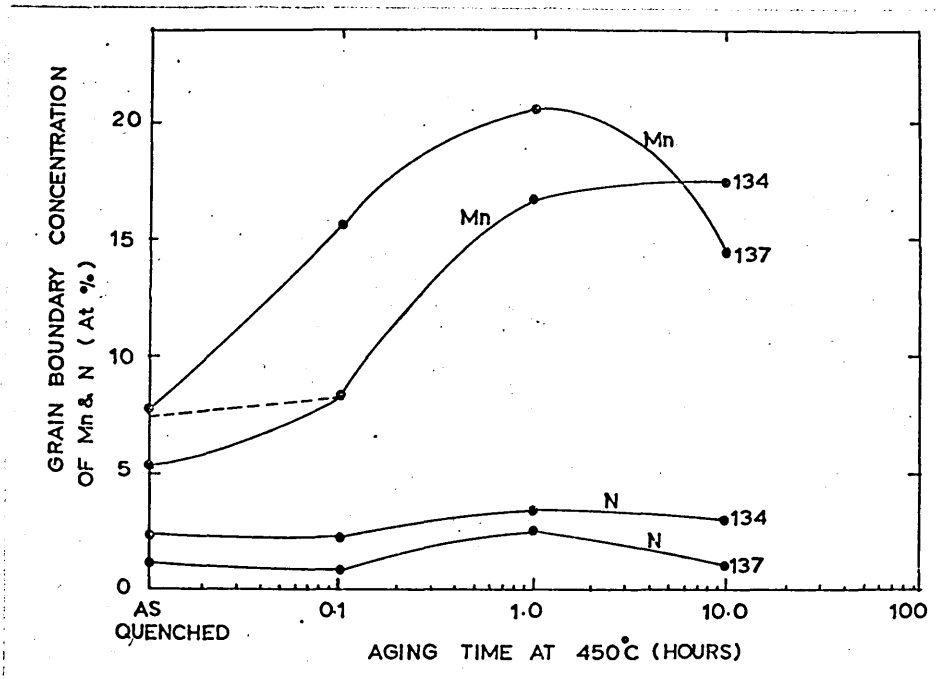


Fig 67. Comparative variation in concentration of Mn and N at the fracture surface in alloys I34 and I37 as a function of aging time at 450C

FIG.68 SCHEMATIC REPRESENTATION OF THERMAL CYCLING TREATMENT CARRIED OUT IN ALLOY K1525 Fe.80 Mn

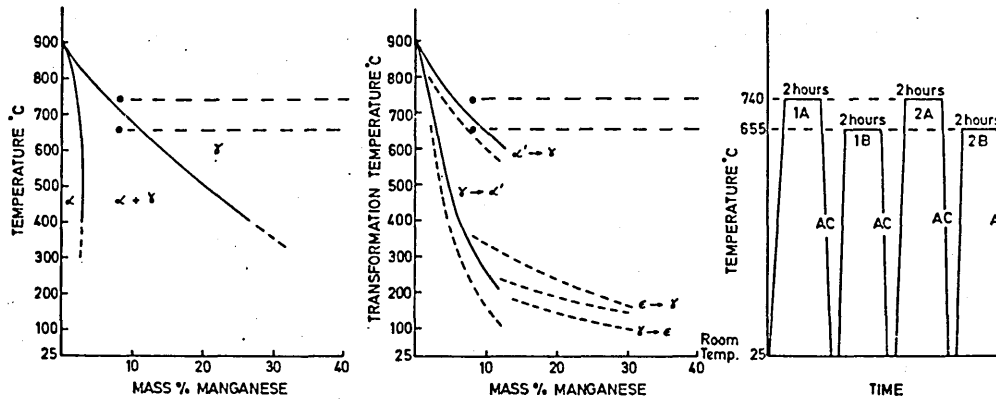
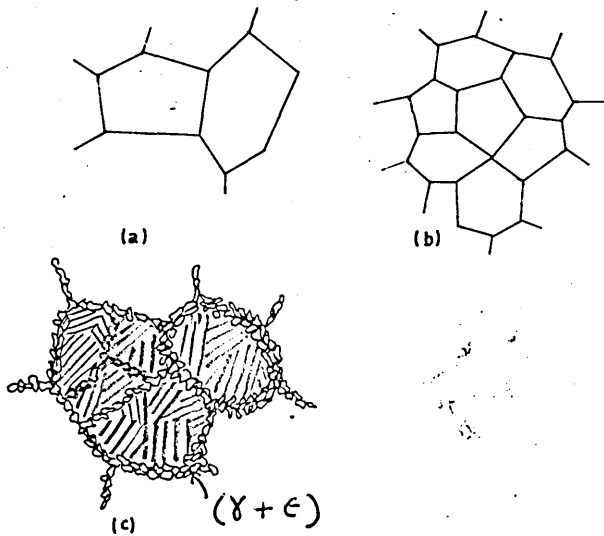


FIG.69. SCHEMATIC ILLUSTRATION OF THE DEVELOPMENT OF MICRO-STRUCTURE ON THERMAL CYCLING TREATMENT



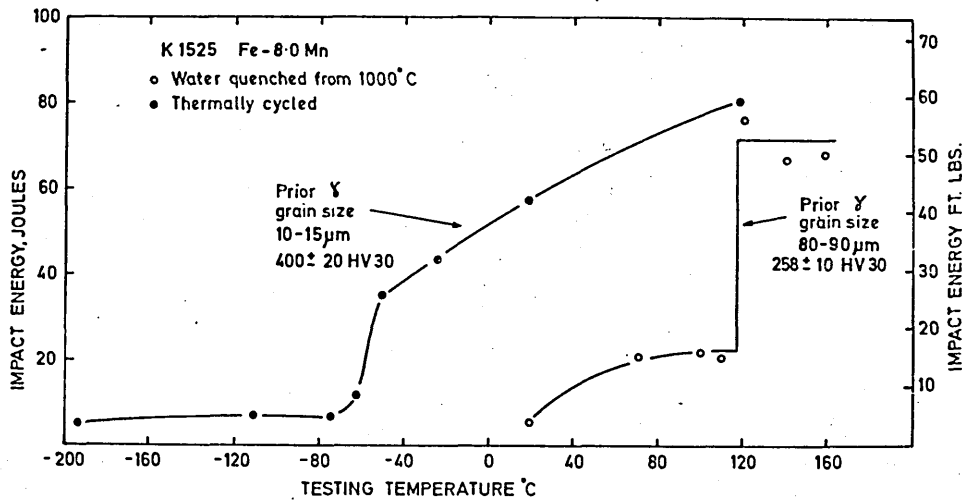


Fig 70(a). Effect of thermal cycling treatment on impact transition temperature in alloy KI525.

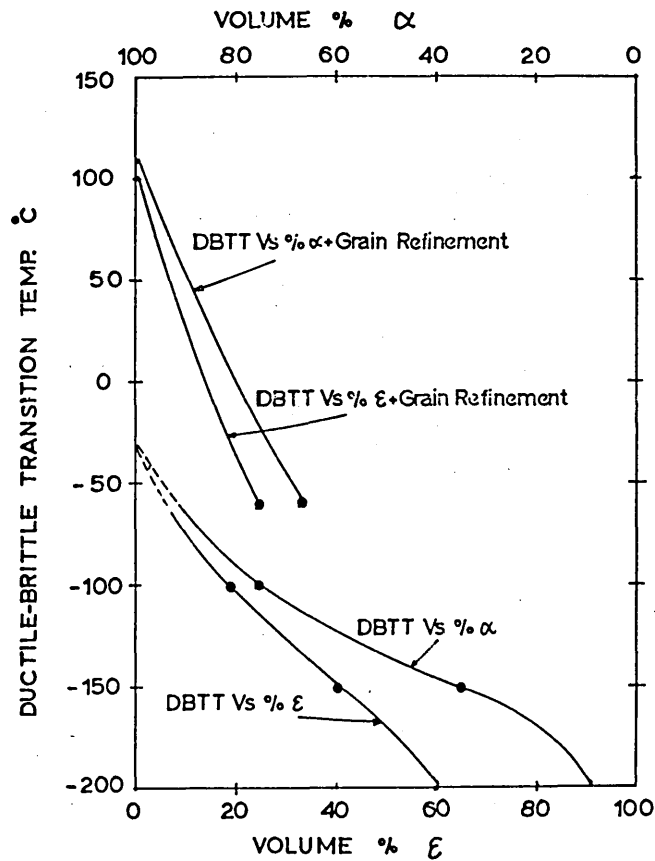


Fig 70(b). Comparison of the shift in DBTT Vs volume percent  $\gamma$  and  $\epsilon$  in Fe-Mn alloys (32) with shift in DBTT Vs volume percent  $\gamma$  and  $\epsilon$  with grain refinement.



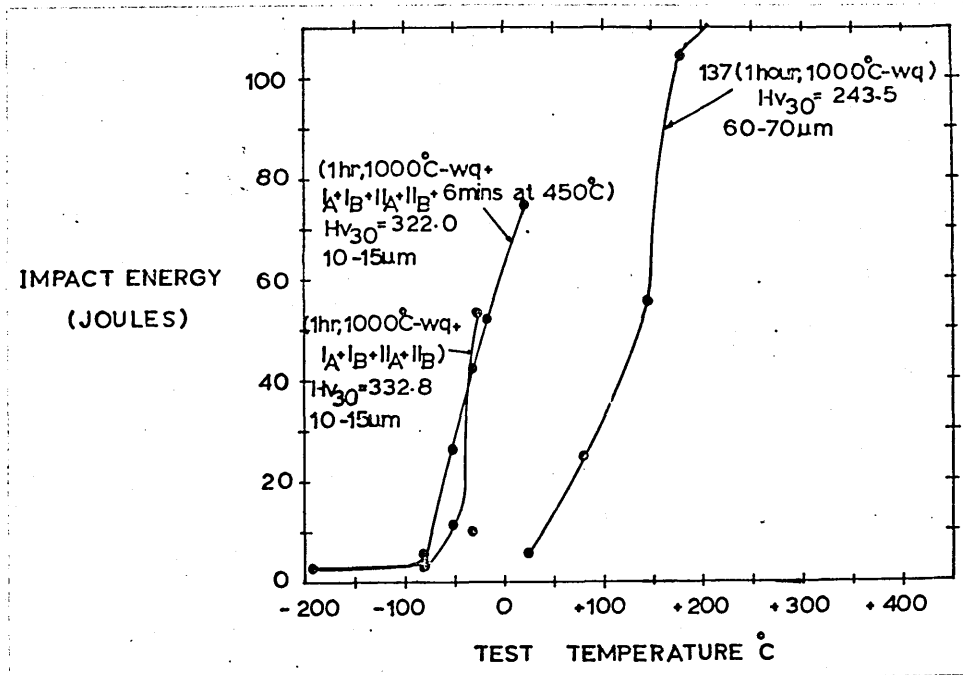


Fig 73. Influence of thermal-cycling treatment on the shift in impact transition temperature in alloy 137 and the effect of holding thermally-cycled alloy for 6min. at 450C

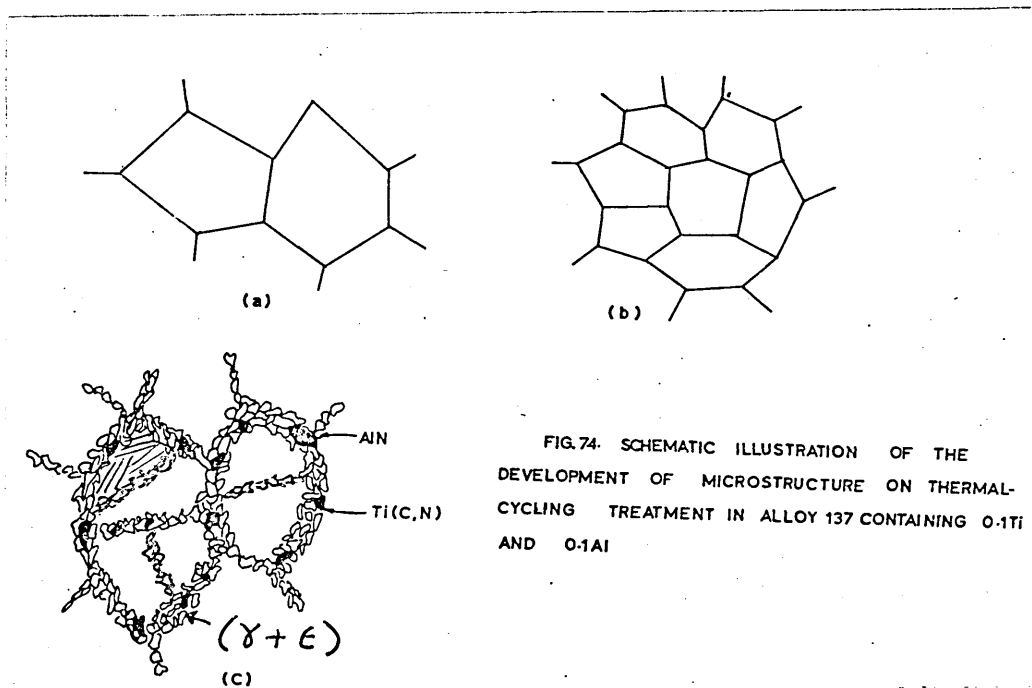
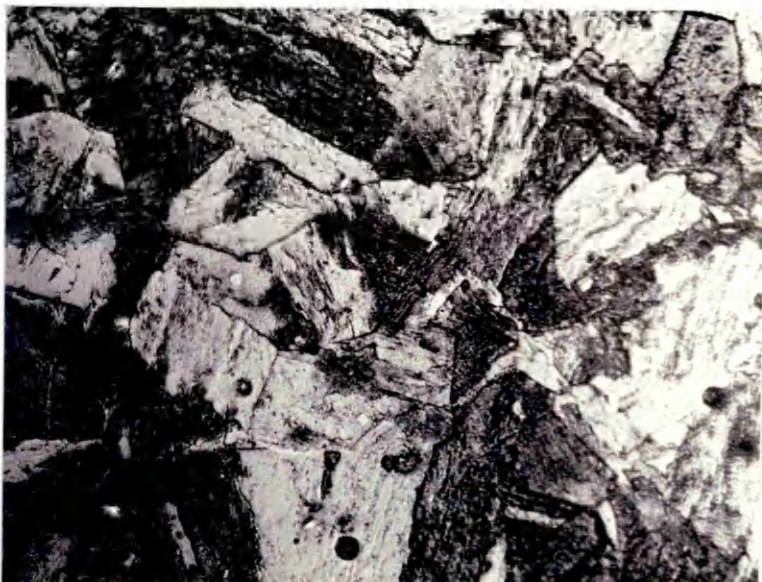


FIG.74. SCHEMATIC ILLUSTRATION OF THE DEVELOPMENT OF MICROSTRUCTURE ON THERMAL-CYCLING TREATMENT IN ALLOY 137 CONTAINING 0.1Ti AND 0.1Al



Fig 75(a). Optical Micrograph in alloy KI525. Solution treated at 1000C/1h-W.Q. Prior Austenite grain size=80-90um Etched in 2pct Nital. X 192



(b) Optical Micrograph in alloy I34. Solution treated at 900C for 1/2 hour-IBQ. X 400



Fig 76. Optical Micrograph in alloy I37. Solution treated at 900C for 1/2 hour-IBQ. Lightly etched in 2pct Nital followed by immersion in Schumann's Reagent. X 400

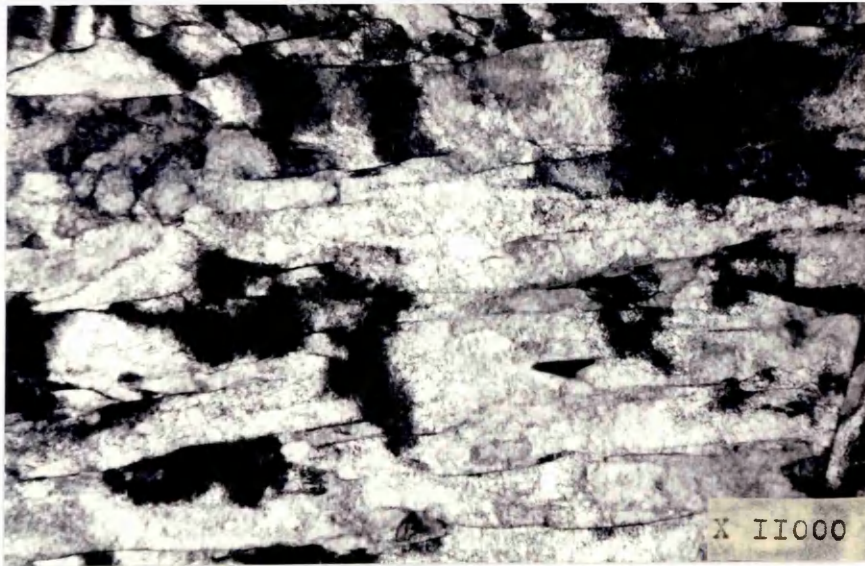


Fig 77. Transmission Electron Micrograph showing dislocated lath-martensitic structure in alloy I37, 1/2 hr, 900°C-A. C.



Fig 78. Transmission Electron Micrograph showing lath martensitic structure in alloy I37, 1/2 hr, 900°C-IBQ.

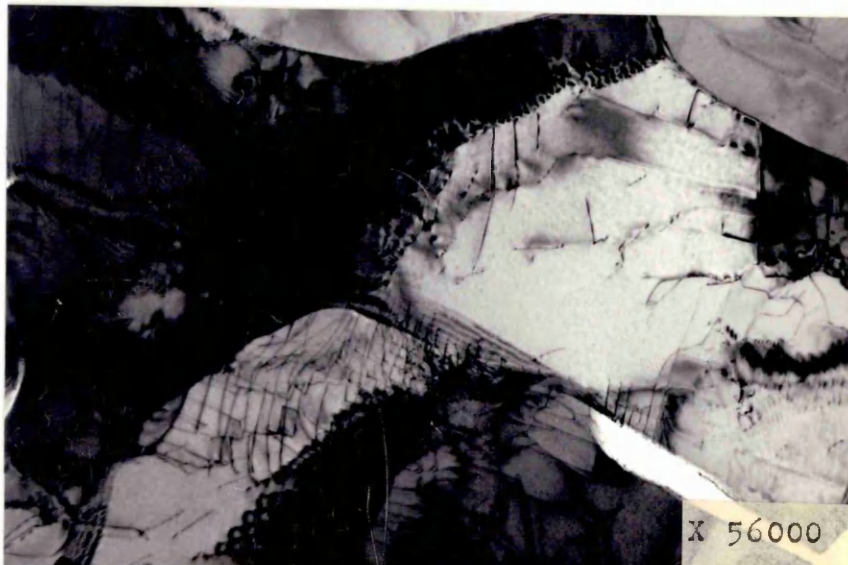
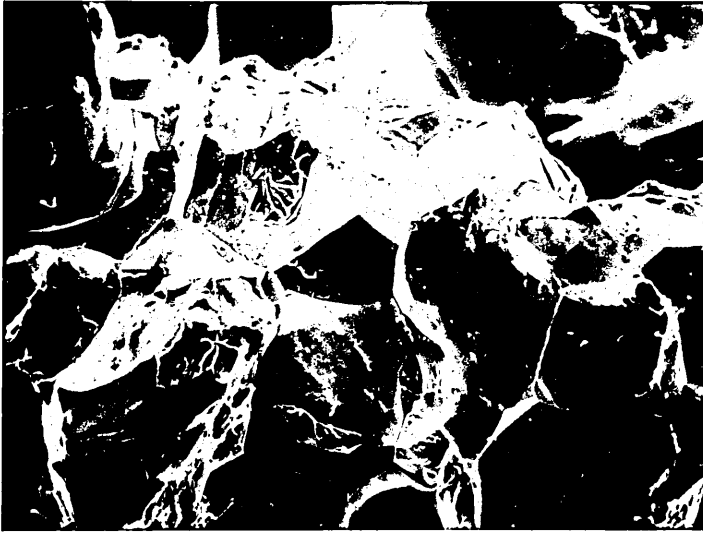
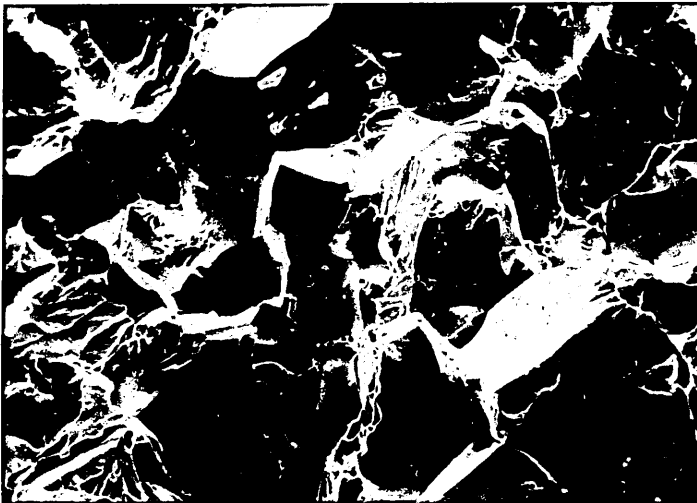


Fig 79. Transmission Electron Micrograph showing highly annealed substructure in alloy I37, 1/2 hr, 900°C-IBQ-aged at 450°C for 1000hrs. Note sub-boundaries in the micrograph.



X 200

Fig 80(a). Scanning Electron Micrograph of the fracture surface in alloy KI525. Solution treated at 1000C/1h-WQ. Impact tested at 25C showing mainly intergranular fracture mode.



X 200

(b). Scanning Electron Micrograph of the fracture surface in the same alloy as above, taken from the random area.

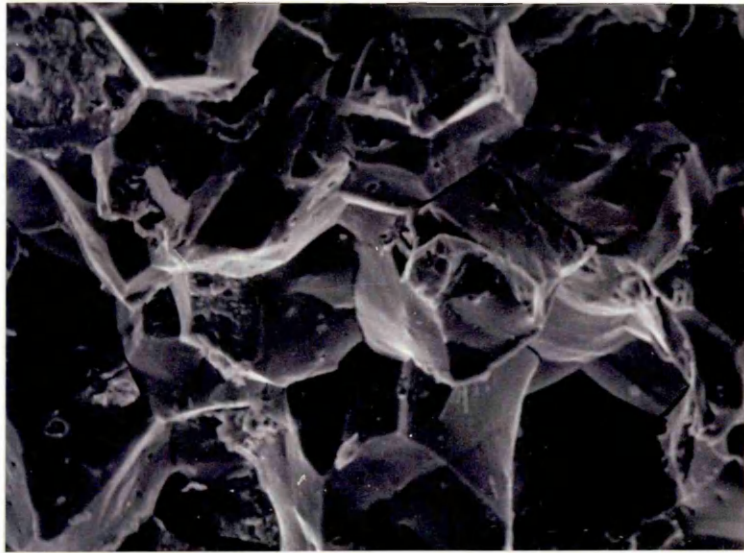
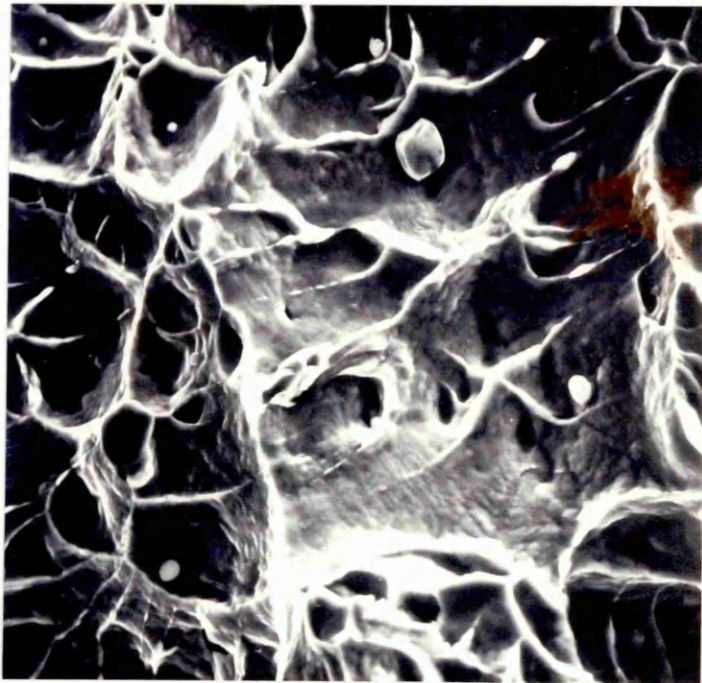


Fig 8I(a). Scanning Electron Micrograph of the fracture surface in alloy I54. Solution treated at 1000°C/1h-W.Q. Fracture mode is predominantly Intergranular. X 260



(b) Scanning Electron Micrograph showing a typical ductile fracture mode above the transition. MnS particles are found on the ductile dimples. X 500



X 240

Fig 82(a) SEM of fracture surface in alloy I34. Solution treated at 1000°C/1h-IBQ. Cleavage fracture mode is predominant. Impact tested at 25°C.



X 480

(b) Same alloy as above but at higher magnification.

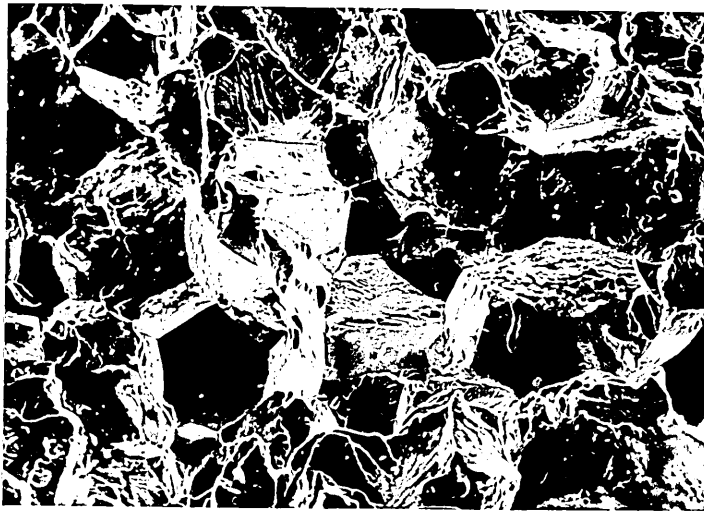
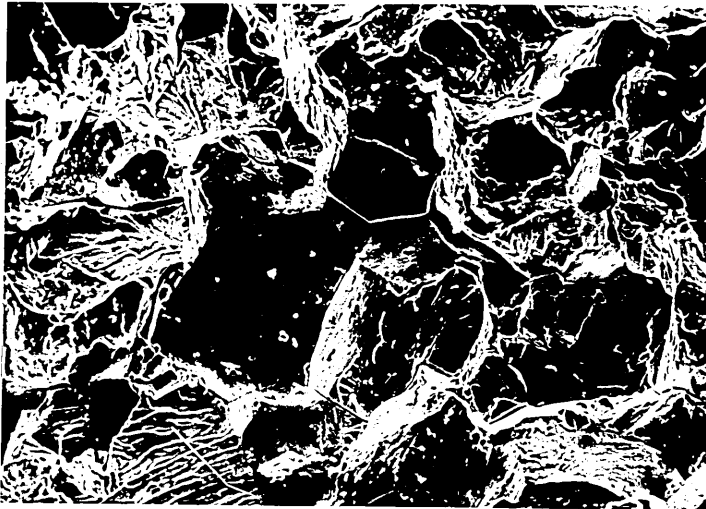
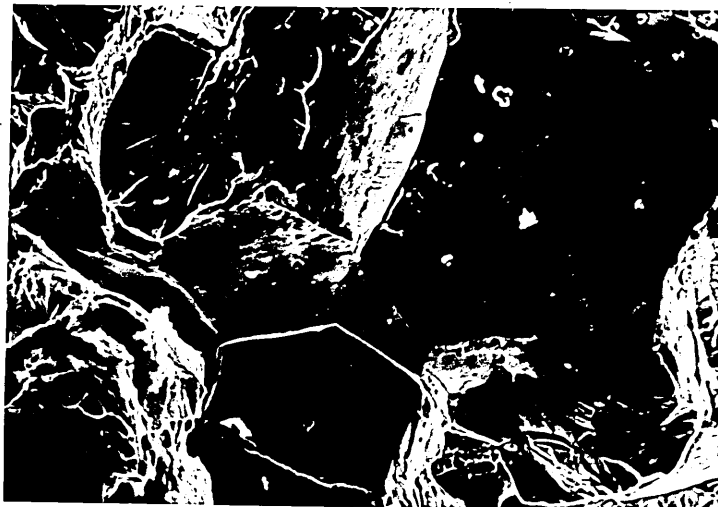


Fig 83(a). Scanning Electron Micrograph of the fracture surface in alloy 137. Solution treated at 1000C for 1 hr-W.Q. Impact tested at 25C. X 260



(b). Random area on the fracture surface.

X 260



(c). Same as shown in (b) but at higher magnification X 520

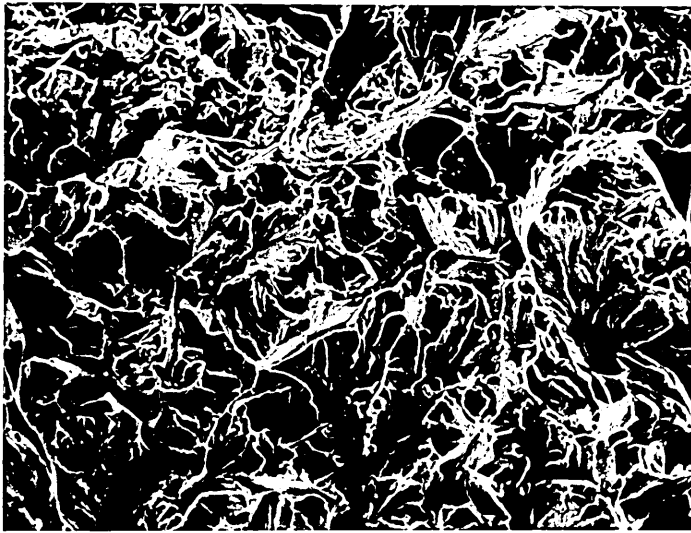
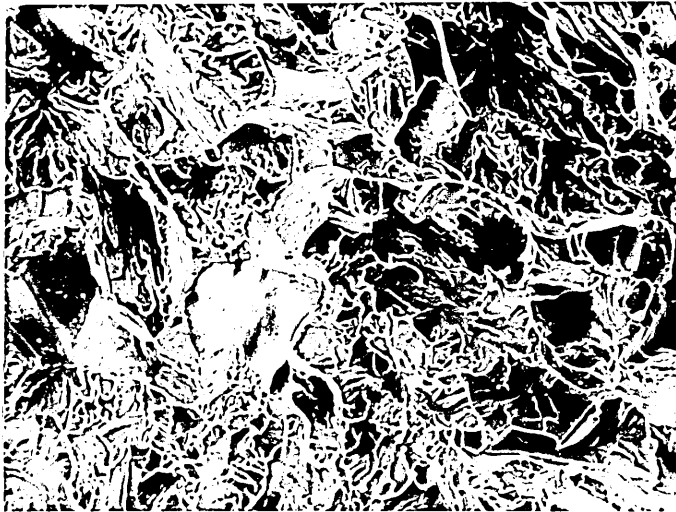


Fig 84(a) Scanning Electron Micrograph of the fracture surface in alloy I34. Solution treated at 900°C for 1/2hr-IBQ. Impact tested at -78°C, showing predominantly cleavage fracture mode. X 480



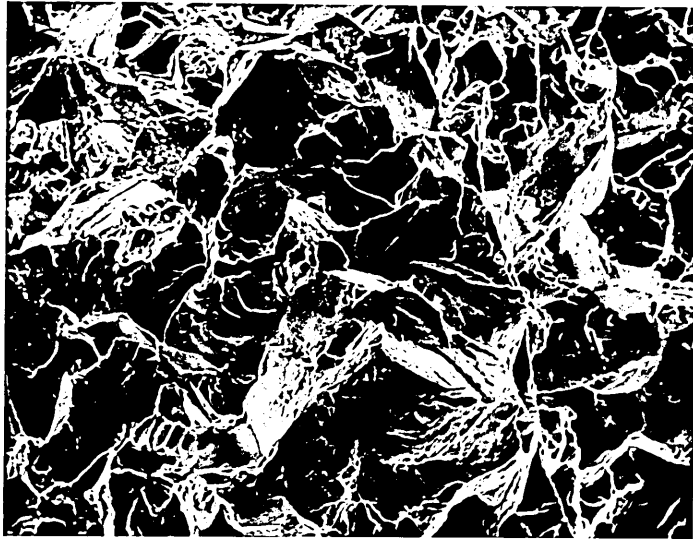
(b) Fracture mode close to V-notch

X 480



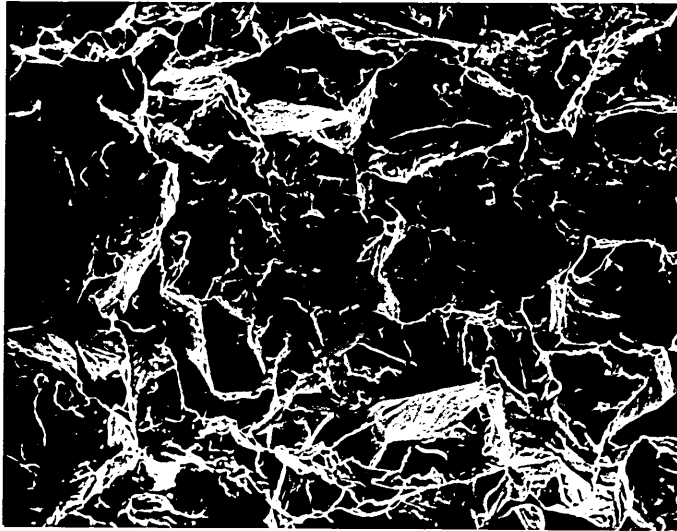
(c) Fracture mode opposite to V-notch.

X 480



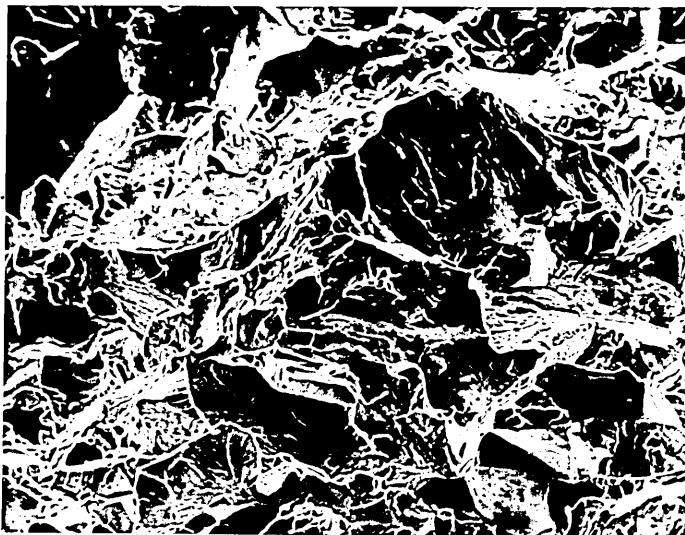
X 520

Fig 85(a). Scanning Electron Micrograph of fracture surface in alloy I37. Solution treated at 900°C for 1/2 hr-IBQ. Almost cleavage fracture with some grain boundary facets. Impact tested at -78°C.



(b). Same as above but close to V-notch.

X 520



(c) Fracture node opposite to V-notch

X 520



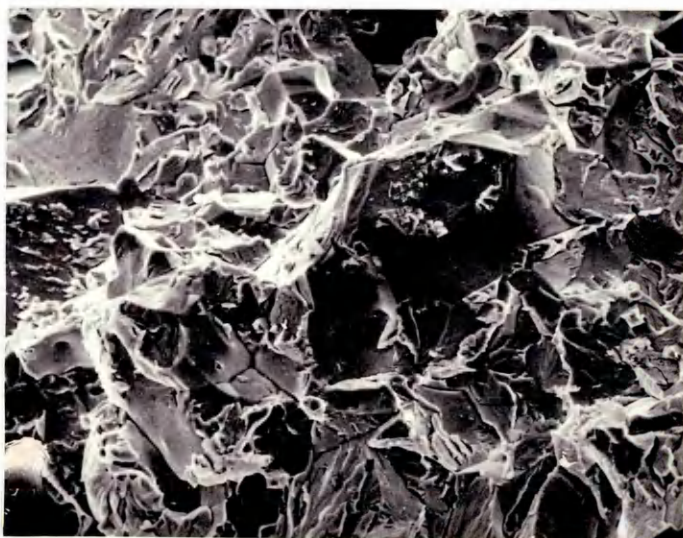
X 520

Fig 86(a). Scanning Electron Micrograph of fracture surface in alloy I34. Solution treated at 900C for 1/2 hr-A. C. Impact tested at -196C. Fracture mode is predominantly intergranular with some quasi-cleavage.



(b). Fracture mode close to V-notch

X 520



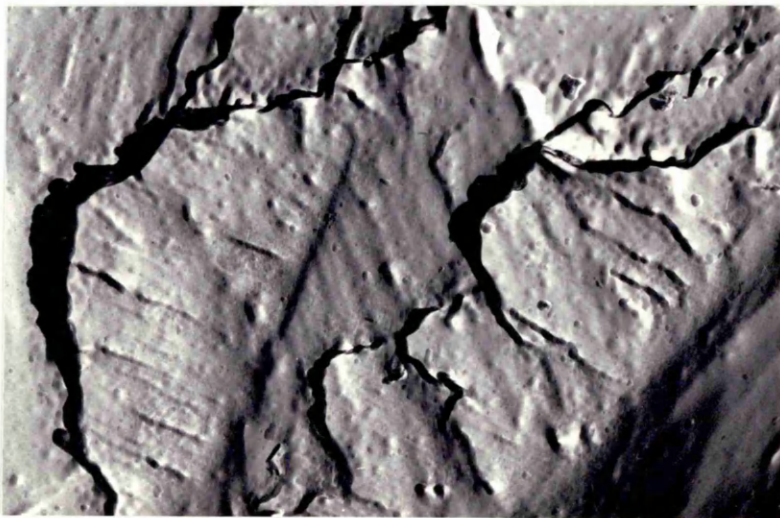
(c) Fracture mode opposite to V-notch.

X 520

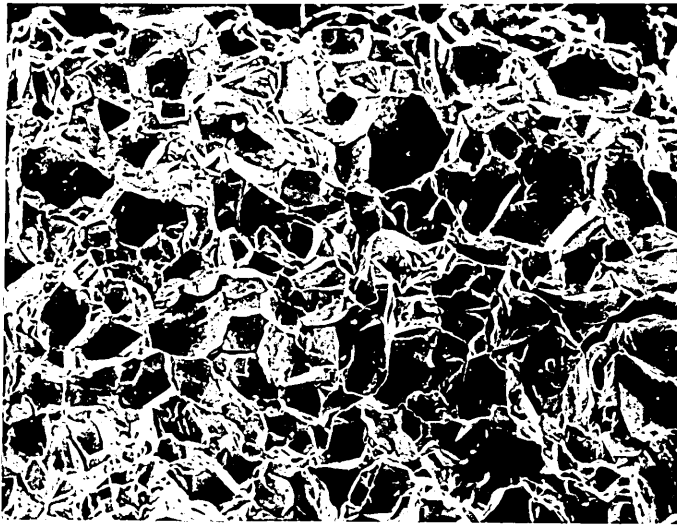


X 4900

Fig 87(a). Carbon extraction replica of the fracture surface in alloy I34 in the air-cooled condition. On this mixed fracture mode, it shows no sign of any kind of pptn at the grain boundaries.

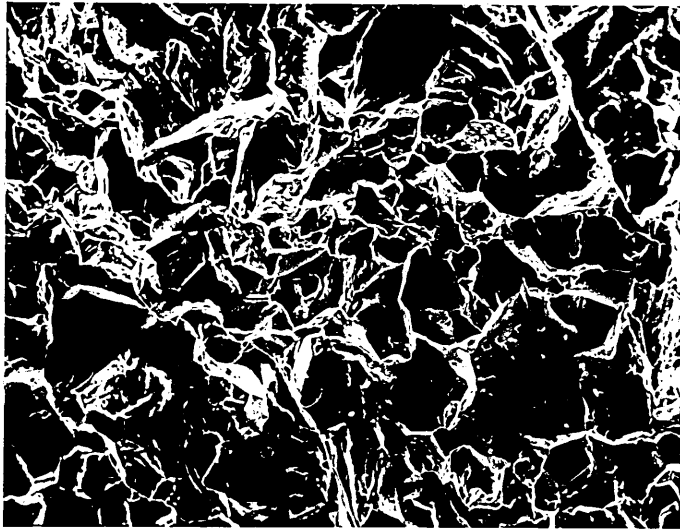


(b). Same as above but at higher magnification. X 10500



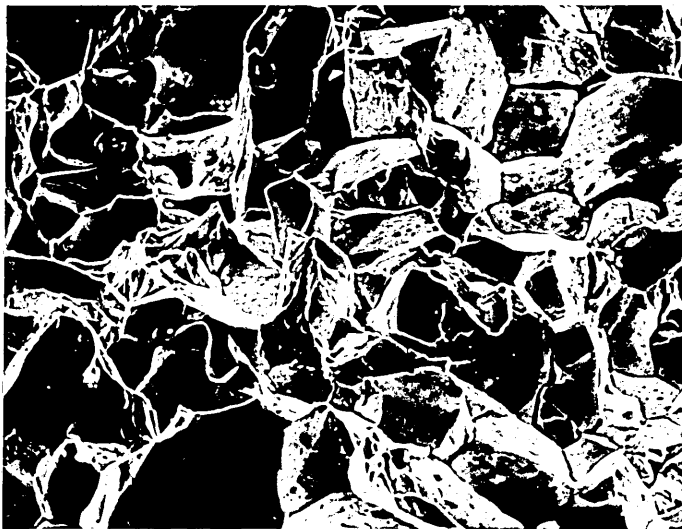
X 260

Fig 88(a). Scanning Electron Micrograph of the fracture surface in alloy I57. Solution treated at 900C for 1/2 hr-A. C. Fracture mode is predominantly intergranular. Impact tested at 20C.



(b). Fracture mode close to V-notch.

X 260



(c). Fracture node in the centre as shown in (a) X 520 but at higher magnification



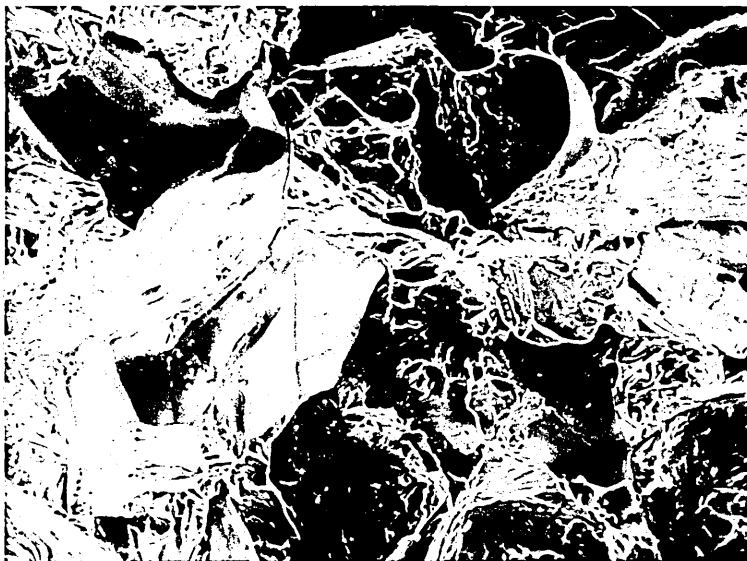
X 240

Fig 89(a). Scanning Electron Micrograph of the fracture surface in alloy I54. Solution treated at 900C for 1/2 hr-IBQ and aged at 450C for 6 mins.-W.Q. Fracture mode is 5-10 percent intergranular. Impact tested at 20C.



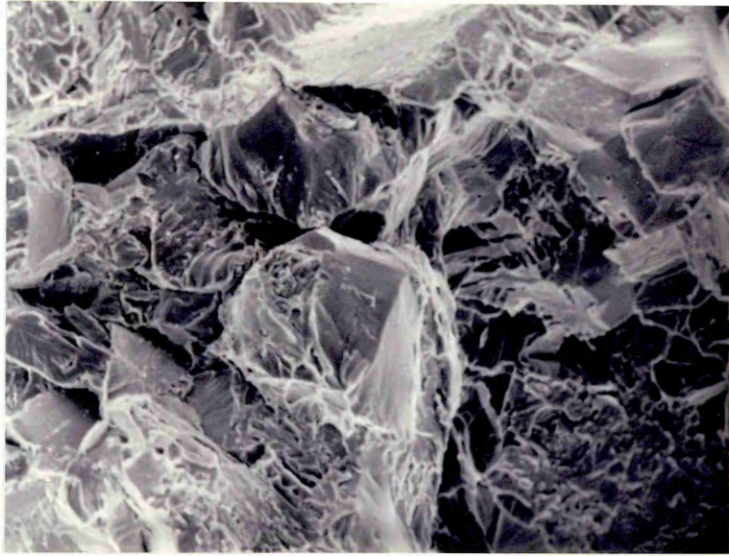
X 520

(b). Same as shown in (a) but at higher magnification



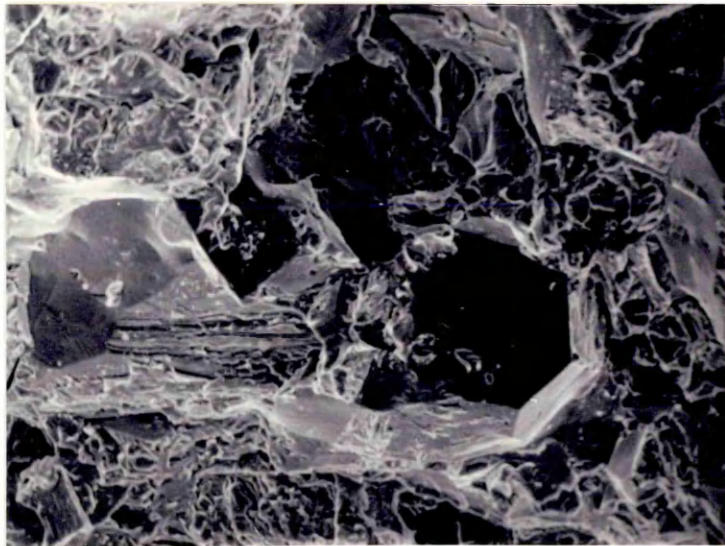
(c). Random area on the fracture surface

X 520



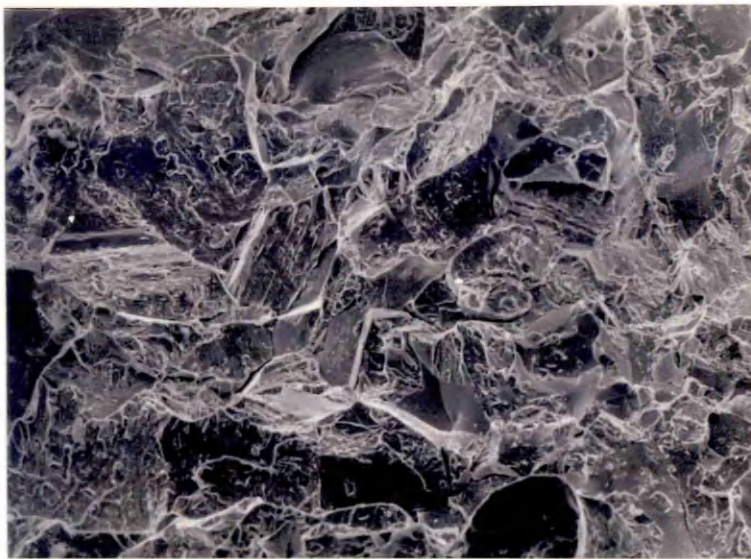
X 520

Fig 90(a). Scanning Electron Micrograph of the fracture surface in alloy I34. Solution treated at 900C for 1/2 hr-IBQ and aged at 450C for 1 hr-W.Q. Fracture mode is approx. 10-15 percent intergranular. Impact tested at 20C.



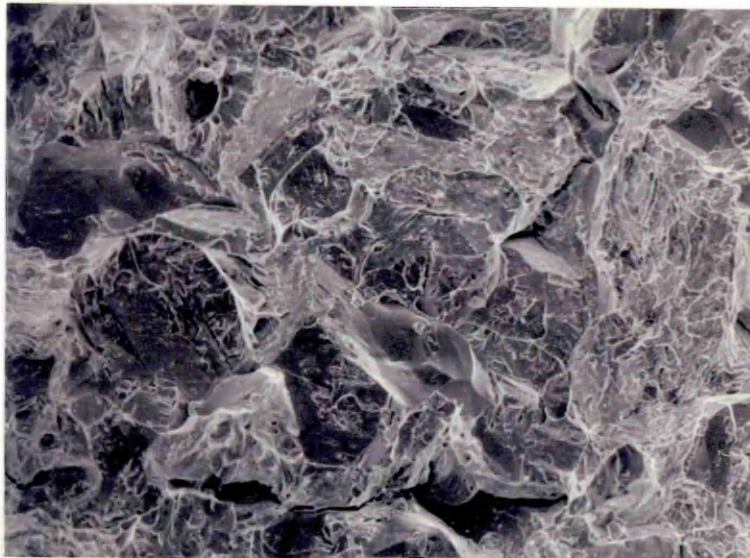
(b). Random area on the fracture surface

X 520



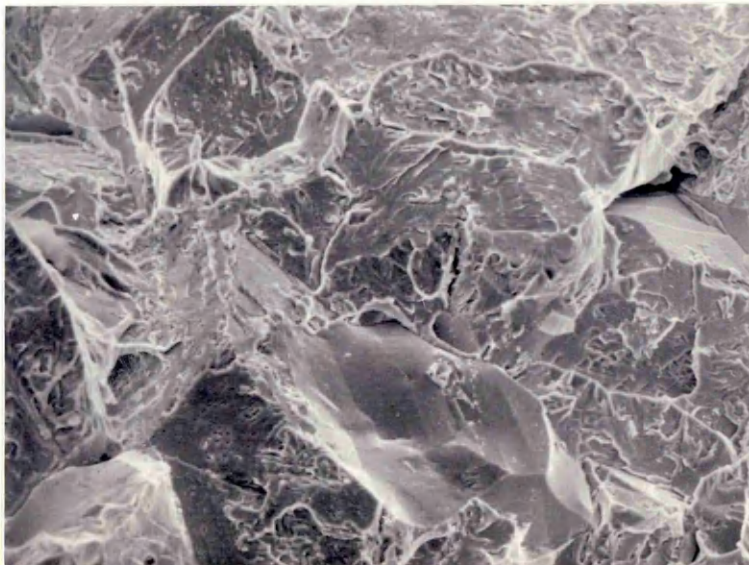
X 240

Fig 9I(a). Scanning Electron Micrograph of the fracture surface in alloy 134. Solution treated at 900C for I/2 hr-IBQ and aged at 450C for 10 hrs-W.Q. Fracture mode is approx. 10-15 percent intergranular. Impact tested at 20C.

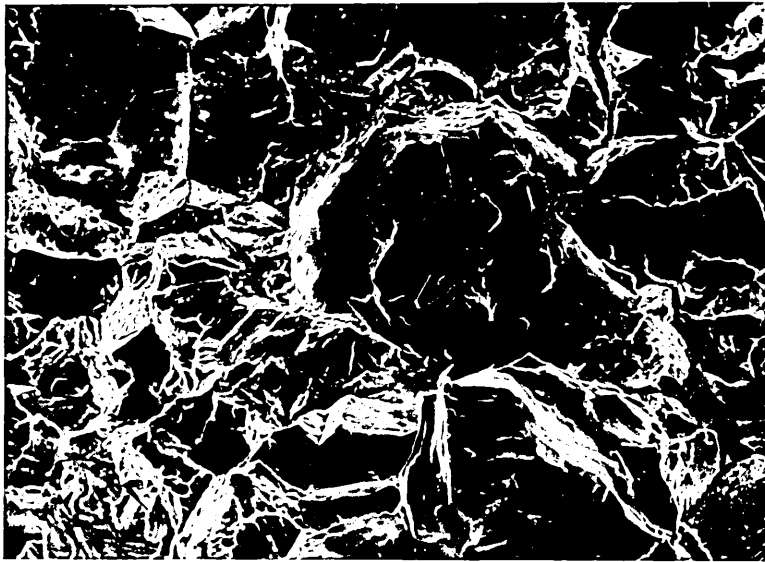


(b). Random area on the fracture surface.

X 240

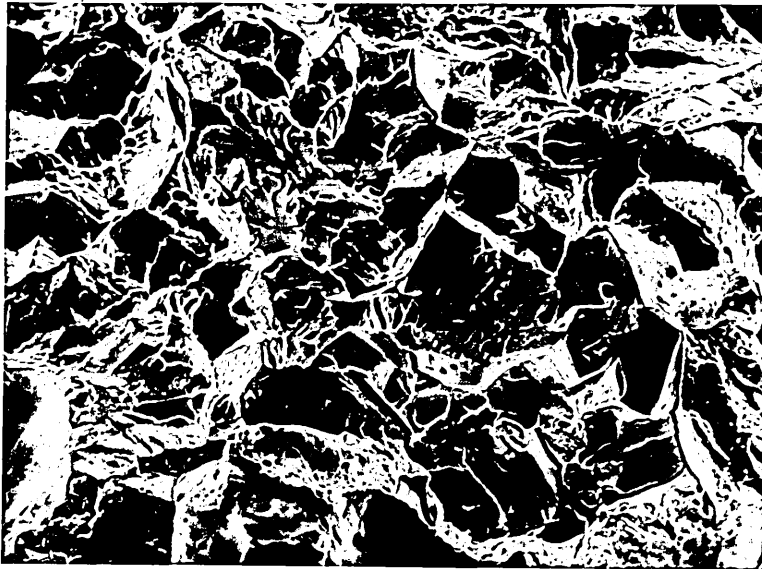


(c). Same as shown in (b) but at higher magnification. X 480



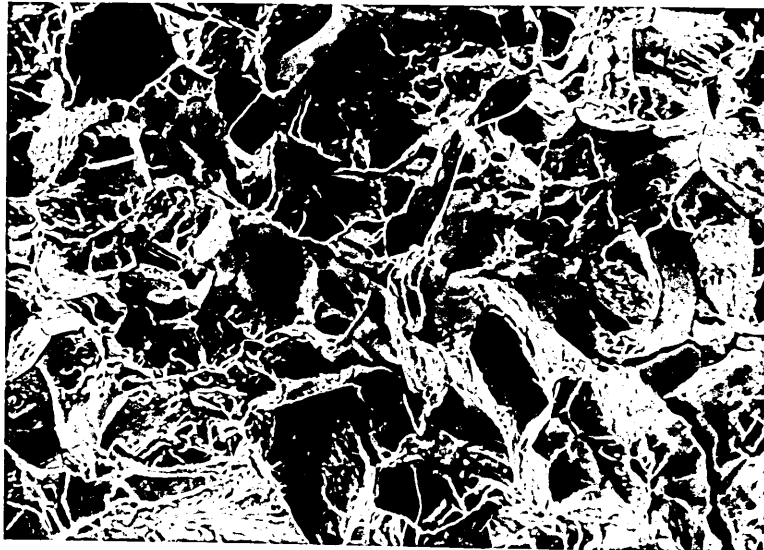
X 480

Fig 92(a). Scanning Electron Micrograph of the fracture surface in alloy I57. Solution treated at 900C for 1/2 hr-IBQ, and aged at 450C for 6 mins. -W.Q. Fracture mode is approx. 50-60 percent intergranular. Impact tested at 20C.



(b). Fracture mode close to V-notch.

X 480



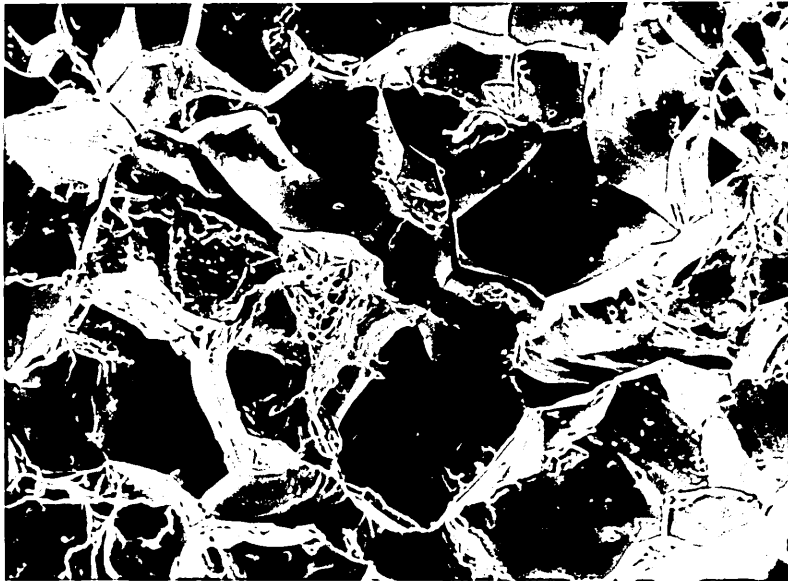
(c). Fracture mode opposite to V-notch.

X 480



X 520

Fig 93(a). Scanning Electron Micrograph of the fracture surface in alloy I37. Solution treated at 900C for 1/2 hr-IBQ and aged at 450C for 1 hr-W.Q. Fracture mode is approx. 80-90 percent intergranular. Impact tested at 20C.



(b). Fracture mode close to V-notch.

X 520



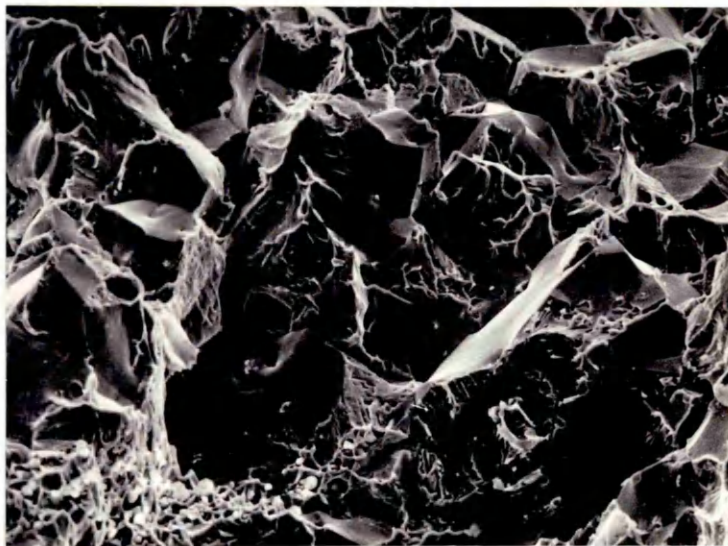
(c). Fracture mode opposite to V-notch.

X 520

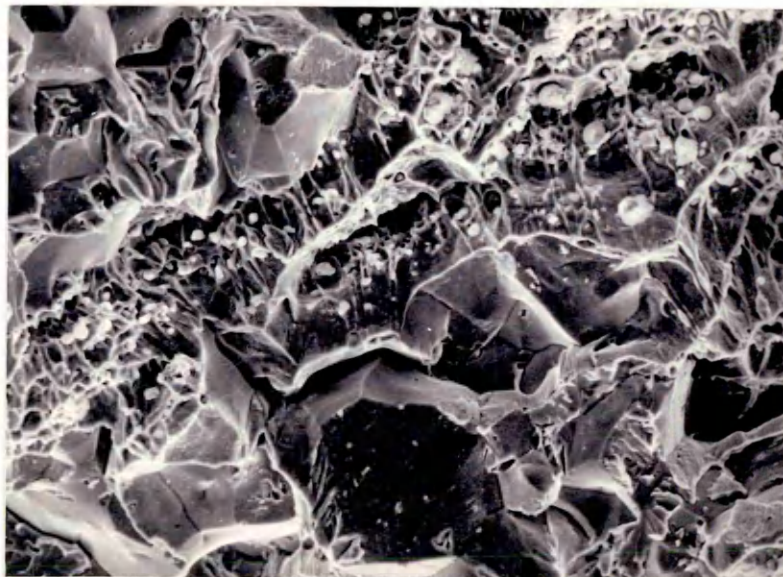


X 520

Fig 94. Scanning Electron Micrograph of the fracture surface in alloy I37. Solution treated at 900°C for 1/2 h-IBQ and aged at 450°C for 10hrs-W.Q. Impact tested at 20°C.



(b) Predominantly Intergranular fracture mode X520



(c) Same as above X520

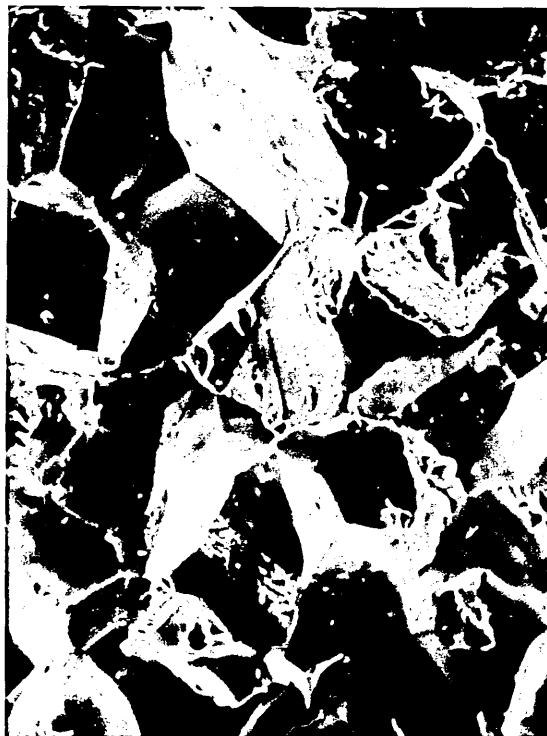
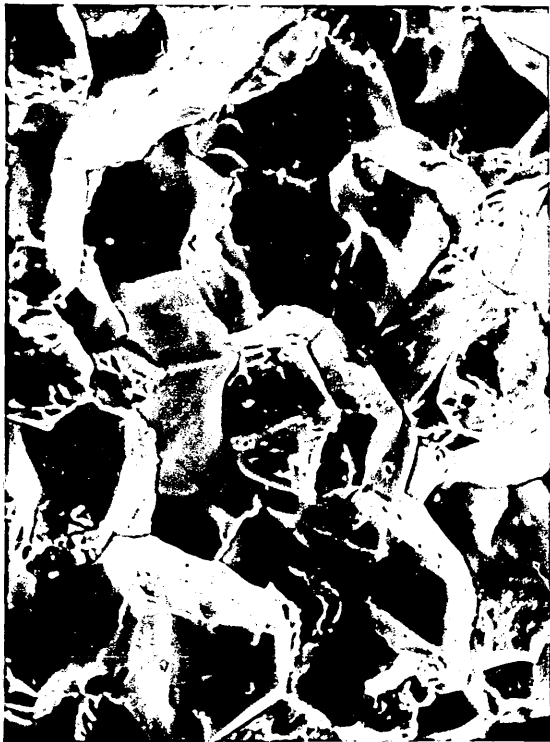


Fig 95. Scanning Electron Micrograph of the fracture surface in alloy KI525. Solution treated at 1000C for 1 hr.-W.Q. and aged at 550C for 10 mins. -W.Q. Hounsefield tensile specimen tested at -78C at a strain rate of 0.5 min. Reduction of area dropped to zero percent with intergranular fracture mode. X 250



Fig 96. Scanning Electron Micrograph of the fracture surface in alloy KI525. Solution treated at 1000C for 1 hr.-W.Q. and aged at 650C for 10 mins. -W.Q. Hounsefield tensile specimen tested at -78C at a strain rate of 0.5 min. Reduction of area dropped to zero percent with intergranular fracture mode. X 250

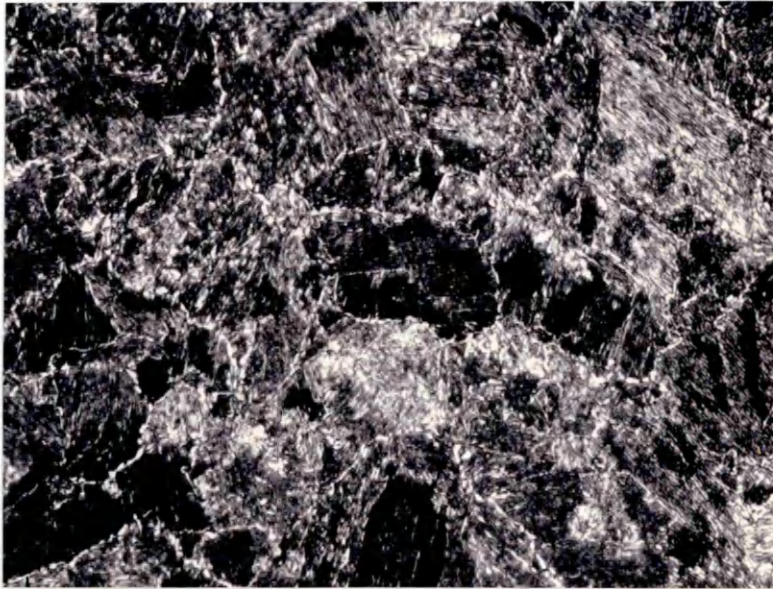


Fig 97(a). Optical Micrograph of alloy KI525. Solution treated at 1000°C for 1 hr-W.Q. Thermally cycled to one complete cycle ( $I_A+I_B$ ). Prior austenite grain size reduced to 2 $\mu$ m as shown by white bead-like nucleation of austenite along the austenite grain boundaries. Lightly etched in 2 pct. Nital followed by immersion in Schumann's Reagent. X 500



(b) Same as above but adjacent region on the metallographic specimen. X 500

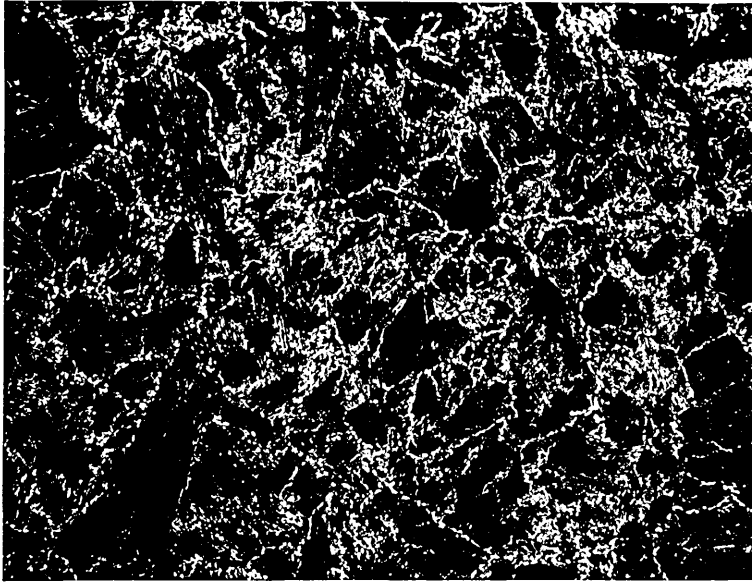
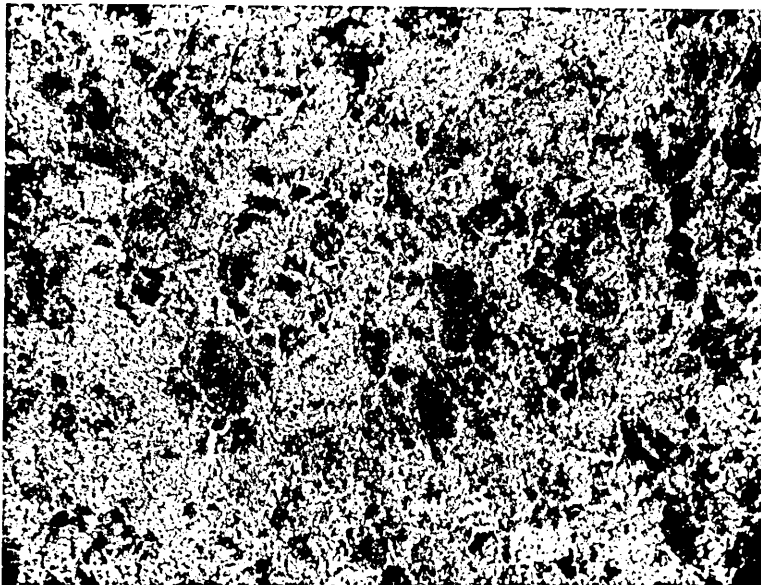


Fig 98(a). Optical Micrograph of alloy KI525. Solution treated at 1000C for 1 hr-W.Q. Thermally cycled to two complete cycles ( $I_A+I_B+II_A+II_B$ ). Prior austenite grain size reduced to 10-15 um as shown by white bead-like nucleation of austenite along the grain boundaries. Lightly etched in 2 pct Nital followed by immersion in Schumanns Reagent. X 500



(b). Same as above but adjacent region on the metallographic specimen. X 500

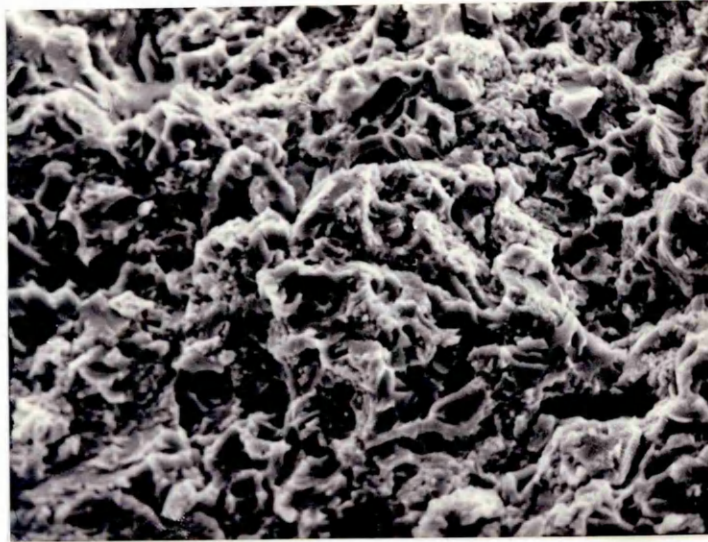
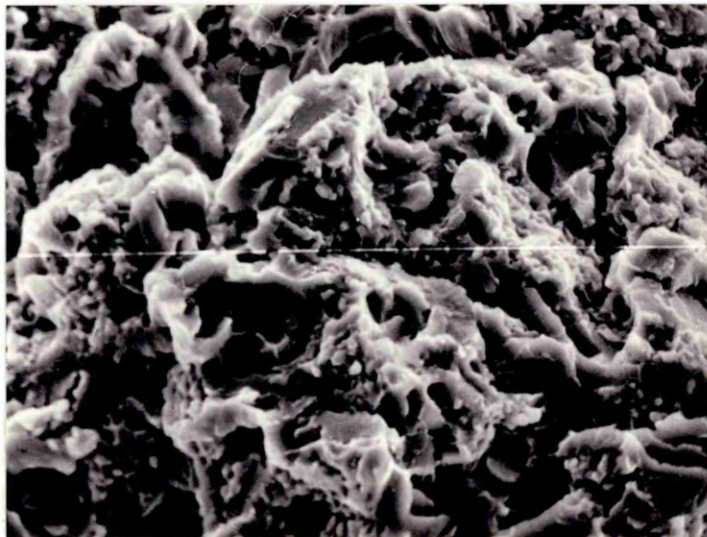


Fig 99(a). Scanning Electron Micrograph of the fracture surface in alloy KI525 after thermal cycling treatment. Impact tested at  $-110^{\circ}\text{C}$  with an impact energy of 7.0 joules. This low energy fracture mode is thought to be ductile+cleavage.  
X 520



(b). Same as above but at higher magnification. X 1040

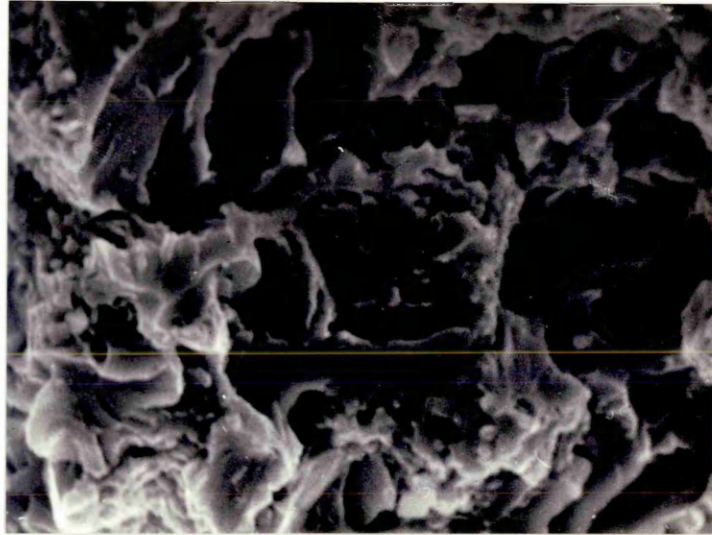
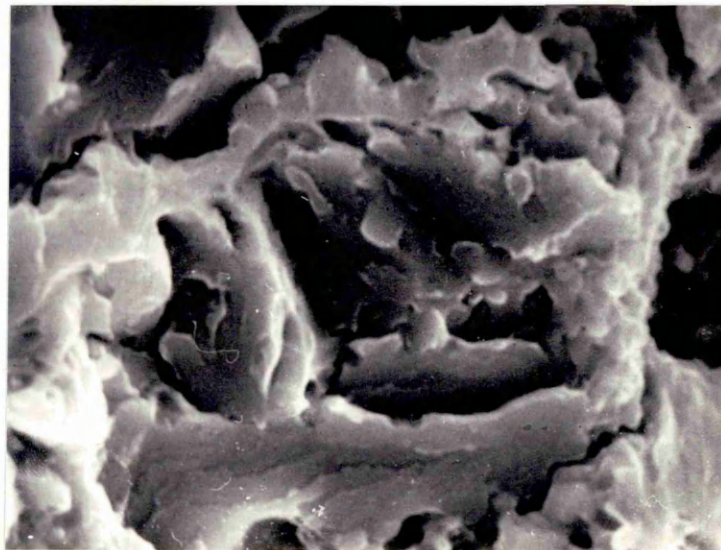
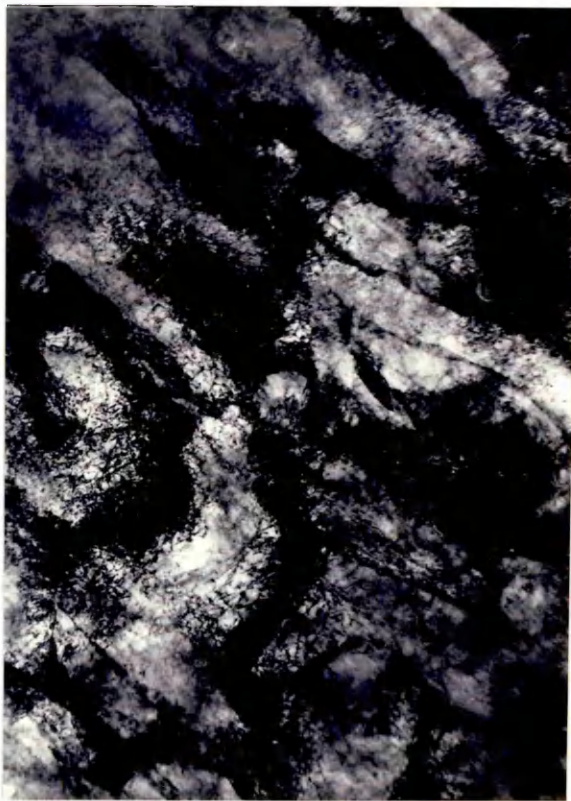


Fig 100(a). Scanning Electron Micrograph of the fracture surface in alloy KI525. Solution treated at 1000C for 1 hr-W.Q. and thermally cycled. Hounsefield tensile specimen tested at -196° at a strain rate of 0.5 min<sup>-1</sup>. Reduction of area dropped to zero percent with a fracture mode having so called flaking effect and resulting in ductile-cleavage type fracture.  
X 640



(b). Same as above but at higher magnification. X 1250



X 28000



X 28000

Fig I01. Transmission Electron Micrograph showing a typical lath-martensitic structure with high dislocation density. Alloy KI525 solution treated 1 hr at 1000C-WQ.

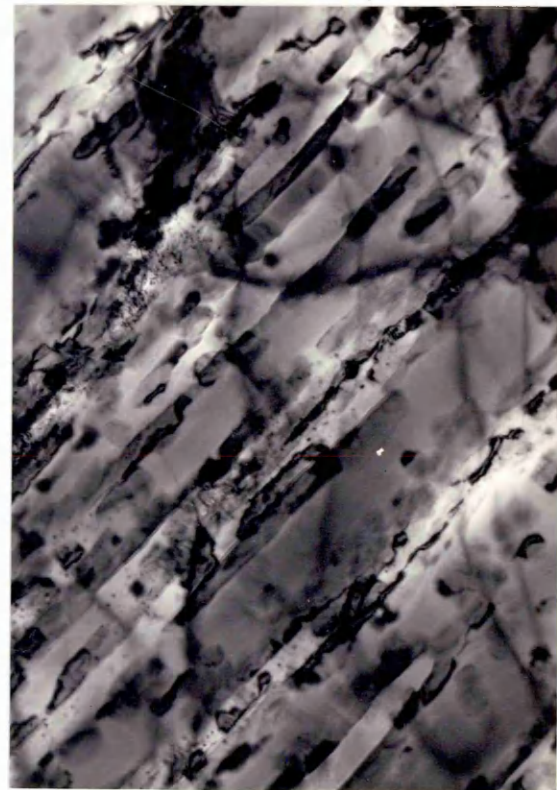
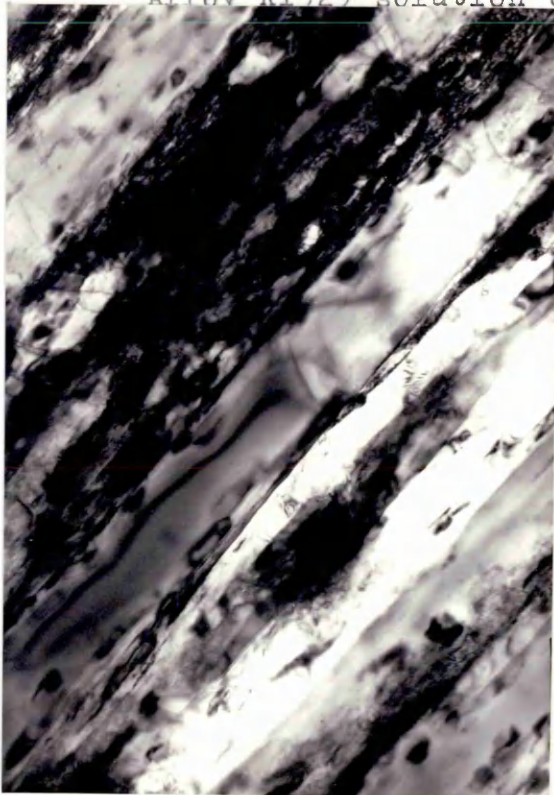
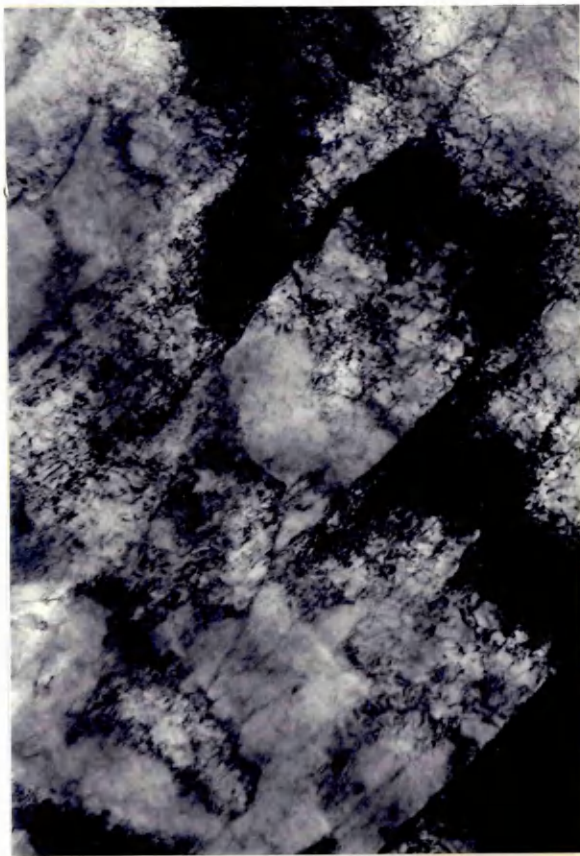
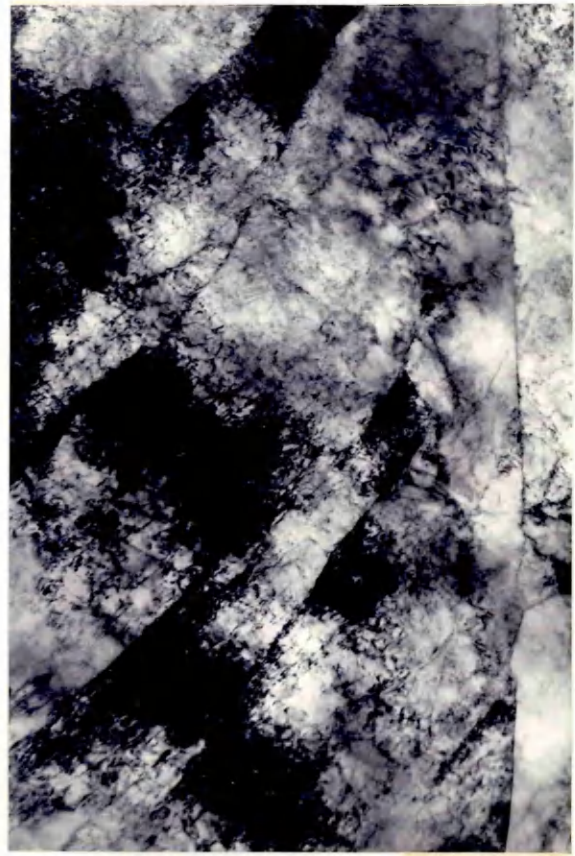


Fig I02. Transmission Electron Micrograph showing interlath precipitation of reverted austenite and epsilon martensite after thermal cycling treatment (I + I<sub>B</sub>) in alloy KI525.

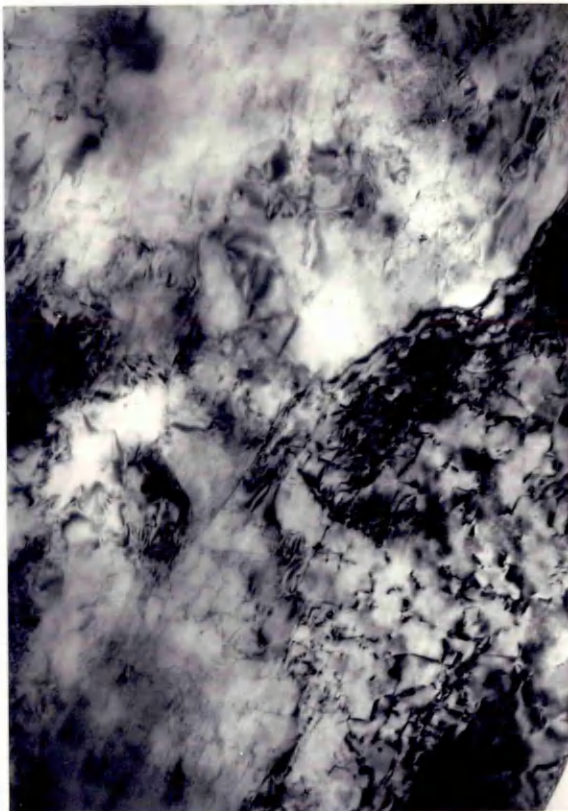
X 70,000



X 49000



X 49000

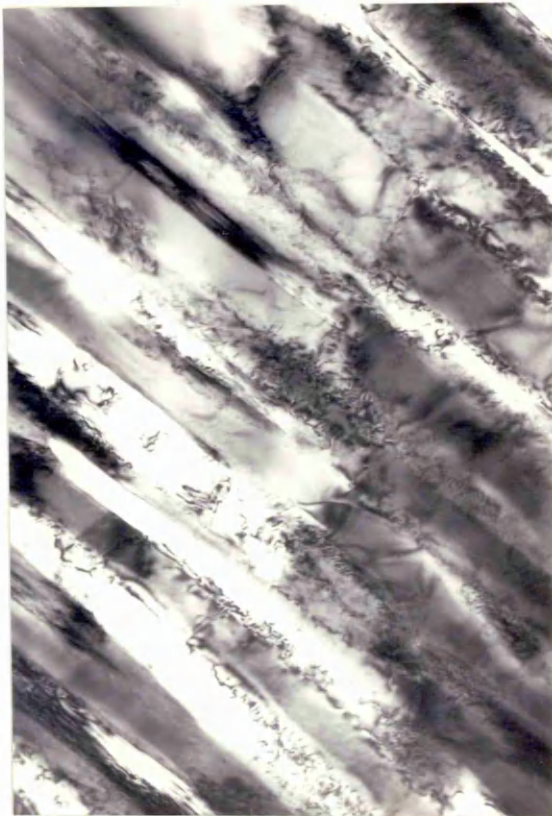


X 70,000



X 35000

Fig 103. Transmission Electron Micrograph showing the generation of tangled dislocations during thermal cycling treatment ( $I_A + I_B + II_A$ ) in alloy KI525.



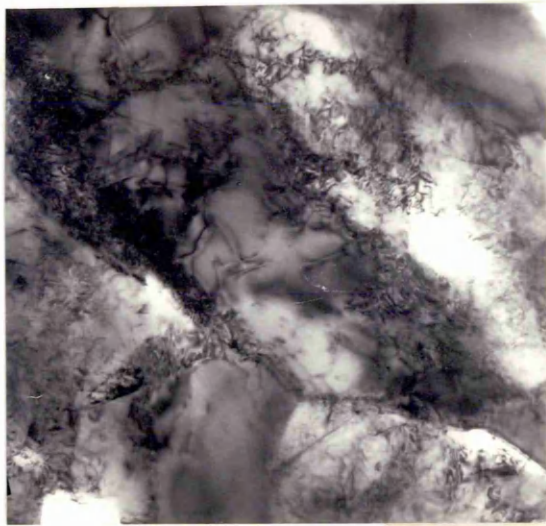
a

X 70,000



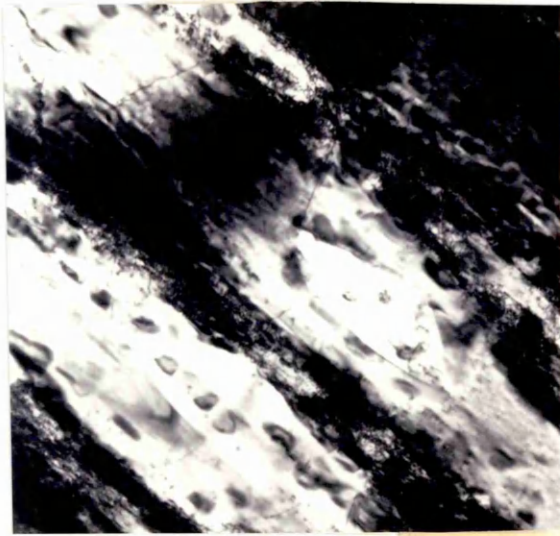
b

X 70,000



c

X 70,000



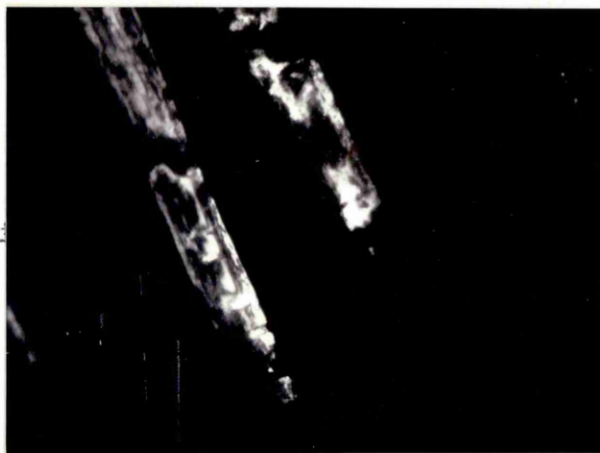
d

X 70,000

Fig I04. Transmission Electron Micrograph showing inter-lath precipitation of reverted austenite and epsilon martensite with some tangled dislocation substructure after thermal cycling treatment (I+I+II+II) in alloy KI525.



Fig I05(a). Bright-field Transmission Electron Micrograph showing the nucleation of  $\epsilon$  band between  $\gamma$  and  $\alpha$  laths. The pointer indicate the formation of  $\epsilon$  band during thermal cycling treatment. in alloy KI525. X 70000

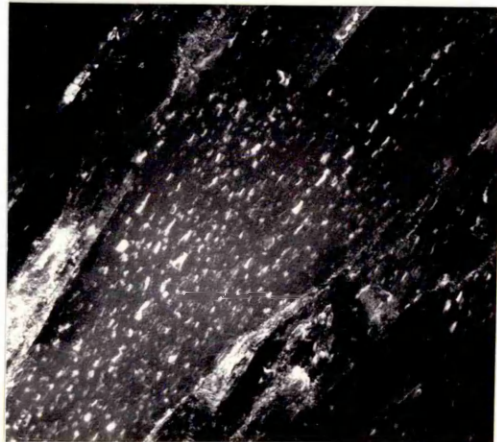


(c) Dark-field image taken from (511) reflection. X 70,000

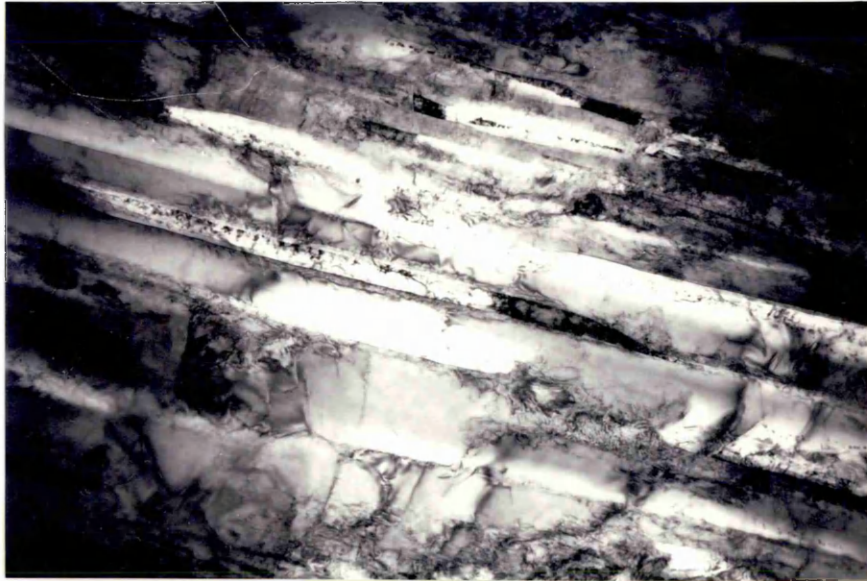
$\gamma$



Fig 106(a). Bright-field Transmission Electron Micrograph showing nucleation of reverted austenite islands within ferrite lath in alloy KI525 after thermal cycling treatment. X 70,000

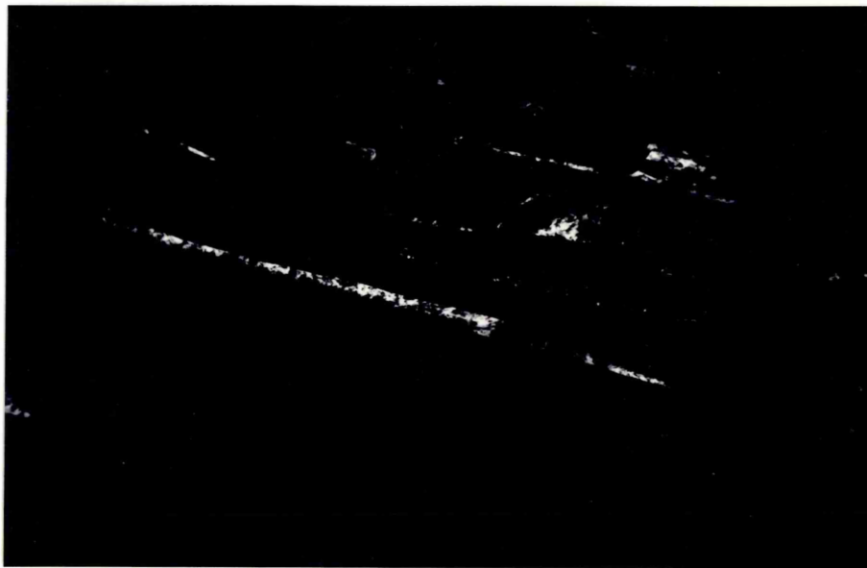


(b). Dark-field image taken from (200) reflection. X 70,000



X 42000

Fig I07(a) Bright-field Transmission Electron Micrograph showing inter-lath nucleation of reverted austenite in alloy KI525 after thermal cycling treatment.



X 42000

Fig I07(b). Dark-field image from (200) austenite reflection.

8

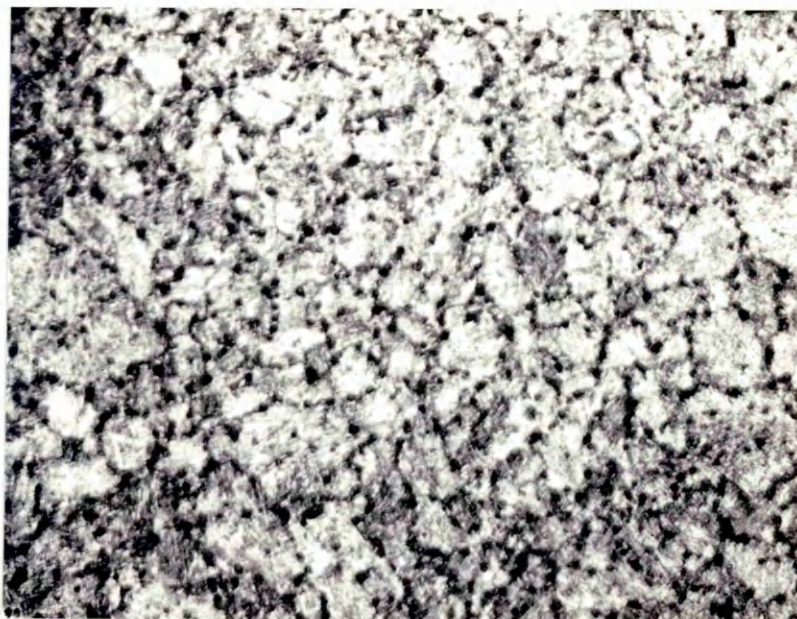
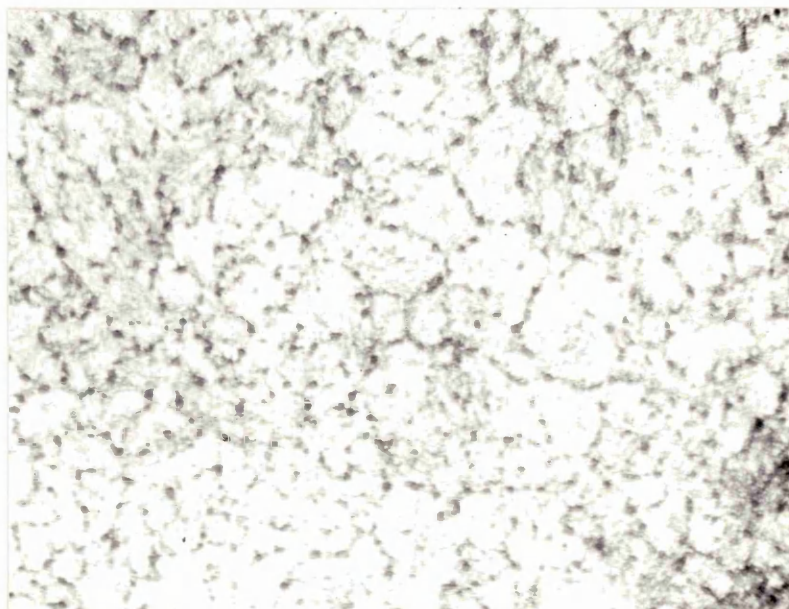


Fig 103a Optical Micrograph of alloy 157. Solution treated at 1000°C for 1 hr-W.Q. and thermally cycled. Prior austenite grain size reduced to 10-15  $\mu$ m as shown by nucleation of reverted austenite and pptn of AlN and Ti(C,N) along the grain boundaries. Etched in 2 percent Nital. X 500



(b). Same as above but adjacent region on the metallographic specimen. X 500

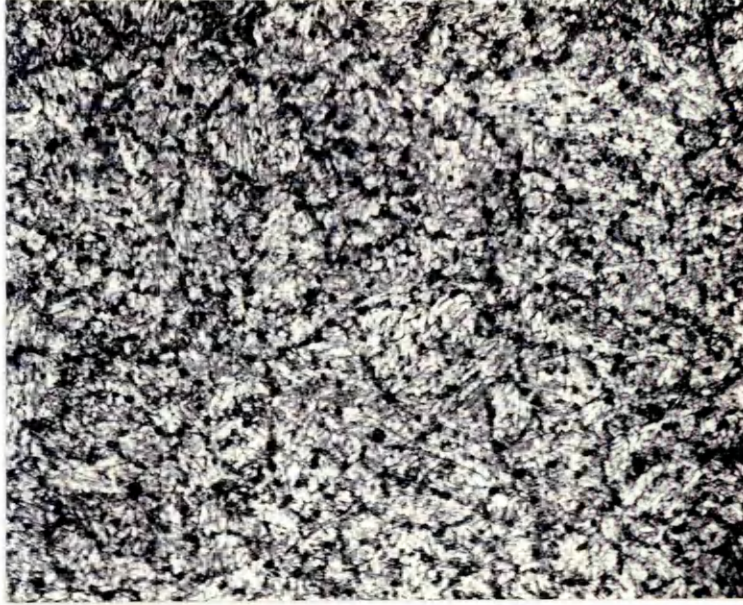
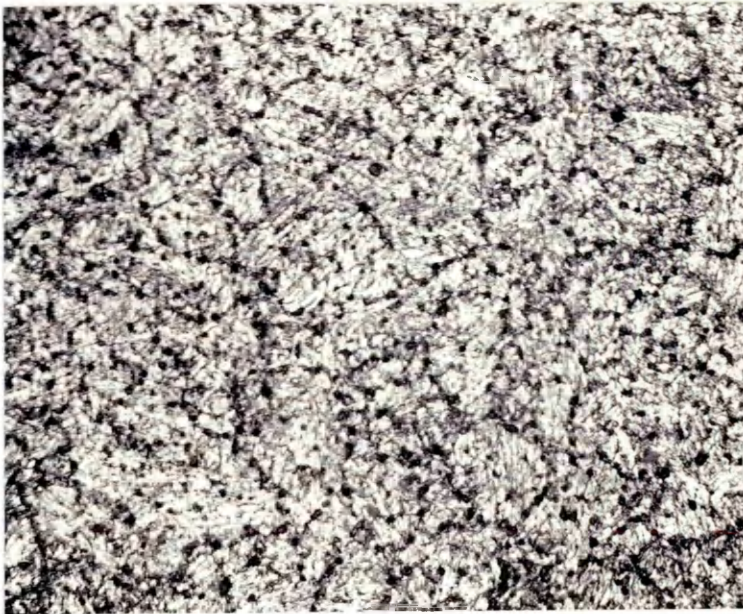
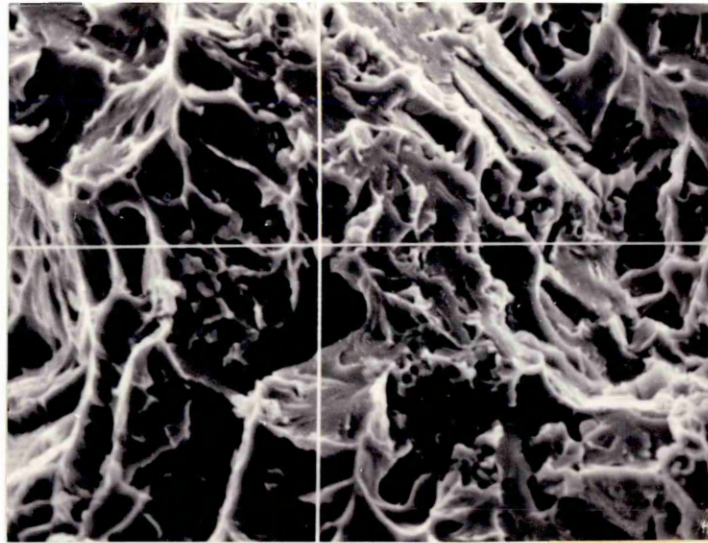


Fig 109(a). Optical Micrograph of alloy I37. Solution treated at 1000C for 1 hr-W.Q. and thermally cycled. Etched in 2 percent Nital followed by immersion in Schumann's Reagent. X 500



(b). Same as above but adjacent region on the metallographic specimen. X 500



X 2000

Fig IIO(a). Scanning Electron Micrograph of the fracture surface of alloy I37 after thermal cycling treatment. Charpy impact tested at  $-78^{\circ}\text{C}$ .

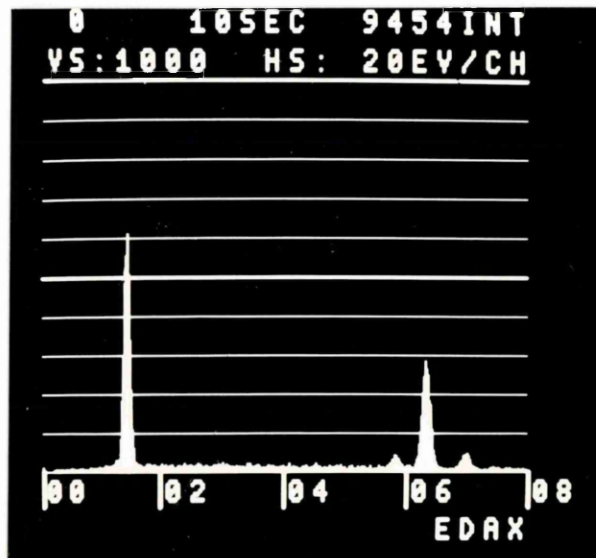
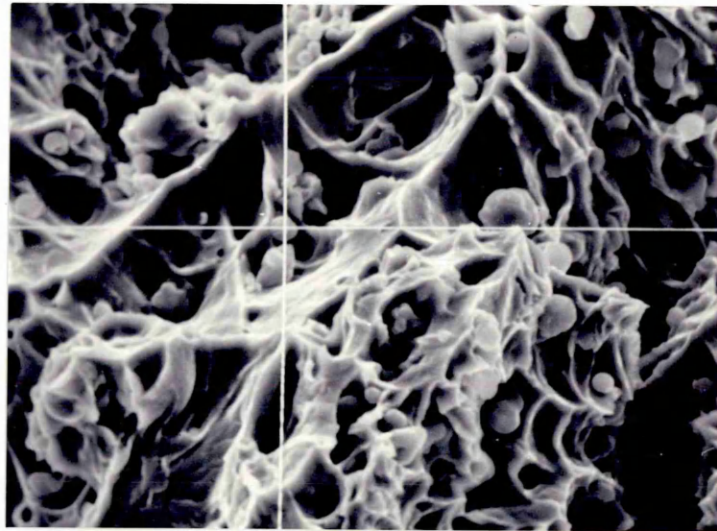


Fig IIO(b) Energy Dispersive X-ray spectra taken from the fracture surface shown above. The Al enriched precipitate is thought to be  $\text{AlN}$ .



X 2000

Fig III(a). Scanning Electron Micrograph of the fracture surface of alloy I37 after thermal cycling treatment. Charpy impact tested at  $-78^{\circ}\text{C}$ .

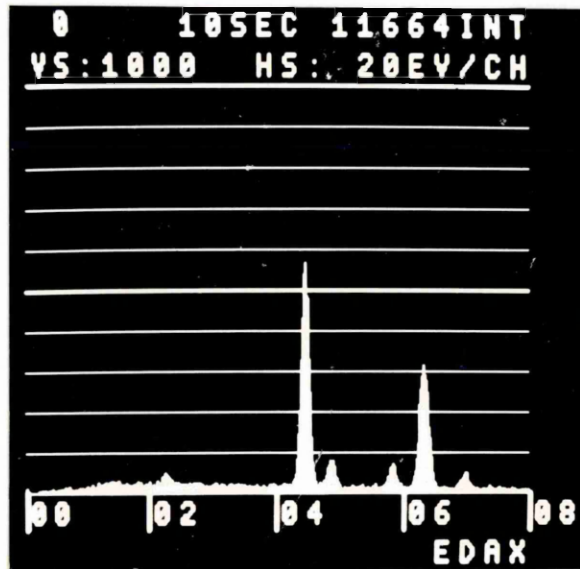
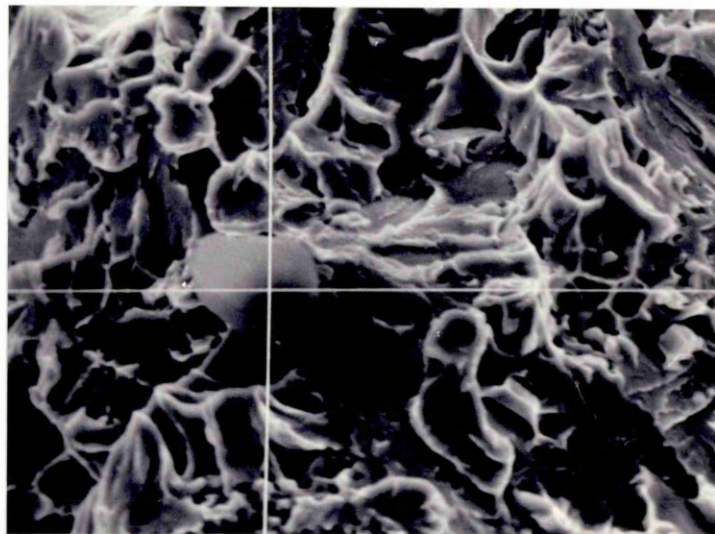


Fig III(b). Energy Dispersive X-ray spectra taken from the fracture surface shown above. The Ti enriched precipitate is thought to be  $\text{Ti}(\text{C},\text{N})$ .



X 2000

Fig II2(a). Scanning Electron Micrograph of the fracture surface of alloy I37 after thermal cycling treatment. Charpy impact tested at  $-78^{\circ}\text{C}$ .

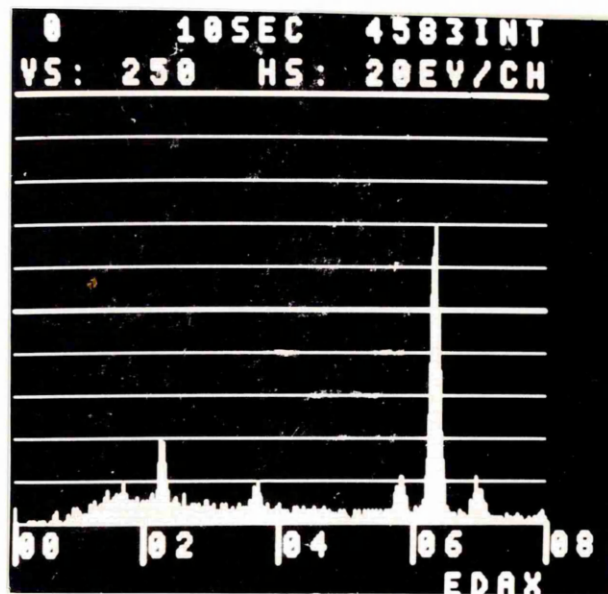


Fig II2(b). Energy Dispersive X-ray spectra taken from the fracture surface shown above. The precipitate is identified as  $\text{MnS}$ .

THE NATURE OF INTERGRANULAR EMBRITTLEMENT IN QUENCHED Fe-Mn ALLOYSB.C. Edwards\*, M. Nasim<sup>†</sup> and E.A. Wilson<sup>†</sup>

\*Metallurgy Division, Atomic Energy Research Establishment, Harwell, Oxon, U.K.

<sup>†</sup>Department of Metallurgy, Sheffield City Polytechnic, Pond Street, Sheffield, U.K.

(Received February 2, 1978)

An economically attractive alternative to the Ni maraging steels is an analogous system based on Fe-Mn. The Fe-Mn and Fe-Ni systems exhibit similar austenite-ferrite transformation products and similar tensile properties are obtained but with the Mn producing a greater solid solution strengthening (1) (similar properties are obtained with 8% Mn as with 18% Ni). In contrast, the Fe-Mn systems have been shown to exhibit poor impact properties characterized by a low temperature intergranular fracture mode (1-4). The embrittlement behaviour is analogous to that of temper embrittled steels, with the fracture propagating along the prior austenite grain boundaries and is enhanced on tempering within the temperature range 400-500°C (1). Transmission electron microscope studies have failed to identify any second phase particles responsible for the embrittlement.

In this paper we wish to report the results of an investigation into the nature of the embrittlement produced on quenching from the austenite field. Two low carbon Fe 8% Mn alloys of differing nitrogen contents were studied; details of the compositions and heat treatments are presented in Tables 1 and 2 respectively. The mechanical impact properties were determined using sub-standard Charpy test pieces. Intergranular embrittlement was characterized using Auger Electron Spectroscopy (AES) to analyse the chemical composition of the intergranular facets produced by in situ impact fracture (5) in the Auger Spectrometer. AES analysis was performed using a CMA analyser with an integral electron gun providing a spot size of 20  $\mu\text{m}$ . The differential energy spectra were recorded at a modulation of 3V peak to peak, a primary energy of 2.5 keV and a specimen current of 4  $\mu\text{A}$ .

A lath martensitic structure was produced by the heat treatments which was essentially free of  $\epsilon$  martensite or retained austenite (<2%). The low nitrogen containing alloy, K1525, exhibited a high ductile-brittle transition temperature (DBTT), 115°C, and an intergranular fracture mode in the lower shelf region of the transition curve (Fig 1). Similar AES analyses were obtained from different intergranular facets of a given impact sample and the intergranular fracture was shown to be primarily associated with the grain boundary segregation of N and P, with no concomitant segregation of Mn. However, on a few samples enhanced N and Mn concentrations were detected with no associated P segregation. These anomalous observations are interpreted as due to a site competition process between P and N in the  $\gamma$  field produced during a slower cooling rate experienced by the AES impact sample. The embrittlement produced on subsequent isothermal ageing at 450°C has been shown (6) to be produced by the grain boundary segregation of Mn and P and therefore site competition between Mn and P in the  $\alpha$  field is considered unlikely.

The impact properties of the high nitrogen containing alloy, A134, were sensitively dependent upon the cooling rate from the austenitization temperature (Fig 1). Brine quenching produced a low DBTT (35°C) and a cleavage brittle fracture mode, consistent with the observations of Roberts (7), whereas in contrast, air cooling produced a dramatic increase in the DBTT (385°C) a decrease in the upper shelf energy and a change in the low temperature fracture mode to intergranular. Auger analysis of the intergranular fracture surface (Fig 3) showed enhanced concentrations of N and Mn but no P segregation was detected. Ion profiling showed that the segregation was confined to the first few monolayers of the fracture surface.

TABLE 1  
Alloy Composition

Alloy	wt% Mn	ppm												
		C	N	Ti	Cr	Mo	Si	S	Ni	Al	P	Sn	Sb	As
K1525	8.10	40	30	-	20	-	115	100	27	-	60	50	10	27
A 134	7.93	100	300	<10	130	130	300	50	70	50	20	50	<10	<100

TABLE 2  
Heat Treatment Schedule

Alloy	Heat Treatment	Grain Size ( $\mu\text{m}$ )	Hv (V.H.N)	DBTT ( $^{\circ}\text{C}$ )	Low Temperature Fracture Mode
K1525 WQ	1h 1000 $^{\circ}\text{C}$ $\rightarrow$ Water Quench	85	250 $\pm$ 10	115	Intergranular
A 134 IBQ	$\frac{1}{2}$ h 900 $^{\circ}\text{C}$ $\rightarrow$ Ice Brine Quench	60	289 $\pm$ 10	35	Cleavage
A 134 AC	$\frac{1}{2}$ h 900 $^{\circ}\text{C}$ $\rightarrow$ Air Cool	60	298 $\pm$ 10	385	Intergranular

TABLE 3  
Summary of AES Results

Alloy	% of Fe(703eV) Peak Height			at%		Grain Boundary Mn
	Mn	N	P	N	P	Bulk Mn
K1525 WQ (i)	4.6	2.9	.2	1.8	.1	1.0
K1525 WQ (ii)	6.6	3.5	-	2.2	-	1.4
A 134 AC	9.1	13.6	-	8.5	-	1.9

The results of the AES analysis are summarized in Table 3, with the N and P concentrations quantified using the procedure described previously (8). The grain boundary enrichment of Mn was indexed by normalizing with respect to the Mn signal obtained from the cleavage fracture, which was equated to that of the bulk. The above embrittlement/segregation behaviour is considered to comprise two distinct types of segregation which are reflected in the degree of grain boundary enrichment of Mn.

(i) Segregation in the  $\gamma$  field

The intergranular brittleness of the low nitrogen containing alloy (K1525) was shown to be due to the grain boundary segregation of N and P, in the  $\gamma$  field, with no concomitant Mn enrichment.

The observation of P segregation in the  $\gamma$  field is consistent with previous work (9-12) and Inoue (11) has shown that the level of segregated P was not significantly influenced by the austenitization temperature. The N segregation in the  $\gamma$  field is also consistent with earlier work (8) but in conflict with the observations of Inoue (11) who reported no influence of N after low austenitizing treatments (930 $^{\circ}\text{C}$ ) in an Fe 1.5% Mn .24% Si alloy; however these obser-

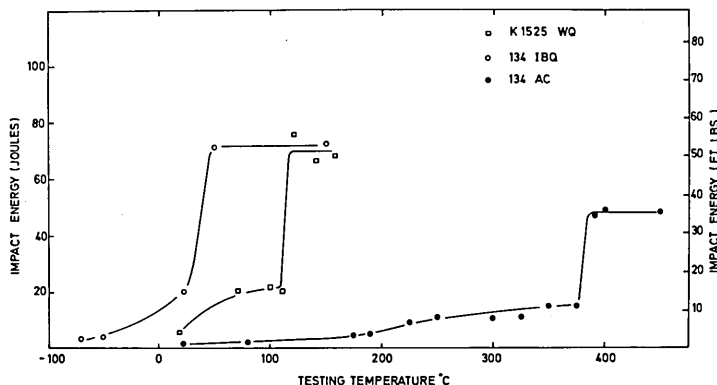


FIG. 1

Impact transition curves obtained using half size Charpy V notched samples of (□) Alloy K1525 - Water quenched; (○) Alloy A134 - ice brine quenched; (●) Alloy A134 - air cooled.

variations may be reconciled by a strong Si-N interaction in the latter alloy. The absence of Mn segregation in the  $\gamma$  field is consistent with the observations of Krahe and Guttmann (13) on an Fe 2% Mn alloy. Cleavage fracture was produced on brine quenching the high nitrogen containing alloy (A134), indicating a lower bulk concentration of P and the limited embrittlement potency of N.

#### (ii) Segregation in the $(\alpha+\gamma)$ field

Embrittlement was markedly enhanced on air cooling alloy A134 from the  $\gamma$  field and was shown to be associated with the grain boundary segregation of Mn and N (with no P detected). On air cooling, the alloy will be in a metastable austenitic condition down to the  $M_s \approx 360^\circ\text{C}$ , and it is postulated that N and Mn segregate to the grain boundaries whilst in this metastable field. Two possible driving forces, or a combination of both, need to be considered: (a) the grain boundary segregation of N which induces Mn segregation due to the strong chemical interaction of Mn-N thus lowering the chemical potential of the system (14). Evidence of this interaction is provided by the work of Fuller and Garwood (15) who reported a strong secondary hardening peak at  $450^\circ\text{C}$  on tempering a Fe-Mn-N martensite; (b) the equilibrium segregation of Mn at the prior austenite grain boundaries in the  $(\alpha+\gamma)$  phase field. However, the bulk reaction  $\gamma$  (metastable)  $\rightarrow (\alpha+\gamma)$  (equilibrium) is extremely slow in the Fe-Mn system (16).

In conclusion, embrittlement in "quenched" Fe 8% Mn alloys has been shown to be due to the grain boundary segregation of N, P and Mn. In rapidly quenched materials embrittlement is due to N and P segregation in the  $\gamma$  field, whereas in slowly cooled air quenched material the embrittlement is enhanced due to segregation of N and Mn in the metastable  $(\alpha+\gamma)$  regime.

#### REFERENCES

1. J.D. Bolton, E.R. Petty and G.B. Allen, *Met. Trans.*, **2** 2915 (1971)
2. W.P. Rees, B.E. Hopkins and H.R. Tipler, *J.I.S.I.*, **169** 157 (1951)
3. W.P. Rees, B.E. Hopkins and H.R. Tipler, *J.I.S.I.*, **177** 93 (1954)
4. B. Freeman, Ph. D. Thesis, University of Cambridge, 1973
5. J.P. Coad, J.C. Pivi re, M. Guttmann and P.R. Krahe, *Acta Met.*, **25** 161 (1977)
6. B.C. Edwards and H.E. Bishop, A.E.R.E. Report No. R 8516, September 1976
7. M.J. Roberts, *Met. Trans.*, **1** 3287 (1970)
8. B.C. Edwards, H.E. Bishop, J.C. Pivi re and B.L. Eyre, *Acta Met.*, **24** 957 (1976)
9. T. Inoue, K. Yamamoto and S. Sekiguchi, *Trans. I.S.I.J.*, **14** 373 (1974)
10. B.J. Schultz and C.J. McMahon Jr. *ASTM STP* 499, p. 104 (1972)
11. T. Inoue, Proceedings of 4th Bolton Landing Conference (1974) p. 533.
12. R.A. Mulford, C.J. McMahon Jr., D.P. Pope and H.C. Feng, *Met Trans* **7A** 1183 (1976)
13. P.R. Krahe and M. Guttmann, *Scripta Met.*, **7** 387 (1973)
14. M. Guttmann, *Metal Sci.*, **10** 337 (1976)
15. B.A. Fuller and R.D. Garwood, *J.I.S.I.*, **210** 206 (1972)
16. A.R. Troiano and F.T. McGuire, *Trans ASM*, **31** 340 (1943)

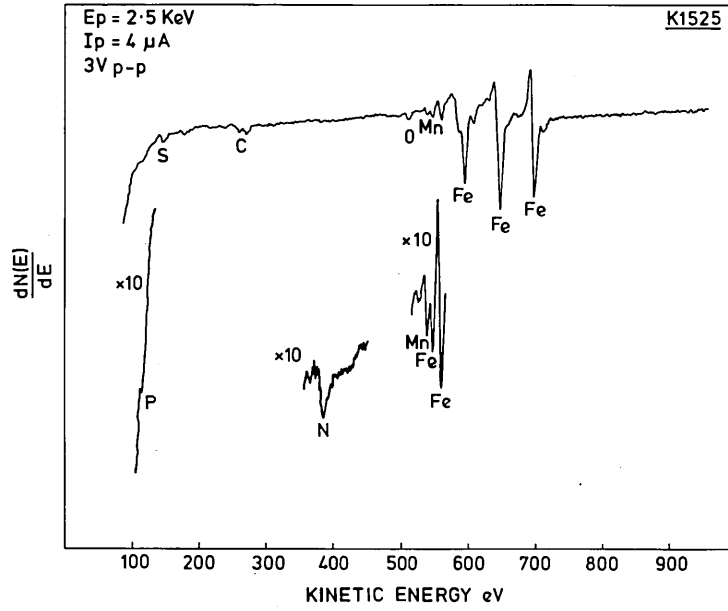


FIG. 2  
AES spectra of Alloy K1525 - water quenched

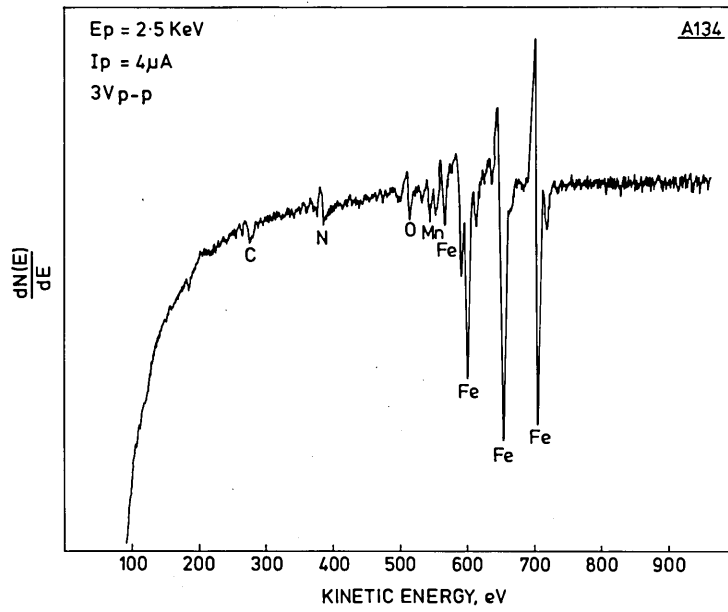


FIG. 3  
AES spectra of Alloy A134 - air cooled

## THE EFFECT OF THERMAL CYCLING ON THE IMPACT TOUGHNESS OF AN Fe-8.0Mn ALLOY

M Nasim and E A Wilson

Department of Metallurgy, Sheffield City Polytechnic, Sheffield, UK

A thermal cycling treatment is described which lowers the impact transition temperature from +115°C to -60°C in an Fe-8.0Mn alloy. Apart from grain refinement, evidence is presented to show that deformation-induced transformation also occurs on tensile testing to improve toughness.

INTRODUCTION

Lath martensite forms the basic microstructure of 9%Ni cryogenic steels and 18%Ni maraging steels (1). The same microstructure is obtained in Fe-8.0%Mn alloys at all cooling rates (2) and therefore may form a cheaper base for alternative steels. However, the Fe-8.0%Mn alloys suffer from grain boundary embrittlement(3). Auger spectroscopy has shown recently that the embrittlement is due to segregation of Mn and N to prior austenite grain boundaries (4). This paper reports the results of attempts to improve the impact toughness of the material studied in (4) by thermal cycling treatments (5-9).

EXPERIMENTAL PROCEDURE AND RESULTS

The composition of the alloy studied is given in table 1.

TABLE 1 Composition of alloy K1525

Mass	ppm												
% Mn	Ti	Cr	Mo	C	N	Si	S	Ni	Al	P	Sn	Sb	As
8.10	-	20	-	40	30	115	100	27	-	60	50	10	27

Transformation points determined by dilatometry at heating and cooling rates of 50°C/min are given in table 2.

TABLE 2 Transformation Temperatures of alloy K1525

$M_s = 360 \pm 5^\circ\text{C}$	$M_f = 336 \pm 5^\circ\text{C}$	$A_s = 677 \pm 5^\circ\text{C}$	$A_f = 723 \pm 5^\circ\text{C}$
---------------------------------	---------------------------------	---------------------------------	---------------------------------

From these transformation temperatures the thermal cycling treatment shown in figure 1 was devised. The holding temperatures and times were selected on the basis that the austenitising temperature should be low enough to minimise grain growth, while the temperature of holding in the ( $\alpha + \gamma$ ) phase region should be high enough to maximise the extent of diffusional transformation to low manganese ferrite and high manganese austenite (reverted austenite).

After two complete cycles, the austenite grain size was reduced from 80-90 $\mu\text{m}$  to 10-15 $\mu\text{m}$ . The impact transition temperature determined from sub-standard Charpy V-notched specimens of 5 x 10 mm section, was reduced from +115°C to -60°C. figure 2.

During holding in the two-phase ( $\alpha + \gamma$ ) region, reverted austenite forms which may subsequently transform to  $\alpha$  lath martensite and/or  $\epsilon$  martensite on cooling, depending on the composition of the reverted austenite formed in the two-phase region. The proportion of phases in the alloy after heat treatment were determined by X-ray diffraction (10)(11) using line intensity measurements from 4 peak combinations. The average values are given in table 3 and are thought to be accurate to better than  $\pm 1\%$ .

TABLE 3 Phase analysis of alloy after heat treatment

Phases	Heat Treatment					
	1h 1,000°C water quench (a)	(a) + 1A (b)	(b) + 1B (c)	(c) + 2A (d)	(d) + 2B (e)	(e) + 15 mins at -196°C
$\gamma$	) <2%	) <2%	5.8%	4.1%	8.0%	6.0%
$\epsilon$	)	)	28.0%	4.0%	24.6%	26.8%
$\alpha$	>98%	>98%	66.2%	91.9%	67.4%	67.2%

It is evident from figure 4 that the reverted austenite forms mainly at the prior austenite grain boundaries and to a lesser extent at the inter-lath boundaries, as shown in the dark field electronmicrograph figure 7.

After thermal cycling, the nature of the brittle fracture changed from intergranular to that shown in figure 5; where fracture was mainly by cleavage with ductile regions apparently corresponding to the grain boundary regions which originally consisted of reverted austenite.

Previous work (12) has shown that alloy K1525 in the initial heat treated condition (ie (a)) rapidly embrittles on ageing at 450°C. On tensile testing at -78°C at a strain rate of 0.5 min<sup>-1</sup>, the reduction of area value dropped to zero after 5 minutes ageing at 450°C. The thermally cycled material was therefore subjected to the same tensile test after ageing at 450°C to see if embrittlement could be induced in these specimens. The results are shown in figure 3 and the corresponding X-ray phase analysis in table 4.

TABLE 4 Phase analysis after ageing thermally cycled material (1A + 1B + 2A + 2B) at 450°C

Phases	Thermally Cycled (Th.Cy.)	Th.Cy + 10 mins 450°C WQ	Th.Cy + 1h 450°C WQ	Th.Cy + 2h 450°C WQ	Th.Cy + 2h 450°C WQ + 15 mins -78°C
$\gamma$	8.0	12.5	9.5	10.6	6.0
$\epsilon$	24.7	11.8	14.5	8.8	9.5
$\alpha$	67.3	75.7	76.0	80.6	84.5

The peculiar stress/strain curves obtained are thought to arise from deformation induced transformation of  $\gamma \rightarrow \epsilon$  martensite and/or  $\alpha$  martensite or  $\epsilon \rightarrow \alpha$ . Such phenomenon has been observed in TRIP steels (13) and increases the toughness of the steel.

DISCUSSION

Holden et al (2) and more recently M J Schanfein et al (14) have reported on the excellent impact toughness of Fe-Mn alloys containing ( $\gamma + \epsilon$ ) phases. Clearly the improved impact toughness of the present alloy can also be attributed to the introduction of these ductile phases into the microstructure as well as to grain refinement. M J Schanfein et al (14) report that the DBTT is lowered by 1.3°C per volume % ( $\gamma + \epsilon$ ). Applying this figure to the present results suggests that of the total shift of 175°C in DBTT,  $\sim 45^\circ\text{C}$  is due to the presence of ( $\gamma + \epsilon$ ) phases and  $\sim 130^\circ\text{C}$  due to grain refinement. This latter figure, (130°C), would appear to be rather large for grain refinement alone (15) and indicates a synergistic interaction between grain refinement and the presence of ( $\gamma + \epsilon$ ) phases. (From figures 2 and 7 of Roberts' work (15) the reduction in prior austenite grain size from 80-90 $\mu\text{m}$  to 10-15 $\mu\text{m}$  in the present alloy, corresponds to a shift in DBTT  $\sim 50^\circ\text{C}$ .)

The exact role of the ( $\gamma+\epsilon$ ) phases in reducing embrittlement is not clear. It has been suggested (16) that:-

- (a) Austenite may act as a sink for impurities, in this case N, reducing embrittlement during heat treatment (17)
- (b) The ductile phases ( $\gamma+\epsilon$ ) may act as crack arresters blunting the propagation of brittle cracks (18-21)
- (c) Transformation of austenite to  $\alpha$ -martensite and/or  $\epsilon$ -martensite may occur during impact testing improving toughness (22,23,24). Evidence for this is provided by figure 3.

Present work on this and other alloys is aimed at establishing the relative importance of such parameters.

#### ACKNOWLEDGEMENTS

The alloy K1525 used in this investigation was kindly manufactured and fabricated by British Steel Corporation, Corporate Laboratories (formerly BISRA). It is a pleasure to acknowledge very useful comments and discussion with Dr D Dulieu of BSC, Swinden Laboratories, Rotherham.

#### REFERENCES

1. Owen W S , Wilson E A and Bell T, 1965 "High Strength Materials", John Wiley & Sons, New York and London, p 167.
2. Holden A, Bolton J D and Petty E R, 1971, JISI 209, 721.
3. Bolton J D, Petty E R and Allen G B, 1971, Met Trans 2, 2915.
4. Edwards B C, Nasim M, and Wilson E A, 1978, Scripta Met 12, 377.
5. Grange R A, 1966, Trans ASM 59, 26.
6. Porter L F and Dabkowski D S, 1972, "Ultrafine Grain Metals", Syracuse University Press, 113.
7. Saul G, Robertson J A and Adair A M, 1970, Met Trans 1, 383.
8. Jin S, Morris J W and Zackay V F, 1975, Met Trans 6A, 141.
9. Nakazawa K, Kawabe Y and Muneki S, 1978, Mat Sci & Eng 33, 49.
10. Durnin J and Ridal K A, 1968, JISI 206, 60.
11. Averbach B L and Cohen M, 1948, Trans AIME 176, 401.
12. Wilson E A, 1970, Unpublished research, Sheffield City Polytechnic.
13. Zackay V F et al, 1967, Trans ASM 60, 252.
14. Schanfein M J et al, 1975, "Properties of Materials for Liquified Natural Gas Tankage", ASM STP 579, 361.
15. Roberts M J, 1970, Met Trans 1, 3287.
16. Kim K J and Schwartz L H, 1978, Mat Sci and Eng 33, 5.
17. Marshall C W, Hehemann R F and Troiano A R, 1962, Trans ASM 55, 135.
18. Rack H J and Kalish D, 1971, Met Trans 2, 3011.
19. Ahlquist C N, 1975, Acta Met 23, 239.
20. Tamate O, 1968, J Fract Mech, 4, 257.

21. Squires D R, Wilson F G and Wilson E A, 1974, Met Trans 5, 2569.
22. Antolovich S D and Singh B, 1975, Met Trans 2, 2135.
23. Lai G Y et al, 1974, Met Trans 5, 1663.
24. Gerberich W W et al 1971, Met Trans 2, 3011.

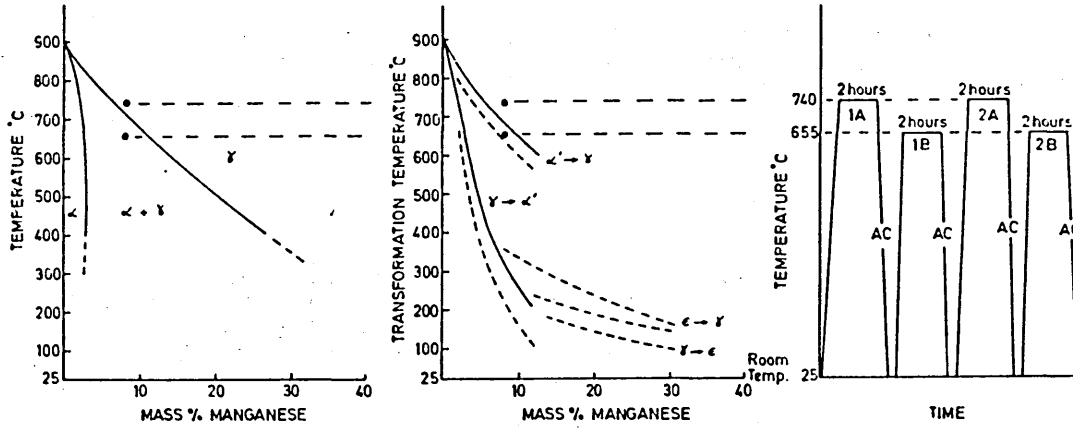


Figure 1 Schematic representation of thermal cycling treatment given to alloy

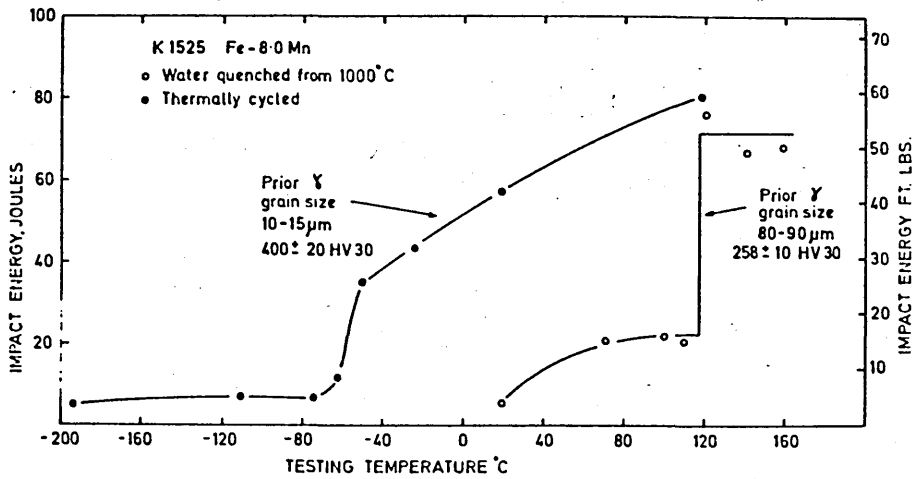


Figure 2 Effect of thermal cycling on impact toughness of alloy

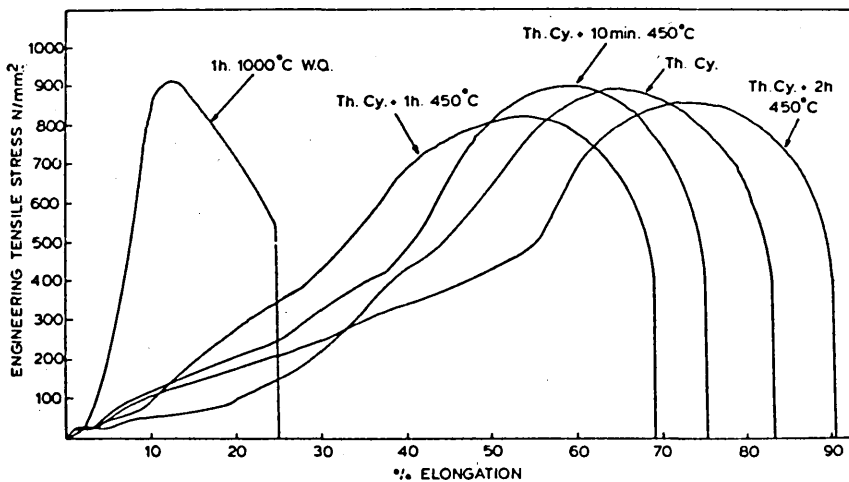


Figure 3 Stress-strain curves of alloy after various heat treatments. Tested at  $-78^{\circ}\text{C}$  and a strain rate of  $0.5 \text{ min}^{-1}$

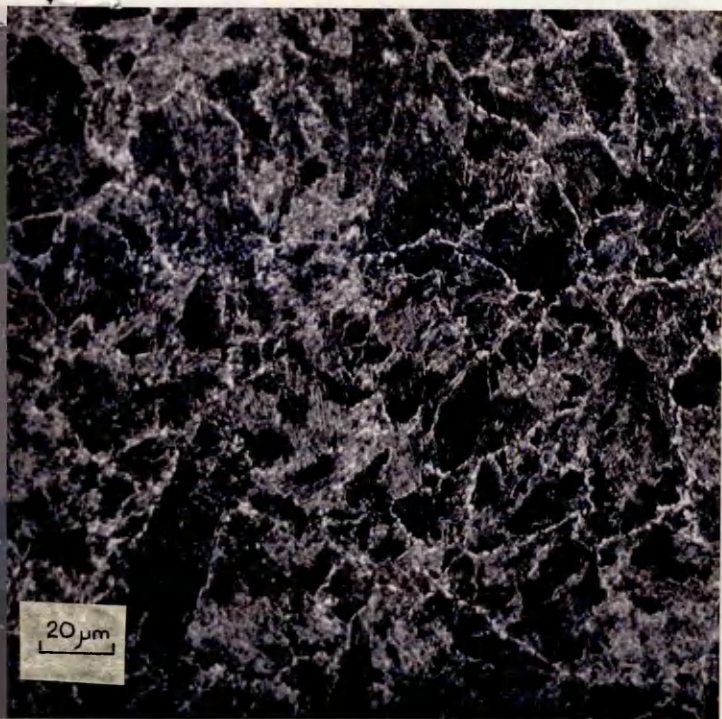


Figure 4 Optical micrograph of alloy K1525 after thermal cycling

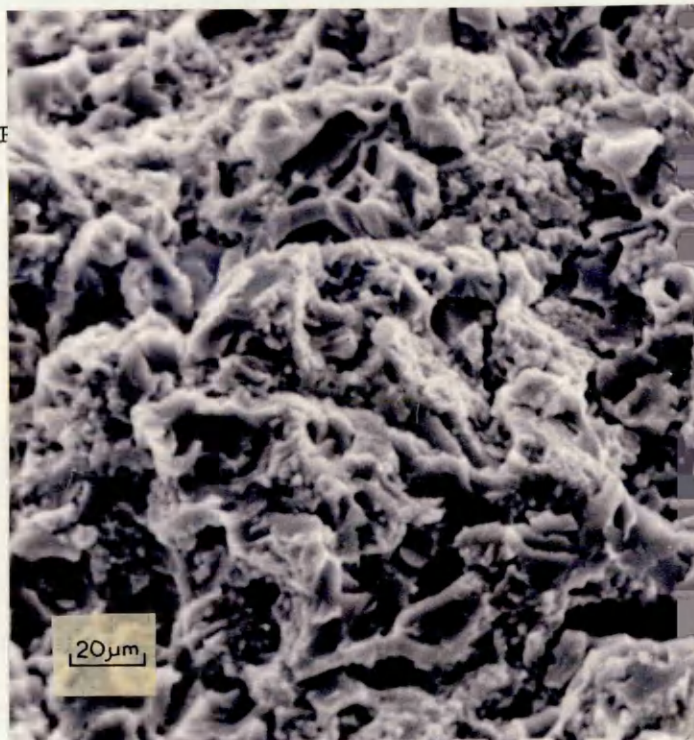


Figure 5 Scanning electron micrograph of brittle fracture of alloy K1525 after thermal cycling



Figure 6 Bright-field transmission electron micrograph of alloy K1525 after thermal cycling



Figure 7 Dark-field image of figure 6 using (200)<sub>γ</sub> austenite reflection illustrating inter-lath formation of reverted austenite